Final Report
LUMEN

Laser-based Uninterrupted Moon Energy Network

AE3200: Design Synthesis Exercise

Group 27

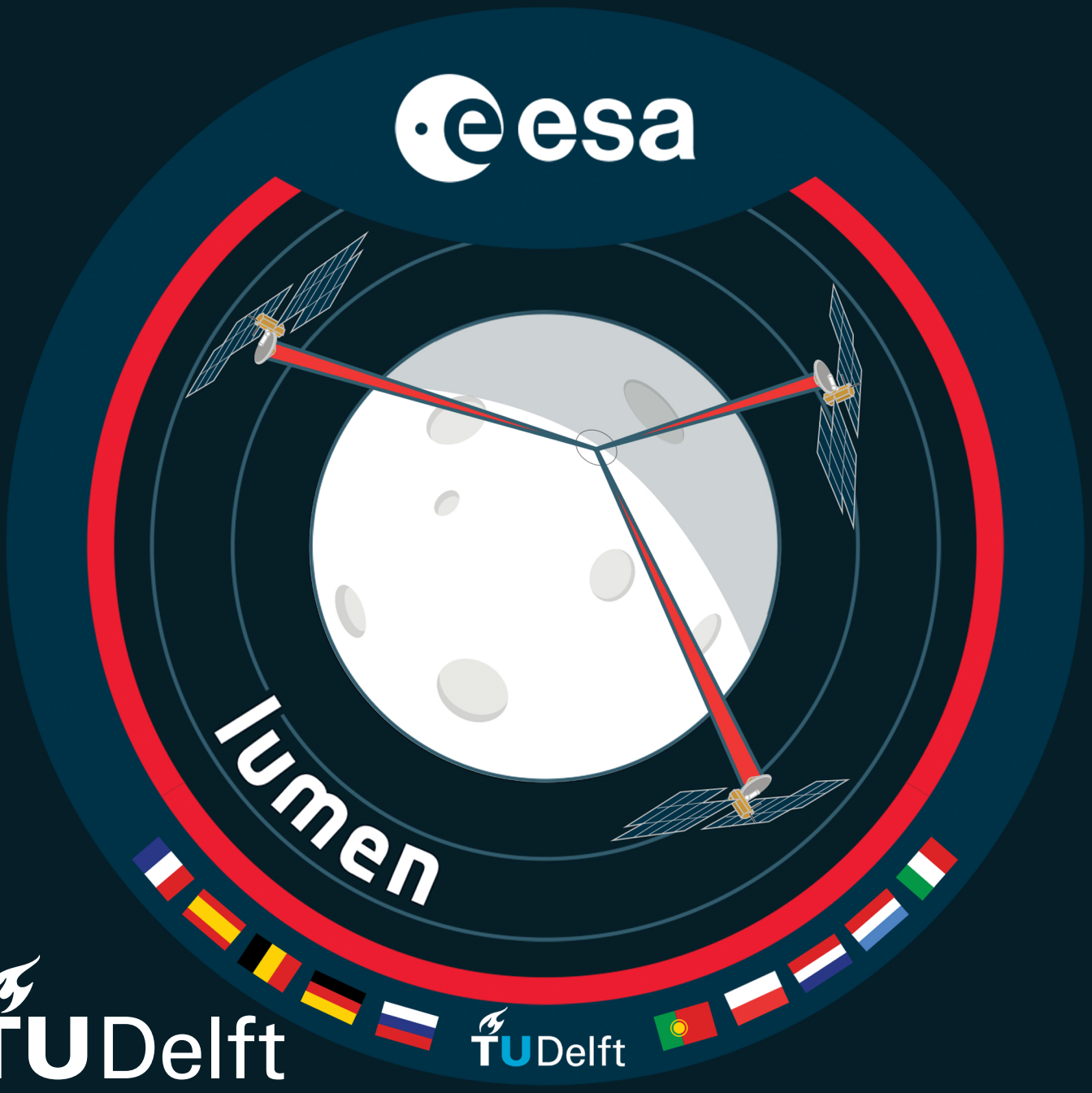

Delft University of Technology

TU Delft

TU Delft

This page intentionally left blank

Final Report
LUMEN

Laser-based Uninterrupted Moon Energy Network

by

Group 27

Name	Student Number
E. Janssen	5043085
K. Kok	5055040
J. Korycki	5218306
M. Maximchuk	5208041
E. Pauwels	4491149
A. Pulimeno	5325455
M. Scaglioni	5301300
D. Schramade	5313694
M. Simoens	5242282
T. Teixeira Pijpers	5025249

Tutor:	Dr A. Cervone
Coaches:	G. Xu, Dr. N. Yue
Project Duration:	April, 2023 - June, 2023
Institution:	Delft University of Technology
Faculty:	Faculty of Aerospace Engineering
Customer:	European Space Agency (ESA)

TU Delft

Preface

This final report is the culmination of 10 weeks of hard work developing a space-based solar power system for lunar assets. The result of this work is not only detailed in this report, but is also summarised on a poster, and will be presented during the 2023 DSE symposium at the TU Delft Faculty of Aerospace Engineering. While this report concludes the project and the collaboration for Group 27, this research lays a basis for further research in this field. We hope that indeed the conclusions and recommendations will be useful to subsequent studies.

Spring DSE 2023, Group 27
Delft, June 2023

"We are star stuff harvesting sunlight."
— Carl Sagan

Figure 1: LUMEN Mission Patch

Executive summary

Over the last decade, travelling to the Moon has re-emerged as a popular topic within the space industry. Missions like the Artemis program are planning to set foot on the lunar ground in the near future. When venturing beyond Earth, energy resources are limited, resulting in missions primarily relying on solar energy or nuclear power. However, generating solar power on the Moon requires large photovoltaic arrays to be deployed, which is very costly. Furthermore, providing power to assets located in perpetually shadowed regions of the Moon, where water is present, is even more difficult. This is where a space-based solar power (SBSP) system becomes a promising solution. Several key industry players are investigating such systems, including the European Space Agency (ESA) with their SOLARIS initiative.

Space-Based Solar Power consists of the generation of solar power in orbit and transferring it to a receiver station on the surface. The main advantage is that the orbit of the spacecraft can be fine-tuned to receive as much sunlight as possible, where it is not yet scattered by a celestial body's atmosphere. In fact, Earth's atmosphere absorbs about 70 % of the incoming sunlight[1]. It can also be used to supply power to hard-to-reach regions which have difficulty generating their own power.

In this report, a conceptual design for a Space-Based Solar Power system for power provision to the lunar South Pole has been made. This project is conducted by 10 TU Delft students and commissioned by the European Space Agency (ESA). This report is mainly focused on the spacecraft design, the mission, power collection and transmission, and the exergy when compared to conventional methods, and less on the power receiver on the Lunar surface. To thoroughly analyse the mission, various examinations were done to conclude whether Space-Based Solar Power is more efficient in various quantities, like total mass, cost and sustainability. Furthermore, an analysis must be done on the exergy of the developed system when compared to conventional, ground-based solar power generation methods.

Project Overview

The mission need statement and the project objective have been defined as:

"To provide Moon assets with a continuous and sustainable source of power."

"To design a Space-Based Solar Power System for Moon assets, intended to supply energy to items operating on the lunar surface."

In order to successfully execute the mission statement, a project plan, a baseline, a midterm and a final design are proposed to the client. When considering the initial requirements provided by ESA, it was made clear that the development must be conducted with an eye on sustainability during both the development and the mission phases, as well as potential future in-situ production of structures or propellants.

Comparable systems have yet to be fully developed, but a recent decrease in per-kilogram launch costs and an increase in the sustainability of launch systems have opened up an ideal opportunity to explore this subject.

Project Design Method

Initially, an overview of the different steps to be taken, both during the design process and during the mission, was made. This was accompanied by a division of the roles and responsibilities. Next, design option trees were set up for the different segments of the mission, which were then trimmed and used in a first round of trade-offs. Several concepts were generated with the winning options of these trade-offs. The main differences between these concepts were transmission via laser or microwave, collection using concentrated solar power cells (CPV) or conventional cells (PV), and high or low orbits, summarised in Table 1. Then a second trade-off round was performed, with the criteria being cost, Technology Readiness Level (TRL), complexity, exergy and sustainability, as can be seen in Table 2. From this trade-off, the winning concept was concept VI which uses a high elliptical

[1] URL: `https://public.wmo.int/en/sun%E2%80%99s-impact-earth` [Cited 04/05/2023]

frozen orbit with concentrated solar power and lasers to transmit the power.

Table 1: Generated feasible concepts

Concept	Transmission	Collection	Orbit
I	Microwave	PV	Frozen low lunar orbit
II	Laser	PV	Frozen low lunar orbit
III	Laser	PV	Frozen elliptical lunar orbit
IV	Microwave	CPV	Frozen low lunar orbit
V	Laser	CPV	Frozen low lunar orbit
VI	Laser	CPV	Frozen elliptical lunar orbit

Table 2: Concept trade-off summary table.

Criterion → Concept ↓	Cost	TRL	Complexity	Exergy	sustain-ability	Total
Weight	20 %	14 %	18 %	37 %	11 %	100 %
Concept I	1	4	4	2	2	2.44
Concept II	2	3	3	2	2	2.32
Concept III	3	3	3	3	3	3.00
Concept IV	1	3	3	2	2	2.12
Concept V	2	3	2	3	3	2.62
Concept VI	3	2	2	2	4	3.16

Concept VI then received its first budget estimations and general subsystem design. A list of system and subsystem requirements was also drafted. In this report, a detailed design has been performed on the different subsystems and a method for integration and iteration has been set up. Different analyses of the market, cost, sustainability, scalability and exergy were then also performed.

Astrodynamics

Astrodynamics plays a vital role in shaping the LUMEN's mission, as its characteristics permeate throughout the design of almost all subsystems. the LUMEN mission will consist of 133 satellites in a frozen elliptical orbit around the Moon. The nominal orbital period is 21.03 h of which the nominal power transmission time of one satellite is 15.82 h, resulting in a transmission percentage of 75.23 %.

The maiden launch, the first of four, will take place on the first of June 2030 from Kennedy Space Center. On the first lap, the Starship launcher will get into an Earth parking orbit where it will perform its pioneering in-orbit refuelling. Once refuelled the Starship will take the first LUMEN batch to a lunar parking orbit with a ΔV-efficient Hohmann transfer. Once in the lunar parking orbit, the Starship will release its payload and the spacecraft will perform their respective insertion manoeuvres. In Figure 2 and Table 3 an overview of the transfer stages can be found.

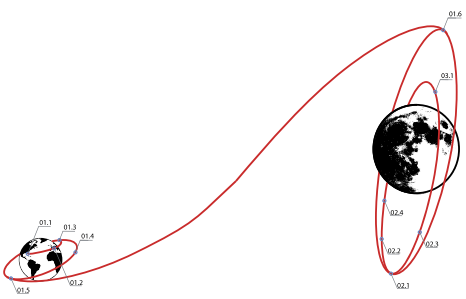

Figure 2: Mission profile

Table 3: Mission profile.

ID	Phase
01.1	Launch
01.2	Booster separation
01.3	Parking orbit insertion
01.4	In-orbit refuelling
01.5	Trans lunar parking orbit injection
01.6	Starship payload separation
02.1	Spacecraft train distancing manoeuvres
02.2	Spacecraft operational orbit injection
02.3	Spacecraft solar panel unfolding
02.4	Initial pointing manoeuvres
03.1	Spacecraft operational mission phase

Subsystem Design

The subsystems and segments that were given a detailed design in this report are Power Transmission, Power Collection, Attitude and Orbit Control, Propulsion, Guidance, Navigation and Control, Thermal Control, Electrical Power, Command and Data Handling, and Communication. While most aspects of the mission were not ground-breaking, its power transmission requirement of 1 MW continuously over 25 years proved a major influence in the design of various subsystems. In the end, a high elliptical frozen polar orbit was chosen, which has a transmission time of 15.82 hours per orbit and an average transmission altitude of $11\,795.73$ km.

A type of concentrating solar panels designed by O'Neill et al. [1] were used to generate the large amounts of power needed, mounted on a mechanism used on the similarly concentrated SCARLET mission [2]. A laser unit consisting of multiple off-the-shelf laser modules and an optic collimation system was designed to continuously and precisely transmit the power down to a receiver on the South Pole. A fine pointing system was designed following Cierny [3], and an orbit determination system, as used on the Jason-1 mission [4], to provide the location and pointing knowledge accuracy required. In order to deal with the heat generated by the different components, a deployable radiator was set up. After the design layout was created, extensive verification was performed to ensure that no calculation mistakes were made and that the values received were representative of reality. Validation methods were then presented for each subsystem, which could be used to prove that the performance is as required. These detailed designs were then used in multiple iterations and alterations to set up an accurate breakdown of mass and power.

Market and Cost Analyses

With these detailed designs, a more in-depth analysis could be performed on the market and cost. For the market, a distinction was made between the Moon and Earth. For the Moon case, no existing energy infrastructure is present, and since certain entities are looking to set up a base on the Moon, the LUMEN system could be an attractive solution to them. The Earth however already has a robust infrastructure in place. As such, serious improvements will have to be made to make the system economically viable outside of niche cases. The power output must be increased by a factor of 1000, with a cost increase by less than a factor of 10.

Sustainability, Scalability and Exergy

Since sustainability was an important aspect to LUMEN's customers, quite a few considerations have been made during the design. In the trade-offs, it was stated as a criterion so that no unsustainable option would be a winner. It was also taken into account when choosing components and a plan to guarantee sustainability during the production phase was constructed. For instance, the propellant was chosen to be LMP-103S, which is a green monopropellant with significantly less toxicity when compared to hydrazine for example.

Scalability and exergy were two considerations which the customer asked for. It was found that the break-even for energy production will occur between years 18 and 19 of the mission lifetime. Scalability for the system both in increasing the power output on the Moon and in placing the same system around the Earth was evaluated. Alongside this, an exergy comparison to regular solar panels on the lunar surface was made. It was found that for Earth applications, specifically the same 133 spacecraft as used for the Moon, the overall BoL efficiency would be $4.22\,\%$. Compared to the BoL efficiency of $5.04\,\%$ for the lunar system, this is slightly lower due to atmospheric extinction and can heavily be worsened depending on weather conditions.

Final Design

With this detailed design and its related analyses, the final design for this phase is presented in Figure 3. Each spacecraft will collect 116 kW, with its 4x concentrated solar arrays of $264.5\,\text{m}^2$, and transmit the power down using 94 lasers. This corresponds to half of the total lasers, the other half is used when the first half's efficiency has degraded after 12.5 yr. Thus, a total of 188 laser modules will be on-board. Overall the efficiency from solar panels on the spacecraft to the receiver on the ground

at the beginning of life is 5.04 % and 3.03 % at the end of life. Considering this, each spacecraft will have a wet mass of 1096.2 kg.

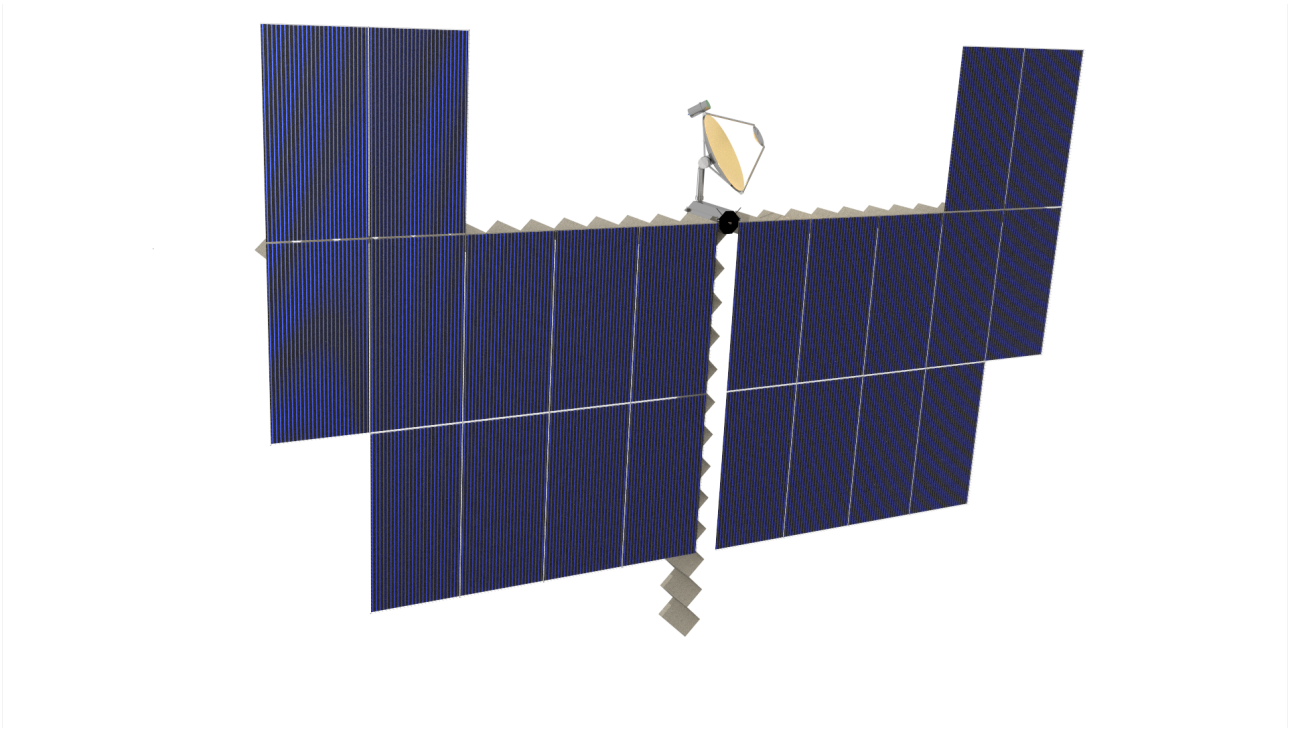

Figure 3: LUMEN final spacecraft design

Contents

Nomenclature

Abbreviations

Abbreviation	Definition
AHP	Analytic Hierarchy Process
AIT	Assembly, Integration and Testing
AOCS	Attitude and Orbit Control System
APC	Automatic Power Control
BOL	Begin Of Life
BC	Boundary Condition
BDF	Beam Dilution Factor
CAD	Computer-Aided Design
CCSDS	Consultative Committee for Space Data Systems
CMDH	Command and Data handling
CNES	Centre National d'Études Spatiales
CPM	Coarse Pointing Mechanism
CPU	Central Processing Unit
CPV	Concentrated Photovoltaics
DC	Direct Current
DoD	Depth-of-Discharge
DOT	Design Option Tree
DSA	Deep Space Antenna
DSE	Design synthesis Exercise
DSN	Deep Space Network
ECSS	European Cooperation for Space Standardisation
EM	Electromagnetic
EPS	Electrical Power System
ETCS	External Thermal Control System
EOL	End Of Life
ESA	European Space Agency
FSM	Fine Steering Mirror
FY	Fiscal year
GMAT	General Mission Analysis Tool
GNC	Guidance, Navigation and Control
HEO	High Earth Orbit
HR	Human Resources
IC	Integrated Circuit
IPC	Instructions Per Cycle
ISS	International Space Station
ISS	Image Stabilisation System
iROSA	ISS Roll Out Solar Array
ISRO	Indian Space Research Organisation
JAXA	Japan Aerospace Exploration Agency
JWST	James Webb Space Telescope
KSC	Kennedy Space Center
LEOP	Low Earth Orbit Procedures
LOI	Lunar Orbit Injection
LOS	Line Of Sight
LPC	Laser Power Converter
LRO	Lunar Reconnaissance Orbiter
LT	Lunar Transfer
LUMEN	Laser-based Uninterrupted Moon Energy Network

Abbreviation	Definition
MLI	Multi Layered Insulation
MTCS	Mounted Thermal Control System
NASA	National Aeronautics and Space Administration
OBC	Onboard Computer
OBDH	Onboard Data Handling
PDH	Payload Data Handling
PCB	Printed Circuit Board
PV	Photovoltaic
RAAN	Right ascension of ascending node
RAM	Random Access Memory
RF	Radio-Frequency
RFDN	Radio Frequency Distribution Network
RMS	Root-mean-square
RTG	Radioisotopic Thermoelectric Generator
RTU	Remote Terminal Unit
SBSP	Space-Based Solar Power
S/C	Spacecraft
SNR	Signal-to-Noise Ratio
SP	Solar Power
SSPTA	Simplified Space Payload Thermal Analyzer
TBC	To Be Confirmed
TBD	To Be Determined
TCS	Thermal Control System
TOI	Transfer Orbit Insertion
TPM	Technical Performance Measurement
TRASYS	Thermal Radiation Analyzer System
TRL	Technology Readiness Levels
TT&C	Telemetry, Tracking and Command
TWTA	Travelling Wave Tube Amplifier
UNAM	National Autonomous University of Mexico
SMA	Semi-Major Axis
SWOT	Strengths, Weaknesses, Opportunities, and Treads

List of Constants

Symbol	Definition	Value
c	Speed of light	$299\,792\,458\,\mathrm{m\,s^{-1}}$
e	Euler's number	2.7183
g_0	Gravitational acceleration	$9.81\,\mathrm{m\,s^{-2}}$
G	Gravitational constant	$6.67 \times 10^{-11}\,\mathrm{N\,m^2\,kg^{-2}}$
k_b	Boltzmann constant	$1.38 \times 10^{-23}\,\mathrm{J\,K^{-1}}$
$\mathcal{R}$	Universal gas constant	$8.314\,\mathrm{J\,mol^{-1}\,K^{-1}}$
μ_{moon}	Standard gravitational parameter of the Moon	$4.905 \times 10^3\,\mathrm{km\,s^{-1}}$
σ	Stefan-Boltzmann constant	$5.670 \times 10^{-8}\,\mathrm{Wm^{-2}K^{-4}}$

List of Symbols

Symbol	Definition	Unit
a	Semi-major axis	[m]

Symbol	Definition	Unit
A	Area	[m^2]
cm	Cntre of Mass	[m]
cp	Centre of Pressure	[m]
c^*	Characteristic velocity	[m s^{-1}]
C_T	Thrust coefficient	[-]
D	Antenna diameter	[m]
$D_{receiver}$	Receiver diameter	[m]
e	Eccentricity	[-]
e	Euler's number	[-]
E	Eccentric anomaly	[rad]
E_x	Exergy	[W]
f_{bd}	Beam dilution factor (BDF)	[-]
$FSPL$	Free Space Path Loss	[dB]
g_0	Gravitational acceleration	[m s^{-2}]
G	Antenna gain	[dB]
h	Angular Momentum	[N m s]
h_t	Transmission altitude	[m]
h_{peri}	Periapsis altitude	[m]
h_{apo}	Apoapsis altitude	[m]
i	Inclination	[rad]
I_{sp}	Specific impulse	[s]
L_n	Nozzle length	[m]
L_l	Transmitter loss	[-]
L_r	Receiver loss	[-]
L_{pr}	Pointing accuracy loss	[-]
L_a	Atmospheric attenuation	[-]
L_s	Free space loss	[-]
$\dot{m}$	Mass flow rate	[kg s^{-1}]
M	Mass	[kg]
M	Beam quality factor	[-]
M	Mean anomaly	[rad]
M	Mach number	[-]
M_W	Molecular mass	[g mol^{-1}]
p	Pressure	[Pa]
r_e	Radius earth	[m]
r_m	Radius moon	[m]
r	Orbital radius	[m]
$\mathcal{R}$	Universal gas constant	[J mol^{-1} K^{-1}]
R	Specific gas constant	[J kg^{-1} K^{-1}]
R	Data rate	[bits/s]
R_M	Radius of the Moon	[km]
R_t	Throat radius	[m]
t	Time	[s]
t_M	Moon eclipse time	[s]
T	Orbital period	[s]
T	Temperature	[K]
T_c	Chamber temperature	[K]
T_d	Disturbance Torque	[N m]
T_s	System noise temperature	[K]
$VF_\perp$	View factor perpendicular suface	[-]
$VF_\parallel$	View factor parallel suface	[-]
v_e	Exhaust velocity	[m s^{-1}]

Symbol	Definition	Unit
v_M	Maximum shadow cone exit velocity	[m s^{-1}]
V	Velocity	[m s^{-1}]
V	Volume	[m^3]
w	Gaussian beam width (radius)	[m]
w_0	Gaussian beam waist (radius)	[m]
z	Beam propagation distance	[m]
α	Absorptivity	[-]
γ	Specific heat ratio	[-]
Γ	Vandenkerckhove function	[-]
ϵ	Expansion ratio	[-]
ε	Emissivity	[-]
ξ	Cartesian component	[m]
η	Cartesian component	[m]
η_{BAT}	Battery discharge efficiency	[-]
η_i	Incidence efficiency	[-]
η_n	Lenght ratio	[-]
η_t	Transmission percentage	[-]
λ	Wavelength	[m]
μ	Gravitational parameter	[m^3 s^{-2}]
ω	Argument of periapsis	[rad]
ω_p	Nodal precession rate	[rad s^{-1}]
Ω	Right ascension of the ascending node	[rad]
ϕ	Angle of Incidence	[rad]
Φ	Solar Irradiance	[W m^{-2}]
ρ	Density	[kg m^{-3}]
θ	True anomaly	[rad]
θ_{beam}	Gaussian beam divergence half-angle	[rad]
θ_e, θ_n	Parabola angle	[rad]
θ_p	Transmitter pointing accuracy	[rad]
θ_{pk}	Transmitter pointing knowledge	[rad]
τ		[-]
ζ	Exergy conversion factor	[-]
ζ	Solar Zenith angle	Deg
ζ_d	Discharge correction factor	[-]

1. Introduction

The idea of Space-Based Solar Power (SBSP) stems from as early as 1923 when Konstantin Tsiolkovsky conceptualised the idea to concentrate sunlight to the Earth[2]. Ever since then, many other scientists and organisations, such as NASA and ESA have researched the idea of collecting sunlight in space and transmitting it to Earth. However, one common problem that was identified each time was the launch cost; such a system will require several launches, and the cost of launching a spacecraft to space was too large to make it competitive with Earth-based power generation methods.
With a recent decrease in launch costs, the idea of space-based solar power has become more attractive. For instance, the European Space Agency is working on project SOLARIS, aiming to develop an SBSP system for Earth applications. Additionally, the ESA has commissioned Design Synthesis Exercise (DSE) Group 27 to design a Space-Based Solar Power system for assets on the lunar South Pole, over a span of ten weeks by ten final-year BSc Aerospace Engineering students at Delft University of Technology.

The objective of the mission, dubbed LUMEN: Laser-based Uninterrupted Moon Energy Network, is to provide 1 MW of power to the lunar South Pole over a mission lifetime of 25 years. The mission is to be designed with an eye on sustainability, considering the energy required to produce the system and comparing it to the energy generated. Furthermore, toxic substances and nuclear power were avoided.

Over these ten weeks, several reports were written. The first, which was the project plan, considered the planning of the work for the remaining nine weeks. After this, a baseline report was made, highlighting the conceptual design phase and the literature study. Next, a midterm report was produced, where the system's preliminary design was performed. Now, the design is at the final stage where the detailed design will be performed in this report.

The outline of the report is as follows. An overview of the project is provided in Chapter 2. After this, an overview of the design is given in Chapter 3. Then, Chapter 4 considers the design of the payload, i.e. the receiver on the lunar surface, the power collection system, and the power transmission system. After this, the astrodynamics will be considered in Chapter 5, which considers the trajectory, orbit, and end-of-life procedures. With the orbit and payload designed, it is possible to perform the detailed subsystem design of the spacecraft bus, which will be done in Chapter 6. After the design chapter, some other aspects will be considered. This includes a cost & market analysis in Chapter 7, a system analysis (exergy & scalability) in Chapter 8, a Reliability, Availability, Maintainability & Safety analysis in Chapter 9, the requirement compliance in Chapter 10, some considerations about future developments in Chapter 11, and lastly the conclusion and recommendations in Chapter 12.

[2]URL: https://www.esa.int/Enabling_Support/Space_Engineering_Technology/SOLARIS/SBSP_history#:~:text=The%20underlying%20concept%20of%20Space,of%20sunlight%20down%20to%20Earth. [Cited 25/06/2023]

2. Project overview

This report is the culmination of the work of 10 students for the spring Design Synthesis Exercise of the Aerospace Engineering bachelor's program at the Technical University of Delft. The LUMEN mission design process started with the definition of the project plan, defining the timeline of the design process, together with its major milestones [5]. The mission need statement and the project objective have been defined as:

"To provide Moon assets with a continuous and sustainable source of power."

"To design a Space-Based Solar Power System for Moon assets, intended to supply energy to items operating on the lunar surface."

Moreover, an extensive literature study was started in this phase and carried on in the second phase of the design process, leading to the baseline report [6]. A comprehensive set of requirements was presented at this stage, both on system and subsystem levels. The major deliverable of this phase was the Design Option Tree (DOT), which allowed the team to identify all possible combinations of segments (Space, Transmission, Collection, Ground, Orbit, Trajectory, and Launch Vehicle) leading to different concepts. Next, the DOT was trimmed to eliminate the unfeasible. All the identified feasible options were the inputs for the third phase of the design process, namely the midterm phase [7].

2.1. Midterm Trade-off Summary

During the midterm phase, a high-level trade-off was performed at a segment level to identify the best scoring options. These options were combined and led to the following concepts:

Table 2.1: Generated feasible concepts

Concept	Transmission	Collection	Orbit
I	Microwave	PV	Frozen low lunar orbit
II	Laser	PV	Frozen low lunar orbit
III	Laser	PV	Frozen elliptical lunar orbit
IV	Microwave	CPV	Frozen low lunar orbit
V	Laser	CPV	Frozen low lunar orbit
VI	Laser	CPV	Frozen elliptical lunar orbit

Five major trade-off criteria were established and weighted using the Analytic Hierarchy Process (AHP) to ensure unbiased evaluation. The criteria are as follows [7]:

- **Cost** (Weight=0.2): Development cost, launch cost, and production cost based on the number of spacecraft are considered. Microwave transmission concepts are less mass effective than laser transmission due to the larger size of required antennas. Production cost is influenced by the type and altitude of the selected orbit.
- **TRL** (Technology Readiness Level) (Weight=0.14): The criterion ensures the use of technologies that have been demonstrated. Low lunar orbit has been demonstrated, while PV (Photovoltaic) technology is widely used and has off-the-shelf products available. CPV (Concentrated Photovoltaic) requires customized development and qualification. Neither microwave nor laser transmission has been used in space for energy transmission purposes.
- **Complexity** (Weight=0.18): High-complexity systems have numerous independent subsystems, require extensive supporting architecture, and have stringent system requirements. CPV concepts are more complex than conventional PVs due to extra lens deployment. Laser transmission is more complex than microwave transmission due to cooling requirements and accurate pointing. Elliptical orbits are more complex than low lunar orbits due to higher altitudes and greater pointing accuracy requirements.
- **Exergy** (Weight=0.37): The energy required to develop, deploy, and operate the system is investigated, along with the useful energy (exergy) it can provide. CPVs require less energy for production than conventional PVs. CPVs also degrade at a slower rate, leading to better end-of-life efficiency. The number of launches and propellant requirements for transfer and orbit

insertion influences exergy. Laser power transmission has lower efficiency at short distances compared to microwaves, but the energy required for the laser transmitters and their thermal control system is higher.

- **Sustainability** (Weight=0.11): Sustainability is a key aspect of the mission. Low lunar orbits require more propellant and emit more CO2-equivalent atmospheric emissions. Low lunar orbits also require more ΔV for a sustainable end-of-life strategy. Elliptical orbits require less propellant and have options for ejection or graveyard orbits until recycling becomes possible. PVs are less sustainable than CPVs due to the need for more semiconductor materials, while materials for concentrator lenses are widely available.

Scores for the different criteria were assigned to each of the six concepts proposed in Table 2.1; scores were based on preliminary budget estimations and overall differences and similarities between the concepts, for which detailed justification can be found in [7]. The results of the trade-off are summarised in the following table:

Table 2.2: Concept trade-off summary table.

Criterion $\rightarrow$ Concept $\downarrow$	**Cost**	**TRL**	**Complexity**	**Exergy**	**SUS**	**Total**
Weight	20 %	14 %	18 %	37 %	11 %	100 %
Concept I	1	4	4	2	2	2.44
Concept II	2	3	3	2	2	2.32
Concept III	3	3	3	3	3	3.00
Concept IV	1	3	3	2	2	2.12
Concept V	2	3	2	3	3	2.62
Concept VI	3	2	2	4	4	3.16

From Table 2.2, Concept VI arose as the winner, which was confirmed using a sensitivity analysis. Moving toward the last phases of the design process, the preliminary design of the different subsystems was presented. The detailed design of those is carried out in this report.

2.2. Stakeholders & Requirements

Now that an overview of the project has been discussed, it is useful to consider the stakeholders and requirements. In Section 2.2.1, the stakeholders of the mission will be discussed. Subsequently, the requirements will be discussed in Section 2.2.2.

2.2.1. Stakeholders

Like any project or mission, one or several organisations will have a certain level of interest. Examples of the stakes can be in the form of revenue, public image, information, influence & power, and social & environmental impact. By analysing the stakeholders, the mission requirements can be set up. In the baseline report [6], the stakeholders were analysed.

The main stakeholder is the European Space Agency, as they are the customer for this study. Their needs have been taken into account during weekly meetings with the team. The TU Delft is also a stakeholder as they provide guidance and support during this Phase A study. For the mission itself, assets on the moon will use the power, hence the moon asset owners are also potential stakeholders.

The stakeholders are not limited to entities directly involved with the project. For instance, energy buyers can be interested in the scalability of the system and its potential applications to Earth, providing cheap and sustainable energy. Scientists may also be interested in the mission, as the potential spill-over of technologies can improve certain future missions.

As can be seen, there are many stakeholders. However, not all of them have the same interest and influence. An overview of this can be seen in Figure 2.1, the influence-interest matrix, which highlights the level of interest and influence of different stakeholders.

As can be seen, ESA, TU Delft, investors, and Moon asset owners have the highest interest and influence in the system. The launch provider and government agencies may not be as interested but still have influence in cost, number of launches, regulations, etc. Energy buyers would be interested

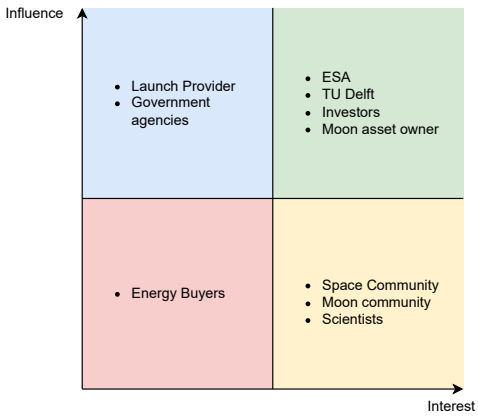

Figure 2.1: Stakeholder influence-interest matrix

in the system for Earth applications, so their interest is moderate and their influence is low.

2.2.2. Requirements

With the stakeholders discussed, it is important to set up the mission requirements. These have been divided into general mission requirements and subsystem requirements. At this stage, all requirements have been finalised and there are no ”TBC” (To Be Confirmed) values remaining. Furthermore, some requirements have been struck out as they are either not possible to validate or are not necessary anymore. They are as follows:

- **LMN.SYS.012** - *The LUMEN system S/C bus propulsion and AOCS subsystems shall be able to provide a ΔV/yr of at least 4.02 m/s [TBC] during mission operations*.
  As no station keeping will be done anymore (see Chapter 5), this requirement is removed.
- **LMN.SUS.005** - *The Earth ground segment shall use on average no more than 10 kW throughout the mission duration.*
  This requirement is removed as several missions use a single ground station, so it is difficult to verify compliance with this requirement.
- **LMN.SUS.006** - *The energy used for the production of the LUMEN system shall be at least 50% renewable energy*.
  Like LMN.SUS.005, this requirement is difficult to trace and verify, as many of the components will be manufactured by companies all around the world. Furthermore, the worldwide renewable energy share is $28.7\,\%$[3], meaning that this would be difficult to attain.
- **LMN.SUS.007** - *The production of all LUMEN systems shall not generate more than 50% of its launch mass in landfill waste*.
  Same reasons as for LMN.SUS.006.
- **LMN.SUS.008** - *The production of all LUMEN systems shall not generate more than 15% of its launch mass in CO2-equivalent atmospheric emissions.*
  Same reasons as for LMN.SUS.006.
- **LMN.PRP.004** - *The propulsion subsystem shall be able to produce at least 200 ± 20 N [TBC] of thrust for the Lunar insertion burn.*
  Since the injection burn will be performed by the launch provider, this requirement is not applicable anymore.
- **LMN.GNC.001** - *The GN&C subsystem shall control and monitor the propulsion subsystem.*
  This will now be done by the CD&H subsystem.
- **LMN.AOC.002** - *The AOCS shall provide a pointing precision of 0.00014° [TBC].*
  Only pointing accuracy will be considered, not pointing precision.
- **LMN.AOC.007** - *The space segment shall have a manoeuvring rate of at least 0.8214°/day.*.

[3] URL: `https://www.iea.org/reports/renewable-electricity` [Cited 21/06/2023]

There was already a requirement for slew rate, rendering this requirement redundant.

- **LMN.PHY.001** - *The space segment shall be modular if several launches for one satellite are required.*
  More than one spacecraft will be used.
- **LMN.LUG.001** - *The LUMEN mission's lunar receiver segment shall be deployed without the use of physical human labour.*
  The customer has confirmed that it can be assumed that the receiver can be deployed with the help of physical human labour.
- **LMN.TRA.001** - *The power transmitter shall have a peak beam intensity of at most 10 W/cm² on the lunar surface.*
  This is not possible to measure.

2.3. Risks

Comprehensive and continuous risk assessment provides an overview of where things can go wrong in the design process and where pitfalls lie. By composing it beforehand, and keeping it up to date, risks can be kept in mind and, in some cases, be mitigated. In previous reports [5–7] the risks were divided into three stages: development, production and testing. Each risk was assigned a likelihood ranging from least likely, A, to most likely, D. An impact value was also assigned, where 1 was the minimal impact and 5 was a very high impact. After this assessment, mitigation strategies and post-mitigation likelihoods and impacts were presented.

While most risks remain unaltered since the midterm report [7], RSK1.05, 'Lack of experience or knowledge of the design team, leading to inadequate design.' had its likelihood increased from C to D, as moving into the detailed portion of the project would undoubtedly lead to more gaps in specific knowledge. Furthermore, three new risks were added. In the development phase, RSK1.14 'Unavailability of relevant documents, - insufficient or inaccurate values used" was added, since trade secrets and a general lack of documents might make it more difficult to find specific values for the detailed design. It was given an initial score of D-4, and could be mitigated by contacting relevant experts or the authors of the documents in question. In the production phase, RSK2.08 'Unavailability of selected components, - design cannot be manufactured' was added. This bears similarities to RSK2.04 'Certain materials cannot be sourced due to geopolitical circumstances, - design cannot be manufactured.' but is more specific to the components selected, as a larger focus on off-the-shelf components was placed during the detailed design. This risk was assigned a score of C-3, with the mitigation method only considering components currently in production. Finally, RSK3.07 'No sufficient testing method available, - some requirements might not be verified' was added to the testing phase, which refers to testing being difficult for some technologies, like the accurate laser pointing system being difficult to validate on Earth. A score of B-3 was thus given, and mitigation could include keeping potential testing methods in mind while selecting certain technologies or concepts. The revised risk map and its mitigated counterpart are presented in Figure 2.2, where the black-coloured risks originate from the baseline report. The risks marked in blue are those that were altered or added in the midterm report and the purple risks were added in this final report.

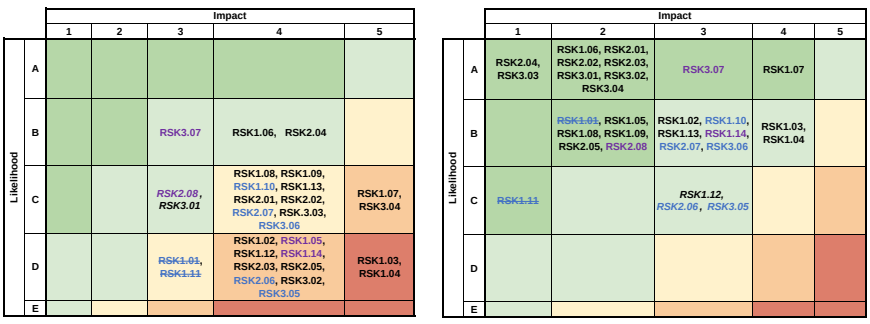

(a) Risk Map **(b)** Mitigated Risk Map

Figure 2.2: Original and Mitigated Risk Map.

3. Design overview

This chapter aims to give the reader a general overview of the LUMEN mission. In particular, the missions' functional analysis is carried out in Section 3.1; the determination of the number of spacecraft within the LUMEN constellation is addressed in Section 3.2 showing the various iterations performed throughout the past 10 weeks; lastly, Section 3.3 dives into the sustainable development approach during each phase of the mission.

3.1. Functional analysis

In order to effectively accomplish the mission objective, it is of utmost importance to establish a systematic breakdown of the required steps. This breakdown was carried out using a waterfall approach, which involves dividing the mission into distinct phases and subsequently breaking down these phases into various functions and sub-functions. The mission at hand has been divided into ten distinct phases, each serving a specific purpose and contributing to the overall success of the mission. These phases are shown in Figure 3.1 and include: "Develop Mission," "Perform 'Assembly, Integration and Testing' (AIT)," "Launch Mission," "Conduct Low Earth Orbit Procedures (LEOP)," "Perform Transfer," "Perform Lunar Parking Orbit Injection," "Perform System Startup," "Perform Transfer into Operational Orbit," "Conduct Operational Phase," and "End-of-Life." Each of these phases encompasses a range of sub-functions, which encompass both nominal operational functions and contingency modes.

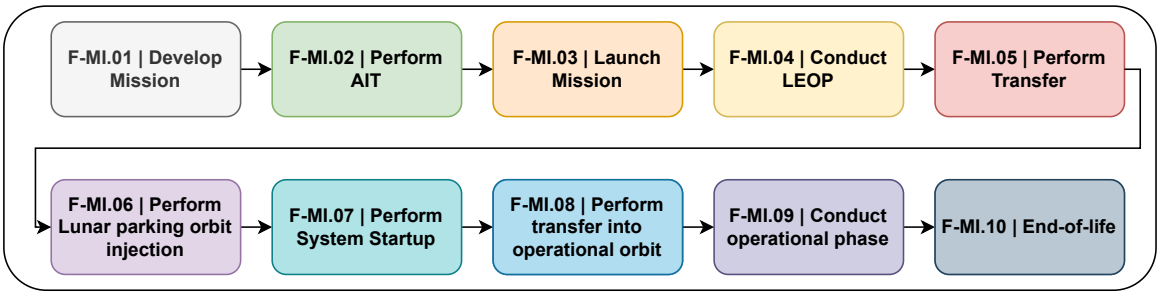

Figure 3.1: High-level mission phases overview

For a more detailed understanding of the flow and the functional breakdown of the mission, an extensive overview is provided in Appendix A and Appendix B respectively. These figures can be referred to in the appendix for a visual representation of the mission's functional breakdown and flow.

3.2. Spacecraft quantification

For the midterm, an initial program was set up that takes as input the overall system efficiency (collection, transmission, receival etc.) and view times of satellites, then outputting a system mass, based on specific powers of subsysytem components ($\mathrm{W\,kg^{-1}}$). The exact intrinsics of the program can be found in Janssen et al. [7]. This mass could be divided among any number of satellites, however, with different implications. Within the midterm, a novel cost estimation method is illustrated, which given a system mass, illustrates the optimal number of spacecraft for cost [7]. This program balanced out the costs between launches, Assembly, Integration & Testing (AIT), production and development costs. Preceeding this report, the optimal number of spacecraft was 80 spacecraft with a dry mass of $608\,\mathrm{kg}$.

However, as of the final detailed design phase, this value does not suffice. The spacecraft dry mass grew extensively from $608\,\mathrm{kg}$ to $1005\,\mathrm{kg}$ to nearly $1400\,\mathrm{kg}$, before dropping again. Though the reasons for this growth are multi-faceted, the main driver is the ever more comprehensive inclusion and scrutinous analysis of efficiencies and degradation involved in the system. This is especially important from an exergetic perspective. A summary is presented in Table 3.1 of the iterations executed with different combinations of spacecraft masses and the number of spacecraft. It is to be noted that for the last two iterations, additional satellites are added in parenthesis, as these are S/C added for reliability purposes. This is explained in more detail in Chapter 9.

As visible in Table 3.1, a growth in the number of spacecraft occurred to counteract the evolution of dry

Table 3.1: Summary of some sample iterations illustrated. Note: Alpha 9.0 is the final design.

	Alpha 3.0	Alpha 5.0	Alpha 6.0	Alpha 6.1	Alpha 7.0	Alpha 7.1	Alpha 8.0	Alpha 9.0
Number of S/C [-]	86	80	80	80	160	160	130+27	110+23
S/C Dry Mass [kg]	700	608.00	1035.60	1434.04	1095.83	652.15	948.76	888.92
Total Dry Mass [kg]	60,200	48,620	82,848	114,723	175,332	104,344	148,955	118,226

mass and preserve subsystem performance. The key subsystems in this regard are: Payload - which includes the large solar arrays, Structures - which need to sustain the additional growth of mass, Propulsion - which needs to quantify the propellant and propellant tank size for the large masses, AOCS - which needs to manoeuvre the large and heavy spacecraft with certain agility. During the design phase, therefore, the number of spacecraft reached 160, where the dry mass was ≈ 750 kg. In Figure 3.2a, the final relation between the number of spacecraft and the dry mass is illustrated. Nevertheless, more spacecraft gives higher costs, therefore the cost estimation program used in the midterm was integrated. As mentioned before, the cost estimation tool also indicates for the given system mass the ideal number of spacecraft to minimise cost. In order to identify the optimal number of spacecraft for the mission, these cost-optimal numbers of satellites are plotted against the design number of spacecraft, see Figure 3.2b. This graph is analogous to a graph of total cost against system mass, however, to include the subsystem performance limitations, it is more indicative to have the design number of spacecraft along the x-axis.

The vertical lines within the figure represent the limits imposed by the various subsystems. The most stringent is the propulsion that sets a desired dry mass below 960 kg, which translates to more than 129 spacecraft (right-most line). This limit avoids negative snowballing effects of increasing the mass of the propulsion system mass and then also the wet mass of the spacecraft. Moreover, the propellant tank is the key driver of the spacecraft bus volume, hence affecting spacecraft packing, addressed in Section 6.9. The second vertical line from the right stems from AOCS, which necessitates a dry mass of less than 1000 kg to preserve the performance, which is equivalent to more than 123 satellites. This limit is set because, with increased spacecraft size, the mass moment of inertia worsens quadratically as the mass is more distributed from the neutral axis. Therefore, to maintain the agility and slew capability of the spacecraft, the limit of 1000 kg is set. Finally, Structures dictate less than 300 kg of photovoltaic arrays. Through the calculations, this equates to a need for more than 66 Spacecraft. The ideal line corresponds to the $x = y$ line, as this translates to the design number of spacecraft being the same as the cost-optimal number of spacecraft. This is represented in the orange line in Figure 3.2b. Therefore, the final ideal number of spacecraft for this project is 110. This value is then submitted for the final detailed design of the subsystems.

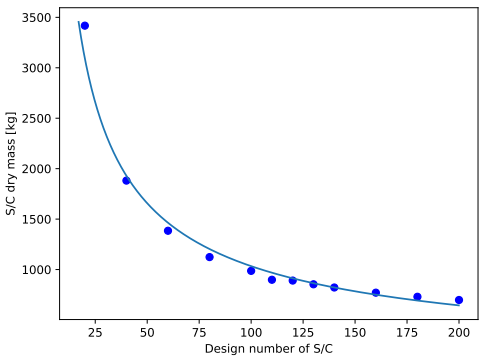

(a) Relation between spacecraft number and individual spacecraft dry mass.

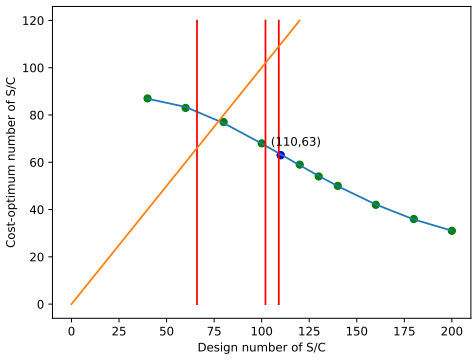

(b) Design number of spacecraft against the cost-optimum number of spacecraft with subsystem performance limitations.

Figure 3.2: Graphs that describe the relation

3.3. Sustainable development approach

The concept of sustainability is becoming more and more important in every aspect of society. The very goal of the LUMEN mission is rooted in this idea as well. By keeping sustainability in mind during the entire design process, all phases of this mission are as economically and ecologically sustainable as feasible. The mission is divided into 4 phases: Design, Production, Operations, and End-Of-Life. These phases have been discussed in the project plan [5], the baseline report [6] and the midterm report [7] and will be reviewed here.

3.3.1. Sustainability during Design

For the design process itself, the guidelines in the above-mentioned reports have been followed consistently. Coffee cups have been reused, reusable water bottles of food containers have replaced single-use ones, and members mostly took the bike, walked, or used other green and sustainable methods of transportation. The whiteboard provided has been used extensively, limiting the use of paper. In summary, the design phase of this mission was generally conducted as sustainably as possible within the power of the members.

3.3.2. Sustainability during Production

During the design, attention was also given to the sustainability pertaining to the production of the satellites. During the trade-off, it was an important criterion, which ensured that unsustainable designs would rank lower in the total score. This criterion was mainly dependent on the type and amount of materials that would generally be required. As for the design itself, while the off-the-shelf components presented might be from a range of different locations and companies, during the more detailed design phases, companies that sustainably produce similar or custom components and that are close to the assembly and launch facilities will be given priority for contracting. Methods of packaging and transportation will also be taken into consideration during the production phase.

In addition, the possibility of in-situ production of materials and propellant was considered for the sustainability criterion. In-situ production means that materials are produced on-site, which would be of great help to a base on the Moon since there is no need to escape the gravity well of Earth and its atmosphere. As sophisticated production infrastructure does not yet exist on the Moon and most likely will not for a long time, the complex components will still have to originate on Earth. However, the telescope and the laser optics are made up of silicon, while the satellite bus consists of aluminium. Both of these are present on the lunar surface and do not require overly complicated production methods[4]. The propellant used will be a green one, meaning that it can be synthesised and does not produce significant amounts of polluting elements. An example of such a green propellant is AF-M315E [8], which consists of Hydrogen, Nitrogen, and Oxygen. All of these components are accessible on the Moon and research is ongoing for a simple and efficient production method. This could mean that it becomes possible to produce this propellant on the Moon during the operation phase. These components take up a large portion of the mass of the spacecraft and as such might make future expansions cheaper and more sustainable to realise.

Another design aspect which factors into sustainability is optimisation. Making sure that the final design is as optimised as possible will help minimise the materials and propellant needed. An interesting example is the orbit. While during the midterm [7], the orbit was chosen as an example of the type selected, in this final report, the orbit has been optimised for multiple factors such as incidence angle, stability and altitude. A stable orbit will allow for no stationkeeping, while altitude and incidence angle affect the transmission methods. This method of design will provide iterations which should each get closer to the true ideal case.

Reliability also plays a part in determining the sustainability of a system. For this mission, components with longer lifetimes were given preference so that redundancy would not be as crucial as it could be in other cases. This means that fewer parts will be needed, which decreases the overall mass and thus launch requirements.

[4] URL: `https://lunarpedia.org/w/In-Situ_Propellant_Production` [Cited 15/06/2023]

3.3.3. Sustainability during Operations and End-of-Life

During the operational phase, not many steps can be taken regarding sustainability. This presents an opportunity to investigate further methods of optimising or increasing the efficiency and decreasing the negative impacts of the design. For the operations on earth, considerations will be made to opt for facilities which are powered by green energy and which do not require ecologically negative transportation methods.

When the mission comes to an end after 25 years, a plan must be devised to decommission each satellite in a non-destructive and non-disruptive manner. This plan will be further explained in subsection 5.6.1.

3.3.4. Sustainability and scaling

The economical potential for the scaling of the LUMEN design is discussed in Chapter 7. Here the potential ecological and social impacts will be discussed. In the previous midterm report [7], it was considered how a similar system could affect Earth. While quite a few changes would have to be made to the transmission system to counter the atmosphere, the overall idea could save surface area on the ground, allowing it to be used for other purposes. Additionally, the system could be used to provide energy to remote locations which have difficulties generating their own energy or connecting to a central power grid. A versatile pointing system could potentially allow for supplementing areas which have been affected by natural disasters or other issues which could cause decreased power generation.

4. Payload Detailed Design

This chapter aims to give an extensive description of the payload's relevance to the LUMEN mission, namely the lunar receiver, spacecraft power collection subsystem and spacecraft power transmission subsystem.

The following general requirements are the most important for the power transmission architecture, affecting the design of the power collection, power transmission and lunar receiver subsystems. An additional requirement for the power transmitter, LMN.TRA.002, is added following the considerations and analysis in section 4.3.

- **LMN.GEN.002** The LUMEN mission shall be capable of providing 1 MW of electrical power to the Moon assets continuously.
- **LMN.SUS.003** The LUMEN system, including its space segment, shall have a lifetime of at least 25 years.
- **LMN.SAR.004** All components of the LUMEN system shall be at least of TRL 6 at the moment of development, as specified by the ESA contact.

4.1. Lunar power receiver

The power receiver, while not designed with equal detail as the space segment, is an integral part of the system as it heavily affects the overall system efficiency. A proposal for its location and sizing is presented in the following section.

4.1.1. Location proposal

The proposed use case for space-based solar power is for extraction of water ice from the Shackleton crater at the lunar south pole. The floor and slopes of this crater may contain significant amounts of water ice (≈ 5 % to 10 % by mass) dispersed in the top 1 m to 2 m of regolith [9]. This ice is an attractive resource as it can be transformed into O2 and H2 - a popular rocket propellant combination. Furthermore, water and oxygen could be used to sustain (permanent) lunar habitats.

However, extracting this ice and converting it into H2 and O2 is energy intensive [10]. As the crater is permanently shadowed and around 4 km deep at its centre, as shown in Figure 4.1, getting the power down to the crater floor is a challenge. This could be done with cables and solar panels on the illuminated crater rim. However, with such a solution the power lines would need to be at least 8.3 km long to reach the crater floor which comes with its own challenges. Hence, employing a space-based solar power system emerges as an appealing alternative, with a receiver strategically positioned at the crater centre to maximise contact time for power transmission. Figure 4.1 illustrates the approximate dimensions of the crater, along with a spacecraft crossing the crater rim. Although the diagram is not to scale, it conveys the inverted truncated cone shape of the crater, measuring 4.2 km in height, with circular face diameters of 6.6 km and 21 km [11]. Based on these dimensions, the minimum elevation for power beaming is estimated to be 21.8 °.

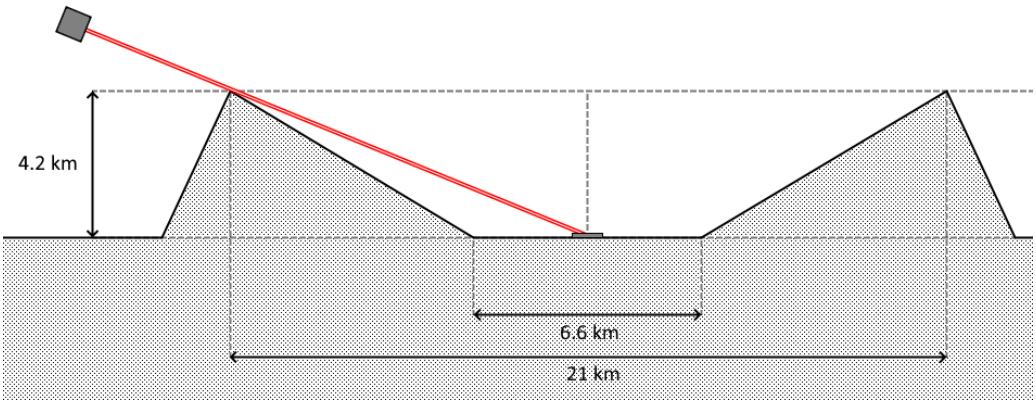

Figure 4.1: Shackleton crater schematic, based on Haruyama et al. [11].

4.1.2. Assumptions and requirements

For the purposes of this report, the receiver is modelled as flat and circular, and the unevenness of the lunar terrain is not considered. The receiver is assumed to be positioned orthogonally to the lunar south pole zenith direction. The size of the power receiver is key for showing the advantage of an SBSP system over other options for power generation for the lunar surface. This design driver was identified in the phases leading up to this Final Report, however, more detailed estimations were necessary to size this receiver. As the estimations became more refined, the large receiver size was discussed with the stakeholders and their feedback was incorporated to establish a compromise.

A compromise with the stakeholders was reached at a diameter of (80 ± 10) m. The purpose of the ± 10 m margin was to allow for iteration to obtain a more optimised result, for instance by varying the orbital elements and power transmitter parameters. Therefore, a new requirement for the receiver was added: LUMEN-REC-001 - The lunar power receiver shall have a diameter between 70 m and 90 m.

4.1.3. Receiver sizing

The receiver size is primarily influenced by the pointing performance of the laser beam from orbit, along with the spot size of the laser beam. The pointing accuracy and pointing knowledge affect the position of the centre of the laser spot with respect to the centre of the receiver. For instance, at a distance of $10\,000$ km and with a RMS pointing accuracy of 10 µrad, the beam can deviate up to 100 m.The deviation is not only limited to the spot moving but also to elongation into an ellipse due to the incidence angle of the beam on the receiver. This effect can significantly increase the required receiver size. As the receiver is sized to capture at least 99 % of the incident laser beam spot these effects must be taken into account.

Based on the beam propagation and pointing accuracy considerations described in Section 4.3.4 and Section 4.3.8, the receiver size dependence on these parameters can be derived. The final estimation for the receiver size takes into account the following parameters:

- z: The distance from the transmitter to the receiver during the mission is considered. Its maximum value influences the maximum static beam spot size on the receiver.
- $w_{99\%}(z)$: The laser beam radius at a distance z encompassing 99 % of the transmitted power. This radius is defined perpendicular to the direction of propagation of the beam - additional corrections must be made to account for the incidence angle. This value includes the initial width of the beam exiting the collimation optics.
- f_{bd}: The beam dilution factor (BDF) resulting from the incidence angle due to the inclination of the spacecraft with respect to the receiver. The BDF can be visualised as the maximum elongation of the beam spot on the receiver during the transmission windows. It is calculated as the maximum width of the elliptical spot during the transit compared to the spot size if the spacecraft were at zenith over the receiver. An example of such elliptical spots due to incidence angle is shown in Figure 4.2 [12].
- θ_p: The transmitter pointing accuracy (RMS) when actively tracking the receiver. This parameter heavily affects the receiver size: for instance, a 10 µrad pointing accuracy at a distance of $10\,000$ km results in a maximum error of ± 100 m. This would require an impractical size of the receiver. To minimise the required receiver size the accuracy must be on the order of 1 µrad (± 10 m at $10\,000$ km). This term includes both the static pointing accuracy and takes into account the maximum jitter for both high and low frequencies.
- θ_{pk}: The transmitter pointing knowledge (RMS) when actively tracking the receiver. This is assumed to have an equal effect as θ_p, as it manifests as an angular offset from the desired pointing. This parameter is dependent on the GNC subsystem.

With these performance parameters in mind, the receiver is sized using the following relation:

$$D_{receiver} = 2 \cdot w_{99\%}(z) \cdot f_{bd} + 2 \cdot z \cdot (\theta_p + \theta_{pk}) \tag{4.1}$$

The selected photovoltaic laser power converters (LPCs) described in the Midterm report, have been

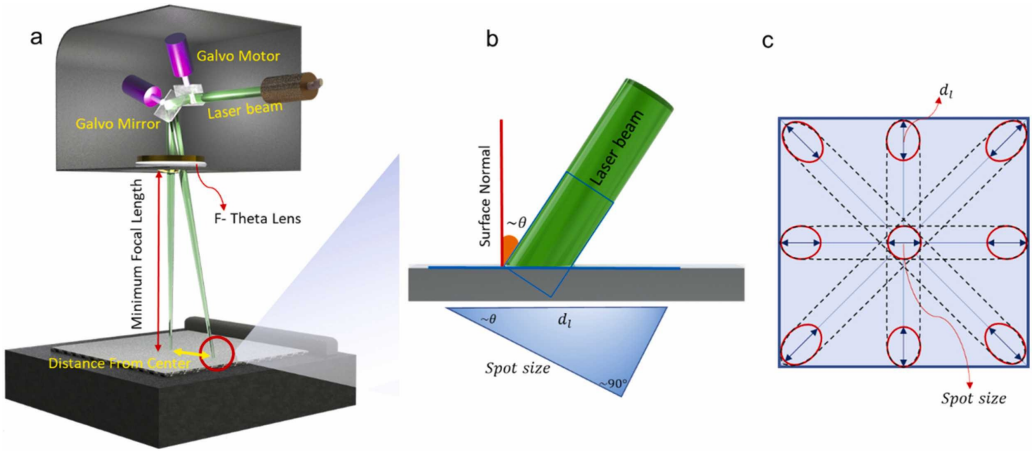

Figure 4.2: Beam spot elongation due to incidence angle, sourced from Fathi-Hafshejani et al. [12].

changed, as an alternative with higher conversion efficiencies at the laser's wavelength was found. While the LPC technology at 976 nm is relatively immature compared to that for other wavelengths, the growing popularity of lasers with this wavelength is a driver for recent improvements. The alternative PV cells promise high efficiencies and are most efficient between 915 nm and 976 nm, with power conversion efficiencies above 40.1 % [13]. Conversion efficiencies in excess of 74.7 % have been demonstrated by Fafard and Masson [14], showing the advantage of PV cells tuned for one specific wavelength compared to broad-spectrum PV cells. As this technology is novel and expensive, employing concentrator lenses on the receiver, such as the ones selected for the power collection subsystem, could significantly reduce its overall cost due to the smaller required PV cell area.

An additional efficiency that must be considered is the reflectivity of the cover glass on the PV cells. This cover glass, intended to protect the cells from radiation and debris, is covered with an anti-reflective coating (ARC). Sharma [15] presents the efficiency versus the incidence angle for PV cells covered with ARC-coated glass. Results from a numerical model predicting the reflectivity for different incidence angles θ as a function of the wavelength are presented by Sharma [15]. From this data, a linear relation for incidence angles between $45\,°$ and $60\,°$ was found (including a safety factor of 1.2) as $R = 5.6e - 4\theta + 0.052$ with R in %. This approximation is considered valid for angles of incidence between $30\,°$ and $60\,°$, which contains the expected angular range of angles of incidence in the orbit. Therefore, for angles between $30\,°$ and $45\,°$, the reflectivity is expected to be overestimated. However, taking conservative values is beneficial for the true performance of the final system.

4.2. Power Collection Subsystem

As documented in the LUMEN Midterm Report [7], a concentrated photovoltaics (CPV) power collection subsystem was selected, primarily due to the reduced mass and cost of this system compared to non-concentrated PV. This section describes this concentrator and the alterations necessary for use in the LUMEN system.

4.2.1. SLA Squarerigger

The design presented in this chapter is based on the Stretched Lens Array (SLA) technology as described by Allen et al. [16]. With flight heritage in the form of the SCARLET array of the Deep Space 1 mission [2] (TRL 9) and an upgraded prototype on the TacSat 4 mission [17] (TRL 7), this is deemed as a sufficiently mature technology to reach the planned launch date of 2030.

The initial SCARLET array design from 1996 underwent a number of iterations and redesigns, both on a component and system level. These include the SLASR array with a compact deployment mechanism [18], improved reinforced lens manufacturing technologies [19] and lightweight 4X and 25X concentrator designs on a telescoping boom [20].

As described in the LUMEN Midterm Report [7], a design based on the SLA SquareRigger (SLASR) [18] is selected for this mission. This design, shown in Figure 4.3 employs 8X concentration flexible

silicone lenses, resulting in ≈8X less required solar cell area compared to non-concentrated PV panels. The PV cells and concentrators are mounted on an aluminium foil and composite radiator used to cool the cells. The PV cells, concentrator and radiator assembly on the flexible substrate form the so-called blanket. Most importantly, the SLASR includes scalable deployment mechanisms for unfolding the large arrays and the flexible concentrator lenses.

Figure 4.3: The SLASR concentrator array. *Adapted from [18].*

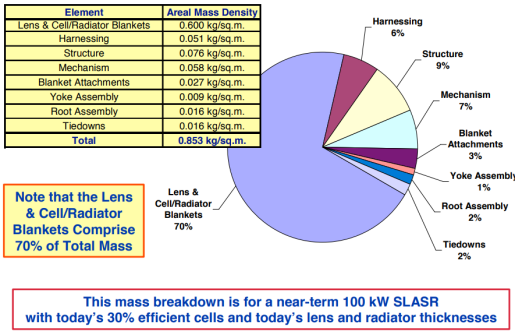

Figure 4.4: Areal density breakdown of SLASR. *Adapted from [18].*

The TRL 6 status of this system was confirmed[5] and will thus be used in the remainder of this report. As can be seen in the areal density breakdown of the original SLASR design presented in Figure 4.4, the lens, PV cell and radiator blankets make up a majority of the mass of the system. This breakdown also facilitates the derivation of the parameters of an upgraded iteration with, for instance, more efficient PV cells.

4.2.2. Upgrades to SLASR

Due to progress in space PV cell efficiencies since 2006, the SLASR [18] will be upgraded with the $32.2\,\%$ efficient triple-junction XTE-SF cells made by Spectrolab[6]. This presents a $2.2\,\%$ increase in efficiency compared to the original SLASR design. With the maturing development of space-hardened quad-junction solar cells such as the $33.3\,\%$ efficient Rocket Lab IMM-β[7], an even higher efficiency could be achieved before the planned launch date of 2030.

Additionally, progress has been made in the production methods of ruggedised stretched lens arrays (SLAs) using stainless steel or titanium meshes [1, 20]. This allows for a thinner, lighter lens that can withstand more stresses, preventing SLA tears such as the one observed on the SLA flown on the TacSat 4 mission [17]. The lenses described by O'Neill et al. [1] achieve a $92\,\%$ transmittance at 4X concentration and are less sensitive to angle-of-incidence losses than conventional PVs. Furthermore, at $0.399\,\mathrm{kg\,m^{-2}}$ the overall areal density of the blankets presented in [1] is significantly lower than the $0.6\,\mathrm{kg\,m^{-2}}$ of the older SLASR design show in Figure 4.4 [18]. Replacing the 8X concentration blanket of the SLASR design with the 4X concentrator blanket [1] can therefore result in significant mass savings.

4.2.3. Performance metrics

The $0.399\,\mathrm{kg\,m^{-2}}$ aerial density value for the 4X blanket was, unfortunately, derived using the assumption of future $35\,\%$ efficient solar cells. This results in a specific power of $1200\,\mathrm{kW\,m^{-2}}$ exclusively for the blankets [1]. As such, efficient PV cells are not yet available and must be corrected for. To do this, a correction factor using the $32.2\,\%$ efficiency of the selected Spectrolab XTE-SF is used. The 4X blanket specific power is therefore scaled with a factor of $\frac{32.2}{35}$, resulting in a corrected specific

[5] Personal correspondence with Mark O'Neill, one of the authors of [18].

[6] URL: `https://www.spectrolab.com/photovoltaics/XTE-SF%20Data%20Sheet%20_07.27.22.pdf` [Cited 18/06/2023]

[7] URL: `https://www.rocketlabusa.com/updates/rocket-lab-begins-qualification-of-highest-performing-space-solar-cel` [Cited 20/06/2023]

power of $1105.84\,\mathrm{kW\,m^{-2}}$. These derived performance characteristics must be verified and validated as described in Section 4.2.4.

A key parameter defining the collector subsystem performance is the degradation in efficiency over the mission lifetime. As a 4X concentrator will be used, four times less PV cell area is required. This allows for heavier radiation shielding coatings while keeping the mass low [16], thereby reducing degradation. Additionally, there is the possibility that the concentrator lens acts as a shield against radiation for the PV cells [21]. However, further investigation is necessary to substantiate this claim.

To establish the degradation value, an in-orbit high-radiation environment experiment utilising the SCARLET array was conducted [16]. It yielded a degradation rate of $0.3\,\%\,\mathrm{yr^{-1}}$ in the GEO radiation environment. Considering the advances in radiation-proofing of PV cells since 1996 [21], no further margin was deemed necessary for this value. The degradation value shall be verified and validated by using the methods described in ECSS-E-ST-20-08C [22].

The stretched lenses, reflect $8\,\%$ of the incoming sunlight, but are also significantly less sensitive to losses caused due to misalignment of the arrays with respect to the incident sunlight. Because of this, even a misalignment of $\pm 2^{\circ}$ results in a drop in power of $<1\,\%$ [1]. To remain conservative, a $1\,\%$ loss is assumed, resulting in a $99\,\%$ angle of incidence efficiency.

Table 4.1: Performance values for the power collection subsystem.

Parameter	Value
Concentration factor	4
PV cell efficiency BoL	$32.2\,\%$
PV cell efficiency degradation	$0.3\,\%\,\mathrm{yr^{-1}}$
PV cell efficiency EoL	$29.867\,\%$
Collector lens transmittance	$92\,\%$
Angle of incidence efficiency	$99\,\%$
Blanket specific power	$1105.84\,\mathrm{W\,kg^{-1}}$
Blanket area density	$0.399\,\mathrm{kg\,m^{-2}}$
Structural area density	$0.253\,\mathrm{kg\,m^{-2}}$

The most relevant performance parameters for this upgraded SLASR-based are summarised in Table 4.1. With these parameters, the collection subsystem is sized parametrically based on the performance of the other subsystems.

4.2.4. Verification and Validation

The characteristics of the collector systems presented in Table 4.1 shall be verified and validated primarily through testing. Firstly, a small-scale prototype will be used, followed by larger-scale collector subsystem assemblies. The following list shows the planned verification and validation activities:

- Testing of the concentration factor of the lenses. This shall be done on small-scale models including first a single concentrator lens, then with multiple lenses in at least a 3x3 grid.
- Testing of the mechanical properties of the concentrator lenses after exposure to high amounts of radiation, similar to radiation exposure testing the methods used for PV cell testing described in [22]. However, mechanical tests shall be used for testing these properties.
- Testing of the transmittance degradation of the concentrator lenses due to radiation exposure.
- Testing of the PV cell efficiency under concentrated sunlight.
- Testing of the PV cell degradation under concentrated sunlight and radiation tests as documented in [22].
- Testing of the concentrator, PV cell and radiator blanket thermal performance at AM0 illumination conditions, as well as at higher illuminations up to 2 AM0.
- Testing of the mechanical properties of the blanket after radiation exposure equivalent to that of the PV cells and concentrator lenses.

4.3. Power Transmission Subsystem

As documented in the previous report [7], a laser-based power transmitter was selected over microwave power transmission. This decision was made to keep the size of the power receiver low and to enable a high contact fraction using a high elliptical lunar orbit. The reader is referred to the LUMEN Midterm Report [7] for additional details. This chapter describes the detailed design of the power transmission system employed on each LUMEN spacecraft, along with a characterisation of the receiver introduced in Section 4.1. First, a description and analysis of the selected laser sources. This is followed by the description of the propagation of the beam. Finally, the design of the collimation optics and its pointing mechanism is presented.

4.3.1. Laser source

As the concept of laser-based defence weapons is gaining in popularity, manufacturers such as Coherent Europe B.V. (formerly DILAS) are developing lightweight, high power and high-efficiency diode lasers [23, 24]. The DILAS IS46.6 $300\,\mathrm{W}$ fibre laser modules [25] were selected as the best option based on the per-segment trade-off described in the Midterm Report [7]. Following a request for the specifications of the module, it was found that these modules were discontinued. However, the DILAS IS53 prototype mentioned by Ebert et al. [25] in 2017 and by Könning et al. [26] in 2022 has matured and is in production as of 2022 [24]. The IS53 modules output $600\,\mathrm{W}$ of single mode $976\,\mathrm{nm}$ infrared light at a mass-power ratio of $0.67\,\mathrm{kg\,kW^{-1}}$, making them around 33% lighter than the older IS46.6 laser for the same power output. By optimising the housing of the IS53 module, their mass can be reduced even further [24].

The possibility of developing a modified version of this module for space-based power-beaming applications was mentioned in an email conversation with the Coherent Sales Manager for Diode Components[8]. Further work is being done to reduce the mass-power ratio of diode laser modules, with prototypes of modified Coherent FACTOR-22 modules reaching $0.4\,\mathrm{kg\,kW^{-1}}$ [24]. This is a result of replacing the original copper housing with a lightweight alternative at the expense of cooling performance and lifetime [24]. However, considering the long required operational lifetime, this was deemed too great a disadvantage, especially in combination with an insufficient TRL. This resulted in the IS53 module (shown in Figure 4.5) being selected as a reference for the laser source. The reason for it being used as a *reference*, is due to the module requiring a significant redesign; It must be ruggedised to perform in the space environment for over 25 years, and its cooling system must be redesigned to use an alternative coolant to water.

Figure 4.5: The Coherent IS53 diode laser module selected for the power transmission system.

4.3.2. Lifetime estimation

Laser diode lifetime is difficult to estimate as it highly depends on its environment and cooling system performance [24, 27, 28][9]. The lifetime and performance of diode laser modules are limited by the various failure modes that may occur. Performance degradation comes in three main variants: rapid degradation, gradual degradation and catastrophic degradation [29]. The most common and easily predictable failure mode is gradual degradation, which occurs throughout the operational lifetime of the laser and is often modelled linearly [29]. In reality, gradual degradation can accelerate and should

[8] Dr. Mario Auerbach - Sales Manager Diode Components EMEA Sales Coherent Shared Services B.V.

[9] URL: `https://worldstartech.com/what-determines-the-lifetime-of-a-laser-module/` [Cited 07/06/2023]

be estimated with more sophisticated models [30]. Considering the 25-year mission lifetime and maiden launch date in 2030, accelerated ageing testing is a key technique for predicting laser module lifetime [31].

The required lifetime of the laser modules is at least 79.05% (from Table 5.7) of the 25-year mission time, resulting in 19.7625 years of operation or more than 173000 hours. This is at the limit of what can be achieved with current lasers, as most lasers have a lifetime far below 100000 operational hours. Nakatsu et al. [32], for instance, mentions a lifetime of 30000 hours or 3.42 years to 50% output power degradation of a $100\,\mathrm{W}$ diode laser. For a Raman diode laser design based on U.S. Patent No. 6,100,975[33], 6-7 years (52500-61300 hours) of continuous operation are claimed before power output degradation of around 15% occurs[10].

The Shenzen Wisely Laser company[11] claims a lifetime of 100000-200000 hours of operation for their $20 - 120$W fibre laser marking machines[12]. However, the part number of the laser module manufactured by IPG Photonics Germany is not mentioned. Because of this, exact degradation per year estimates were not found and this data raises doubts.

Less powerful laser sources with exceptional lifetimes have been demonstrated both on the ground and in space [34]. Four Non-Planar Ring Oscillator (NPRO) lasers were tested, starting with $40\,\mathrm{mW}$ of output at BoL. Continuous firing lifetimes with a power output degradation of less than 20% of more than 21.75 and 11 years on the ground and in space, respectively, have been observed [34]. Furthermore, an accelerated lifetime test estimate before power drops below 80% of the BoL level results in an expected 27-year lifetime [34].

This shows that lasers used in space have the potential for long lifetimes, but no lifetime test data for diode lasers of the same type as the IS53 is available. As the NPRO lasers presented by Asbury et al. [34] operated at a power level significantly lower than the IS53, these lifetimes must be critically reviewed. Nonetheless, with a lack of further test data, the 11 year lifetime of Flight Laser A to reach 80% of BoL power is used as reference [34]. This results in a target degradation of $2.008\,140\,5\,\%\,\mathrm{yr}^{-1}$. Based on this estimation, after 25 years of operation, the efficiency of the laser modules is reduced by a factor of around 0.66, resulting in an efficiency of $30.11\,\%$ and power output of $361.341\,\mathrm{W}$ per module.

4.3.3. Design considerations to extend lifetime

To counter laser power degradation through all three failure mechanisms, and extend the lifetime of the laser diodes, their temperature must be kept as low as possible, and thermal cycling should be minimised[13]. The materials and dimensions used in the different layers of the diode stack, solder, and substrate must be chosen such that thermal stresses are minimised.

Additionally, the lifetime is affected by the quality of the power supplied, with power fluctuation potentially accelerating degradation [27]. To mitigate power fluctuations, an automatic power control (APC) system that monitors the laser output with photodiodes will be used. Temperature sensors will be added to each laser module to allow for the mitigation of thermal cycling. Additionally, the laser modules must be reinforced against the accelerations and vibrations encountered during the launch and transfer, to prevent misalignment or degradation of the fibres and other optical components.

The following strategy is implemented to mitigate the laser module efficiency degradation. The number of laser modules is doubled and the lasers are split into two sets. The first batch will operate for half of the mission or 12.5 years, after which their efficiency is expected to degrade to $38.8\,\%$. The second batch will be kept inoperative for the first half of the mission lifetime, with active temperature control of these inoperative modules to reduce temperature fluctuations and slow degradation. After 12.5 years, the first batch of laser modules is deactivated and the second batch begins operations.

[10] URL: https://www.process-instruments-inc.com/support/products/Raman-Lasers/Laser-Lifetime/ [Cited 07/06/2023]

[11] URL: https://www.wiselylaser.com [Cited 15/06/2023]

[12] URL: https://www.wiselylaser.com/IPG-Fiber-Laser-Marking-Machine-Type-III.html [Cited 08/06/2023]

[13] URL: https://www.lasercomponents.com/de-en/news/long-lifetime-laser-diodes-for-space/ [Cited 15/06/2023]

The efficiency of the second batch of modules is expected to reduce by $10\,\%$ during storage, but due to a lack of data this will need to be confirmed experimentally. Therefore, the second batch of modules will start with an efficiency of $45\,\%$, resulting in an expected EoL efficiency of $34.9\,\%$. This approach to extending the laser lifetime can likely be optimised further, but more research and testing are required.

To confirm the lifetime, accelerated ageing tests such as those described by Joyce et al. [31] will be performed on these modules throughout the development of the modules to verify their performance. Further tests of the power transmitter assembly and thermal control system in a relevant environment will be performed to validate the system.

4.3.4. Beam propagation

The ideal, diffraction-limited laser beam is typically modelled as a Gaussian, with its radius w defining where the intensity of the beam drops to $1/e^2$ of its peak value. This region encompasses $86.5\,\%$ of the transmitted power, $1.224 \cdot w$ corresponds to $95\,\%$ and $1.52 \cdot w$ contains $99\,\%$. As the exergy of the system should be maximised, the losses should be minimised. Therefore, the system is designed to capture at least $99\,\%$ of the transmitted power. Hence, the factor of 1.52 on the beam radius will be used. This radius will be referred to as $w_{99\%}$. The smallest radius of this beam w_0 is called the waist.

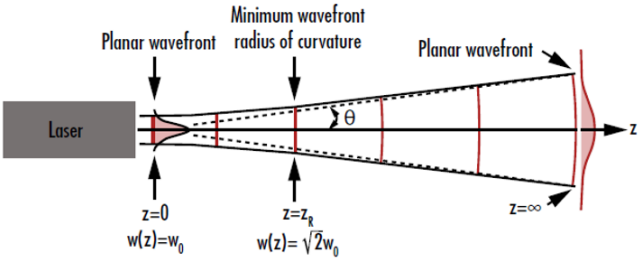

Figure 4.6: Gaussian laser beam propagation, adapted from Edmund Optics[14].

At a distance z from the beam waist, the beam is said to be diffraction-limited and diverges linearly as depicted in Figure 4.6. The divergence half-angle of the diffraction-limited beam is given by:

$$\theta_{beam,dl} = \frac{\lambda}{\pi \cdot w_0} \tag{4.2}$$

with λ the laser wavelength and w_0 the beam waist radius. However, real beams diverge more than the diffraction limited beam. To correct for the added divergence, the beam quality factor M^2 is typically used. While it may be defined differently by different authors, in its typical definition it is a factor scaling the beam divergence compared to the diffraction limited case. Furthermore, different measurement methods exist, necessitating experimental verification of the beam quality factor.

$M^2 = 1$ is the minimum theoretically possible value, while a $M^2 = 2$ beam diverges with twice the angle, resulting in:

$$\theta_{beam} = M^2 \frac{\lambda}{\pi \cdot w_0} \tag{4.3}$$

The beam radius $w_{99\%}$ at a distance z, assuming a small angle θ_{beam} and containing 99% of the transmitted power, is therefore:

$$w_{99\%}(z) = w_0 + z \cdot 1.52 \cdot \theta_{beam} = w_0 + z \cdot 1.52 \cdot M^2 \frac{\lambda}{\pi \cdot w_0} \tag{4.4}$$

For the remainder of this report, the beam radius refers to $w_{99\%}$.

[14] URL:https://www.edmundoptics.com/knowledge-center/application-notes/lasers/gaussian-beam-propagation/ [Cited 17/06/2023]

4.3.5. Collimation considerations

The beam spot size on the receiver influences the power receiver size and must, thus. be kept small. To do this, the beam radius at the receiver must be reduced through a reduction of the divergence angle. The selected laser module's exit fibre has a high divergence on the order of $5 - 20°$ and must be reduced. Based on Equation (4.3), this can be done by increasing the beam waist w_0. To do this, collimation optics must be employed, where the beam is first expanded, then collimated into a low-divergence beam[15]. This system can be based on mirrors and/or lenses, with the beam's radius at the collimator exit defining the divergence of the beam.

To compensate for the beam deforming through the optics, a conservative M^2 is applied. Typical M^2 values for single-mode fibre lasers range from $1.1 - 1.2$ [35]. A safety factor of 1.2 is applied to this value accounting for the beam quality degradation due to the optics and possible diffraction of poorly combined laser beams, resulting in an M^2 of 1.44.

4.3.6. Collimation sensitivity

The beam waist w_0 versus the spot radius $w(z)$ (Equation (4.4)) is plotted in Figure 4.7. The maximum transmission altitude of $14\,522.70$ km is assumed, (from Table 5.7, derivation explained in Chapter 5) along with an M^2 of 1.44 and $\lambda = 976$ nm. It can be seen that the beam radius at a distance decreases steeply until a waist radius of around 1 m. Furthermore, after a waist radius of around 3 m the waist size becomes more driving for the beam size than the divergence angle and the beam radius at a distance begins to increase again. At a waist radius of 0.5 m, the beam radius at distance is around 20 m. This was deemed as an unacceptably large driver of the receiver size (Equation (4.1)) in combination with preliminary pointing accuracy values. For a beam waist radius of 1 m, the beam radius at the maximum distance is 10.5 m. This is deemed acceptable both in terms of receiver sizing as well as collimation feasibility as monolithic optics of similar sizes have been achieved. The Hubble space telescope, for instance, has a primary mirror with a diameter of 2.4 m. As a starting point for iterations, an initial required beam-radius $w_0 = 1$ m was decided.

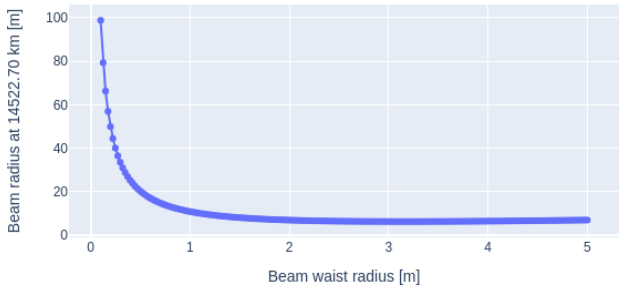

Figure 4.7: Beam radius at $14\,522.70$ km versus the beam waist radius.

4.3.7. Collimator design

As mentioned before, collimation can be done with either lenses, mirrors or a combination of the two. Large mirrors have seen ubiquitous use in space telescopes such as the Kepler, Hubble and James Webb Space telescopes. Furthermore, for this high-power application, the supporting structure of the mirrors can easily be cooled, while active cooling of lenses can only be applied at the lens edges, resulting in significant thermal gradients, deformation and potential degradation. Therefore, it was decided to use a mirror-based collimator over refractive optics.

The mirror collimator used for LUMEN is loosely based on the design of the Boeing Yal-1 Airborne Laser Testbed. This system employed a Cassegrain telescope collimator [36], an example of which is depicted in Figure 4.8.

The collimator used for the LUMEN mission is a Ritchey-Chrétien reflector telescope, a derivative of the Cassegrain design. This design uses hyperbolic mirrors to reduce spherical aberration compared

[15] URL: `https://www.edmundoptics.eu/knowledge-center/application-notes/lasers/beam-expanders/` [Cited 16/06/2023]

to the classic Cassegrain [37]. Spherical aberration dilutes the laser beam by effectively increasing its divergence angle and becoming more significant with shorter focal lengths. The spherical aberration not mitigated by the use of this design is assumed to be included in the safety factor of 1.2 on the beam quality factor M^2.

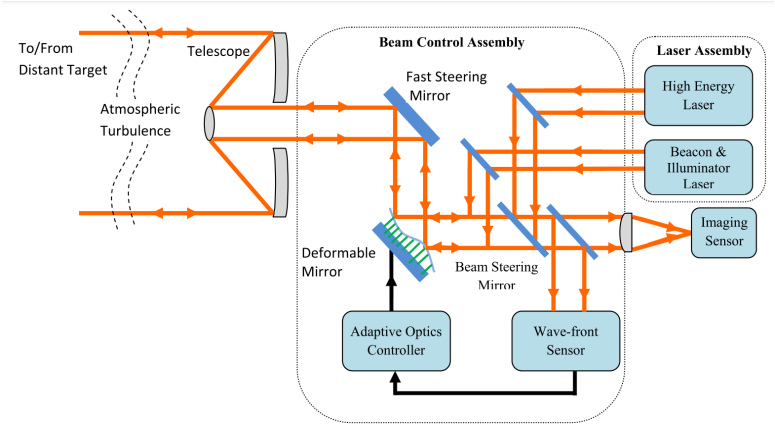

Figure 4.8: High-power laser weapon system architecture [36].

Similarly to the mirrors of the James Webb Space Telescope (JWST), the collimator mirrors will be coated with gold, as it can reflect >99% of 976 nm light. As the JWST operates in a wide range of infrared wavelengths (600-2800nm), its mirrors are made to reflect this wide band [38]. However, at 800 nm and 1000 nm, the mirror reflectivity is only 96% and 97.3%, respectively [38]. Therefore, mirrors tuned closer to 976 nm are employed - based on the EKSMA 035-0980 45° mirrors, a 99.5% reflectivity at 976 nm is assumed [16]. Between the output of the laser sources and input of the collimator, the laser beam must be reflected at least three times: by the primary and secondary mirrors, along with the Fine Steering Mirror. Due to the pointing mechanism, at least one more reflection is necessary. In this draft report, the pointing mechanism is not fully modelled, so four reflections are assumed, resulting in a mirror reflection efficiency of 98.015 %.

Each mirror reflecting the laser beam requires integrated liquid cooling pipes to transport the absorbed heat away to radiators. Furthermore, the supporting structure of the primary and secondary telescope mirrors will be coated with a high-emissivity material to take advantage of the significant area to radiate heat away.

The primary mirror is sized based on the initial beam radius by multiplying this radius by a safety factor of 1.2 to prevent vignetting by collimating the beam away from the mirror edges. This results in a primary mirror diameter of 2.4 m at a beam waist radius of 1 m. The path of the laser beam through the collimator is shown schematically in Figure 4.9.

The individual laser modules are packed closely together in the laser assembly shown on the right. Thermal management is done with a liquid cooling loop and dedicated radiators. The optical fibres coming out of the laser modules are bundled together. Shown with blue lines is the beacon laser, which is part of the GNC subsystem. It operates at a lower wavelength than the power lasers - because of this, the beacon beam diverges less than the power beam, aiding in the pointing determination of the GNC subsystem. This beacon laser is placed at the centre of the optical fibre bundle. The laser emanating from the end of the fibre diverges heavily as described before. This heavily diverging beam is reflected by the fixed parabolic mirror. This mirror will be fine-tuned to focus the beam down onto the Fast Steering Mirror (FSM), which is placed at the focus of the telescope. The FSM will be curved to expand the beam appropriately for the secondary mirror. The distances between the mirrors and their curvatures will be optimised to minimise losses. Past the FSM, the laser beam enters the Ritchey-Chrétien collimator and is collimated down to a divergence angle of $\approx 4.473\,65 \times 10^{-7}$ nm resulting from the 2 m beam waist.

[16] URL: `https://eksmaoptics.com/optical-components/dielectric-mirrors/bk7-laser-line-mirrors/` [Cited 15/06/2023]

The exact sizing of the components, including the curvature of each mirror is considered out of the scope of this stage of the design. However, the laser propagation distance from the laser fibres to the effective focal point of the collimator can be adjusted together with the focal ratio of the telescope mirrors. By doing this, a compromise between the distance between the mirrors and their curvature can be achieved. For this stage of the design, the collimator inter-mirror distance is assumed to be $1\,\mathrm{m}$. However, for the next design phase, this value will be optimised to reach a balance between launcher packing considerations and collimation performance.

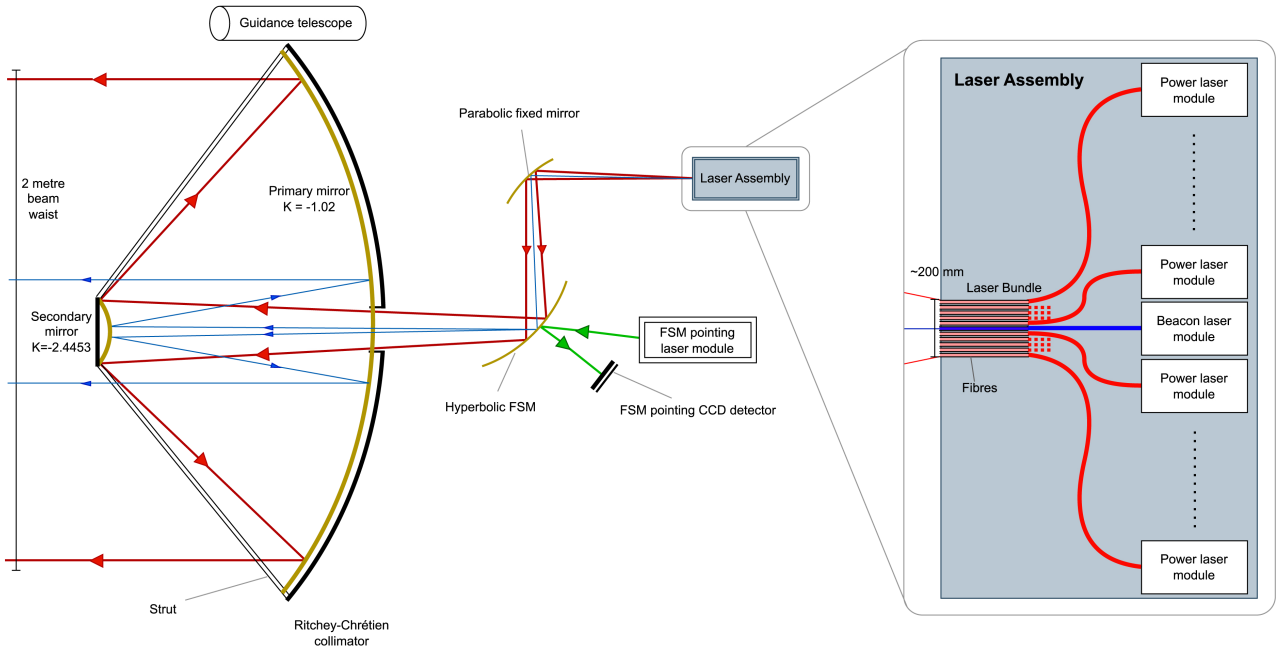

Figure 4.9: A diagram for the transmission segment of the LUMEN spacecraft showing the path of the lasers from their generation to when they exit the spacecraft.

4.3.8. Pointing performance

The pointing accuracy of the power transmitter drives both the system efficiency and receiver size, as it results in a random excursion of the beam pointing from the desired position at the centre of the receiver. To maximise the efficiency of the system, an increase in receiver size is preferred over a lower efficiency. To quantify an estimate of the required receiver size, a sensitivity analysis on the pointing accuracy and transmission distance was performed for a maximum excursion $\pm 20\,\mathrm{m}$ from the centre of the receiver. The resulting graph is depicted in Figure 4.10, where it can be seen that the required pointing accuracy becomes more stringent with increasing transmission distance.

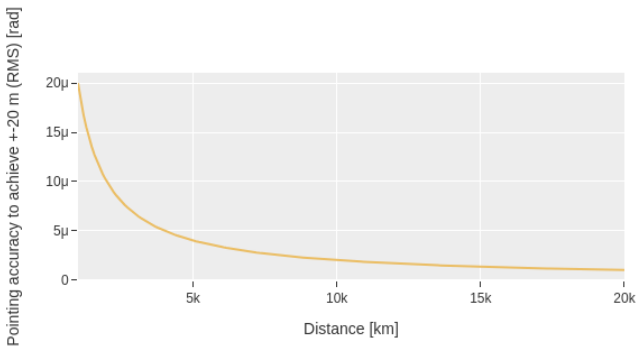

Figure 4.10: Required pointing accuracy to achieve a maximum beam excursion of $\pm 20\,\mathrm{m}$ versus the transmission distance.

A complication that arises when using lasers to transmit power is mechanical pointing. Lasers must be pointed with extreme accuracy, in order for a receiver to capture the complete beam. Despite the

receiver design being beyond the scope of this project, considerations are made to keep this as small as possible for customers to further adopt for a limited expense. Nevertheless, the accuracy requirement for the pointing mechanism cannot be excessively advanced, due to the effects this has on the cost of the spacecraft. Therefore, the adopted method relies on the use of sophisticated technology for the pointing, on top of which a margin is applied. This maintains the performance competitive while including relatively mature technology, instead of cutting-edge. TRL is also considered within this method.

Firstly, a key characteristic of the laser transmission of the spacecraft is the large angular movement over a single orbit. This calls for the use of a gimbal system as a coarse pointing mechanism (CPM). This system cannot achieve accuracies close to the required pointing accuracy for the laser beams. Rather, it provides the large angular excursions of $\approx \pm 70^{\circ}$ that are experienced during orbit. Research on readily available laser gimbal systems integrated into previous spacecraft, shed light on the LCT-135 component by TESAT. This laser communication component is used on more than 8 ESA missions and has been readily tested and qualified, thus giving a TRL of 9. Due to the large experience present with this component, it is assumed that a modified scaled-up version can be adapted for the current mission with similar performances. Ideally, the exact architecture shall adopt a non-off-centre design to reduce the disturbance torque for the rest of the spacecraft. Nevertheless, the LCT achieves a pointing accuracy of ± 100 µrad [39].

For the more precise pointing of the lasers, the industry standard is the use of Fine Steering Mirrors (FSM). These, however, can only be implemented by using a feedback loop in which data flows from the receiving end back to the transmitting end, where then corrections are conducted and the cycle repeated. This closed-loop cycle is then designed by the GNC subsystem, from which a certain pointing knowledge can be derived. Han et al. [40] demonstrate the practical performance of closed-loop FSM. Han et al. [40] find the pointing accuracy to be 0.96 µrad. Moreover, this FSM has an operational range of ± 2 mrad.

However, this does not account for the jitter of the FSM, for which [41] was consulted. In the second paper, the line-of-sight (LOS) jitter of a tracking mechanism with and without FSM is measured over a range of more than 100 Hz. With the FSM, the maximum LOS jitter along any axis was 0.1 µrad (see figure 16 of [41]). It is also worth noting that the largest jitter values occur at low frequencies.

In case these jitter values are insufficient for payload functionality, it is recommended to include a further component, such as the Image Stabilisation System (ISS) of the Solar Dynamics Observatory spacecraft. The ISS acts as a low-pass filter and greatly attenuates frequencies over a certain threshold. This could be tuned for the specific frequencies of the highest jitter, therefore increasing accuracy. However, this is not necessary in the current transmission design.

Combining the aforementioned performances, a total accuracy of 1.06 µrad can be achieved also accounting for jitter. This performance is then multiplied by the design factor of safety of 1.2 to both account for more mature technology, and allow for design margin. Therefore, the final pointing accuracy used for design is 1.26 µrad. This is expressed as an additional requirement: ”LMN.TRA.002 The power transmitter shall have a pointing accuracy better than 1.26 µrad.”.

4.3.9. Summary of power transmitter parameters

The parameters of the transmitter subsystem described in this chapter are summarised in Table 4.2. The power output can be scaled by changing the number of laser modules. The size of the collimator optics is only dependent on the desired spot size on the lunar surface and the distance, meaning this design does not need to be scaled with laser power. However, the thermal management system does have to remove more heat for a higher power level, increasing complexity.

4.3.10. Power transmitter verification

The following verification activities shall be performed for the power transmitter:

- Accelerated ageing tests shall be performed on the laser modules to verify their degradation rate using methods from [31]. Due to the long required lifetime of the laser, non-accelerated testing is impractical. This accelerated ageing will be done through radiation exposure, vibrations and

Table 4.2: Power transmitter subsystem parameters.

Parameter	Value
Laser wavelength	976 nm
Laser module specific mass	0.67 kg kW^{-1}
BOL laser module efficiency	50 %
Laser efficiency/power degradation	2.008 % yr^{-1}
EoL laser module efficiency with 2-batch strategy	34.92 %
Beam quality factor M^2	1.44
Expanded beam waist (radius)	1 m
Reflectivity efficiency for 4 mirrors	98.01 %
Primary mirror diameter	2.4 m
Pointing accuracy (RMS)	1.26 µrad

thermal cycling. As these lasers require a significant redesign for space environment use, this testing shall be repeated during the development of these upgraded modules.

- The beam quality factor M^2 of the laser beams emerging from laser modules' fibres must be determined experimentally. This will be done through testing with a knife-edge test as described by E Siegman Edward L [42]. This testing shall again be performed following laser module accelerated ageing tests as described in the previous item.
- The beam quality factor M^2 of the laser beam emerging from the collimator will be measured and verified through testing with varying numbers of laser modules, increasing this number past the required number of modules up to 1.5 times the number of modules that shall fire at the same time.
- The reflectivity of the collimator mirrors of 99.5 % at the laser modules' operating wavelength of 976 nm shall be verified through testing.
- The pointing accuracy of the collimator assembly, resulting from the combination of the coarse pointing gimbal and the fine steering mirror shall be verified through testing. To reach the required 1.26 µrad pointing accuracy, a test in conjunction with the active feedback loops of the GNC subsystem shall be performed.
- The divergence angle of the laser beam emerging from the collimator optics shall be measured at a variety of locations along the beam, with the maximum measurement distance as large as allowable depending on the available facilities. This is done to verify the analytical beam divergence calculations.

4.4. Combined power transmission validation

A small-scale prototype of the power transmission architecture shall be used to verify the combined functioning of the three parts of the power transmission architecture described in this chapter. A key factor to be measured is the combined efficiency of the three subsystems. The power collector prototype will provide power from sunlight, which is then converted and passed to the power transmitter prototype, which fires its laser beam at the lunar power receiver prototype. The power received and lost at every step in the conversion will be either measured or estimated analytically. For instance, the power coming out of the collector shall be measured, while the power in the laser beam shall be derived analytically based on the power at the receiver and sampling of the laser beam intensity at different points.

5. Astrodynamics

Prevalent challenges in designing any system to be operating in the vicinity of the Moon are getting the system from the Earth to the Moon, ensuring the system can stay around the Moon for its intended lifetime, and disposing of the system at the end of its life in a responsible manner. It should therefore come as no surprise that the system's astrodynamics is an important driver for all other aspects of its design. This chapter aims to give an overview of LUMEN's astrodynamic design, from launch to end-of-life.

5.1. Elliptical Lunar Frozen Orbits: A Brief Overview

Choosing an orbit for LUMEN requires knowledge of what kind of characteristics would be desired for such a system, and which options for orbit design would be available in the first place. This section will give an overview of the class of Elliptical Lunar Frozen Orbits and why this class is identified as being the most suitable for the LUMEN mission.

5.1.1. Frozen Orbits about the Moon

The lunar neighbourhood is a peculiar region for orbit design: this seemingly empty environment in the absence of a strong magnetic field and atmosphere may seem deceivingly simple, while the opposite is true. Due to the Moon's significantly irregular mass distribution, dubbed mascons, most lunar orbits below 500 km altitude are highly unstable [17], causing spacecraft stationed in these orbits to be doomed to crash into the Moon after times on the order of weeks to months unless kept there manually using lots of stationkeeping (>$50\,\mathrm{m\,s^{-1}\,yr^{-1}}$) [43]. Although switching the focus to higher lunar orbits can mitigate these effects, other perturbations start to become more noticeable at these altitudes. Most notably, third-body perturbations due to the Earth start dominating over perturbations due to lunar mascons for altitudes above 500 km, again leading to unstable orbits [44]. This leaves the design space for long-term viable lunar orbits (orbits with limited needs for stationkeeping) restricted to frozen lunar orbits.

Frozen orbits refer to all orbits in which perturbations on average cancel out over a given timescale. Seeing as for these orbits the semi-major axis a, eccentricity e, inclination i and argument of periapsis ω remain constant on average, in principle no stationkeeping is required, making these orbits viable for long-term missions. Here, it should be noted that the right ascension of the ascending node Ω for frozen lunar orbits does not remain constant over time, seeing as viable solutions for selenocentric orbits do not exist: nodal precession over the mission lifetime should thus be expected in any case. Frozen orbits exist at both lower altitudes, the Frozen Low Lunar Orbits (FLLO) for which the perturbing effects of lunar mascons cancel out, and at higher altitudes, the Elliptical Lunar Frozen Orbits (ELFO) for which the perturbing effects of the Earth cancel. As discussed by Janssen et al. [7], for the LUMEN mission ELFOs are preferred over FLLOs due to their longer contact times, shorter eclipse times and reduced ΔV costs for orbit insertion.

5.1.2. ELFO Constraints

The ELFO family is quite limited in terms of freedom in the choice of orbital elements: for the net perturbing effect of the Earth to cancel out, specific choices of orbital elements are required [44]. First of all, to keep e constant over time, ω must be set to either $0\,°$, $90\,°$, $180\,°$ or $270\,°$. Also, to keep the chosen value for ω constant over time itself, its value is restricted to either $90\,°$ or $270\,°$. In principle, no restrictions on the semi-major axis a on its own exist, apart from the general constraint that all orbital altitudes should remain within the range of 500 km to $20\,000$ km: at lower altitudes, perturbations due to lunar mascons start dominating over the Earth's third-body perturbations, and at higher altitudes, the problem starts approaching a three-body problem as opposed to a two-body perturbed problem [45]. For e, i and Ω more complex constraints exist.

Orbit designers have the most amount of freedom in selecting an ELFO's semi-major axis and the combination of its eccentricity and inclination. For ELFOs, the orbit's eccentricity e is directly related

[17] URL: `https://science.nasa.gov/science-news/science-at-nasa/2006/06nov_loworbit/` [Cited 02/06/2023]

to its inclination i, following Equation (5.1) [45]:

$$e = \sqrt{1 - \frac{5}{3}\left(\frac{\cos(i^{ep}) + \sin(i_M^E)\sin(i^{op})\cos(\Omega^{op})}{\cos(i_M^E)}\right)^2} \tag{5.1}$$

Here, i^{ep} denotes the ELFO's inclination with respect to the Moon's equatorial plane (the usual definition for an orbit's inclination), i_M^E denotes the inclination of the Earth's apparent orbit (in a Moon-fixed frame) with respect to the Moon's equatorial plane, i^{op} denotes the ELFO's inclination with respect to the Earth's apparent orbit, and Ω^{op} denotes the ELFO's right ascension of the ascending node as measured from the Earth's apparent orbital plane. These angles are also shown in Figure 5.1, where the x-axis of the frame points at the intersection of the Moon's equatorial plane with the Earth's apparent orbital plane (it thus points towards the ascending node of the Earth's apparent orbit).

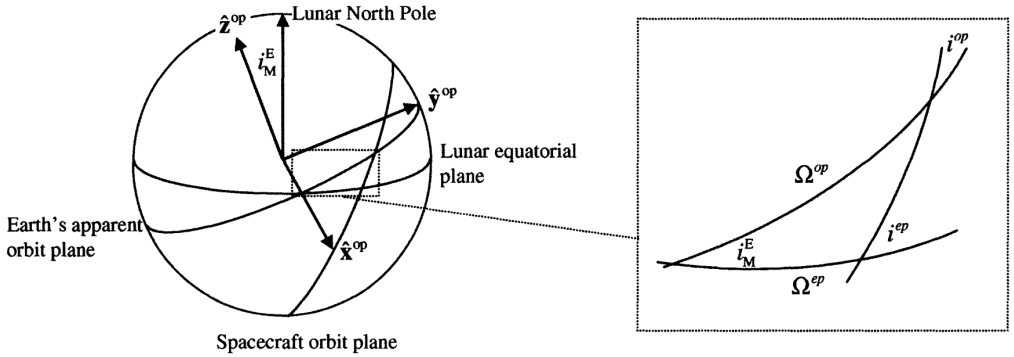

Figure 5.1: The lunar equatorial and Earth orbit planes taken from Ely [45].

By setting Ω^{op} equal to $90\,°$ and by considering $sin(i_M^E) \approx 0$ and $cos(i_M^E) \approx 1$, as the Moon's declination i_M^E $=6.68\,°$ is small[18], this expression may be simplified to the one given in Figure 5.2 [44], with the superscript ep dropped:

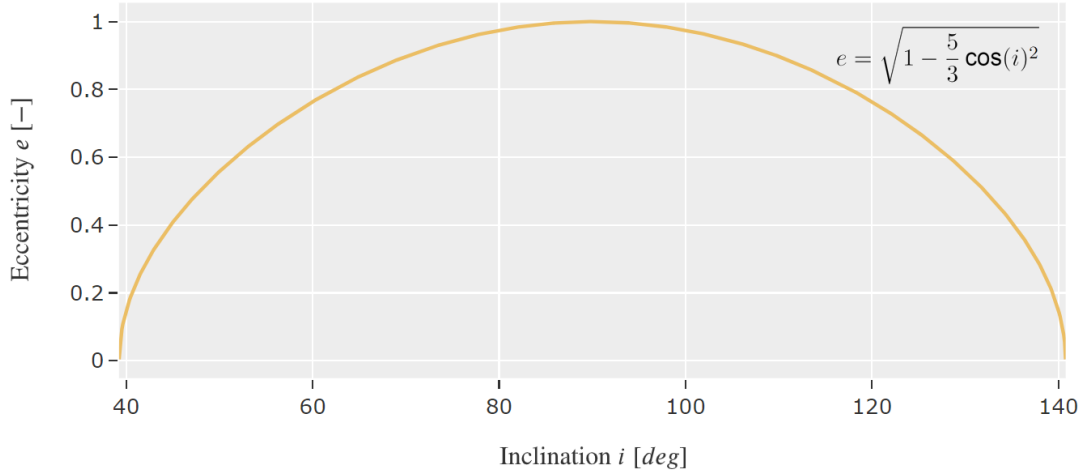

Figure 5.2: Eccentricity - inclination relation for ELFOs.

Again, this assumes Ω^{op} equals $90\,°$, which has important implications for the ELFO's required right ascension of the ascending node Ω. Seeing as the ELFO's right ascension should equal $90\,°$ as measured from the x-axis, and seeing as the x-axis points towards the ascending node of the Earth's orbital plane, the ELFO's right ascension should be equal to the right ascension of the ascending node of the Earth's apparent orbit plus $90\,°$. As this condition should be satisfied at orbit insertion, and as

[18] URL: `https://nssdc.gsfc.nasa.gov/planetary/factsheet/moonfact.html` [Cited 22/06/2023]

the Earth's apparent right ascension varies with time, the ELFO's required value for Ω is dependent on the launch date and transfer time.

5.1.3. Other Orbit Considerations

Although the orbital elements of ELFOs are highly constrained, their combinations can still be tailored towards desirable performance characteristics for SBSP applications. One of the most important performance characteristics of LUMEN's spacecraft is the percentage of each orbital period spent in contact with the lunar South Pole. Seeing as a spacecraft moves slowest through its apoapsis, this contact time can be maximised by choosing a highly eccentric orbit having its apoapsis lie over the lunar South Pole, achieved by setting ω equal to $90\,°$ (complying with the ELFO constraints). For further maximising this contact time, it is then logical that choosing a near-polar inclination with a high eccentricity, as given by the central region of Figure 5.2, and choosing a high value for a is beneficial. It should however be noted that choosing a high a and near-polar i (and thus a high e) comes at the cost of increasing the average altitude during laser transmission of power to the lunar South Pole, thus making accurate laser pointing more difficult. There thus exists a general trade-off between increasing transmission time and increasing average transmission altitude, which will also be explored in Section 5.3.

Another remark that should be made at this stage is the observation that Figure 5.2 is symmetrical about $i = 90\,°$, meaning ELFO constraints allow for both prograde ($i < 90\,°$) and retrograde ($i > 90\,°$) orbits. In general, any perturbed orbit will experience nodal precession in the direction opposite to its direction of rotation about its central body. Seeing as retrograde orbits, when seen from above (North), are characterised by counterclockwise rotation about the Moon, while the Moon's rotation about the Sun is clockwise, this gives retrograde orbits the unique property of nodal precession in the direction of the Moon's rotation about the Sun (positive nodal precession). This same principle is responsible for Earth's Sun-Synchronous Orbits, where the orientation of these orbits with respect to the Sun is constant due to their precession rate equalling $\frac{360\,°}{365.25\,\text{days}} = 0.986\,°/\text{d}$, alleviating the need for slewing manoeuvres to keep the Sun in view. As selecting a perfectly Sun-Synchronous ELFO will not be possible due to the oscillatory nature of its orbital elements over time, positive (clockwise) spacecraft slewing manoeuvres will inevitably be necessary for LUMEN to keep the Sun in view over its mission lifetime. Seeing as a positive precession rate, and thus a retrograde orbit, would already (partially) account for this required motion, any retrograde orbit is preferred over any prograde one having an equally polar inclination. This argument is further explained using Figure 5.3:

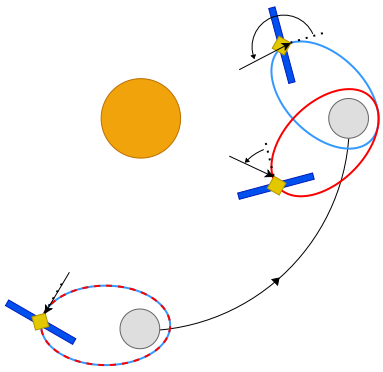

Figure 5.3: Nodal precession and required slewing manoeuvers of prograde (blue) versus retrograde (red) orbits.

This figure shows the nodal procession over a period of 3 months (the Earth and thus also the Moon has rotated 90 degrees around the Sun) for a prograde (blue) and a retrograde (red) orbit. While the spacecraft's arrays initially face the Sun, its relative orientation will change because of the Moon's rotation. For both the prograde and retrograde orbit, the spacecraft's orientation will be off after the 3 elapsed months: however, as shown by Figure 5.3, for the retrograde orbit the spacecraft's

required slew angle to counteract this rotation will be smaller. Also, from a preliminary assessment using NASA's GMAT software, a very slight reduction in required injection ΔV was observed for lunar retrograde orbits over prograde orbits, reinforcing the choice to limit future analysis to retrograde ELFOs. As a consequence, the design space for LUMEN's optimal orbit will be limited to the right side of the central part of Figure 5.2.

Finally, for the LUMEN mission, a tandem orbit of spacecraft equally spaced in time would be preferred. Such a configuration would be characterised by having all spacecraft orbit in the same orbital plane, rather than using a constellation (e.g. two orbital planes spaced $180\,°$ apart). While choosing a constellation of multiple orbital planes can be a powerful tool for achieving global coverage, the requirement to provide power just to the lunar South Pole makes this advantage irrelevant for the sake of this mission. Also, a constellation would inevitably add points of intersection between the orbital planes, increasing the risk of collision between two spacecraft. Lastly, while selecting a constellation could solve the problem of overcrowded orbits, where the spacing between spacecraft becomes too small to manage, due to the large perimeters of ELFOs this problem is only expected to become relevant for numbers of spacecraft on the order of multiple hundreds to thousands. Spacing the spacecraft equally in time over the orbit's orbital period would have the advantage of leading to the most constant contact performance over time.

5.2. Orbit Performance Calculations

From just knowledge of an orbit's Keplerian elements and the number of spacecraft used, a lot of information about the spacecraft's performance can be deduced via a range of calculations. Estimating these values is not only important in finding spacecraft performance for a given orbit, but also allows for comparing the performance of spacecraft in different orbits. This section will give an overview of the tool that was set up for these performance calculations.

5.2.1. Orbit Performance Tool Description

The system's orbit is a very important driver for the design of its subsystems, making quantifying its characteristics crucial for the overall system design. To achieve this goal, an extensive Python code was written, dubbed the orbit performance tool.

A lot of any orbit's most important performance characteristics, like contact times, eclipse times and transmission angles, can be estimated from knowledge of just a spacecraft's position and orientation relative to other bodies in space. The orbit performance tool is an exclusively geometrical tool, requiring only the orbit's Keplerian elements and its number of spacecraft as inputs. Then, using a combination of derived geometrical relations and linear algebra, a datasheet of numerical performance characteristics is outputted, allowing for making comparisons between different types of orbits. The tool also contains various plotting functionalities.

Seeing as the orbit performance tool is purely geometrical in nature and does not model any physics other than simple relations from orbital mechanics, it can not be used for assessing the motion of spacecraft over their orbital period, or to assess the temporal evolution of a spacecraft's orbit. For full functionalities, the orbit performance tool may be used in conjunction with other software like NASA's General Mission Analysis Tool (GMAT), an open-source tool for space mission design[19]. A general procedure could be to model the temporal propagation of a spacecraft and its orbit using GMAT, resulting in a dataset showing the evolution of the orbit's Keplerian elements over time. By then analyzing each data point of this dataset using the orbit performance tool, the temporal evolution of an orbit's performance characteristics may then be determined as a function of time.

5.2.2. Orbit Assumptions

In setting up the orbit performance tool, a number of simplifying assumptions were made. An overview of these assumptions is given in Table 5.1, where assumptions have been split up into those affecting transmission (T) and eclipse (E) performance.

[19] URL: `https://software.nasa.gov/software/GSC-17177-1` [Cited 22/06/2023]

Table 5.1: Orbit performance tool assumptions.

Index	Assumption	Effect	Justification
T1	The receiver is located exactly at the lunar South Pole	Contact time and laser pointing are not affected by nodal precession	The centre of the Shackleton crater is actually located at $89.54\,°$S $0.0\,°$E)[20], very close to the true South Pole, and the cut-off elevation for contact is quite low ($\approx 21.8\,°$)
T2	Treat each spacecraft's array of laser modules as producing a single, infinitely thin laser beam	Simplified laser beam angle of incidence calculations by neglecting variations in the laser's angle of incidence due to its finite beam width	The laser's beam width is negligible compared to the orbital altitude
E1	Neglect the Moon's penumbra and antumbra	Moon eclipse detection is simplified (cylindrical shadow), light intensities are simplified (0% in eclipse, 100% out of eclipse)	Because of the large Sun-Moon distance and the Moon's relatively small size, the Moon's penumbra is very small and its antumbra is located very far behind the Moon
E2	For Moon eclipse considerations, the Moon lies in the ecliptic plane	Moon eclipse detection is simplified, as the Moon's shadow will always be parallel to the ecliptic plane	The inclination of the Moon's orbital plane around the Earth is certainly not negligible at $5.145\,°$ [21]. Yet, because of the large Sun-Earth distance as compared to the Earth-Moon distance, with respect to the Sun, this inclination may be neglected.
E3	The light intensity inside the Earth's penumbra is equal to 50% of the light intensity out of eclipse	Simplified Earth eclipse calculations	The real light intensity lies somewhere between 0% and 100%, where 50% is an average value
E4	Neglect the number of spacecraft for Earth eclipse calculations	Simplified assessment by considering all spacecraft to be eclipsed when any spacecraft is eclipsed by the Earth	The Earth's shadow at Earth-Moon distance is large compared to the size of the Moon

Considering the assumptions from Table 5.1, a couple of remarks should be made. First of all, note how assumption E1 is conservative: the implications of this assumption are that the size of the Moon's shadow is slightly overestimated, while the eclipsed light intensity is underestimated. A similar consideration can be made for assumption E4. Also, note how assumption E2 only applies to Moon eclipse detection: when considering eclipses due to the Earth, this assumption can no longer be made, seeing as this would lead to a significant overestimation of the amount of Earth eclipses. Finally, while assumption E1 indicates the penumbra and antumbra of the Moon are neglected, this assumption is not made for the penumbra of the Earth, which is very significant in Earth eclipse calculations.

5.2.3. Three-Dimensional Position Determination

With the orbit performance tool's functionalities mostly relying on geometrical relations in three-dimensional space, perhaps its most important functionality is being capable of accurately modelling the 3D position of LUMEN's spacecraft. This is achieved by first specifying a discretization in time, spanning one

[20] URL: `https://www.esa.int/Science_Exploration/Space_Science/SMART-1/Shackleton_crater_SMART-1_s_search_for_light_shadow_and_ice_at_lunar_South_Pole` [Cited 22/06/2023]

[21] URL: `https://nssdc.gsfc.nasa.gov/planetary/factsheet/moonfact.html` [Cited 22/06/2023]

orbital period and equally split up across the total number of spacecraft used for an equal spacing in time. From this discretization in time t, the orbit's two-dimensional Cartesian components ξ and η may be determined using the equations given below [46]:

$$M = 2\pi \frac{t}{T} \tag{5.2}$$

$$E - e\sin(E) = M \tag{5.3}$$

$$\theta = 2\arctan\left(\frac{\tan(\frac{E}{2})}{\sqrt{\frac{1-e}{1+e}}}\right) \tag{5.4}$$

$$r = \frac{a(1-e^2)}{1+e\cos(\theta)} \tag{5.5}$$

$$\xi = r\cos(\theta) \tag{5.6}$$

$$\eta = r\sin(\theta) \tag{5.7}$$

As shown, the discretization in time is first converted to mean anomaly M, eccentric anomaly E, true anomaly θ and orbital radius r in intermediate calculation steps. Here $T = 2\pi\sqrt{\frac{a^3}{\mu_M}}$ denotes the orbital period, where μ_M represents the Moon's gravitational parameter. Also, note how Equation (5.3) is transcendental, and as such solving for E must be done numerically.

Finally, estimating a spacecraft's three-dimensional position as a function of time is done by means of transforming the obtained 2D position to 3D space using the transformation matrix given in Equation (5.8) [22]. This matrix is comprised of values computed using the orbit's Keplerian elements.

$$\begin{bmatrix} x \\ y \\ z \end{bmatrix} = \begin{bmatrix} l_1 & l_2 \\ m_1 & m_2 \\ n_1 & n_2 \end{bmatrix} \begin{bmatrix} \xi \\ \eta \end{bmatrix} \tag{5.8}$$

Here $l_1 = \cos(\Omega)\cos(\omega) - \sin(\Omega)\sin(\omega)\cos(i)$, $l_2 = -\cos(\Omega)\sin(\omega) - \sin(\Omega)\cos(\omega)\cos(i)$, $m_1 = \sin(\Omega)\cos(\omega) + \cos(\Omega)\sin(\omega)\cos(i)$, $m_2 = -\sin(\Omega)\cos(\omega) + \cos(\Omega)\cos(\omega)\cos(i)$, $n_1 = \sin(\omega)\sin(i)$ and $n_2 = \cos(\omega)\sin(i)$.

5.2.4. Transmission Characteristics

LUMEN's goal of providing 1 MW of power continuously to the lunar South Pole is highly dependent on the amount of spacecraft in view of the receiver at any given moment, the time available for power transmission per orbit, and the efficiency at which this is done. These characteristics, as well as constraints on laser pointing during contact, will be analysed below. Transmission logic is explained using the notion of a "transmission cone", a cone extending from the receiver (lunar South Pole) characterised by a view angle of $68.2\,°$, as obtained from the receiver's cut-off elevation of $21.8\,°$. Transmission is then only considered possible when a spacecraft lies within this transmission cone. A visualisation of this transmission cone for an example orbit housing 30 spacecraft can be found in Figure 5.4.

Transmission Time

The transmission time t_t is estimated by finding the difference in time between the points of intersection between the orbital plane and the transmission cone. Although this parameter is useful in itself, it might be more descriptive for characterising the orbit's performance to express transmission time as a percentage of the orbital period, denoted by transmission percentage η_t. Because of the design choice of spacing spacecraft equally in time across the orbit, the minimum number of spacecraft in view of the receiver at any given time is easily determined. First, t_t is divided by the temporal spacing, itself obtained by dividing the orbital period T by the number of spacecraft. By then rounding this value down to the nearest integer (half spacecraft do not exist) and by subtracting 1 to account for the time in which one spacecraft has left the transmission cone while the next spacecraft has not entered yet, the number of spacecraft in view can be obtained.

[22] URL: https://ocw.tudelft.nl/wp-content/uploads/AE2104-Orbital-Mechanics-Slides_10.pdf [Cited 02/06/2023]

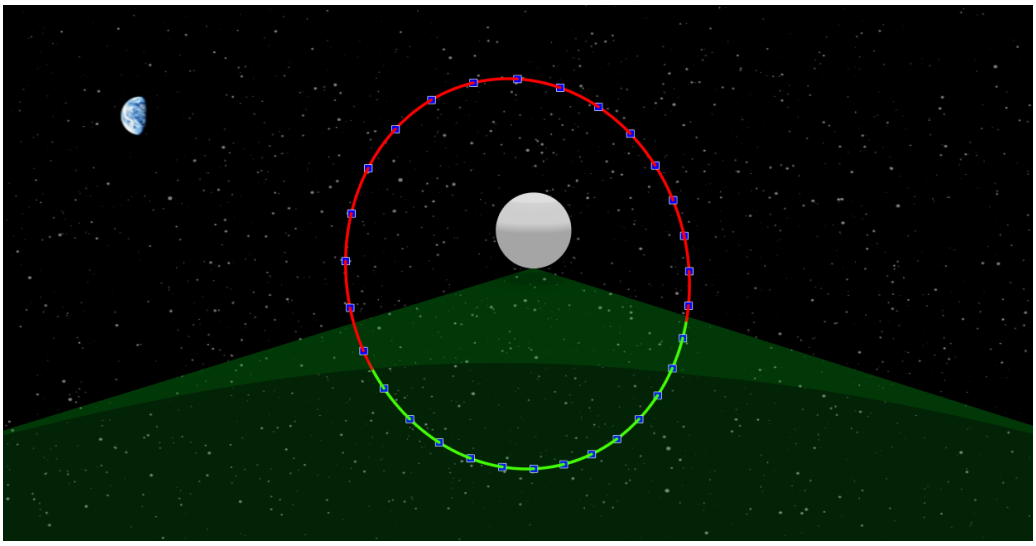

Figure 5.4: Orbit performance tool visualisation of the transmission cone.

Transmitter-Receiver Efficiency

The efficiency of transmission is directly affected by the angle of incidence between the receiver and the incoming laser beams: for a given laser beam, this efficiency is modelled by considering the reflectance of the incidence angle of that beam, as was explained in Section 4.1.3. To find the angle of incidence between the receiver and a laser originating from a certain point in the transmission cone, the angle of the vector pointing from that point to the receiver with respect to the vector normal to the receiver's plane is evaluated. By computing the reflectance for this angle, repeating this procedure for every time-discretized point lying in the transmission cone, taking the average value of these reflectances and finally subtracting this value from 1, the incidence efficiency η_i may be computed.

Another parameter indirectly affecting transmitter-receiver efficiency is the required receiver diameter, which can be estimated assuming spacecraft pointing accuracy is already known. As may be concluded from Equation (4.1), the required receiver diameter depends on the chosen orbit, seeing as it depends on the combination of distance from the transmitter to the receiver z (from now on referred to as the transmission altitude h_t) and the beam dilution factor f_{bd}. Here, h_t is easily calculated by evaluating the length of the vector pointing from a given point in the transmission cone to the receiver, and f_{bd} is calculated from knowledge on this transmission altitude and the incidence angle. Estimating h_t and f_{bd} for each time-discretized point lying in the transmission cone, applying Equation (4.1) and taking the maximum value, the minimum required receiver diameter can be evaluated.

Laser Pointing

Seeing as the position and orientation of spacecraft relative to the receiver can be computed at all times, the required angles over which the laser should be rotated to keep pointing at the receiver can also be computed, given a specified coordinate system. For the sake of laser pointing, a body-fixed coordinate system was chosen, as represented in Figure 5.5 by coordinate system "b": from this figure, it is obvious that each orbital revolution, some rotations of the laser over the x_b and z_b axes will be necessary to keep pointing at the lunar South Pole.

To estimate the required rotations over the x_b and z_b axes for each orbital revolution, the incidence angles for all points of transmission are decomposed along the x_b and z_b axes. It is then assumed that to reset the laser to its original position, the full time outside of the transmission cone is used, at constant angular velocities about the x_b and z_b axes. Seeing as the spacecraft body is constantly slewing about the z_b axis for pointing its solar arrays at the Sun, while the position of the laser is defined relative to the spacecraft body, the required z_b angle for laser pointing will also constantly be changing. More specifically, for a positive slew angle of $90\,°$, all required z_b angles for laser pointing should be decreased by $90\,°$ to counteract these slewing manoeuvres. As over the mission's lifetime the spacecraft will have to perform full slewing rotations about the z_b axis a number of times, this also

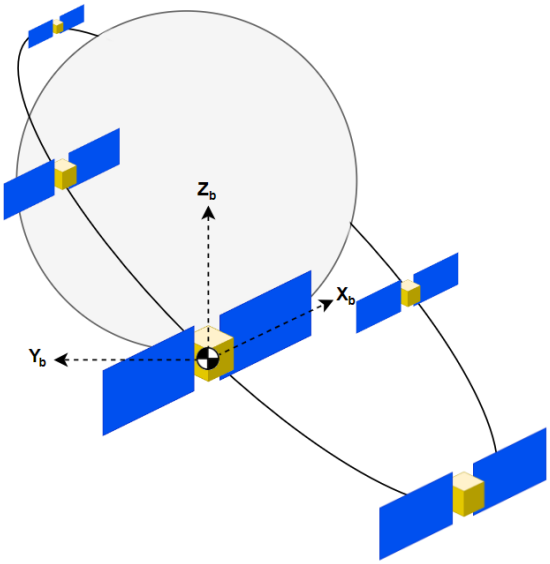

Figure 5.5: Laser pointing coordinate system.

requires the laser to be capable of rotating $360\,^{\circ}$ about the z_b axis.

5.2.5. Eclipse Characteristics

Eclipses form situations in which no solar power is available for certain periods of time, affecting the battery size for LUMEN's spacecraft, the receiver or both. When considering eclipses, the distinction between Moon and Earth eclipses should be made, which occur on entirely different timescales, drive the design in completely different ways and are estimated using different procedures. Eclipse logic is explained using the notion of a "shadow cylinder", a cylinder extending from a body's side opposite to the Sun, parallel to the incoming light, and representing the shadow that body would cast over space. A visualisation of this shadow cylinder for an example orbit housing 30 spacecraft can be found in Figure 5.6.

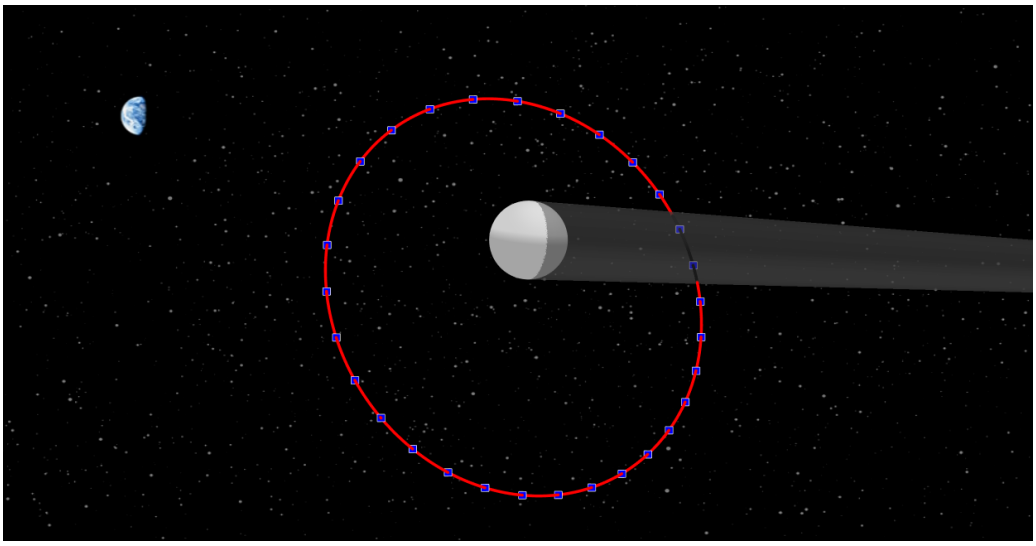

Figure 5.6: Orbit performance tool visualisation of the shadow cylinder.

Moon Eclipses

Eclipses by the Moon occur (almost) every orbital period, and last for times on the order of minutes to hours. A Moon eclipse is a spacecraft-specific event: due to the large amount of spacecraft in orbit, when a specific spacecraft is eclipsed, most others will not at that same instant. Seeing as the transmission cone extends downwards from the lunar South Pole, starting from an elevation of

$21.8\,°$, and considering that the shadow cylinder extends sideways from the Moon, always at an angle shallower than $6.68\,°$ (the Moon's declination), intersection of the transmission cone and the Moon's shadow cylinder is impossible. As a result, spacecraft capable of transmitting can never experience a Moon eclipse at the same time, meaning Moon eclipses will not hinder power transmission and as such will not affect required battery size for power transmission, either at each spacecraft or at the receiver. Rather, Moon eclipses are an important driver for a spacecraft's required battery size for providing its own subsystems with sufficient levels of power during eclipse.

For estimating Moon eclipse characteristics, a spacecraft is considered eclipsed when lying within the perimeters of the Moon's projected shadow cylinder. This cylinder is coincident with the centre of the Moon, has a radius equal to the Moon's radius of $R_M = 1737.4\,\text{km}$ and extends from the Moon's current dark side to infinity, parallel to the vector pointing from the Sun to the Moon. By assessing whether points of intersection between the orbital plane and the shadow cylinder exist, Moon eclipses can be identified. Then, by finding the difference in time between these points of intersection, the spacecraft's Moon eclipse time t_M can be found. Also, the maximum velocity when entering or leaving the shadow cone, denoted by v_M, can be calculated to estimate temperature gradients encountered when entering or leaving eclipse.

As the Moon orbits around the Earth, which in turn orbits around the Sun, over the mission's lifetime light will always come from different directions relative to the orbital plane. Also, seeing as the Moon has a declination of $6.68\,°$ with respect to the ecliptic plane, the Moon's shadow cone will in general not be parallel to its equatorial plane. As each spacecraft should be designed for the maximum (worst-case) eclipse time it will encounter over its mission lifetime, the aforementioned procedure is performed for all possible directions of incoming light, where the longest eclipse time encountered across all iterations is used to size the system.

Earth Eclipses

Eclipses by the Earth are quite rare, occurring only twice a year on average, and last for times on the order of hours[23]. An Earth eclipse is a Moon-wide event: because of the large size of Earth's projected shadow cylinder relative to the Moon, during each Earth eclipse most (if not all) spacecraft are eclipsed at the same time. This also means that during an Earth eclipse, spacecraft capable of transmitting could be shadowed, hindering the transmission-receiver segment. Earth eclipses thus pose a serious challenge for LUMEN, making power transmission next to impossible for hours at a time.

For estimating Earth eclipse characteristics, GMAT's EclipseLocator functionality was used, considering both partial and total eclipses. By propagating a spacecraft for its mission lifetime of 25 years (from 2030 to 2055), and by estimating each eclipse time as the time spent in umbra plus 50% of the time spent in penumbra (arising from assumption E3), the longest Earth eclipse over the spacecraft's lifetime can be estimated. The minimum time between two Earth eclipses was also estimated, seeing as this could drive receiver battery size.

5.3. Orbit Optimisation

While the orbit chosen during an earlier stage of LUMEN's design showed good performance, as described by Janssen et al. [7], its orbital elements were never formally justified, having been selected based on initial engineering judgement. This section will describe the procedure used to formally select an orbit, based on the optimisation of an orbit efficiency score. An overview of the optimised orbit's characteristics will also be given.

5.3.1. Boundary Conditions

Before giving an overview of the orbit optimisation procedure, the used boundary conditions for the optimisation are discussed. These values are important in limiting computational effort by discarding

[23] URL: `https://solarsystem.nasa.gov/moons/earths-moon/lunar-phases-and-eclipses/#:~:text=a%20Lunar%20Eclipse%3F-,During%20a%20lunar%20eclipse%2C%20Earth%20comes%20between%20the%20Sun%20and,Earth's%20shadow%20covers%20the%20Moon` [Cited 02/06/2023]

obviously unfeasible options, and in ensuring the eventually selected orbit still meets all requirements. For the orbit optimisation, the following boundary conditions were considered:

- **BC1**: Periapsis altitude $h_{peri} > 500$ km.
- **BC2**: Apoapsis altitude $h_{apo} < 20\,000$ km.
- **BC3**: Maximum transmission altitude $h_{t,max} < 14\,150$ km.
- **BC4**: Inclination $110\,° < i < 140.75\,°$.
- **BC5**: Eccentricity e follows Figure 5.2.
- **BC6:** Argument of periapsis $\omega = 90\,°$.

Here, BC1 and BC2 arise from the requirement to keep all orbital altitudes within the range of 500 km to $20\,000$ km, based on the ELFO constraints presented by Ely [45] and as explained in Section 5.1.2: this ensures the Moon remains the orbit's central body (two-body perturbed problem as opposed to a three-body problem) and mitigates the effect of lunar mascon perturbations, which could lead to unpredictable perturbations by only affecting the orbit's periapsis. These constraints also indirectly help in mitigating the risk of colliding with the Moon, in mitigating the effect of the lunar dust present at lower altitudes, which could decrease solar array performance, and in making sure laser pointing remains feasible by setting an upper limit on the transmission altitude [47]. A boundary condition more directly related to the feasibility of meeting pointing requirements is BC3: this constraint was imposed to ensure the orbit's required receiver diameter would remain below the 80 m value imposed in Section 4.1.2. The specific value of $14\,150$ km was obtained assuming the overestimated f_{bd} of 1.286 corresponding to the orbit described by Janssen et al. [7]. Finally, BC4 and BC5 restrict the choice in orbit to near-polar retrograde ELFOs, as were deemed optimal in Section 5.1. No inclinations between $90\,°$ and $110\,°$ were considered, seeing as this would lead to eccentricities greater than 0.9, which could over-complicate the system by increasing the transmission altitude and by leading to even higher variability of the spacecraft's environment.

5.3.2. Orbit Optimisation Procedure

In general, to be able to optimise something, the parameter to be optimised for should first be defined. In this case, the orbit efficiency score, defined as equalling the product of transmission percentage η_t and incidence efficiency η_i, was selected to be optimised for. This choice was made as η_t and η_i are considered to be the orbit's most important characteristics, having the largest influence on LUMEN's design. For example, a higher value for η_t can significantly reduce the total required system mass: if LUMEN's spacecraft are sized according to the orbit's minimum number of spacecraft in view at any given time, the total number of these spacecraft required to be in orbit should be significantly higher to account for times at which these spacecraft do not lie in the transmission cone. Having a higher value for η_t will then bring this required number of spacecraft closer down to the number of spacecraft in view, decreasing the total system mass. A higher value for η_i will directly influence the amount of power received at the lunar South Pole, allowing for downscaling each spacecraft's solar arrays.

At this moment, the oscillatory nature of ELFOs should be re-emphasized. While a specific combination of optimal orbital elements, adhering to the ELFO constraints, can be found by maximising the orbit efficiency score, this optimal performance will most of the time not be observed due to oscillations of these orbital elements over time. In fact, this optimal performance will not even be observed over the mission lifetime on average, seeing as an ELFO's initial conditions do not necessarily exactly correspond to its observed equilibrium values. This seriously brings the final orbit's computed optimality into question, seeing as it was not its average performance that was optimised for, but only its beginning-of-life performance. However, through comparing the orbital performance characteristics of ELFOs at beginning-of-life with their long-term averaged performance, initial conditions corresponding to higher orbit efficiency scores were confirmed to correspond to orbits showing higher orbit efficiency scores on average. As such, the optimisation procedure was considered acceptable for finding a high-performance orbit for LUMEN's applications, though future recommendations could be given to optimise the orbit for its lifetime-averaged performance directly.

Another consequence of ELFOs' oscillatory nature has to do with orbits not always meeting the imposed boundary conditions: while the optimised ELFO at beginning-of-life will always meet the im-

posed boundary conditions, its oscillatory nature could in principle lead to some boundary conditions no longer being met at later moments in time along LUMEN's lifetime. However, as will also be shown in Section 5.4, these moments are infrequent, last for relatively short times and undershoot or overshoot the boundary conditions by only small margins. Also, seeing as the worst-case performance of the orbit over its entire lifetime will be used to size LUMEN anyways, this effect was not considered to form a problem for LUMEN's design.

Finally, the general outline of the orbit optimisation procedure can be represented as follows:

1. Constrained by the boundary conditions, find all allowed combinations for a, e, i and ω.
2. Calculate the orbit efficiency score for each allowed combination of orbital elements.
3. Find the combination of orbital elements resulting in the highest orbit efficiency score: this could be the optimal orbit.
4. Propagate the orbit showing the highest orbit efficiency score for 25 years using GMAT: export the evolution of its orbital elements over time.
5. For this same orbit, calculate the minimum required receiver diameter for every point in the mission's lifetime.
6. Find the highest value for the minimum required receiver diameter over the mission's lifetime: verify that this calculated receiver diameter meets the imposed (80 ± 10) m requirement.
7. In case the (80 ± 10) m receiver diameter requirement is met over the orbit's entire lifetime, the optimal orbit has been found: if the receiver diameter requirement is not met, repeat steps 4-7 for the next best orbit option.

5.3.3. Optimised Orbit Description

The described orbit optimisation procedure converged to an orbit having an orbit efficiency score of 72.07: this ELFO is characterised by beginning-of-life orbital elements equal to $a = 8934.37$ km, $e = 0.7438$, $i = 121.18\,°$ and $\omega = 90\,°$. A visualisation of this orbit including the orbital path (red), the transmission cone and transmitting path (green) and the shadow cylinder and ecliped path (grey) can be found in Figure 5.7. This orbit houses 133 spacecraft, equally spaced in time, represented as blue squares of solar array: note how these have not been represented to scale, where in reality the spacecraft would always be spaced apart at a distance larger than 164.47 km. A more complete overview of the optimised orbit's performance, including variations of this performance over its lifetime, will be given in the next sections.

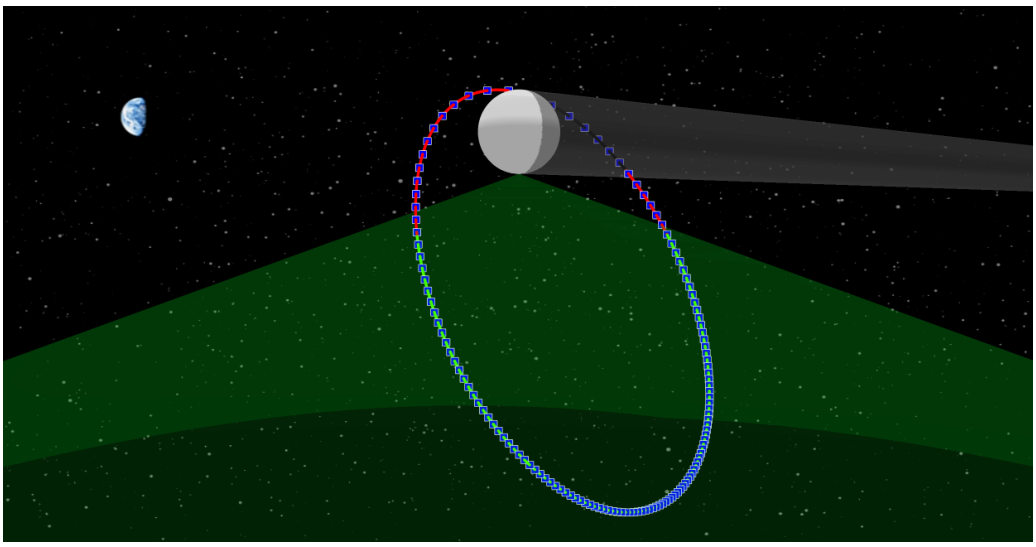

Figure 5.7: Orbit performance tool visualisation of 133 spacecraft in the optimised orbit.

5.3.4. Orbit Optimisation Sensitivity

As for any optimisation procedure, questions regarding the optimisation's confidence naturally arise; as the optimal orbit is a result of its boundary conditions, how would changing these boundary con-

ditions change the optimisation's outcome? Also, how does the optimal orbit perform relative to the other options? When considering these questions, it should first be noted that the optimal orbit arising from the orbit optimisation might not necessarily be the most optimal one in all regards: rather, it is the most optimal ELFO for maximising the product of transmission percentage and incidence efficiency, constrained by the receiver size and pointing accuracies given in Chapter 4.

To assess whether the right optimisation procedure was applied, the sensitivity of the imposed boundary conditions is analysed. Although changing BC1, BC2, BC4, BC5 and BC6 would have a large impact on the optimisation's outcome, all of these values are based on previously conducted studies on ELFOs: as selecting an ELFO has already been justified to be the optimal choice for LUMEN, complying with these values is necessary, and as such the effect of changing these boundary conditions is irrelevant. While BC6 could in theory be alleviated to also allow for $\omega = 270\,°$, orbits making use of this option would never be selected, seeing as placing the orbit's periapsis over the lunar South Pole would severely decrease the transmission percentage that was optimised for. The most interesting boundary condition to analyse is BC3, seeing as it is not inherent to ELFOs: rather, this boundary condition is the direct result of the system's receiver and pointing characteristics. The effect of changing this boundary condition on the selected orbit's efficiency score, and thus on the selected orbit, is graphically represented in Figure 5.8.

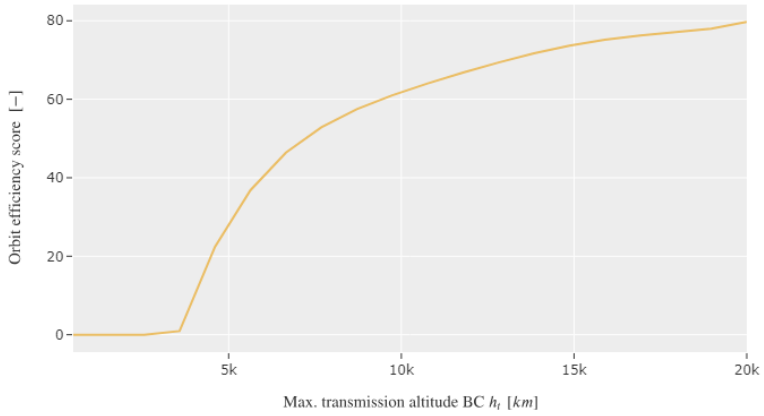

Figure 5.8: Orbit efficiency score for varying transmission altitude boundary conditions.

From this graph, it may be concluded that the less stringent the transmission altitude constraint, the higher the maximum achievable orbit efficiency score: this makes sense, seeing as increasing the average transmission altitude will increase both the transmission percentage and the incidence efficiency. Theoretically, a more optimal orbit could thus be found if this boundary condition was changed to a higher altitude. This is however not possible when considering the receiver size constraint, indeed making the selected orbit the most optimal one for this specific use case. It should also be noted that in case the $14\,150$ km value was slightly over or underestimated, the outcome of the optimisation would not significantly change anyways: within the range of $14\,000$ km to $14\,300$ km, the orbit efficiency score is only observed to vary by 0.6, which comes down to only about 0.83% of the selected orbit's efficiency score.

To assess whether for the presented optimisation procedure the most optimal choice was selected, the relative performance of the optimal orbit with respect to all other options is analysed for the presented optimisation procedure using the same boundary conditions. A graph showing the distribution of obtained orbit efficiency scores for a total of 10000 orbit options, where only the 1665 options meeting all boundary conditions have been included, can be found in Figure 5.9.

As can be concluded from this graph, high-scoring orbits are quite rare, with only 18 other orbits lying in the same bin as the selected orbit. Although all of these 18 orbits are very similar to the selected orbit, they also all show slightly longer eclipse times. It can therefore be concluded that the optimal orbit for the given boundary conditions has been selected with high confidence.

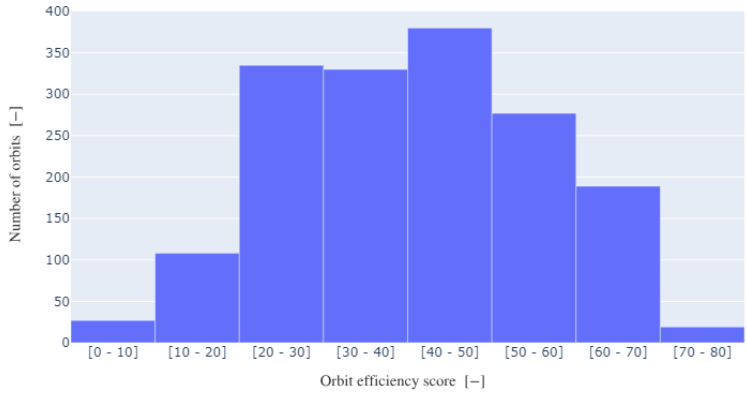

Figure 5.9: Distribution of orbit efficiency scores for orbits meeting optimisation boundary conditions

5.4. Orbital Oscillatory Ranges and Stationkeeping

As previously indicated, the ELFO constraints result in highly stable orbits, meaning orbital elements remain bounded on long timescales. It is important to note that this does not mean the orbital elements are constant over time: rather, orbital elements are observed to oscillate about certain nominal values, making them constant on average. This section will analyse the observed oscillatory ranges for the optimised orbital elements over the entire mission lifetime, discuss the need for stationkeeping, and quantify the implications these oscillatory ranges may have on LUMEN's performance as a function of time.

5.4.1. Temporal Evolution of Orbital Elements

When considering the entire mission lifetime, the optimised orbital elements only mark the first point on a graph spanning 25 years. To assess the orbit's characteristics, it is thus of uttermost importance to consider the temporal evolution of these orbital elements, rather than trying to deduce the orbit's characteristics from just this first point in time. To assess the temporal evolution of the optimised orbital elements, NASA's GMAT software was utilised, used to propagate the orbit from 01/01/2030 to 01/01/2055. For this simulation the PrinceDormand78 method was used to propagate a singular spacecraft for 25 years, under the influence of the Moon (degree 16 LP-165 gravity model), the Earth, Jupiter and the Sun (all point masses), at a temporal resolution of 1 day. The most extreme values for a, e, i and ω encountered over this period have been reported in Table 5.2; graphs showing their full evolution can be found in Figure 5.10 and Figure 5.11.

Table 5.2: Temporal evolution of optimised orbital elements.

Parameter	Unit	Initial	Minimum	Average	Maximum
Semi-major axis a	[km]	8934.37	8910.10	8930.43	8951.56
Eccentricity e	[-]	0.7438	0.6573	0.7085	0.7633
Inclination i	[°]	121.18	115.37	123.26	131.56
Argument of periapsis ω	[°]	90	75.32	90.02	103.96

Clearly, all orbital elements show oscillatory behaviour, and this behaviour is comprised of both short-period and long-period oscillatory motion. Also, while the amplitude of the semi-major axis is quite limited, the observed oscillations for all other orbital elements are more significant.

The temporal evolution of the orbit's right ascension of the ascending node Ω may also be interesting to analyse: although Ω does not oscillate, it does show precession, relevant in determining the required slew rates for LUMEN's spacecraft to always face the Sun. This nodal precession is the combined result of the Moon's J2 effect and the Earth's third-body perturbations, although the Moon's J2 only has a very limited influence. The temporal evolution of the nodal precession rate ω_p can be found in Figure 5.12.

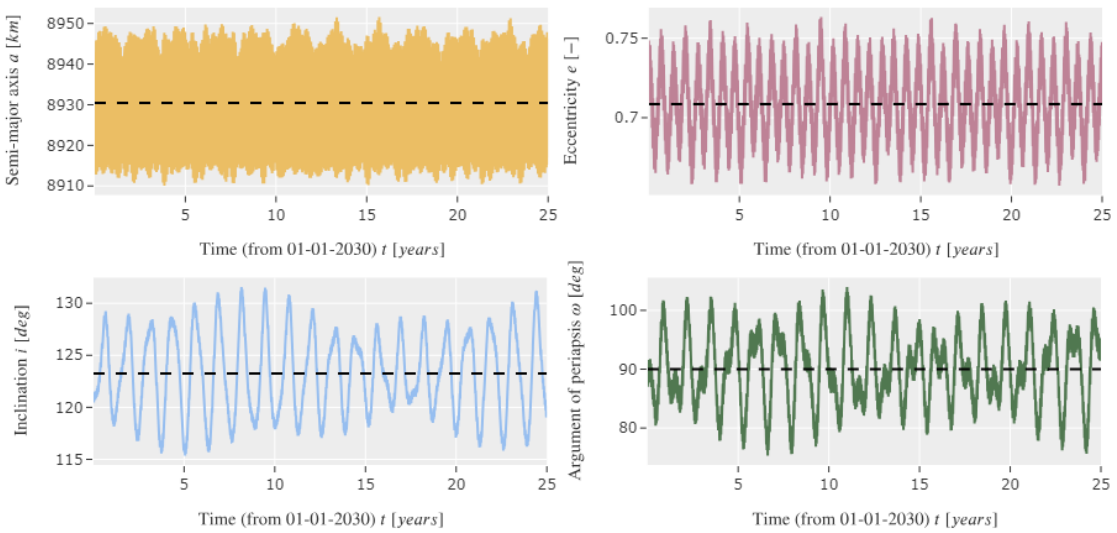

Figure 5.10: Long-term oscillation of optimised orbital elements.

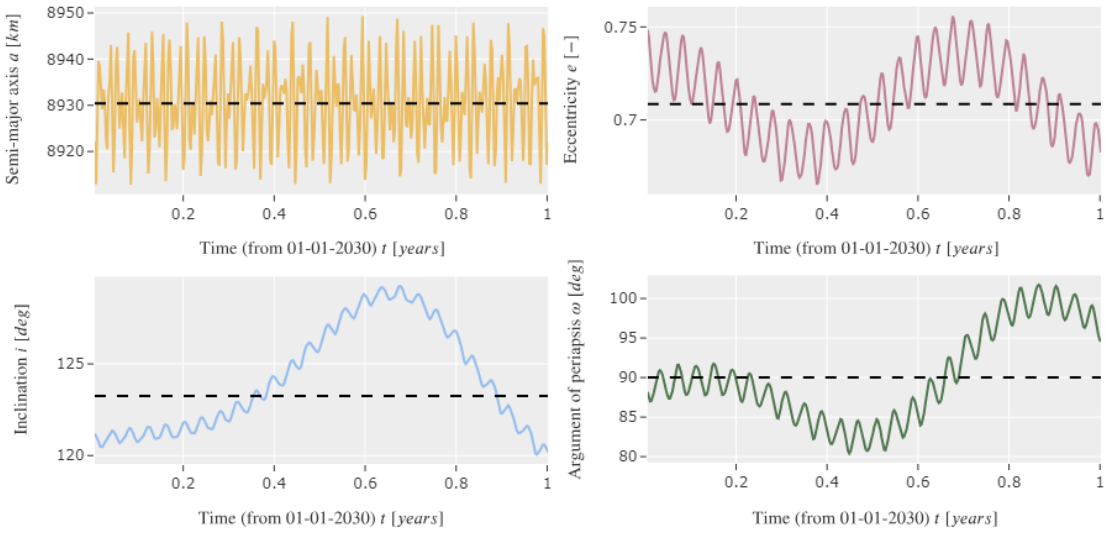

Figure 5.11: Short-term oscillation of optimised orbital elements.

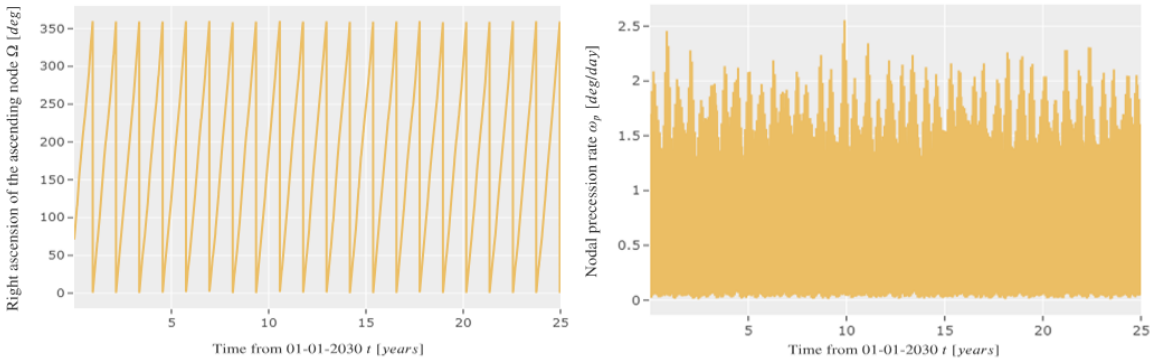

Figure 5.12: Long-term evolution of right ascension of the ascending node and nodal precession rate.

As may be concluded from this figure, the nodal precession rate is highly variable over time, ranging from $0.0851\,°/\text{d}$ to $2.5559\,°/\text{d}$. However, the average observed value of $0.8214\,°/\text{d}$ is quite close to the value of $0.986\,°/\text{d}$ required for Sun-Synchronous Orbits, resulting in the optimised orbit only requiring limited slewing manoeuvres over its lifetime.

5.4.2. Temporal Evolution of Performance Characteristics

Oscillations of the orbital elements will also induce oscillations of the orbit's performance, seen as the orbit's elements are the only inputs for the orbit performance tool. By feeding the results presented in Figure 5.10 through the orbit performance tool, these performance oscillations were obtained. The most important results have been divided into five categories, which will be treated below.

Altitudes

The temporal evolution of the orbital altitude is important for various reasons: the periapsis altitude should not drop too low to avoid collisions with the Moon, and the maximum transmission altitude should not get too high to comply with pointing accuracy and receiver size constraints. Also, the period-averaged transmission altitude is important to consider when characterising the system's nominal performance. A graph showing the temporal evolution of the periapsis, apoapsis, minimum transmission, average transmission and maximum transmission altitudes can be found in Figure 5.13. Although the maximum transmission altitude at times reaches values greater than $14\,150$ km, the maximum receiver diameter requirement is never violated. Also, as the periapsis altitude remains above 376.97 km at all times, there is no real risk of crashing into the Moon.

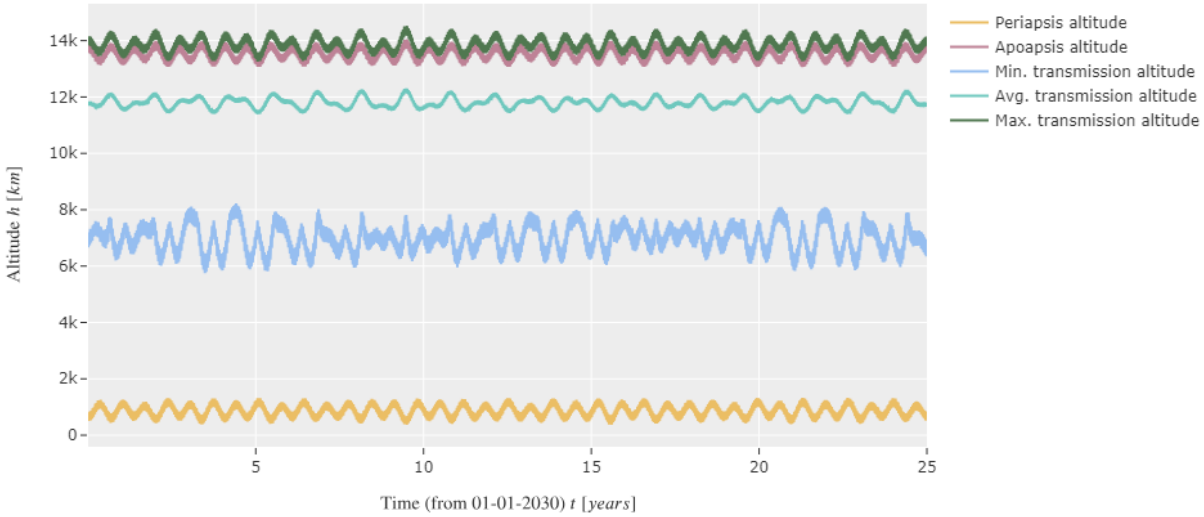

Figure 5.13: Evolution of periapsis, apoapsis and transmission altitudes over time.

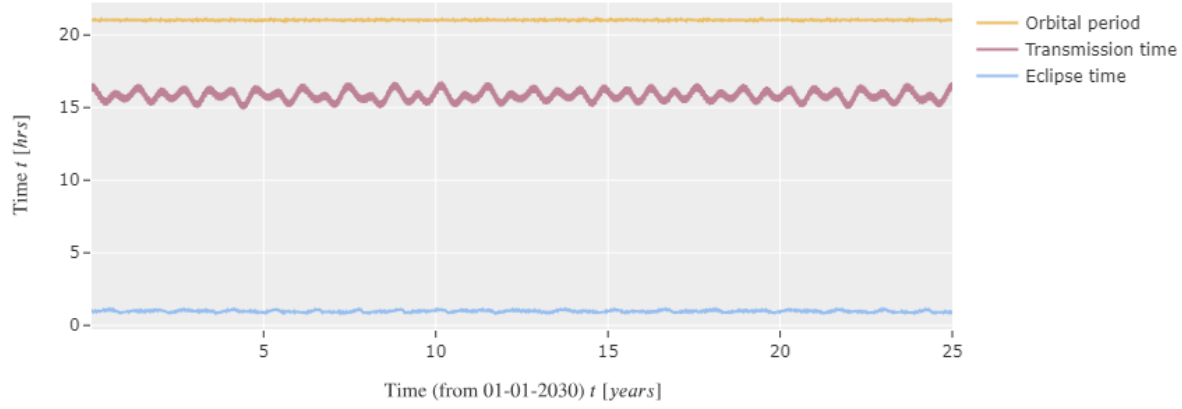

Figure 5.14: Evolution of orbital period, transmission time and eclipse time over time.

Times

Analysing how the transmission time, eclipse time and orbital period (total time) per orbit vary relatively to each other can be indicative of losses in system performance. A graph showing the temporal evolution of these parameters can be found in Figure 5.14. As is immediately apparent, the orbital period and eclipse time remain quite constant throughout the mission's lifetime. The transmission time shows the most significant oscillations, ranging from 14.89 h to 16.77 h.

Satellites in view

The number of satellites in view is an important parameter to consider for LUMEN's design: for a given total number of spacecraft, the greater the minimum number of spacecraft in view of the receiver, the less system mass is "wasted" by not being able to transmit power. For LUMEN, a tandem configuration of 110 spacecraft was chosen, along with 23 additional spacecraft for system reliability. A graph showing the temporal evolution of the minimum number of spacecraft in view, for 110 and for 133 spacecraft, can be found in Figure 5.15. As the 23 additional spacecraft have purely been added for the sake of system reliability, the system should not be reliant on their performance: as such, the system should be designed by considering the minimum value of the minimum number of spacecraft in view for the 110 spacecraft, which comes down to 77 spacecraft. It should however be noted that the real number of spacecraft in view is significantly higher, with an average value of 99 and a maximum value of 105 spacecraft. In the most extreme case, the receiver will thus have 28 more spacecraft in view than what was designed for, which would increase the power received by about 36.4%.

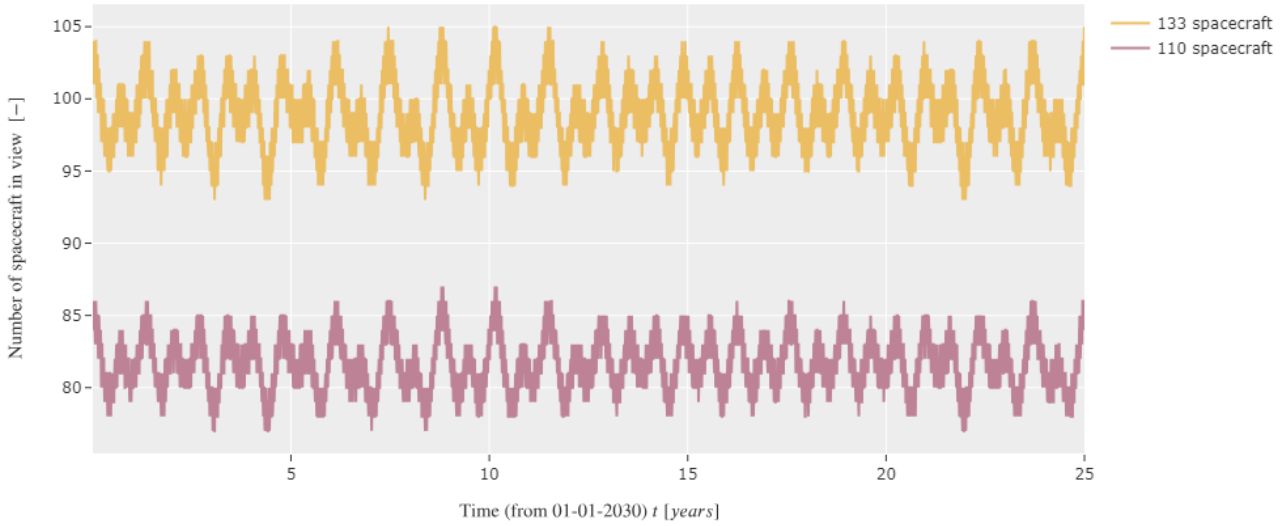

Figure 5.15: Evolution of the number of spacecraft in view over time.

Laser pointing

The required angles, angular velocities and angular accelerations for laser pointing are important for the design of LUMEN's AOCS and laser pointing gimbal mechanism. In detail, the angles are important in designing how the gimbal mechanism should look and in finding the clearance angle for the spacecraft's solar arrays, while the angular accelerations are important in finding the torques that should be applied. A graph showing the pointing angles, angular velocities and angular accelerations over the course of one orbital period, both about the z and x axes as defined by Figure 5.5, can be found in Figure 5.16. Here, the coloured lines represent the pointing graphs generated based on the orbit's time-averaged orbital elements; the grey lines were generated for the specific combinations of orbital elements that would lead to the lowest and highest angles, angular velocities and angular accelerations. Note how θ_z first increases and then decreases, indicating the laser is first pointed to the left and then to the right relative to the spacecraft's body, which is characteristic of retrograde (clockwise) orbits.

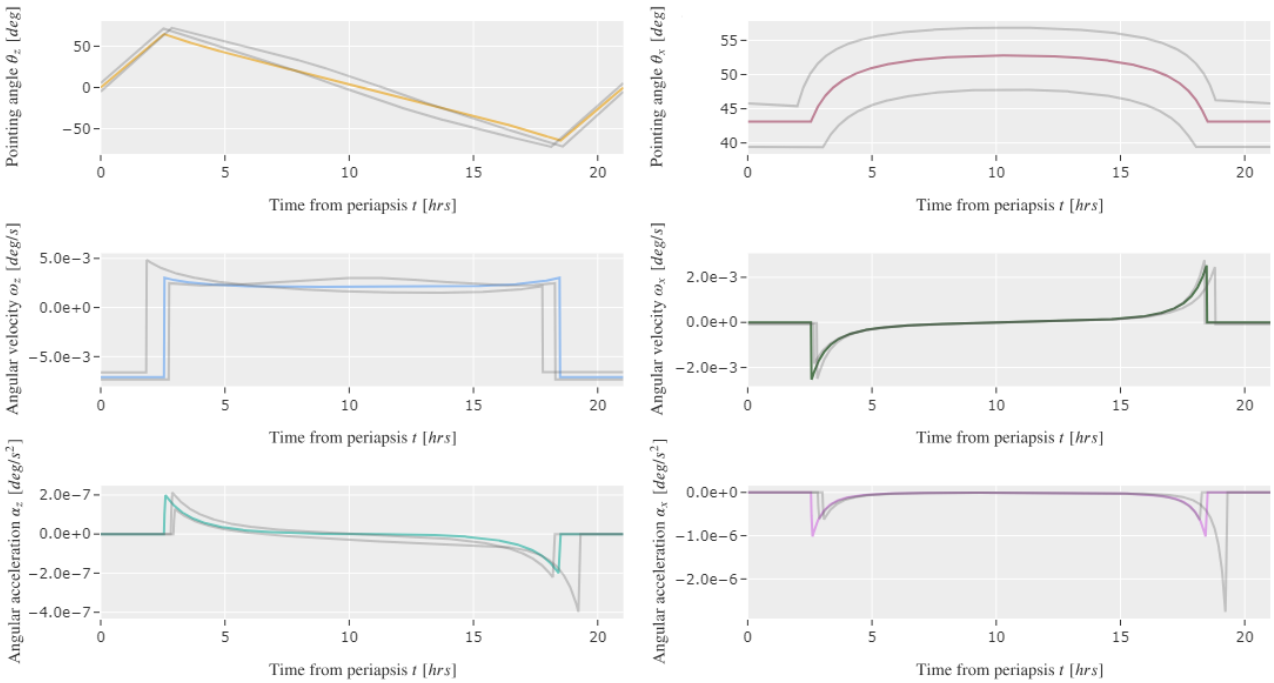

Figure 5.16: Pointing angle, velocity and acceleration ranges.

Orbit efficiency score

One of the most important parameters for tracking the orbit's performance over time is the orbit efficiency score, the product of the incidence efficiency and the transmission percentage, which was used to find the optimal orbit. A graph showing the temporal evolution of this score, along with the evolution of its components, can be found in Figure 5.17. As may be concluded from this figure, the transmission percentage is highly variable over time, which was also observed in Figure 5.14; the incidence efficiency remains a lot more constant for the mission's duration.

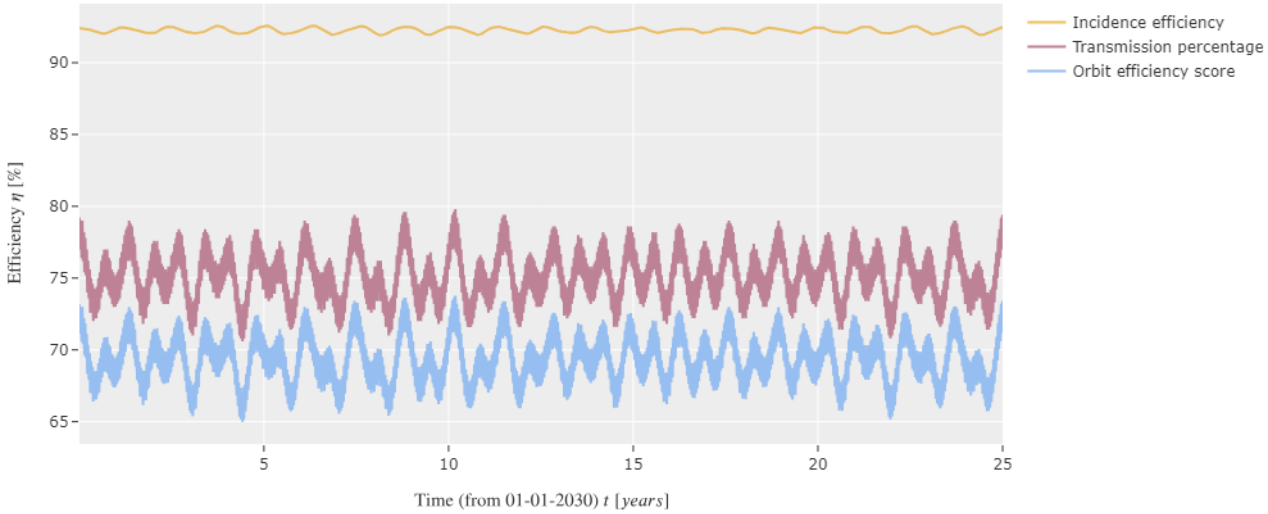

Figure 5.17: Evolution of orbit optimisation parameters over time.

5.4.3. Stationkeeping

The main appeal of frozen lunar orbits is their property of being frozen, meaning their orbital elements on average remain constant over time. This unique property makes it such that theoretically, a spacecraft could remain in such an orbit indefinitely. However, while analytical ELFO solutions have shown this behaviour, numerical simulations in literature have shown slight distortions of shape and slight drifts on the order of years [44, 45]. As this behaviour could distort the orbit's frozen property, turning

it unstable, this could facilitate the need for small amounts of stationkeeping over long timescales: however, for the performed GMAT simulations spanning 25 years, no limiting

Another consideration that could facilitate the need for stationkeeping, is the notion that the selected orbit's performance will not be constant over time, as emphasized in Section 5.4.2. LUMEN should be designed for the worst-case performance observed over its entire lifetime, thus ensuring requirements are complied with for the full mission duration: the presence of these performance oscillations would make LUMEN's design more constrained, seeing as its worse orbital performance would require the system to be overdesigned for all other conditions. Using stationkeeping to keep the orbit's performance within certain bounded regions around the average performance could be an interesting way of mitigating this effect. However, it should be noted that a procedure like this would only make sense on the condition that LUMEN's worst-case performance can significantly be improved and that stationkeeping is easy to realise.

Regarding the notion that performing stationkeeping only makes sense when LUMEN's worst-case performance can significantly be improved, the performance evolution given in Section 5.4.2 should be considered. From the graphs presented, the general conclusion can be drawn that performing stationkeeping might not be a very efficient way of alleviating LUMEN's design constraints, seen as most oscillatory ranges are quite limited. For example, the periapsis altitude and minimum spacecraft spacing remain above 376.97 km and 164.47 km respectively at all times, meaning mitigating the risk of collision with the Moon or other spacecraft would not require any stationkeeping ΔV to be budgeted. Also, although the maximum transmission altitude overshoots the imposed boundary condition of $14\,150$ km at times, this is only observed up to a transmission altitude of $14\,522.70$ km: here, required receiver diameters of up to 85.92 km are observed, which still meets the (80 ± 10) m requirement and thus does not impose the need for stationkeeping either. Finally, increasing the worst-case value for the orbit efficiency score to its lifetime average, which can be seen as an indicator of general orbit performance, would only lead to an improvement of about 5%. Also considering the notion that relying on stationkeeping would increase the system mass by adding propellant mass, such a marginal increase in efficiency by relying on stationkeeping would have a high probability of proving to be futile.

To apply stationkeeping for worst-case performance mitigation, the easiest parameter to control would be the orbit's apoapsis altitude (and thus also its maximum transmission altitude). The most obvious way to perform this kind of stationkeeping would be to increase or decrease the semi-major axis with burns applied at the periapsis, at moments in time at which the maximum transmission altitude is deemed too low or too high. This correction has been visualised in Figure 5.18, where the satellite is shown as an X, the green solid line shows the propagated path and the dotted red line represents the satellite's orbit. Here it can be seen that this station-keeping method will alter the orbital elements for the remainder of the mission. As these orbital elements are also oscillating around an average value, it could mean that due to the stationkeeping-induced alteration of the average value, the orbit is no longer frozen and gets into an unstable domain, which would jeopardise the mission.

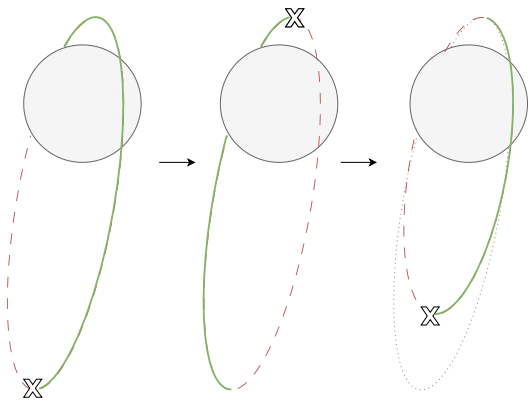

Figure 5.18: Maximum transmission altitude station-keeping by decreasing the semi-major axis.

On the basis of these now outlined considerations, it may be concluded that LUMEN will formally not require any stationkeeping and that relying on stationkeeping would only lead to marginal increases in performance compared to the added system mass and complexity. Therefore, the choice has been made to let LUMEN follow the oscillatory motion shown in Section 5.4.1 freely, and to consequently design its subsystems for the worst orbital performance given in Section 5.4.2. Although stationkeeping will thus not be necessary, situations may still arise in which spacecraft will have to perform evasive manoeuvres, or small orbit corrections due to unforeseen circumstances. $5\,\mathrm{m\,s^{-1}\,yr^{-1}}$, or a total ΔV of $125\,\mathrm{m\,s^{-1}}$ over the mission lifetime, is therefore budgeted for unforeseen manoeuvres (including stationkeeping corrections) per spacecraft. This value was based on the stationkeeping ΔV budgeted for the Lunar Reconnaissance Orbiter, a similar spacecraft currently placed in a frozen low lunar orbit [48].

5.5. Trajectory Design

Starship will bring the LUMEN system into a lunar parking orbit of a radius equal to the apocenter of the mission orbit, $13\,520.16\,\mathrm{km}$. To do so, the starship must perform an impulsive burn of $0.5819\,\mathrm{km/sec}$ ΔV. In Table 5.3 and Figure 5.20 the whole mission profile until the operational phase is shown. The starship will take care of phases 01.1, launch until 01.6, payload separation. After the payload is separated the starship will make manoeuvres to return back to earth to be reused, as SpaceX wil have planned [24].

SpaceX is planning on using two launching sites for the starship launches, the Boca-chica starbase and the Kennedy Space Center (KSC). For both of the launch sites, there are azimuth limitations in which the starship can be launched, due to the landmass fly-over limitations. The Boca Chica constraint is to launch in either a $93\,^\circ$ or a $112\,^\circ$ flight path. For KSC this constrain ranges from $35\,^\circ$ to $120\,^\circ$ flight path. Figure 5.19 shows the azimuth contains for both launch centres, and it can be seen that SpaceX' starbase launch option is more constraining than the KSC launch option. Thus KSC is chosen as the main launch site, to eliminate the need for dog-leg turns [49], induced by the launch constraints. The $35\,^\circ$ to $120\,^\circ$ azimuth range of KSC produces an inclination range from $28.5\,^\circ$ to $59\,^\circ$[25] for which the trajectory will be designed.

(a) Boca Chica **(b)** Kennedy space centre

Figure 5.19: Launch azimuth limitations [49].

The maiden launch date has been chosen to be the 1st of June 2030 at 12:00:00, thus complying with the LMN.SCH.001 requirement [50]. This launch datum still leaves some room for launch delays and launch scrubs with a maiden launch margin of 6 months. A second, third, and fourth launch will be planned 3, 6, and 9 months after the maiden launch. Although these data have been chosen now, it can still be due to change closer to 2030, due to scheduling constraints of both SpaceX and Kennedy Space Centre.

[24] URL: `https://www.nasaspaceflight.com/2018/09/SpaceX-announces-bfr-lunar-passenger-earths-artists/` [Cited 19/06/2023]

[25] URL: `http://www.satobs.org/faq/Chapter-09.txt` [Cited 19/06/2023]

Table 5.3: Mission profile.

ID	Start time (dd hh:mm)	Duration	Phase
01.1	T+00 00:00	00 00:03	Launch
01.2	T+00 00:03	00 00:05	Booster separation
01.3	T+00 00:08	00 00:30	Parking orbit insertion
01.4	T+00 00:38	00 04:00	In-orbit refuelling
01.5	T+00 04:38	04 11:27	Trans lunar parking orbit injection
01.6	T+04 16:05	00 00:30	Starship payload separation
02.1	T+04 16:35	02 00:00	Spacecraft train distancing manoeuvres
02.2	T+06 16:35	01 17:26	Spacecraft operational orbit injection
02.3	T+08 10:01	01 00:00	Spacecraft solar panel unfolding
02.4	T+09 10:01	01 00:00	Initial pointing manoeuvres
03.1	T+10 10:01	9125 00:00	Spacecraft operational mission phase

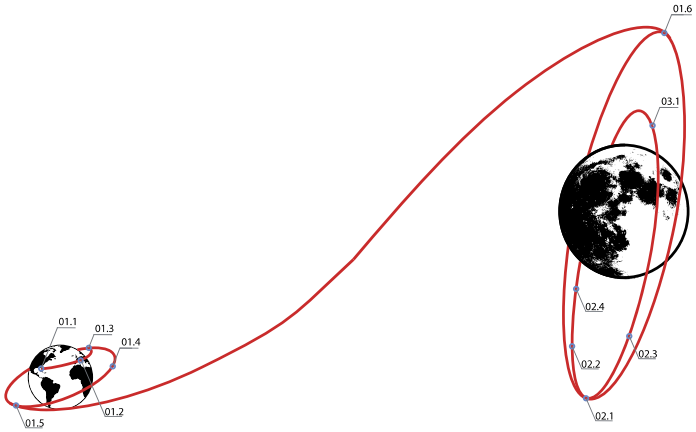

Figure 5.20: Mission Profile

The Starship will launch in an azimuth direction of $35\,^{\circ}$ to go to a circular Earth parking orbit with an $28.5\,^{\circ}$ inclination and an altitude of $500\,\mathrm{km}$, as specified to be the maximum LEO orbit value by starships user manual [51]. In this orbit, the starship will perform in-orbit refuelling, as will be explained in Section 6.9, after which it will perform its trans-lunar trajectory insertion. When arriving in the lunar plane of influence, the starship will perform a lunar parking orbit insertion.

The ΔV that is needed to get into the parking orbit is $9816\,\mathrm{m\,s^{-1}}$ from Janssen et al. [7]. To the transfer orbit, from the parking orbit, the ΔV is $3.063\,\mathrm{km\,s^{-1}}$. To go from the transfer trajectory to the lunar parking orbit an impulsive burn with a ΔV of $0.5958\,\mathrm{km\,s^{-1}}$ is needed, both calculated by GMAT. A detailed trajectory and lunar parking orbit insertion can be seen in Figure 5.21a and Figure 5.21b, respectively. A summary of the parking orbit characteristics can be seen Table 5.4

Table 5.4: Parking orbit characteristics

Parameter	Unit	Value
Semi-major axis a	[km]	15579
Eccentricity e	[–]	0
Inclination i	[°]	121.18
Orbital Period T	[s]	174449

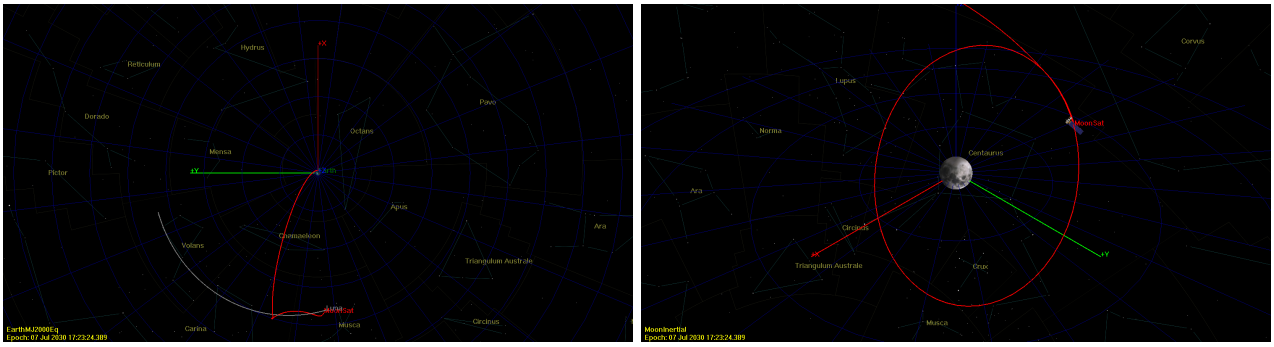

(a) Starship trajectory design for a launch date of 01 June 2030, propagated for 1 parking orbit rotation, generated by GMAT

(b) Parking orbit injection, propagated for one orbit, generated by GMAT

The parking orbit has an orbital period of about $48.5\,\text{h}$, in which the starship will release LUMENs spacecraft one for one with a spacing of $568.48\,\text{s}$ in time, based on the target temporal spacing for the selected orbit at the moment of injection (period divided by 133). The spacecraft will not stay in this parking orbit for more than one obit, as this is not a frozen orbit and thus perturbations will affect the orbit characteristics. If multiple launches are needed then it is assumed that the insertion will need to be timed correctly to avoid collisions with already orbiting satellites. After which they will need to be inserted into the operational mission orbit, which is visualised in Figure 5.22 where the starship and the spacecraft are shown as an arrow and an X respectively. The ΔV needed to do so has been calculated by Equation (5.9), with the data from Table 5.5, resulting in $277.1\,\text{m}\,\text{s}^{-1}$ confirmed with GMAT.

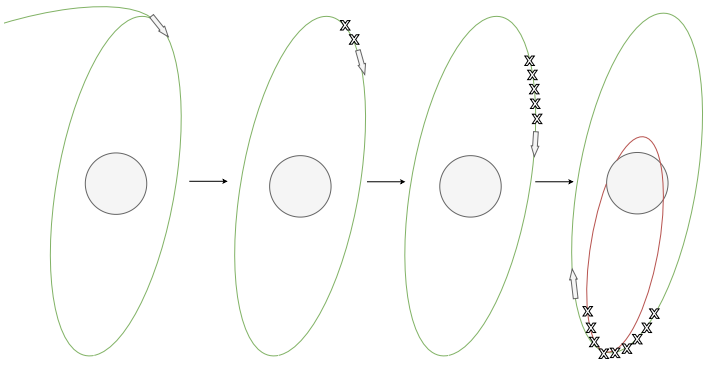

Figure 5.22: Parking orbit spacecraft spacing

$$|| \Delta V ||=| V_{apo_2} - V_1 |= \left| \sqrt{\mu \left(\frac{2}{r_{apo_2}} \frac{1}{a_{apo_2}} \right)} - \sqrt{\frac{\mu}{r_2}} \right| \tag{5.9}$$

Table 5.5: Operational orbit insertion calculation data, from Section 5.7.1

μ	$4.905 \times 10^3\,\text{km}^3\,\text{s}^{-1}$
r_1	$13\,520.16\,\text{km}$
r_{apo_2}	$13\,520.16\,\text{km}$
a_2	$8934.37\,\text{km}$

5.5.1. End-of-Life

At the end of the life of a satellite, a plan must be set-up to avoid polluting the orbit and abide to present regulations. So a proper disposal strategy has to be established. There are different kinds of EOL strategies, of which three were considered for the LUMEN mission [52]:

- Stable graveyard orbit;

- Perform an Earth atmospheric re-entry
- Crashing into the moon.

Until recently, the most common way to dispose of satellites orbiting the Moon has been to either crash them into the Moon or leave them in their unstable lunar orbit, which eventually results in an uncontrolled crash [52]. The Earth's atmospheric re-entry has not been performed by any non-crewed or sample collection missions. The graveyard orbit is frequently used for satellites orbiting the Earth when the ΔV for de-orbiting is too large, valid for GEO satellites. These GEO satellites are brought to an orbit that is 300 km higher than the altitude of a GEO orbit[26]. This method however is not possible for lunar orbits, as the frozen lunar orbits are favourable for future missions and unstable lunar orbits will still result in an uncontrolled crash in the end. This is why a controlled crash has been decided upon for the disposal strategy for the LUMEN mission. To make sure no historical sites and safety zones are hit, and to enable future recycling of debris materials on the moon a crash zone will be instated.

The Lunar Resources Registry has already theorised a space debris landing zone, also called a space debris graveyard in the Gambert crater ($1.0\,^\circ$ N, $15.2\,^\circ$ W). The Gambert crater is roughly 20 km wide and its walls are about 100 km high. The Lunar Resources Registry notes that high-speed impacts will cause a crater of about 12 m wide and a debris field of about 300 m of which there is a small chance that the debris and regolith cloud reach over the crater walls. Furthermore, recycling possibilities have also been taken into account by the authors [27].

This crater, however will cost a large ΔV, which ranges from 80 m/sec to 518 m/sec. When designing for the worst case, it would mean that a big portion of the propellant would need to be dedicated to the EOL phase. This is why for the LUMEN mission another crater will be used, with the same goal as the Gambert crater, but closer to the projected latitude of the pericenter of the orbit.

In Figure 5.23 the maximum latitude that the orbit projects on the lunar surface is approximately $60\,^\circ$N. To match this ground-track the Gamow ($65.30\,^\circ$N, $145.30\,^\circ$E) has been chosen for the EOL strategy. This crater has a depth of about 11 km and is 129 km wide.

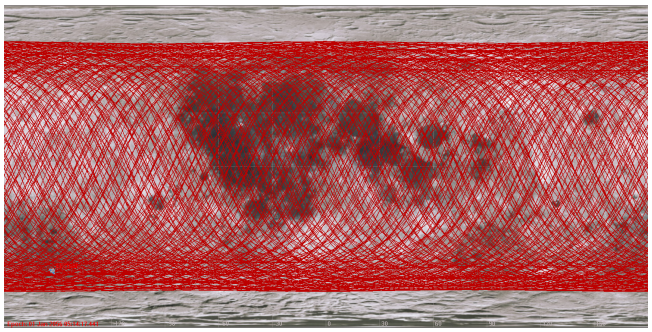

Figure 5.23: Ground plot, epoch 2050, propagated for 1 year

Different EOL manoeuvres can be seen in Figure 5.24, for which the left-most will cost the most ΔV, as a plane change is needed and the right-most will cost the least amount of ΔV. Taking into account that for ESA standards the EOL procedure must take a maximum of 25 years in earth orbit [28], but to keep the frozen lunar orbits free as soon as possible, and to meet th LMN.SAR.005 requirement [50] the EOL manoeuvre will have to be done within 1 year. In Figure 5.23 it can be seen that propagating the satellite for 1 year results in a high coverage, so the EOL will be planned to stay idle, until in the correct orbital plane and then start its de-orbiting manoeuvre. The ΔV that is needed for this transfer is calculated by Equation (5.10) with the values in Table 5.6 from Table 5.7, and results in a ΔV of $33\,\mathrm{m\,s^{-1}}$, verified through GMAT.

[26] URL: https://www.esa.int/ESA_Multimedia/Images/2008/03/Mitigation_scenarios_Graveyard_orbit_300_km_above_GEO [Cited 09/06/2023]

[27] URL: https://lunarresourcesregistry.com/infrastructure/space-debris-graveyard/ [Cited 09/06/2023]

[28] URL: https://www.esa.int/Space_Safety/Space_Debris/Mitigating_space_debris_generation [Cited 18/06/2023]

$$\|\Delta V\| = \mid V_{apo_2} - V_{apo_1} \mid = \left| \sqrt{\mu \left(\frac{2}{r_{apo_2}} - \frac{1}{a_2} \right)} - \sqrt{\mu \left(\frac{2}{r_{apo_1}} - \frac{1}{a_1} \right)} \right| \tag{5.10}$$

Table 5.6: EOL calculation data

μ	$4.905 \times 10^3\,\text{km}^3\,\text{s}^{-1}$
r_{apo_1}	$15\,579\,\text{km}$
a_1	$8934.37\,\text{km}$
r_{apo_2}	$15\,579\,\text{km}$
a_2	$8658.20\,\text{km}$

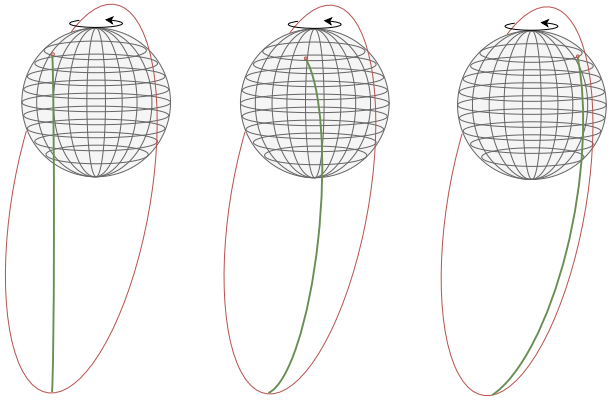

Figure 5.24: Rotation of the moon, w.r.t. the orbital plane

5.6. Astrodynamic Sustainability

As for all other areas of LUMEN's design, sustainability is an important driver. Considering sustainability aspects in designing the system's astrodynamics can aid in reducing the greenhouse gas emission and energy consumption encountered in spacecraft manufacturing: through astrodynamic design, the required amounts of ΔV, and thus the required amounts of spacecraft propellant to be produced, may be reduced. Also, taking into account sustainability for end-of-life considerations is necessary to avoid contributing to spaceflight's problem of space debris.

Orbit and Trajectory Sustainability

LUMEN's selected orbit is very sustainable compared to the other options for lunar orbits. This should come as no surprise: in the orbit trade-off presented by Janssen et al. [7], ELFOs were found to require no ΔV for stationkeeping, and to require about 5.6% less ΔV for orbit injection than the other considered options. Also, maximising the criterion for which the orbit was optimised, a combination of high transmission percentages and low incidence losses, results in a more sustainable orbit overall. As previously explained, through selecting an orbit with higher transmission percentages the system's total size and mass may be reduced, reducing greenhouse gas emission and energy consumption in spacecraft manufacturing, and reducing the required launch propellant mass. By minimising incidence losses, the system's efficiency is increased, requiring less solar array area for the same amount of power received at the lunar South Pole. Furthermore, the system's retrograde orbit helps to reduce the amount of manoeuvres necessary for letting LUMEN's spacecraft face the Sun, resulting in less stringent AOCS constraints, which could help in reducing its complexity and thus its required energy for manufacturing. Finally, a Hohmann transfer orbit has been selected to get LUMEN from the Earth to the Moon, which is known to be a highly energy-efficient way to move between two orbits.

5.6.1. Future EOL Recyclability

As all the satellites will be crashed into one crater, a future recyclability programme can be set up, which targets the Gamow crater. This programme can be based on what is already planned by the Lunar Resources Register[29] with the Gambert crater. Here they developed a driving plan for lunar rovers, which will collect the debris and bring it back to a lunar base. As the Gamow crater will not be close to the lunar south pole carter, it is assumed that this plan can only be used when a lunar base is close by. Possible rover paths have already been identified, by looking at the terrain height map, and can be seen as red arrows in Figure 5.25. Recycling the crashed systems will be more sustainable than either leaving them in space or having them crash uncontrollably onto the lunar surface.

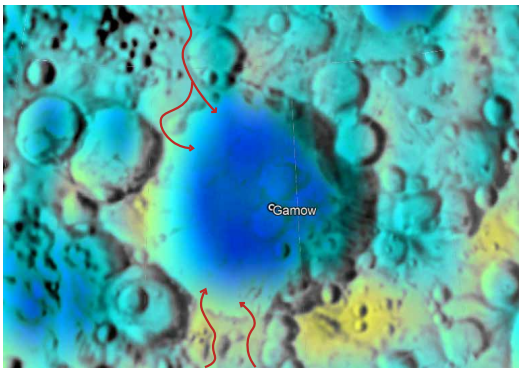

Figure 5.25: Possible lunar rover paths into the Gamow crater

5.7. Astrodynamic Summary

The aim of this section is to give a clear and concise overview of all relevant numerical values estimated for the final orbit. These values drive the design of LUMEN and its subsystems significantly, leading to the need for a database of these driving values.

5.7.1. Orbit Performance Datasheet

In this chapter, LUMEN's orbit was selected by optimising for the product of transmission percentage and incidence efficiency. The orbit this analysis converged to is characterised by a semi-major axis of 8934.37 km, an eccentricity of 0.7438, an inclination of $121.18\,°$, an argument of periapsis of $90\,°$ and a right ascension of the ascending node of $76.94\,°$ (Moon right ascension + $90\,°$), all given for the anticipated moment of injection (the 6th of June 2030 at 04:35:00).

An overview of all of the selected orbit's most important orbital characteristics can be found in Table 5.7. This table is loosely split up into 5 categories: distances, transmitter-receiver segment, laser pointing, eclipse, and other, from top to bottom. Minimum (min.), maximum (max.) and average (avg.) in the parameter column refer to the minimum, maximum and average values as encountered over one orbital period, for one specific choice of a, e, i and ω: the numerical values in the "Nom. value" column then refer to these values as averaged over the entire mission lifetime (2030-2055), the nominal values, while the values in the "Con. value" column refer to the most constraining values encountered for these parameters over the mission lifetime. The minimum spacecraft spacing (in space and time) was estimated for the full 133 spacecraft; the minimum number of spacecraft in view was reported for 110 spacecraft, seeing as the additional 23 spacecraft were added for reliability reasons, and as such should not be considered for sizing the final design.

[29] URL: `https://lunarresourcesregistry.com/infrastructure/space-debris-graveyard/` [Cited 19/06/2023]

Table 5.7: Overview of orbital characteristics.

Parameter	Unit	Nom. value	Con. value
Periapsis altitude h_{peri}	[km]	865.91	376.97
Apoapsis altitude h_{apo}	[km]	13520.16	14041.79
Avg. altitude h_{avg}	[km]	9428.20	9428.20
Min. transmission altitude $h_{t,min}$	[km]	6966.31	5754.48
Max. transmission altitude $h_{t,max}$	[km]	13850.01	14522.70
Avg. transmission altitude $h_{t,avg}$	[km]	11795.73	12304.98
Min. spacecraft spacing (133 S/C)	[km]	185.44	164.47
Orbital period T	[hrs]	21.03	21.03
Temporal spacecraft spacing (133 S/C)	[s]	569.28	567.33
Transmission time t_t	[hrs]	15.82	14.89
Transmission percentage η_t	[%]	75.23	70.90
Min. number of spacecraft in view (110 S/C)	[−]	82	77
Avg. receiver angle of incidence θ_i	[deg]	45.38	51.54
Incidence efficiency η_i	[%]	92.26	91.91
Orbit efficiency score	[−]	69.41	65.17
Max. beam dilution factor f_{bd}	[−]	1.5696	1.8470
Required receiver diameter	[m]	78.92	85.92
Pointing z-angle range	[deg]	-64.74 — 64.74	-72.51 — 72.64
Pointing max. z velocity	[deg/s]	$7.030 \cdot 10^{-3}$	$9.060 \cdot 10^{-3}$
Pointing max. z acceleration	[deg/s^2]	$2.427 \cdot 10^{-7}$	$4.799 \cdot 10^{-7}$
Pointing x-angle range	[deg]	42.20 — 52.79	34.13 — 61.42
Pointing max. x velocity	[deg/s]	$2.934 \cdot 10^{-3}$	$4.614 \cdot 10^{-3}$
Pointing max. x acceleration	[deg/s^2]	$1.228 \cdot 10^{-6}$	$2.434 \cdot 10^{-6}$
Max. Moon eclipse time t_M	[hrs]	0.950	1.074
Max. Moon eclipse velocity v_M	[km/s]	1.7351	2.0222
Max. Earth eclipse time	[hrs]	4.94	4.94
Min. time between Earth eclipses	[days]	29.05	29.05
Nodal precession rate ω_p	[deg/day]	0.8214	2.5559
Stationkeeping ΔV	[m/s/year]	0	5

Designing a system to comply with average performance does not always make sense: for example, if at a given point in time the number of spacecraft in view drops below its average value, while the system was designed for the average number, too little power will be received at the South Pole. The constraining values in Table 5.7 are the most extreme values obtained over the mission lifetime, making them important inputs for the design of LUMEN. Only the most limiting values have been reported: for example, while the maximum eclipse velocity can at times also be lower than the value reported in Table 5.7, only its highest value will lead to the most extreme temperature gradients, and thus only its highest value will drive the design. As for the orbital period and average altitude on their own no clear constraining values exist, their nominal values have been repeated. This was also done for the Earth eclipse values, seeing as these numbers were only simulated based on the orbit's average orbital elements.

5.7.2. ΔV Budget

The total ΔV budget for both the Starship and one LUMEN satellite have been listed in Table 5.8. Here it can be seen that the starship needs to be able to give a ΔV of $3.66\,\mathrm{km\,s^{-1}}$, consisting of the Transfer Orbit Insertion (TOI) and the Lunar Parking Orbit Insertion (LPOI). One LUMEN satellite needs to provide $310.1\,\mathrm{m\,s^{-1}}$, consisting of the operational orbit insertion and the EOL manoeuvre.

Table 5.8: Starship (post in-orbit refuelling) and one LUMEN satellite ΔV budget

Manoeuvre	Δ**V** [m s^{-1}]
Starship TOI	3063
Starship LPOI	595.8
Total Starship	3658.8
Operational orbit insertion	277.1
End-of-Life manoeuvre	33
Unforeseen manoeuvres	125
Total LUMEN	435.1

5.8. Astrodynamics Verification & Validation

As for all other segments designed for the LUMEN mission, the accuracy and reliability of obtained results should be confirmed by means of Verification and Validation (V&V). This section describes the V&V procedure for LUMEN's astrodynamics.

5.8.1. Software Verification & Validation

The generated orbit performance tool was verified by means of a plethora of unit- and system tests, the exact details of which lie outside of the scope of this report. In general, verification was focused on finding errors in used logic and errors in wrong implementation of this logic. Both GMAT and the orbit performance tool were also verified by means of comparing results with those obtained using calculations by hand. All unit and system tests conducted on the final versions of the utilised tools were passed.

To validate the results obtained using GMAT, efforts were made to reproduce orbits as reported in literature to assess the correlation between results produced by GMAT and those from literature. In particular, this was done for the example orbits presented by Folta and Quinn [44] and Ely [45], seeing as correspondence with results obtained for other ELFOs is the most valuable for this mission. The results of a representative analysis can be found in Figure 5.26.

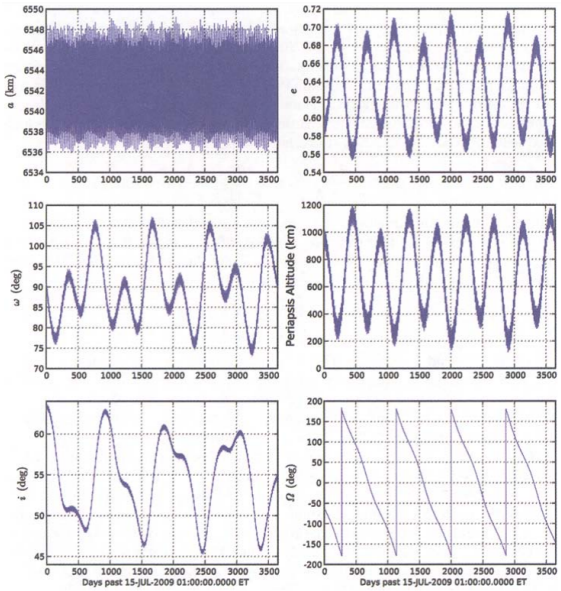

(a) 10-year evolution of ELFO elements, taken from Ely [45].

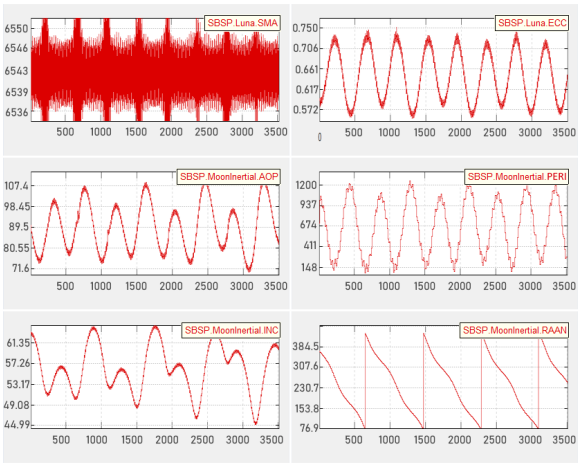

(b) 10-year evolution of the same ELFO elements, estimated using GMAT.

Figure 5.26: GMAT validation by reproduction.

As may be concluded from this figure, GMAT is able to reproduce the results obtained by Ely [45] quite well, even for long propagation times (here about 10 years). These results, along with previously conducted analyses on GMAT's validity such as the one presented by Hughes et al. [53], lead to

sufficient confidence in GMAT's validity for the sake of this conceptual design.

Seeing as the orbit performance tool almost exclusively makes use of geometrical relations, visual inspection using the 3D orbit graphs it is capable of generating is a powerful tool in validating the tool's numerical results. The correctness of these 3D orbit graphs themselves is validated via visual inspection using GMAT, where GMAT was already regarded as valid to a degree considered sufficient for the system's current design stage. From visual inspection of the 3D graphs generated by the orbit performance tool, the correctness of many of the tool's outputs can quickly be validated. For example, the arclength of the orbit lying inside of the transmission cone or the shadow cylinder as compared to the orbit's total arclength can be used to quickly get a feel for the right order of magnitude of produced numerical results. Also, it was assessed whether results obtained for extreme initial conditions, such as very low or very high inclinations, make sense when compared to the values obtained for other initial conditions.

5.8.2. Future Considerations

To not only validate the use of GMAT and the generated orbit performance tool, but also the orbit itself before launch, a first step could be to bring a smaller spacecraft into the desired orbit, in an analogous fashion to what was achieved for the Near-Rectilinear Halo Orbit using the CAPSTONE mission[30]. The orbit chosen in this report was indicated to require no stationkeeping for the course of the mission's lifetime, while it has not been used yet as of 2023: sending a dedicated lunar orbiter to verify its characteristics beforehand could thus prove worthwhile, especially if ELFO's are to be reused for other future missions.

After launch, LUMEN's orbit could be validated using the upcoming Cislunar Autonomous Positioning System (CAPS)[31], a navigation technology for relative tracking between multiple spacecraft, first demonstrated by CAPSTONE and the Lunar Reconnaissance Orbiter. Combining data obtained on the relative positions of LUMEN's spacecraft using CAPS with data obtained from the lunar South Pole and the Earth, sufficient infrastructure should be in place to determine the system's orbital positions at any time to a high accuracy.

[30] URL: `https://www.nasa.gov/directorates/spacetech/small_spacecraft/capstone` [Cited 22/06/2023]
[31] URL: `https://advancedspace.com/caps/` [Cited 22/06/2023]

6.1. Attitude and Orbit Control System

The Attitude and Orbit Control System's (AOCS) main responsibility is to control the spacecraft attitude, given the attitude information from the Guidance and Navigation system (GNC). The design approach taken from the midterm was already to include reaction wheels and thruster control for desaturation. From [7], the allocated mass and power budget was of 23.1 kg and 112 W. Below the subsystem design approach is described.

6.1.1. Control Modes

Throughout the mission lifetime of each individual spacecraft, the conditions encountered vary greatly and so do also the operational modes of each subsystem. Hence for the functioning of the AOCS and GNC five main control modes were identified:

1. Acquisition Mode

   This mode is the first to be activated, coarsely determining and stabilising the attitude of the spacecraft, in order to initiate communication with ground after insertion by Starship.

2. Orbit Correction Mode

   After communication has been set-up, the larger orbit correction manoeuvre instructions are communicated and performed. The spacecraft needs moderate determination and precise stabilisation during these larger manoeuvres, hence this control mode.

3. Nominal Operational Mode

   This is the standard operation control mode during the operations of the spacecraft. The operational requirements of this control mode will drive the design of the GNC and AOCS. Both accurate and precise determination and stabilisation is required.

4. Slew Mode

   This mode is required during the re-orienting manoeuvres of the spacecraft, for example during station keeping.

5. Safe Mode

   This is the low power control mode initiated when major anomalies are detected onboard. Here the orbit determination and stabilisation is still present, but very coarse.

As mentioned above, the main driver for design is the Nominal Operational Mode for both GNC and AOCS.

6.1.2. AOCS Performance Requirements

The AOCS requirements are dependent on several further factors, including the orbit, payload, S/C geometry etc. Below both system and performance requirements are derived from the various needs of the many parts of the spacecraft for the AOCS subsystem design.

As mentioned in the section introduction, the AOCS is given technical budgets, especially for mass and power. These are converted into updated AOCS requirements to design for:

1. LMN.AOC.001: The AOCS subsystem shall in total have a mass of no more than 70 kg.
2. LMN.AOC.002: The AOCS subsystem shall use no more than 112 W of average electrical power.

The main system level requirement derives from Section 5.3, where slew manoeuvres are required to combat the precession of the orbit. This would shift the orbit with respect to the payload target (South Pole), introducing great variations in the angles perceived by the receiver. Also in combination with the NASA regulations for constellation systems described in [54], slew manoeuvres are to be performed a maximum of every 4 weeks. Therefore, orbit precession countering manoeuvres every 4 weeks must be performed:

1. LMN.AOC.003: The LUMEN spacecraft shall slew at least 22.4 deg every 4 weeks.

From the same regulation paper [54], the positional and velocity knowledge necessary to maintain a safe inter-satellite distance can be derived using the orbit parameters into Table 5.7:

1. LMN.GNC.007: The three-axis apogee position knowledge of the S/C shall be known with a three sigma accuracy better than 700m.
2. LMN.GNC.008: The three-axis apogee velocity knowledge of the S/C shall be known with a three sigma accuracy better than 11.6 mm/s.

Moreover, from Section 5.3, further performance requirements can be derived, for the angles, angular velocities and angular accelerations that the payload transmission needs to perform over a singular orbit. Also from the solar collector payload, performance requirements on the attitude of the spacecraft can be derived.

Table 6.1: Performance requirements on two axes of the payload transmission

	Payload Transmission Requirements	
	Z angle	X angle
Range	$\pm$ 70 °	$\pm$ 7 °
Slew Rate	± 0.027 °/s	$\pm$ 0.032 °/s
Slew Acc.	$\pm$81.72 μ° s^{-2}	$\pm$160.3 μ° s^{-2}

6.1.3. Quantifying Disturbance Environment

In order to size the specific AOCS instrumentation necessary, the disturbance environment of the S/C must be analysed and thus the disturbance torques quantified. The disturbance environment entails both the external disturbances by third body effects and the internal disturbances caused by other components of the S/C. These are analysed, each with their assumptions and foci.

External Disturbances

Within an orbit around the Moon, the disturbances are limited in comparison to orbits around the Earth; no drag and negligible magnetospheric considerations. As mentioned in [55], the main perturbations to be considered in orbits around the Moon are the solar radiation pressure and the gravity gradient.

The solar radiation pressure, though neglected in some papers, is a sizeable force given the dimensions of the solar arrays of each S/C. However, due to the symmetric nature of the spacecraft, the torques around the local z-axis and x-axis can be neglected, simplifying the equation from vectorial to scalar, see Equation (6.1). Here Φ is the solar irradiance, c the speed of light, A_s the area illuminated (array 1, S/C bus, array 2), $c_{p_s} - c_m$ is the difference between centre of pressure and centre of mass and ϕ is the incidence angle, assumed to be zero to compute the worst-case load. Hence, the main torque generated by the solar radiation pressure is around the y-axis and stems from the difference between centre of mass of the spacecraft and centre of pressure of the arrays and S/C bus. These computations were programmed to account for the interdisciplinary design evolution of the S/CS/C. This also entailed a critical verification of the code through unit-tests to ensure the correctness of the program. After this verification, the total solar radiation pressure torque was calculated to be 1.480×10^{-3} N m.

The gravity gradient experienced by the S/CS/C is a further major external disturbance. Here the main complications arise from the fact that, with respect to the orbital reference frame, the spacecraft's attitude remains constant. This results in large angle excursions between the spacecraft and the nadir axis direction, which is the gravitational gradient direction. The equation to compute the disturbance torque caused by gravity gradient is Equation (6.2), where μ is the gravitational parameter of the moon, r and $\vec{r}$ are the scalar and vectorial distances of the spacecraft from the centre of the Moon, and $\vec{I}$ is a vector containing all the moments of inertia of the S/C. The maximum total gravity gradient disturbance torque is equal to 1.018×10^{-4} N m.

$$T_s = \frac{\Phi}{c} A_s (1+q)(cp_s - cm)cos(\phi) \tag{6.1}$$

$$T_{gg} = \frac{3\mu}{r^5}\vec{r} \times \vec{I}\vec{r} \tag{6.2}$$

Furthermore, another area of analysis includes the entering and exiting of eclipses. Due to the large area of the solar arrays, the solar pressure acting only on one side of the spacecraft may induce a significant torque while entering or leaving the eclipse. To calculate this magnitude, the force of the solar pressure was integrated over the growing area of the solar array exposed to the sun at the speed of the spacecraft while leaving the eclipse. Moreover, this implies a changing moment arm, which further must be accounted for in the integration. Using a solar array area of $331.1\,\mathrm{m}^2$ and a velocity of $1896\,\mathrm{m\,s}^{-1}$, the solar pressure shock torque is $1.638 \times 10^{-3}\,\mathrm{N\,m}$.

Internal Disturbances

The spacecraft's AOCS shall also be able to counteract the disturbance torques from within the spacecraft, stemming from its own instruments. Most important for this disturbance torque is the movement of the payload transmitter. Of the transmitter, the parts which are actively moved by the gimbal include the optics and the large mirror. A conservative mass estimation of $75\,\mathrm{kg}$ and movement arm of $1.2\,\mathrm{m}$ was used to model a worst-case scenario disturbance. These values are updated as the Payload design is updated; Thus, the design undergoes several updates. Moreover, essential to the transmitter are the angular accelerations the laser must undergo to remain in direct contact with the receiver on the South Pole. This value is taken from the constraining performances documented in Table 5.7. Calculated from these values is an internal disturbance torque of $1.48 \times 10^{-4}\,\mathrm{N\,m}$.

Further internal disturbances of the reaction wheel jitter, misalignment of thrusters or uncertainty of the centre of gravity are not computed, as they are found to be minimal in comparison to the most prominent disturbance torques evaluated previously. Moreover, the uncertainty of the values are attributed to implementing factors of safety. As discussed in Section 9.1.2, for load-driven designs the factor to be used is 2.25. This is substantial enough to also attribute for the minor uncertainties mentioned previously.

The maximum total disturbance torque on the spacecraft is $9.92 \times 10^{-3}\,\mathrm{N\,m}$. The total disturbance torque to design for is thus $0.0223\,\mathrm{N\,m}$.

6.1.4. AOCS subsystem design

It is to be noted that the pointing mechanism and the detailed design of the transmission mechanism are included in the Payload design in Section 4.3.8. Whereas the main component to design within the AOCS subsystem are the reaction wheels. To increase reliability and include redundancy in the design for each axis, a 4-wheel assembly is designed.

According to [55], the gravity gradient torque must also be accounted for by over a quarter of the orbit, considering the momentum build-up that the reaction wheels must tolerate. This builds up over a quarter of the orbit and the gravity gradient torque behaves as a sinusoid due to the varying altitude, explaining the 0.707 factor. Moreover, for these calculations, unlike the maximum disturbance torques mentioned before, the average altitude value is taken into account, instead of the maximum. This is because the equation models the orbit as a circular orbit, and modelling the current highly eccentric orbit as a circular orbit at the lowest altitude is unrealistic and unfeasible.

$$h = T_d P(0.707)/4 \tag{6.3}$$

Hence, a gravity gradient torque of $0.000\,101\,8\,\mathrm{N\,m}$, acting over a quarter of the period, results in an angular momentum build up of $3.066\,\mathrm{N\,m\,s}$.

For these values, an off-the-shelf component was identified by consulting Rinard et al. [56]. This paper is a thorough analysis by NASA on all of the possible providers of reaction wheels for any of the missions. Therefore, comparing the performances and the required output of the reaction wheels, the choice was made to use the HC7 reaction wheel by Honeywell Commercial (see Figure 6.1a). This has a torque output of $0.2\,\mathrm{N\,m}$, and momentum saturation of $6\,\mathrm{N\,m\,s}$. Moreover, this wheel has

also advantageous power performances, such as a steady state power draw of only 25 W. However, considerations for the total power necessary in an assembly of 4 reaction wheels, cannot be simply quadrupled. The most power draw that may occur at a given time is the use of two wheels at the same time during a manoeuvre, since otherwise the wheels would be counteracting each other. Additionally, this component has been used previously on several missions, giving it a TRL of 9.

Nevertheless, for any reaction wheel assembly a complementary consideration to be made are thruster sets to desaturate the momentum buildup in the reaction wheel assembly. For redundancy reasons on all axes, the total number of thrusters is set to be 12. To generate the necessary amount of output torque and balance the build-up of momentum, the actual needed amount of thrust is small, on the order of 0.2 N. However, to simplify the internal structure of the spacecraft, and to make use of the same hardware as the Propulsion subsystem, it was opted to use 1 N HPGP thrusters. Though these have a thrust range between 0.25 and 1 N. These use the same fuel and similar inlet pressure to the system in place for the propulsion system, hence reducing the complexity of the spacecraft. A singular thruster can be seen in Figure 6.1b.

(a) HC7 Reaction Wheel. **(b)** 1N Thruster to be used 12 times on S/C.

Figure 6.1: AOCS comnponents

6.1.5. Performance Summary

Below, the performance of the AOCS is summarised for the reader.

Table 6.2: AOCS performance and major information summary.

AOCS Parameter	Value	Unit
Budgets		
Mass	70	[kg]
Avg. Power	112	[W]
Performance		
N. Reaction Wheels	4	[-]
Torque/Wheel	0.2	[N m]
Momentum storage/ wheel	6	[N m s]
N. of Thrusters	12	
Thrust/Thruster	0.25-1	[N]

6.2. Guidance, Navigation and Control

The Guidance, Navigation and Control subsystem for the LUMEN mission is treated as the suite of sensors whose data will be used by the AOCS and the pointing mechanism of the transmission laser. It has a range of different responsibilities, each related to the 3D positioning and attitude of the satellite, which were initially covered in the midterm report [7]. Where possible, off-the-shelf components are used to provide a benchmark for what is possible. Most of these sensors will come in pairs of two, to ensure redundancy and to cross-check for errors. To note is that the selected components will most likely not be optimised for the mission and requirements in question, and as such more fitting components could be designed at a later stage.

6.2.1. Operational modes

For the GNC, while the operational modes are the same as those for Section 6.1, they can functionally be divided into two major ones. These are transmitting and not transmitting. When not transmitting, the responsibilities of the GNC are timekeeping, inertial data, solar panel pointing knowledge, attitude and orbit determination. During the transmitting mode, fine laser pointing determination is added to this list. While each responsibility will be governed by a single sensor type or design, the sensors chosen often are capable of extracting additional data which can be used to verify the readouts from other sensors.

6.2.2. Requirements for GNC

Looking at the initial requirements set up for the GNC, they covered autonomy (LMN.GNC.002 and LMN.GNC.003), TRL (LMN.GNC.004), mass (LMN.GNC.005) and power consumption (LMN.GNC.006). While they govern budgets and design constraints, they are not sufficient to guarantee a spacecraft can navigate and operate safely. The requirements to design for mainly come from the AOCS subsystem (Section 6.1) and the payload subsystems, Section 4.3 and Section 4.2 as they have close interplay with the GNC subsystem and can only truly fulfil their accuracy requirements with adequate knowledge.

6.2.3. Timekeeping

Timekeeping is an important aspect of navigation, ensuring that the time in between measurements can be taken into account by the different algorithms. The passage of time will cause delays in signals and the laser reaching its target. The Ultra Stable Oscillator from AccuBeat [57], provides accurate time updates at 57.5 MHz, or once every 17.4 ns. It has a nominal power consumption of 6.5 W, a peak power consumption of 8 W and a mass of 2 kg. Currently, it is being used on the JUICE mission, which requires high fidelity and highly accurate time measurements for its science experiments. The location for the installation of these clocks is not crucial, so the two clocks should be placed as close as possible to the centre of gravity of the spacecraft to interfere as little as possible with AOCS management.

6.2.4. Attitude

The attitude is a measure of the overall pointing direction of the spacecraft. A commonly used method of determining attitude is star trackers. These are optical sensors which identify stars in their field of view and compare them to a stored star catalogue. This comparison allows for the determination of the orientation of the star tracker on the satellite. The off-the-shelf unit considered here is the T1 Star Tracker from Terma [58]. These have a cross-axis accuracy of 2.2", and a proven lifetime of at least 15 years. Their theoretical failure rate at 25 years is 7 % at $35\,^{\circ}$C, which decreases at lower operating temperatures. The baffle and electronic unit add up to a mass of 0.76 kg and require 3.3 W of power. These star trackers should be installed on opposite sides of the spacecraft, at an angle where strong light sources such as Earth, the Moon and the Sun are in view as little as possible during regular operations.

6.2.5. Acceleration

The accelerations of the satellite, both linear and rotational, will be measured by an inertial sensor. The HG9900 from Honeywell [59] makes use of Ring Laser Gyroscopes and Quartz Accelerometers on all three axes. It provides a gyro bias of $0.0035\,^{\circ}\,\mathrm{h}^{-1}$ and an accelerometer bias of 25 µg, which has been rated for high-speed manoeuvres performed by military platforms and other satellite missions. It weighs 2.7 kg and consumes power equivalent to 10 W. For these inertial measurement units to be as accurate as possible, they should be installed at or near the body's centre of gravity.

6.2.6. Solar panel pointing

To ensure that the solar panels are accurately pointed, sun sensors will be employed. The BiSon64-ET-B from Lens R&D [60] is one such sensor, which employs multiple photovoltaic units to determine the direction of the incoming sunlight. About the size of a 2€coin, a mass of 0.033 kg and no power consumption, this sensor offers an accuracy of 0.5° over a 58° 2-axis coordinate frame. As the con-

centrator solar panel type chosen has a self-correcting factor at most 2°, the accuracy this sensor gives is sufficient. Their small size will allow them to be installed directly on the solar panels which ensures that the measurements received coincide with the solar panel's actual angle. In total, four of these sensors will be installed, two on each array.

6.2.7. Orbit determination

While the other responsibilities are straightforward in their design, the orbit determination is less so. Traditionally, satellites use GPS systems or other networks to determine their orbit and position in 3D space. Other satellite missions around the moon have made use of the Deep Space Network, or in the case of the Lunar Reconnaissance Orbiter, a guiding laser from Earth [61]. However, due to the large variation in altitude during transmission and the high pointing accuracy required by the transmitting laser, a separate system will have to be designed. Two options were considered: a laser tracking system and a radio wave beacon system. The laser tracking system was let go as it would require a separate module per satellite, each with its individual moving parts and tracking system. This would add a considerable amount of mass and power to be added to the receiver, even more when taking redundancy into account. In comparison, radio beacons can be omnidirectional, use no moving parts and use less power. The Jason-1 mission [4] employed the DORIS subsystem to use the signal received from radio beacons on Earth in order to determine its orbit at 1336 km with a radial accuracy of 0.3 m. This gives it an accuracy of 0.11 µrad. From Section 6.1, the orbit knowledge requirement for the LUMEN mission was 700 m, which would be 0.87 µrad for the orbit chosen, and is thus possible to achieve. In order to recreate a version of the DORIS system, three beacons with their signature frequencies will be placed around the receiver. The satellite will then use the Doppler effect and respective signal arrival times in order to determine the satellite's position both in an absolute sense and relative to the receiver. This will also double as a rough, initial pointing determination for the transmission laser. For the receiver on the satellite to be able to pick up the signals, all gains and losses must be calculated and a configuration chosen which provides less loss than the receiver sensitivity. Regarding frequency, the S-band (2-4 GHz) was chosen in order to minimise Free Space Path Loss (FSPL) and it is a well know frequency band with numerous off-the-shelf components. On the beacon side, the TX-2400 from AAC [62] is able to transmit radio wave frequencies of 2-2.4 GHz, with channels available in steps of 25 kHz. The signal is then sent through a PA 200270-10 A amplifier from Kuhne [63] which has a gain of 47.5 dB. Finally, the signal is sent out through an OMNI-A0142 high gain omnidirectional antenna from Kuhne [64], with a gain of 4 dB. For the three beacons 2050 MHz, 2200 MHz and 2350 MHz were chosen as their signature frequencies. These would then send out pulses containing the time data gotten from their clocks, the same model as in Section 6.2.3.

The $FSPL$ can be calculated using Equation (6.4), where d is the distance, f is the frequency and c the speed of light.

$$FSPL = 20\log_{10}(d) + 20\log_{10}(f) + 20\log_{10}\left(\frac{4\pi}{c}\right) \tag{6.4}$$

On the satellite side then, the antenna used is the AC-2000 from AAC [65], with a gain of 2 dB. From the antenna the signal gets transferred through another amplifier, this time the LNA 200250 A-SMA from Kuhne, giving a gain of 35 dB. Finally, the receiver at the end of the signal will be the RX-2000 from AAC [66], which has the same frequency range as the transmitter and can have 26 preset channels with a 20 MHz bandwidth. It has a sensitivity of about -110 dB.

In Table 6.3, an SNR analysis is performed similar to what will be explained and used in Section 6.4. It can be seen that the total gain budget of this chosen system is thus sufficient for the receiver to detect and recognise the signal. In total, each beacon will have a mass of 2.77 kg and a power consumption of 37 W while for each satellite this will be 0.41 kg and 1.501 W respectively.

6.2.8. Fine laser pointing

By far the system that requires the most accurate knowledge is the fine laser pointing system. In order to limit the size of the receiver on the lunar surface to acceptable levels, a laser pointing knowledge

Table 6.3: The link budget losses and gains for the RF Beacon capturing system.

Source	RF Beacon
RF Power [dB]	47.50
Circuit L [dB]	-0.30
Cable L [dB]	-0.26
Tx Ant. G [dB]	4.00
EIRP [dB]	**50.94**
Frequency [Hz]	2.35E+09
Distance [m]	1.50E+07
FSL [dB]	-183.39
Atmospheric L [dB]	0
Pointing Offset L [dB]	-0.12
Propagation L [dB]	**-183.51**
Receiver G [dB]	2.00
Receiver Noise [dB]	200.64
Data Rate [dB]	-51.76
Circuit L [dB]	-0.30
Cable L [dB]	-0.20
Total Rx G [dB]	**150.4**
SNR [dB]	**17.81**

of at least $1\,\mu$rad is required. In order to achieve this, a combination of different proposed methods will be used. In [3, 67, 68], a method is proposed and expanded upon where a laser beacon is shone upon a nanosat as seen in Figure 6.2.

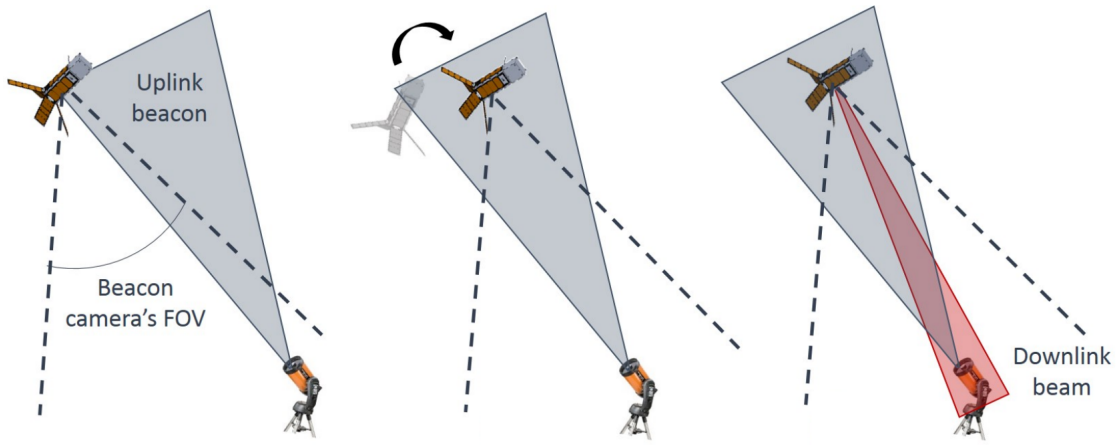

Figure 6.2: Depiction of the closed-loop system from [3]

On the satellite a camera with a charged-couple device (CCD) is then used alongside a focusing lens to determine the location of the beam and with that the current pointing angle, which is depicted in Figure 6.3.

For the LUMEN mission a similar system will be used, but the laser beacon is placed in the middle of the transmission laser segment. This guiding laser will have a wavelength different from the neighbouring transmission lasers in order to avoid interference and to be able to differentiate it from the others. In the middle of the receiver on the Moon a $1\,$m radius circular retro-reflector array will be placed which will reflect the guiding laser back to the satellite, where a telescope placed on top of the transmission segment will catch part of it. Using the angle retaining properties of lenses, illustrated in Figure 6.4, a CCD will then be able to sense where this concentrated beam is and thus extrapolate

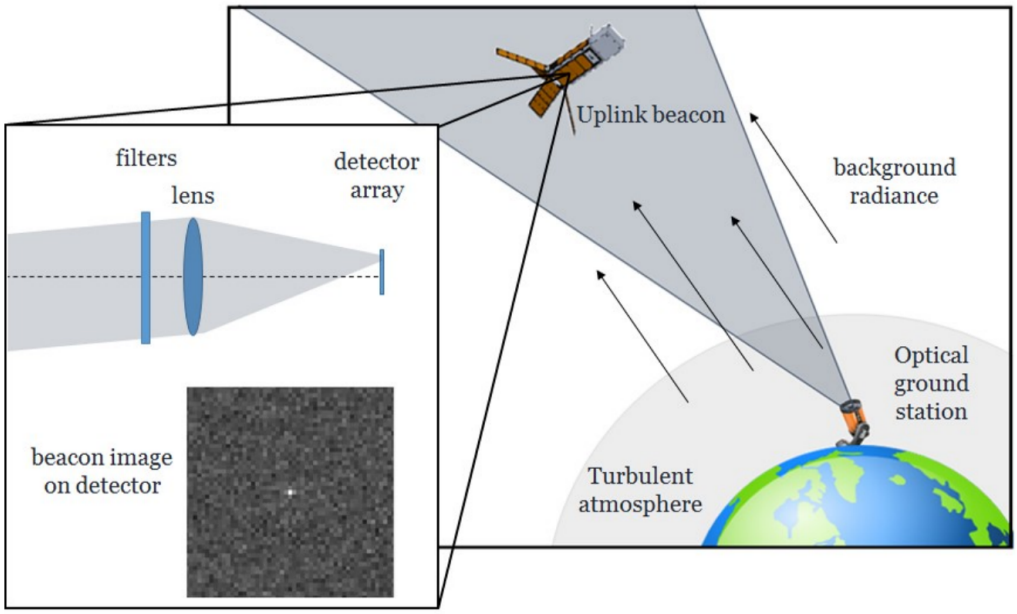

Figure 6.3: Depiction of the beacon receiving function from [3]

the current pointing angle (Figure 6.5).

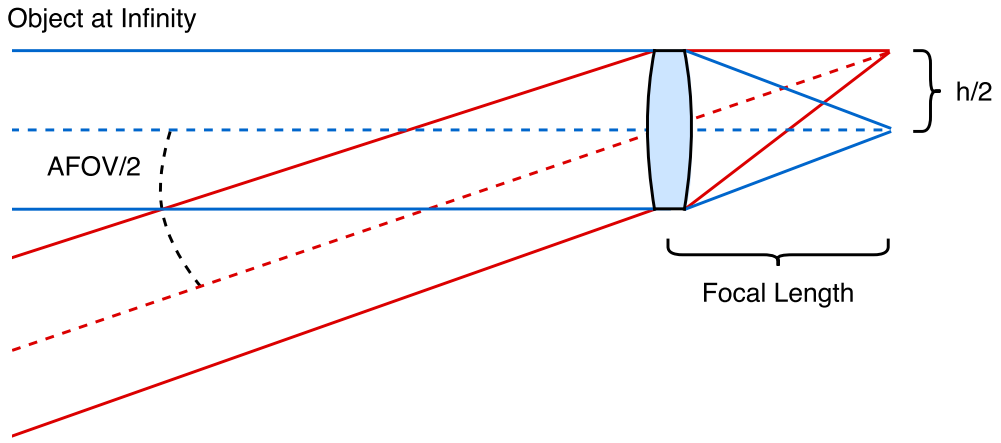

Figure 6.4: Depiction of the relation between angles, focal length and pixel size from [3]

In [3], an MT9P031 CCD from Aptina [69] was used integrated in a Matrix Vision mvBlueFox-IGC camera [70]. This had a pixel height of $2.2\,\mu$m, a quantum efficiency of 30% at $635\,$nm and a resolution of 2592H X 1944V. The lens that was employed had a focal length of $22.5\,$mm and an aperture of $16\,$mm. Finally a $1\,$mW laser with a wavelength of $635\,$nm was used for the beacon. Using Equation (6.5), each pixel had a field of view of $97.78\,\mu$rad. This would represent the pointing knowledge if the beam was focused on a single pixel and the change in angle had to be detected in steps by the beam moving over to the next pixel. In reality, it is better to increase the spot size on the sensor in order to differentiate between the centre and the outer edges of the beam. The paper then discusses extrema searching and error correction algorithms to further increase the accuracy of the knowledge down to $20\,\mu$rad.

$$\frac{FOV}{2} = \tan^{-1}\left(\frac{\text{Pixel height}}{\text{focal length}}\right) \tag{6.5}$$

This method can be adapted to fit the LUMEN mission. First, Aptina has since the writing of this paper released a updated CCD. This is the MT9J003 [71]. While still the same size, its pixels are now $1.67\,\mu$m across, with a resolution of 3856H X 2764V and the pixels themselves are also more

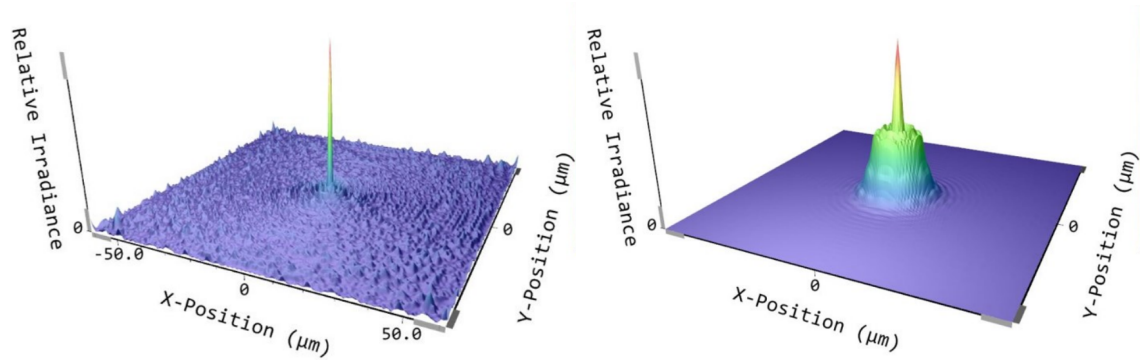

Figure 6.5: Depiction of the read-out of the CCD from [3]

sensitive. This CCD is incorporated into the Basler acA3800-14um/uc camera [72]. Using only this new camera, the rough pointing knowledge would decrease to 74.22 µrad. This CCD can also drive the choice of the guiding laser. Inspecting the data sheet, the CCD is shown to have the highest quantum efficiency at 455 nm, for which an appropriate laser can be selected. Since this laser will not be used to transmit power, a 5.5 W, 455 nm Collimated Laser Diode from RPMC [73] is selected. Another aspect that can be changed is the lens, which will affect the focal length. To find what was possible, a star gazing telescope was searched for. The Celestron Advanced VX 700 [74] has a focal length of 2.8 m, a tube length of 0.56 m, an aperture diameter of 0.22 m, a mass of 12.7 kg and a power consumption of 42 W. With this focal length, the rough estimate of the knowledge accuracy can be calculated using Equation (6.5) to be 0.62 µrad. This could later be further refined using the extrema searching algorithms and shows that with current technology it is certainly feasible to achieve the required 1 µrad pointing knowledge. Only the guiding laser should enter the CCD, so a bandpass is placed, preferably in front of the telescope. A 455 nm bandpass from Edmund Optics [75] is capable of almost completely blocking every wavelength other than 455 ± 2 nm, of which it only blocks 15%. Finally, to verify the pointing of the fine steering mirrors and provide a second feedback loop, a low-power laser reflecting off of the FSM's backside into a camera will be used with the same measuring concept as above.

6.2.9. Global GNC

With each responsibility of the GNC now covered, Table 6.4 shows the total mass and power required by the satellite and the beacon. For three beacons, this means that the total extra mass and power required at the receiver is 8.01 kg and 110.7 W.

6.2.10. GNC Verification & Validation

Verifying the calculations performed in this section was done by performing a step-by-step manual calculation and comparing them with the output in each step of the process. Validation of these different sensors and measurement systems will be done by lab testing their response in different conditions which could occur during the mission. Most of the components chosen are off the shelf and have proven flight capabilities. The two more complex systems, orbit determination and fine-pointing knowledge can be further validated by way of a separate cubesat mission if necessary.

6.2.11. Sensitivity Analysis

As most elements in the GNC subsystem rely on off-the-shelf components, its mass and power consumption per spacecraft is almost fixed. Only if a required knowledge accuracy were to become smaller than what the related component is capable of, will a change be required. This does not necessarily rely on the number or size of spacecraft, but more on technology type, and thus the GNC subsystem is not very sensitive to minor and quantitative changes in the overall design. Most components are used by a large fraction of satellites, and as such a new off-the-shelf component should not prove too difficult to find.

Table 6.4: mass and Power for each satellite GNC component and Beacon.

Component	Nr.	Mass [kg]	Power [W]
Satellite GNC			
Clock	2	2	6.5
Star tracker	2	0.76	3.3
Inertia sensor	2	2.7	20
Sun sensor	4	0.033	0
Antenna	1	0.1	0
Amplifier	1	0.11	0.01
Receiver	1	0.2	1.5
Guiding laser	2	0.05	5.5
Bandpass filter	1	0.05	0
Telescope	1	12.7	42
CCD camera	2	0.09	2.8
Total		24.492	119.71
Budget		74	120
Beacon			
Clock		2	6.5
Transmitter		0.07	2.4
Amplifier		0.5	28
Antenna		0.1	0
Total		2.67	36.9

6.3. Command & Data Handling

The command and data handling is the 'brain' and 'nervous system' of the satellite. It ensures that all subsystems execute their tasks as intended and data can be transmitted to and from the different components. To be able to design a working command and data handling system, it is necessary to know which subsystems and components are present in the spacecraft. This dictates both connection types and data processing capabilities. In this section, the communication flow will be presented from which the telemetry generation can be established. Finally, the architecture of the onboard computer will be presented.

Setting up the telemetry generation overview starts with knowing the communication flow within the system. In such a communication flow diagram, the different subsystems, together with their respective components, are presented with the data flows between them.

Every subsystem has its controller for direct control loops within the subsystems. This alleviates the operations that the onboard computer has to execute and increases the responsiveness of components that are dependent on a feedback loop. The telemetry from all the components within a subsystem is routed through the controller to the onboard computer which can store and downlink it. This is also in accordance with the requirements of LMN.CDH.001 and LMN.CDH.002.

6.3.1. Onboard Computer

The onboard computer is responsible for handling all the data that the subsystems produce, be it telemetry, scientific measurements, or commands. In the case of the LUMEN mission, the spacecraft do not produce scientific data and as such the system only has to be sized for telemetry and commands.

The onboard computer consists of multiple components responsible for different tasks in the process of data handling. From receiving the data to permanent storage, to communication with other subsystems they communicate with the central processor in their own way. A diagram of the connections and communication protocols of the components can be found in Figure 6.7

On commercially available data handling system boards, the memory, storage, and CPU (Central Processing Unit) are all integrated, thus their connections are soldered to the printed circuit board

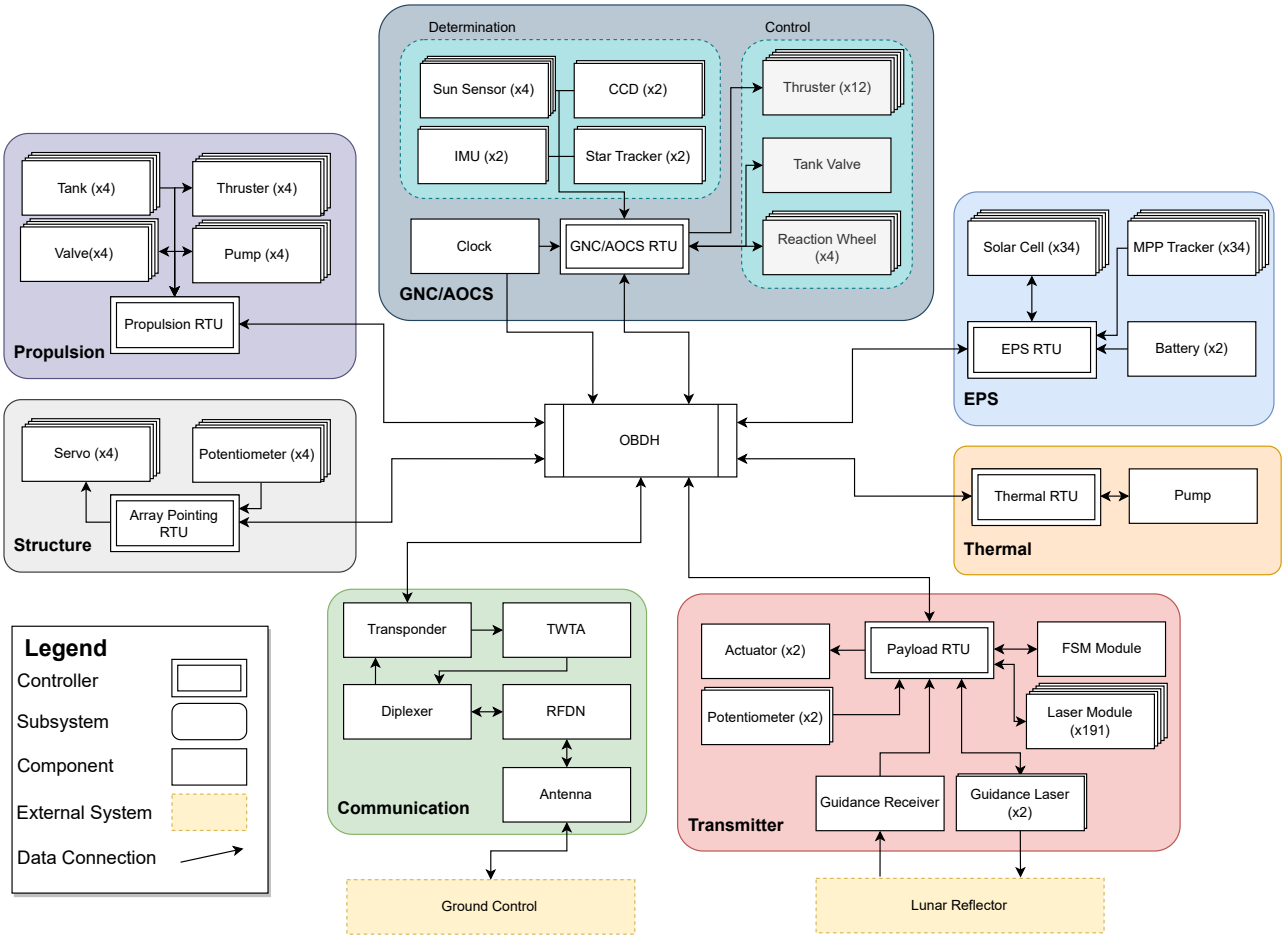

Figure 6.6: A diagram of the data connections between the onboard data handling unit and the subsystems.

(PCB). For simplification purposes, communication between these components is handled entirely by the bus controller, though modern architecture may provide a direct connection between RAM (Random Access Memory) and CPU for increased performance. This is also more efficient as well as sustainable as there are fewer losses along the circuit which is beneficial for stability and power draw.

The CPU is responsible for the calculations that have to be done with the data, encoding, and processing the commands as well as commanding the entire spacecraft with the programmed instruction set. This ensures autonomous operations in accordance with requirement LMN.OPS.005. It is also responsible for monitoring the health of the subsystems and for the maintenance of the operating system. To do that a watchdog process is continuously active to detect faults and engage fault mitigation measures. This ensures that requirement LMN.OPS.001 is complied with.

The bus is not only responsible for communication between the components on the PCB, but also with other components in the system. By means of connection ports on the PCB, wired connections with other subsystems can be established. The components transmit and receive data through these connections and the bus is responsible for routing the data between the subsystems and the CPU.

For communication between systems, an agreement must be made on data rate, voltage levels, and the meaning of those voltage levels (i.e.: which voltage level indicates a 0 or 1 in bit code). For the data rate, a timing element should be present. This can be achieved by having a clock at both components or having one of the two components supply the timing information. These two methods are called asynchronous and synchronous respectively. Furthermore, only serial communication will be considered for the wired connections as parallel communication is too costly at this scale. Only the components that are integrated into the circuit (RAM, CPU, storage) will have parallel communication and are indicated as such by the amount of lanes they will use, as seen in Figure 6.7. The communication protocols between these latter components will not be discussed in further detail as this is

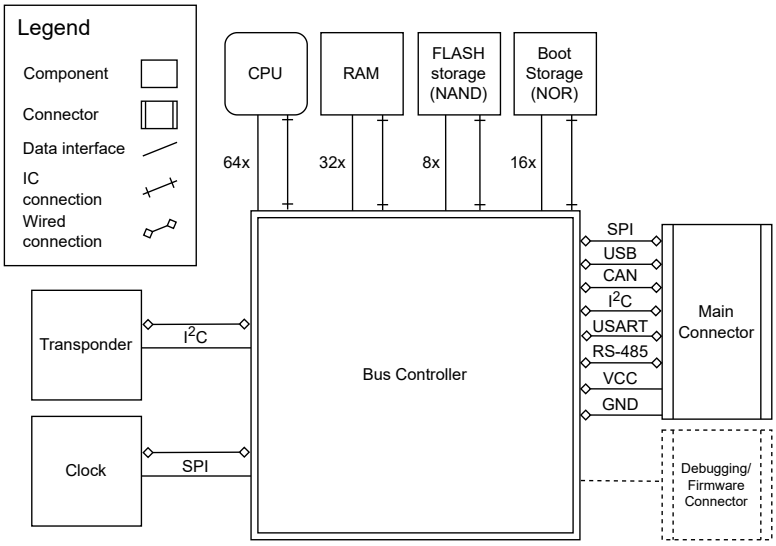

Figure 6.7: A diagram of the onboard computer with its physical connections and communication protocols (sourced from the author).

outside the scope of this report and is often dictated by the system architecture of the commercially available boards.

The clock is necessary for calculations onboard the spacecraft, as well as time stamping telemetry, and giving a clock for the CPU. This connection must be serial synchronous as the clock itself is the input of the system clock. The accuracy of time should be very high and, consequently, the sampling rate should also be high. The SPI connection has all these characteristics and is therefore a suitable choice for the clock connection.

The transponder, which is only active during up- and downlink and does not necessarily have a continuous data stream during that time, requires a serial synchronous connection. This way the data will be handed to the CPU in the most reliable way, using the CPU clock for the communication agreement. The I^2C connection fits these requirements and has the added benefit of reducing data throughput when the CPU cannot process the data fast enough.

Finally, the main connector contains multiple connection types. This gives a wide range of possible connections for other components and subsystems that are present in the spacecraft. At this stage, it is not yet known what other components must interface directly with the onboard computer. However, using the communication flow diagram as seen in Figure 6.6, the onboard computer will mainly interface with the subsystem remote terminal units (RTUs) otherwise known as microcontrollers. These microcontrollers have integrated clock crystals, dictating their own time, which means asynchronous communication is possible. To accommodate for both synchronous and asynchronous communication, as well as other benefits from the differing connection architectures, multiple connectors are present on the main connector. As soon as the requirements from the other subsystems and components are known, the unused connection types can be removed.

Data Generation

Sizing the memory and storage is fully dependent on the data generation rate of the telemetry of the components on the spacecraft. Thus, it is important to create an overview of all data-generating components, their sample rate, and the packet size they produce. Taking the components that are present in Figure 6.6 and compiling their data gives information on the data generation rate on the spacecraft. The overview of the data rate of the different components is given in Table 6.5.

The total data rate for the spacecraft is $40.6\,\mathrm{kb/s}$. This value will increase due to packetisation which will be discussed in Section 6.3.2. Accounting for this factor, the virtual data rate is $95.0\,\mathrm{kb/s}$. In a single orbit of 75708 seconds, the satellite will produce approximately $6.20\,\mathrm{Gbit}$ of data.

Table 6.5: An overview of the data generation of the components of the subsystems for the LUMEN spacecraft.

Item	TM type	Qty.	Sample Rate [Hz]	Packet Size (bits)	Data Rate (bps)	Item	TM type	Qty.	Sample Rate [Hz]	Packet Size (bits)	Data Rate (bps)
Power						**Propulsion & AOCS**					
Solar cell voltage in	voltage	22	1	8	176	Tank gauge	voltage	5	10	8	400
Solar cell voltage out	voltage	22	1	8	176	Propellant flow	voltage	5	2	8	80
Battery charge	voltage	1	1	8	8	Thruster valve status	on/off	16	5	1	80
Power on/off	on/off	22	1	1	22	Thruster control	voltage	16	1	8	128
Battery temp.	voltage	1	1	8	8	Reaction wheel state	voltage	4	5	8	160
MPP tracker	voltage	22	5	8	880	Reaction wheel control	voltage	4	1	8	32
Cell temp.	voltage	22	1	16	352						
						Structure					
Thermal						Potentiometer	voltage	4	1	8	32
Pump speed	voltage	1	1	16	16	Servos/steppers	voltage	4	5	8	160
Coolant temp.	voltage	1	1	8	8						
						GNC & AOCS					
Comms						Star tracker	voltage	2	10	8	160
RF network temp	voltage	1	1	8	8	Sun sensor	voltage	1	10	8	80
Transponder temp.	voltage	1	1	8	8	IMU	voltage	1	10	8	80
Antenna temp.	voltage	1	1	8	8	Temp.	voltage	4	10	8	320
Transmit power	voltage	1	1	8	8						
Timekeeping	serial	1	1	32	32	**Payload**					
						Power system	voltage	1	10	8	80
C&DH						Payload commands	serial	2	100	8	1600
CPU power	voltage	1	1	8	8	Payload on/off	on/off	1	1	1	1
CPU temp.	voltage	1	1	8	8	Laser module temp.	voltage	191	10	8	15280
Fault detection	on/off	1	5	1	5	Laser module power	voltage	191	10	8	15280
Fault status	on/off	1	5	1	5	Guidance receiver	voltage	1	10	8	80
TM out	serial	1	100	8	800	Potentiometer	voltage	2	100	8	1600
TM in	serial	1	100	8	800	Guidance laser temp.	voltage	1	10	8	80
RAM temp	voltage	1	1	8	8	Guidance laser power	voltage	1	10	8	80
Storage temp	voltage	1	1	8	8	FSM module	serial	1	100	8	800

RAM Sizing

The RAM must be able to store the incoming telemetry, the incoming commands, and the necessary data for the operating system simultaneously, as well as temporary data that comes as a byproduct of the calculations that have to be done on board.

To size the RAM two points must be discussed; size and error correcting code (ECC) functionality. The RAM for the CPU must be sufficiently large to store the data that the CPU must actively and quickly access. Having larger RAM means more data can be quickly accessed by the CPU. However, larger RAM is more expensive and requires more power. This impacts both the cost budget as well as the power budget. As such the RAM size must be chosen to not significantly bottleneck the CPU processes while not becoming overly large.

Taking a data generation rate of $90.1\,\mathrm{kb/s}$, as previously determined, together with an estimated $1.6\,\mathrm{kb/s}$ command rate for incoming data, gives a rate of $\approx 91.7\,\mathrm{kb/s}$. For the LDPC code, a 4096^2 matrix must be loaded into memory which has a size of $134.2\,\mathrm{Mbit}$ (assuming 8-bit precision). Assuming the processor will work on a single codeword at a time, only one of these matrices will be present in memory at any given moment. At this stage it is still unknown what the subsystems will require in terms of computational operations and the associated memory requirements. The LDPC code will, however, most likely be one of the most demanding operations. Combining the mentioned rates, and adding a safety factor of 2 to account for a second demanding process from one of the subsystems, a final memory capacity of $268.5\,\mathrm{Mbit}$ is required. Important to note is that in case the memory capacity is insufficient, data can be paged to the mass storage temporarily acting as additional memory. This reduces performance but can be used incidentally when more RAM capacity is necessary.

The ECC aspect is another point to keep in mind. While ECC memory does decrease the risk of corruption, it comes at the cost of being more expensive as well as being more power-demanding. If the processes are deemed sufficiently sensitive, and should therefore not be corrupted, ECC RAM should be chosen. Consequently, the ECC method should be appropriately chosen so as to not be too demanding in terms of power, while still providing reliability for data integrity.

As telemetry is not a critical part of the mission, data integrity is not of the highest importance. However, it is important to minimise system faults that occur due to quantum interactions known as bit-flips, for example. By using ECC RAM with the least demanding type of ECC these system faults can be minimised while not increasing the power draw by a large factor.

Storage Sizing

The storage is split into two parts: the boot storage, and the mass storage. Both storages should be non-volatile as the data must be maintained during power loss. However, they can be optimised differently as the chip architecture can be specially selected for the operations that must be executed with those chips. By separating the boot storage and mass storage potential faults can be isolated, increasing reliability.

Furthermore, only Flash-based storage will be considered. This is due to the fact that the alternative, hard-disk based storage, contains moving parts. The reliability of such systems is lower compared to electronically rewritable storage (Flash storage) especially when considering the vibrations during launch that the system must withstand. Moreover, electronic storage is both lighter and has a lower profile than hard-disk storage. While electronic storage is more expensive in terms of cost per storage bit, the lower mass and profile compensate for that production cost.

The boot storage is the dedicated storage location of the spacecraft operating system. As it contains only the operating system, and it will not have many write operations, the architecture can be optimised for this. NOR-type storage is optimised for read-only operations providing superior read times compared to the more conventional NAND-type storage. Write operations are slower, but as the boot storage will only be written to when first loading the operating system onto the chip, and possibly later on during incidental updates, it is beneficial to choose a read time-optimised chip. The sizing for the boot storage is entirely dependent on the size of the operating system. It should be sized to fit it as best possible leaving 30% extra capacity for potential updates later on in the mission in accordance with requirements LMN.OPS.002 and LMN.OPS.004.

The mass storage must be able to store processed telemetry until it can be downlinked to the Earth, as well as any paged data that is not loaded onto RAM. This storage chip will have both read and write operations. NAND-type FLASH storage is optimised for both of these operations. Taking the data generation rate of 6.20 Gbit per orbit, the mass storage should be able to store an entire orbit's worth of data. For redundancy, a second orbit should also be able to be stored on the mass storage, in case a transmission window is missed. This increases the required capacity to 12.4 Gbit. This is more than stipulated in requirement LMN.CDH.002, but increases reliability without increasing mass or power requirements by a significant amount as the FLASH storage chips are neither heavy nor power consuming.

Finally, capacity degradation should be taken into account. Using a capacity degradation rate of 5% per year and a mission lifetime of 25 years, the required capacity should be divided by $0.95^{25} = 0.277$ giving a capacity requirement of 44.8 Gbit.

C&DH Final configuration

Taking all the previous sizing into account, a final configuration can be obtained for the Command and Data Handling unit. An overview of the system can be found in Table 6.6. This system approximates commercially available boards such as the *Volkh processing platform* [32].

Table 6.6: An overview of the configuration of the Command and Data Handling subsystem.

CPU	20 MHz SmartFusion 2 SoC
Memory	268.6 Mbit
Boot Storage	2 Gbit [TBC]
Mass Storage	44.8 Gbit

Power	Volume	Mass
3 W	0.02 l	0.021 kg

With a power of 3 W and a mass of 0.021 kg, this falls well within the budgets allocated for the command and data handling subsystem. Furthermore, the power consumption complies with requirement

[32] URL: `https://infinityavionics.com/products/volkh/` [Cited: 13/06/2023]

LMN.CDH.003. Important to note is that these values are based on the Volkh processing platform that was previously mentioned. Designing a similar board might change these values, though it is expected that the custom board will not deviate significantly from these presented. The mass presented in Table 6.6 does not take the cables between the subsystems and components into account, which can increase the mass of this subsystem substantially. Keeping the length of the cables as low as possible is beneficial for mass, stability, and power draw as less power is lost over the cables. This is beneficial both for the performance of the spacecraft as well as the sustainability goals.

Finally, for reliability reasons, a full second board can be integrated to ensure that the satellite can remain operational, should the primary board fail. As the board has a mass of 21 grams, a second board can be added without exceeding the mass budget allocated for the command and data handling subsystem. The power budget will not change as the boards will not be used in parallel.

6.3.2. Encoding and Packetisation

Transmitting data does not occur as a continuous stream of data. Limited transmission windows and physical obstructions prevent that. Rather, data is split into *packets* and transmitted in parts to the receiver. Using metadata from in the packets (pointers to its origin, relative location, and timestamp), the data can be reconstructed to what it originally was at the receiver end.

The packets in and of themselves are not transmittable as these are only meaningful in a virtual space. To be able to transmit the data, the packets must be 'translated' to a physical representation as a signal. This process is called encoding and has multiple methods to be achieved. Special types of encoding exist that are able to reconstruct (partially) corrupted data by sending extra data in the signal; so-called 'parity overhead'. This puts more strain on the required data rate, but ensures that all transmitted data can be read. Depending on the amount of parity that is added to the signal, different coding gains can be achieved. The larger the amount of parity data, the larger the coding gain. This comes at a cost of an increased required data rate as the parity data must be sent on top of the metadata and real data. A visualisation of the structure of the encoded packet can be found in Figure 6.8.

For this mission the LDPC[8192,4096] (Low Density Parity Check) code [76] was chosen which has a data rate of 1/2. This means that for every bit of data a parity bit is sent.

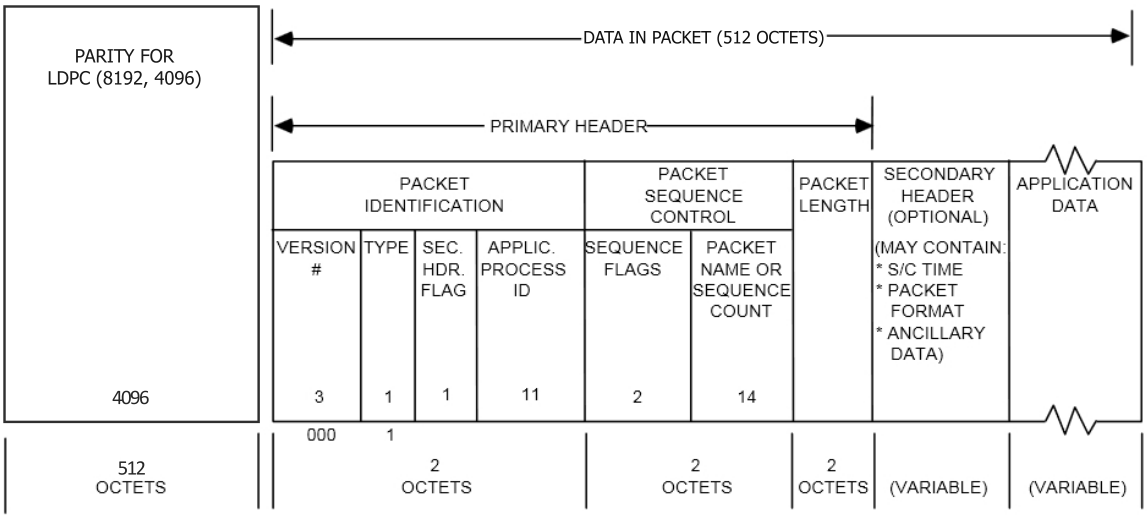

Figure 6.8: A visualisation of the data packets, including header sizes, that can be stored, and transmitted to the ground. (Adapted from CCSDS [77]).

Using the sizes for the header metadata and parity information as presented in Figure 6.8, it can be calculated that for every 4096 bits of data 4168 bits are needed for metadata and parity. Taking all items from Table 6.5, gives a raw data rate of $40.1\,\mathrm{kb/s}$. This data rate can be packetized in 10

codewords, which gives the virtual data rate of $90.1\,\mathrm{kb/s}$. In a single orbit of 75708 seconds, the spacecraft produces approximately $6.20\,\mathrm{Gbit}$ of data.

The lower rate/higher gain coding was used as the communication window is quite large which results in relatively low required data rates. The increase in gain from the coding was larger than decreasing the required data rate, making it a more economical choice for the communication system budget. Moreover, adding more parity ensures that the data can be reconstructed at the receiver minimising lost telemetry.

Verification of the subsystem can be done using analysis and testing. By means of a simulation, the software can be verified. This ensures that the software architecture is correct and can be integrated with the hardware. When installing the software on the hardware, an integration test should be performed to confirm that both the hardware is working correctly and that the software can indeed interface with the hardware and perform its function.

6.4. Communication

Communicating with satellites orbiting the moon occurs over a large distance, therefore a wireless communication method is necessary. The communication subsystem is responsible for this communication, sending telemetry to the Earth, and receiving commands from the ground station. Usually, the communication subsystem would provide a means for communication for the crew of the transmission, or scientific data from the payload. In the case of the LUMEN mission, which neither transports humans nor performs any scientific measurements, the communication will be limited to commands and telemetry. In this section the link budget will be analysed, a system architecture will be presented, and the subsystem sizing will be performed.

6.4.1. Link Budget

The communication link must be designed carefully to ensure that telemetry and commands can indeed be received and sent successfully as per requirements LMN.OPS.003 and LMN.COM.001-004. This means that specific parameters must be chosen to establish a link, such as power, antenna size, transmission frequency, and data rate. To determine if the combination of parameters results in a functional communication link, a link budget analysis can be performed.

The link budget is based on the fact that to detect a signal, it must be significantly more powerful than *noise* sources. The noise sources are, for example, the inherent system temperature of the receiver, background radiation, etc. Enough energy must be present in the communication signal to be able to distinguish the actual signal from the noise signal. The link budget also reflects this, as it focuses on increasing the signal-to-noise ratio (SNR) to a sufficiently high level.

The signal-to-noise ratio can be determined from the relationship that can be found in Equation (6.6) as given by Zandbergen [78].

$$\frac{E_b}{N_0} = \frac{P \cdot L_l \cdot G_t \cdot L_a \cdot G_r \cdot L_s \cdot L_{pr} \cdot L_r}{R \cdot k_b \cdot T_s} \tag{6.6}$$

In this equation $\frac{E_b}{N_0}$ is the signal-to-noise ratio, P is the radio frequency power output, L_l and L_r are transmitter and receiver system loss factors, G_t and G_r are transmitter and receiver antenna gain, L_a is the atmospheric attenuation, L_s is the free space loss, and L_{pr} is the pointing loss. In the denominator, R is the data rate, k_b is the Boltzmann constant, and T_s is the system noise temperature.

The power of the system is mostly free to choose within the subsystem budget. Of course, it is ideal to minimise power consumption. However, reducing power means that gain has to be obtained through other means, such as a larger antenna. This in turn increases the mass of the subsystem. Therefore a balance should be struck between power and mass dependent also on which is more stringent.

The transmitter and receiver losses are an inherent property of an electrical system. Energy will be lost within the circuits of the system due to inefficiencies. Minimising this is important though completely eliminating it is not possible. Having said that, the losses within the system circuits are minimal compared to the losses incurred during free space loss.

The antenna gain on the spacecraft can be changed depending on its size. This of course comes at a cost of increased mass. The equation for antenna gain can be found in Equation (6.7) as given by Zandbergen [78].

$$G = \frac{\pi^2 \cdot D^2}{\lambda^2}\eta \tag{6.7}$$

Where D is the antenna diameter, λ is the transmission wavelength, and η is the antenna efficiency. For the ground station, existing infrastructure will be used. The Deep Space Network (DSN) and Deep Space Antenna (DSA) provide multiple 34-meter dishes with a gain of 68 dB. This limits communication to the 8.5 GHz frequency [79]. This is also in accordance with the spectrum allocation as described by CCSDS [80] and requirement LMN.REG.003.

Due to the spread of the antenna of the DSN or DSA, a receiver will always be in view of the transmitting satellites. This configuration, associated with the DSN and DSA antennae, will be used for the remainder of this section also in accordance with LMN.COM.010-011.

Atmospheric attenuation occurs due to the interaction between the radio waves and the molecules in Earth's atmosphere. Depending on the radio frequency used the attenuation changes due to the different resonant frequencies of the molecules. This attenuation reaches a maximum of 0.5 dB for an elevation of $5\,^\circ$ according to Speretta [81].

The most significant contribution to signal losses is the free space loss. This is due to the fact that the energy of the emitted signal spreads over a larger area the further it travels. How strong this loss of energy is also depends on the wavelength the signal is transmitted at. The equation for free space loss is presented in Equation (6.8)

$$L_s = \left(\frac{\lambda}{4\pi S}\right)^2 \tag{6.8}$$

Where λ is the wavelength of the signal and S is the distance between the transmitter and receiver.

The pointing loss is due to the inaccuracy of aligning the transmitting and receiving antenna. Due to the lobe pattern of antennae, they are better at transmitting and receiving in certain directions. If the antennae are not aligned with these patterns, there will be a pointing loss. This loss is calculated using the relation in Equation (6.9).

$$L_{pr} = -12\left(\frac{e_t}{\alpha_{1/2}}\right)^2 \tag{6.9}$$

Where e_t is the pointing offset angle, and $\alpha_{1/2}$ is the half-power angle. For omnidirectional antennae, this loss is zero as its lobe pattern does not favour any particular direction. The total pointing loss is found by multiplying the pointing loss of the receiver and the transmitter.

The data rate is dependent on how much data must be transmitted in what time frame. For large amounts of data and short transmission windows, this rate must be very high. For the LUMEN mission, only telemetry is generated, thus the data rate requirement is relatively low. In Section 6.3 a detailed description of the generated data is presented. For LUMEN the expected data rate will be around 40.1 kb/s.

The final parameter is the system noise temperature. This temperature is a constant value depending on the brightness of other sources in the antenna's field of view. For the DSN 34 m dishes, the system noise temperature is approximately 28 K [79]. The system noise temperature for the spacecraft communication subsystem was assumed to be 614 K [55].

Filling in these parameters and converting to decibels, the link budget as presented in Table 6.7 was generated. This link budget was done for two low-gain omnidirectional antennae placed orthogonally for coverage and redundancy. As the antennae are omnidirectional, they do not require pointing, though they do not benefit from the increased gain of a directive antenna. To compensate for this lack of gain, either the data rate must decrease or the RF power must increase. For the safe mode, it is assumed that low power is required, thus the data rate is decreased.

Finally, a channel coding gain can be applied by using an error-correcting code. While this increases the signal-to-noise ratio, the effective data rate is decreased as parity data must also be sent. Depending on the type of error-correcting code, the data rate changes. Using LDPC (8192,4096) the

Table 6.7: The link budget calculations for the LUMEN system for uplink, downlink, and safe mode.

	Downlink	**Safe Mode**	**Uplink**
DC-RF η [-]	0.2	0.2	-
RF Power [dB]	0	-6.99	73.00
Circuit L [dB]	-0.30	-0.30	-0.30
Cable L [dB]	-0.26	-0.26	-0.26
Tx Ant. G [dB]	1.00	1.00	68.00
EIRP [dB]	**0.44**	**-6.55**	**140.44**
Frequency [Hz]	8.50E+09	8.50E+09	8.50E+09
Distance [m]	4.07E+08	4.07E+08	4.07E+08
FSL [dB]	-223.23	-223.23	-223.23
Atmospheric L [dB]	-0.03	-0.03	-0.03
Pointing Offset L [dB]	-0.12	-0.12	-0.12
Propagation L [dB]	**-223.38**	**-223.38**	**-223.38**
Receiver G [dB]	68.00	68.00	1.00
Receiver Noise [dB]	-214.13	-214.13	-200.64
Data Rate [dB]	51.76	30.00	51.76
Circuit L [dB]	-0.30	-0.30	-0.30
Cable L [dB]	-0.20	-0.20	-0.20
Total Rx G [dB]	**229.9**	**251.6**	**149.4**
Coding G [dB]	10.00	0.00	10.00
SNR [dB]	**16.93**	**21.70**	**76.44**

effective data rate is 0.5. Adding to this, the data generated during eclipse cannot be immediately uplinked, and should also be transmitted, adding to the data rate. Thus, to transmit the necessary data, the required data rate is $95.0\,\mathrm{kb/s}$. Requirement LMN.COM.018 states a data rate of $150\,\mathrm{kb/s}$ should be obtained and was thus used for the budget link. For the safe mode, the coding gain is not present as it is assumed that in safe mode the onboard computer will not be available for encoding.

As can be seen in Table 6.7, the SNR is above $7\,\mathrm{dB}$ for all links. This means communication is possible for the above configurations. The link budget having an SNR above $7\,\mathrm{dB}$ is in accordance with the minimum margin of $1\,\mathrm{dB}$ with an additional margin of $6\,\mathrm{dB}$ as per requirements LMN.COM.012 and LMN.COM.014.

6.4.2. Communication System Architecture

To be able to go from data to a transmittable signal, multiple steps are necessary. Various components are present in the communication system to encode, convert, amplify, and beam the data.

The first step already begins at the onboard computer (OBC) that generates and encodes the data. A more detailed description of the encoding of the data can be found in Section 6.3. When the data is ready to be transmitted, it is sent to the transponder which converts it to RF. This RF signal is then sent through the Travelling Wave Tube Amplifier (TWTA) which amplifies the signal. This then goes on through the duplexer which makes sure an incoming and receiving signal can be present in the circuit simultaneously. Finally, the signal goes through the RF Distribution Network (RFDN) which sends the signal to the antenna so it can be transmitted.

Vice versa, an incoming signal arrives at the antenna which is passed to the RFDN and the duplexer. Next, it arrives at the transponder which converts it to a signal that the OBC can read. The OBC then decodes the signal and processes the incoming data.

A diagram of this communication system architecture can be found in Figure 6.9. Both the antennae operate at a frequency of 8.5GHz (X-band). They are present orthogonally due to the fact that they do not emit fully omnidirectionally, but rather as a ring. By placing two omnidirectional antennae orthogonally, there is full coverage without having to point an antenna.

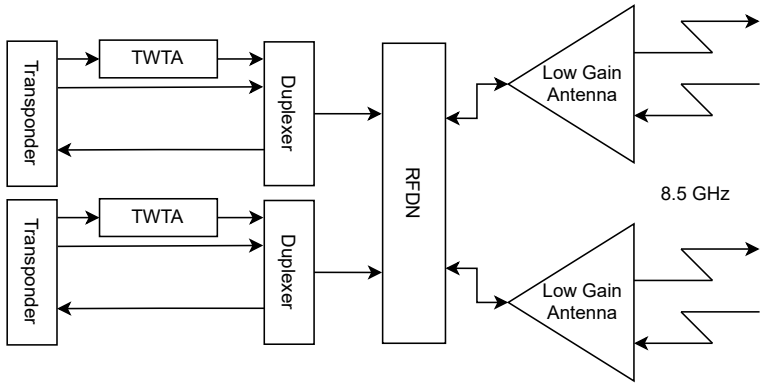

Figure 6.9: A diagram for the communication subsystem for the spacecraft of the LUMEN mission (sourced from author).

For redundancy, it might be valuable to have an additional transponder, tweeter and duplexer. During sizing, more information will be available on the mass of the system. Should the mass of a redundant communication system fit within the mass budget, no modifications have to be made. The redundant part can still make use of the same RFDN and antennae.

6.4.3. Communication System Sizing

Knowing all the components and the requirements they must meet, the system can be sized. Using the mass and volume relations as presented by Zandbergen [78] the following dimensions for the components were found: For a redundant system, the total mass equals 8.4 kg with a volume of a least

Table 6.8: A breakdown of the mass, volume, and power per component of the communication subsystem of a LUMEN spacecraft.

Component	Qty.	Mass [kg]	Volume [l]	Average Power [W]
Antenna	2	0.5	ext. (0.08)	-
Duplexer	2	0.5	0.29	10
RFDN	1	1.07		-
Transponder	2	1.72	2.3	1
TWTA	2	0.93	0.72	5
Total	-	8.37	>6.7	16

6.6 litres which satisfies requirement LMN.COM.017. Note that the power draw does not increase for the duplicate components as they will never be used simultaneously. The largest contribution to mass and volume is, as expected, the two transponders. The average power is 16 W with a minimum power draw of 11 dB during safe mode.

Verification for this subsystem can be done by means of analysis and testing. By simulating the orbit virtually, the communication windows can be simulated to check if the system can indeed establish a communication link. Testing of the subsystem is more challenging as it is not possible to simulate the relevant environmental conditions on Earth. However, certain segments of the communication subsystem can be tested to see if they perform correctly as well as testing the established link on the correct frequency.

6.5. Thermal Control System

In this section, the Thermal Control System, TCS, will be presented. To ensure the requirement LMN.THE.001, ”The thermal control system shall maintain all subsystem temperatures within their allowable windows”, a thermal analysis is done. In free space, there is no temperature, as there is no atmosphere. Therefore all radiation will be absorbed, reflected, or equal to the energy incident of the surface. However, the surfaces of the LUMEN spacecraft are assumed to be opaque as all used materials for the skin do not transmit light. Heat absorbed by the outside of the spacecraft is distributed over the subsystems based on the internal conductance gradients. The internal heat

must be compliant with the operational temperatures of the subsystems in order for them to function correctly.

In this section, first the method used to estimate the heat distribution in the spacecraft is explained. Then, the radiator system used to radiate internal heat to free space is identified. Afterwards, the internal thermal control system is presented in order to create the required thermal balance inside the spacecraft bus.

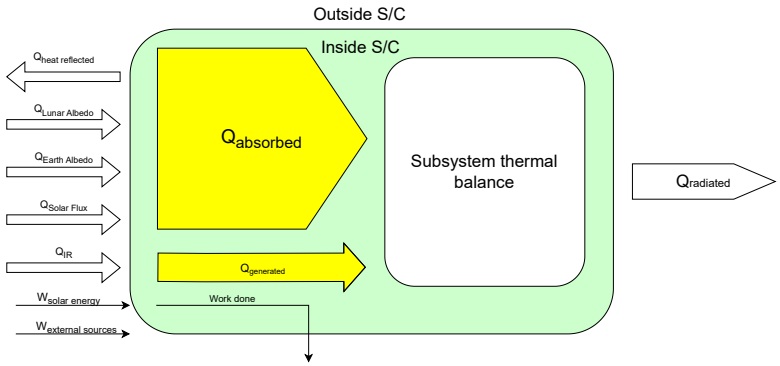

Figure 6.10: Thermal balance spacecraft bus.

The thermal balance of the spacecraft is presented in Figure 6.10, with the heat in net balance Equation (6.10) resulting in Equation (6.11). The highest contribution of heat is the solar flux, which is $1367\,\mathrm{W\,m^{-2}}$, and its intensity is varying based on the distance from the Sun to the surface. Furthermore, albedo heating is the solar flux radiated as a reflected source from non-black bodies. Regarding spacecraft heating, the albedo of the Moon and Earth are taken into account. Lastly, additional heat will be generated internally coming from the efficiency of the subsystems, where the losses will be converted into heat. This heat is indirectly coming from the solar flux absorbed by the PV cells, and battery energy being generated into work. Therefore, the solar panel heat balance will be treated separately. From all heat coming in, a part will be absorbed, while the rest should be passively reflected, or actively radiated, resulting in the operational temperature of all subsystems.

$$Q_{in} = Q_{out} \tag{6.10}$$

$$Q_{SF} + Q_{AM} + Q_{AE} + Q_{gen} + Q_{IR} = Q_{rad} \tag{6.11}$$

For all heat coming in, the distance of the heat source to the spacecraft will be accumulated. Secondly, the outside material, the Multi Layer Insulation (MLI), absorbs only approximately 5% of the solar spectrum that interferes with its surface. The ability to absorb the solar flux, therefore including the albedo flux, is the absorbtivity. For the infrared flux, this parameter is characterised by the emissivity, which indicates the ability of a material to radiate the infrared energy as thermal radiation. The heat absorbed is also dependent on the area the energy is reflected on, which differs on the configuration of the heat bodies with respect the spacecraft. In order to accumulate the true radiation that hits the surface of the spacecraft, the geometric view factor was considered. Two surfaces of a model can see each other based on their distance and relative angle and thus radiate heat. Such an exchange depends on the geometric factor, also named view factor, and is based on trivial geometries as can be seen in Figure 6.11b[33]. The view factors were calculated using integrals, formulated based on the different sides of the spacecraft with respect to the heat source. This can be seen as an example in figure Figure 6.11a, where the heat source in this figure is the lunar surface, reflecting the lunar albedo. The surfaces facing orthogonal and towards the heat source are in view of the most radiated power and have a view factor described in Equation (6.12) [82]. The $VF_{\perp}$ is represented by the N

[33]URL: https://abaqus-docs.mit.edu/2017/English/SIMACAETHERefMap/simathe-c-viewfactor.htm [Cited 07/06/2023]

side in Figure 6.11a. All four surfaces parallel to the heat source experience less radiation, so the effective area is adapted by the factor Equation (6.13) [82]. The $VF_{\parallel}$ surfaces are represented by the P, A and S sides in Figure 6.11a. The area opposite to the heat source is assumed to be zero, as the significance is in the order of 10^{-5}. This side is represented by the Z side in Figure 6.11a.

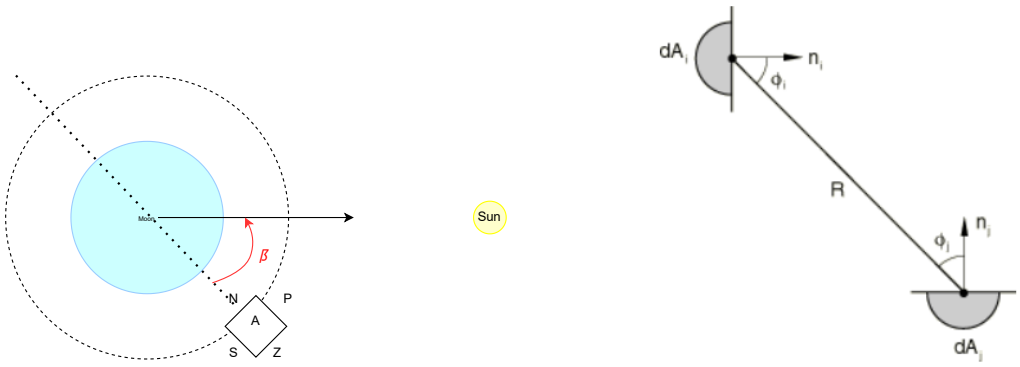

(a) View factors **(b)** Geometric view[34]

Figure 6.11: Critical distances

$$VF_{\perp} = \left(\frac{1}{2\pi}\right)\left[\pi - 2\sin^{-1}\left(\sqrt{1-\left(\frac{r_e}{r_e+h}\right)^2}\right) - \sin\left(2\sin^{-1}\left(\sqrt{1-\left(\frac{r_e}{r_e+h}\right)^2}\right)\right)\right] \tag{6.12}$$

$$VF_{\parallel} = \left(\frac{re}{re+h}\right)^2 \tag{6.13}$$

Furthermore, the angle ζ, called the solar zenith angle, provides an additional factor on the heat, taking into account the relative orbital plane between the primary and secondary heat source with respect to the spacecraft [83]. The configuration is shown in Figure 6.12. In the complete lunar albedo heat equation, only the ζ angle of the Earth with respect to the sun was accumulated, as the influence of the Lunar angles with respect to the Earth is relatively small with a significance of 10^{-3}.

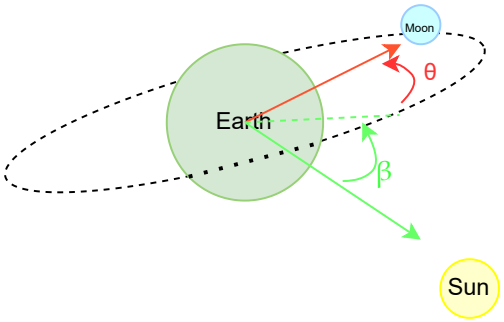

Figure 6.12: ζ angle

$$\cos\zeta = \cos\theta\cos\beta \tag{6.14}$$

- $-90° < \beta < 90°$
- $-90° < \theta < 90°$

Adding all mentioned factors together, a complete list of all in-, and output heat equations is shown in Section 6.5. In this list, Q_{AE} is the albedo heat of the Earth, Q_{AM} is the albedo heat from the lunar surface and Q_{gen} is the heat generated by the internal subsystems.

[34] URL: https://abaqus-docs.mit.edu/2017/English/SIMACAETHERefMap/simathe-c-viewfactor.htm [Cited 07/06/2023]

$$Q_{solarflux} = \frac{L}{4\pi d^2}(VF_{\parallel}A_{\parallel} + 4VF_{\perp}A_{\perp})\alpha_{MLI} \quad (6.15)$$

$$Q_{AE}{=}Q_{sol}\alpha(\tfrac{r_e}{r_e+D_{e-m}})^2(VF_{\parallel}A_{\parallel}{+}4VF_{\perp}A_{\perp})\alpha_{MLI}cos\zeta \quad (6.16)$$

$$Q_{AM}{=}Q_{sol}\alpha(\tfrac{r_m}{r_m+D_{m-s/c}})^2(VF_{\parallel}A_{\parallel}{+}4VF_{\perp}A_{\perp})\alpha_{MLI}cos\zeta \quad (6.17)$$

$$Q_{gen} = \eta_{subsystem}W_{done}A \quad (6.18)$$

$$Q_{IR} = Q_{IRmoon}\varepsilon_{MLI}(VF_{\parallel}A_{\parallel} + 4VF_{\perp}A_{\perp}) \quad (6.19)$$

$$Q_{rad} = \varepsilon_r\sigma(T_{rad}^4 - T_{space}^4)A_r \quad (6.20)$$

$$Q_{rad} = \varepsilon_r\sigma(T_{rad}^4 - T_{space}^4)A_r \quad (6.21)$$

In these calculations, the free space temperature is 2.7 K, which is caused by the cosmic background radiation. In order to identify the critical circumstances for the TCS, a cumulative analysis of critical values is performed. Secondly, the area of the MLI was beforehand fixed to be $2.75\,\mathrm{m}^2$ as by the placement of the outside subsections, like thrusters, sensors, the laser and antenna, only one-sided was decided to be feasible for the placement of the radiator. If this area is not sufficient enough, the radiator will be built with increased surface area, like a deployable system or louvre configuration. The optimum cold temperature configuration with its assumed critical circumstances is presented in Figure 6.13a, called the cold case. The optimum hot temperature configuration with its assumed critical circumstances is presented in Figure 6.13b, called the hot case. All associated circumstances regarding the S/C relative positioning of both the hot and cold case are presented in Section 6.5.

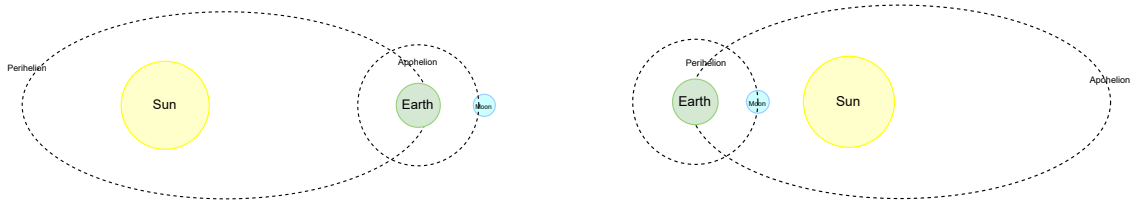

(a) Cold case. **(b)** Hot case.

Figure 6.13: Critical distances

- Minimum bond albedo
- Spacecraft at moon orbits apogee
- Earth located at aphelion
- Maximum angle ζ
- Minimum absorption heat area

- Maximum geometric albedo
- Spacecraft at moon orbits perigee
- Earth located at perihelion
- Minimum angle ζ
- Maximum absorption heat area

For the accumulated circumstances taken into calculation regarding the hot and cold case provided in Section 6.5, a few assumptions were made. First of all, it is assumed these circumstances can occur simultaneously. This is all dependent on the orbital locations and rotation of the aircraft. This must be researched in thermal optimization. Secondly, the surface of the spacecraft skin is assumed to be opaque, therefore the energy incident, τ_λ of the spacecraft is assumed to be zero. Another assumption is that the material properties are assumed to stay constant at the spacecraft temperature range, with the exception of the Phase Change Material (PCM). Lastly, it is assumed the subsystems do not have temperature gradients meaning the complete subsystem has an identical temperature.

6.5.1. Internal-External thermal regulation

First of all, the MLI of the passive thermal control system was already implemented into the calculations, as this is a passive radiator. The MLI reflected the vast majority of the heat by its small absorption, and high reflectivity values. However, even after taking this into account, additional radiators must be considered as there is more heat than the MLI can reflect. This is done by integrating a Mounted Thermal Control System (MTCS), onto the surface of the spacecraft bus. The spacecraft will be kept rotated with the same surface facing the sun, this side will be the heat source of the spacecraft. On the opposite side surface, the spacecraft will be used as the heat sink. As can be seen with the view factors, this side is the least exposed to radiation and also has a large area, together with a continuous view to free space, making the radiator more efficient. A 5 mm thick silver teflon surface

finish radiator will be used. This radiator has an ε_{rad} of 0.78, a $\sigma_{radiator}$ of 0.05, and a maximum ε_{radIR} of 0.15[35]. The operational temperatures of all subsystems are noted in Table 6.9, concluding in a general equilibrium operational inside temperature of $27°$, or 300 K.

Table 6.9: Subsystem temperatures

Subsystem	Operational range (C°)	Survival range (C°)
PV cells	-100/125	-100/125
Laser	20/30	0/55
Antenna	-100/100	-120/120
AOCS	-30/70	-10 - 40
Batteries	-20/60	-40/60
power box baseplates	-20/60	-20/80
Digital electronics	0/50	-20/70
Propulsion system	-8/60	-20/70
C&DH	-20/50	-40/75

All in and outgoing power of the spacecraft is presented in Table 6.10. The required power output can be calculated for both the hot and cold cases. The output power is constant undependent on its location in orbit. The area of the MTCS is the only unknown and can be optimised on the required heat inside the spacecraft.

Table 6.10: Power balance values

	IN (Watts)		OUT (Watts)	
	hot case	cold case	hot = cold	
$Q_{\text{Solar flux}}$ RAD	0.371 · A	0.347 · A	Q_{rad}	345.27 · A
$Q_{\text{Albedo Earth}}$ RAD	0.0051 · A	0.000059 · A		
$Q_{\text{Albedo Moon}}$ RAD	2.859 · A	0.048 · A		
Q_{IR} RAD	64.5 · A			
$Q_{\text{Solar flux}}$ MLI	14.268	13.34	Q_{MLI}	121.73
$Q_{\text{Albedo Earth}}$ MLI	0.00388	0.0000446		
$Q_{\text{Albedo Moon}}$ MLI	2.144	0.0364		
Q_{IR} MLI	118.25			
Q_{gen}	234			

This results in a required surface radiator area of $0.657\,\text{m}^2$ for the cold case and $0.8897\,\text{m}^2$ for the hot case. The critical case is the hot case and thus the $0.75\,\text{m}^2$ side should contain a constellation of a $0.8897\,\text{m}^2$, which can be achieved using louvres or deployable systems. This radiator is passive, which is preferred over active cooling with regard to mass and power budgeting. However, NASA developed a louvre system based on springs, making the system passive [84]. When the temperature of the satellite rises, the louvre opens, and the emissivity of the surface increases. However, in an eclipse, when the temperature in the spacecraft bus decreases, the louvre can be closed. This technology currently has a TRL of 5, however, in the final design the TRL can be reconsidered. The mass of the MLI skin will be 4.125 kg [85], and the mass of the MTCS will be 9.68 kg.

The most critical subsystem of the spacecraft, with a heat of 72.8 kW to be dissipated, is the laser system. This heat loss is significantly bigger than the needed heat dissipation of the spacecraft bus, therefore this subsystem will be cooled separately. The heat generated at the laser system of the LUMEN spacecraft equals $(1 - \eta_{laser}) \cdot Q_{in}$, assuming all power losses are converted to heat. The laser is mounted on the cold side of the spacecraft bus, therefore being optimal for heat dissipation and an insulation material needs to be integrated between the spacecraft bus and the laser system. Therefore, layers of aerogel will be used, as this is a lightweight material with a low thermal conductivity [86]. Based on the manual of the off-the-shelf diode laser module, which has a built-in connection for

[35] URL: `https://www.nasa.gov/smallsat-institute/sst-soa/thermal-control#_Toc120613722` [Cited 11/06/2023]

heat pipes, liquid cooling is considered for the dissipation of all heat in the laser system. With graphine-fibre-carbon-matrix heat pipes, an External Thermal Control System, ETCS, with an emissivity of 0.9, the double-sided area of radiators required is $88.05\,m^2$, having a mass of $103.84\,kg$ [87]. This is only the mass of the radiator component, not with deployment structure. To factor in the deployment structure, a mass of 16.73 kg was added. The mass of the deployment structure is proportional to the deployment mass of the solar panels and is considering both the support and deployment structure. To take into account reliability, a safety margin of 1.2 was added, as presented in Section 9.1.2, resulting in a total radiator of $105.66\,m^2$ and $144.678\,kg$. Ammonia will be used as a coolant, as it has a high latent heat of vaporization and a low boiling point, which makes it favourable to extract heat from subsystems. The liquid inside the heat pipe radiators will be pumped with a pump module, circulating the ammonia through its loops and also keeping the ammonia in a liquid state. The ETCS will be parallel to the solar arrays, behind the solar panels to decrease the solar absorbance as can be seen in Figure 6.14.

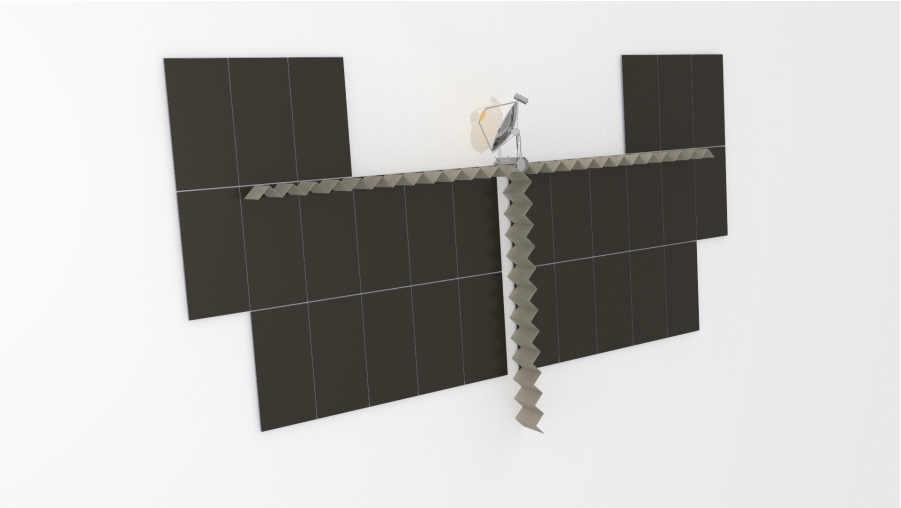

Figure 6.14: Deployable radiators

6.5.2. Internal storage thermal subsystem

The heat inside of the S/C bus needs to be distributed based on the generated, based on the power budget presented at Table 6.23, and the operational temperature presented in Table 6.9. The laser pointing is the subsystem that needs the most energy. However, this is outside the bus and thus will not be taken into account in the internal thermal balance. The maximum value of heat that is required to be dissipated by radiators, taking into account worst-case efficiencies of 40% is $234.8\,W$. Assuming not all subsystems are in direct contact with radiators, heat needs to be distributed to the outside surfaces. The liquid cooling system will consist of one loop, from all subsystems, absorbing heat, to the radiator, dissipating heat. The heat pipes will have an average heat transfer capacity of $100\,W/m$ based on ammonia and a heat pipe density of $1.45\,kg/m$[36]. This results in a mass of $4.78\,kg$.

6.5.3. Temperature gradient

Occurring every orbit, the satellite is exposed to big power changes of $235.53\,W$ caused by the loss of solar flux at the time of the eclipse. To comply with the requirement LNM.THE.001, the TCS is sized for critical conditions, which occur during eclipse and the maximum heat configuration Section 6.5. The eclipse is approximately an hour and during this hour the spacecraft subsystems have to stay at their operational temperature, not losing too much heat.

For energy storage, to make up for the energy losses during eclipse, Phase Changing Material (PCM) will be used, as this method has a high storage density in small temperature intervals [88]. PCMs store latent heat by changing phases, either solid, liquid or gas. In this phase change, enthalpy

[36] URL: https://www.arquimea.com/products/thermo-structural-panels-satellite-space/#content Cited 10/06/2023

stays stored which will release slower than the temperature change in the rest of the spacecraft. It is assumed that the required thermal energy that needs to be stored during eclipse is $235.53\,\mathrm{W}$. This is calculated taking the cold case, extracting the solar flux resulting in a total Q_{in} of $94.6\,\mathrm{W}$. The chosen PCM is Climsel-C18. This material has a heat of fusion of $306\,\mathrm{kJ\,kg^{-1}}$, which is under the one of H_2O. However, Climsel-C18 has a lower phase-changing temperature of $-18\,^{\circ}\mathrm{C}$, beneficial for the spacecraft operational temperatures. The mass of the PCM will therefore be $2.77\,\mathrm{kg}$. The PCM will be integrated into the liquid cooling system. After looping through the heat source, the liquid will be at its maximum and the PCM can absorb the heat in a circular way as shown in Figure 6.15. Around the PCM material, a highly insulating material will be placed in order to keep the heat in the liquid loop during eclipse.

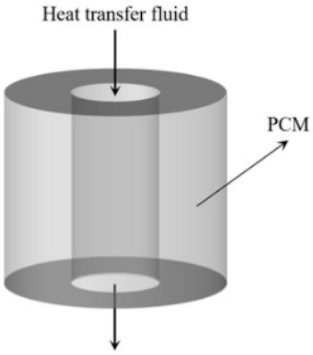

Figure 6.15: PCM around cooling pipes [89].

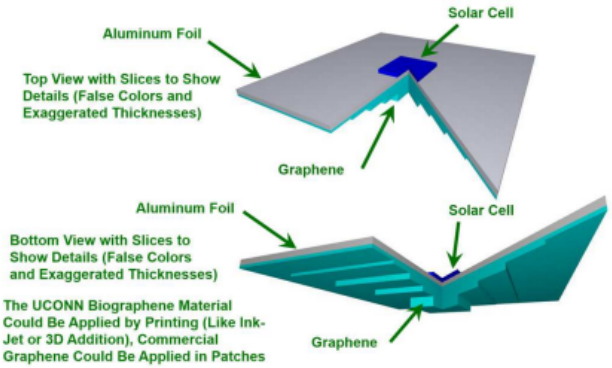

Figure 6.16: PV cell radiator [19]

6.5.4. PV cells

The PV cells already have independent TCS built into the design. The radiator is made from a composite Graphene sheet [18]. This material has extremely in-plane thermal conductivity and is deposited on the backside of the aluminium foil of the photovoltaic cells. The radiator is integrated into the solar blanket design and will deploy synchronously. If desired, the heat needs to be stored, for example, eclipse, material of the radiator will curl due to differential thermal contraction values both present in the radiator sheet. This reduces the view factor to deep space and thus keeps the photovoltaic cell in its operational temperature range [19].

Currently, an improved version of this radiator design is being tested by NASA where the thickness of the graphene composite is not evenly thick on the surface of the complete radiators, but peaks under the concentrated solar cell. This optimizes the heat generated over the area.

The total mass budget if the TCS is given in Table 6.11. The complete mass is $166.06\,\mathrm{kg}$, excluding the PV cell radiators, as they are build into the solar cells and therefore including in the mass budget of Section 4.2. Redundancy is taken into account by calculated values for worst-case scenario's and including safety factors.

Table 6.11: Complete TCS

Component	Mass (kg)
Skin	
MLI	4.13
MTCS	9.68
Inside	
Pipes	4.78
PCM	2.77
Lasers	
ETCS	144.68
Total	166.04

6.5.5. V&V Thermal system

In order to correctly verify the TCS, a thermal tolerance analysis can be done. This analysis ensures the thermal performance and limits of the spacecraft ensuring its thermal reliability, as is required by LMN.SAR.002, which will be 95% or higher. In further research and the prototype testing phase, several tests can be conducted on the TCS:

First of all, a thermal model needs to be made of the subsystem and integrated system. These models can be made on finite element software systems, for example, Thermal Radiation Analyzer System (TRASYS) and Simplified Space Payload Thermal Analyzer (SSPTA). In this model, a sensitivity analysis needs to be done by changing material, environmental and geometric values. Also, all worst-case scenarios should be modelled and analysed.

Secondly, on the prototype, a thermal cycling test can be conducted on the individual subsystems and complete spacecraft. This test involves repeated cycles of temperature variation to test the reliability of the system in terms of thermal expansion and thermal lifetime [90]. These tests are most important for the MLI and coatings.

Shock tests will also be done on the design. This test is allowing more rapid changes on the spacecraft, giving the material a thermal shock. This is important as during eclipse, the design is exposed to rapid temperature changes. This test is done in a dual compartment chamber [37].

The long-term reliability of the thermal system will be tested using a hot and cold soak test. In this test, the prototype will be exposed to critical temperatures with additional margins. Therefore, the environmental temperatures of eclipse and launch can be simulated [38].

Lastly, all radiators should be checked by analysis and testing. This can be done by measuring the heat it can dissipate and how different operating temperatures have an effect on the efficiency of the heat dissipation. Also, life degradation of the radiators, as the PCM and MLI need to be tested with the use of testing and extrapolation, as comparisons to similar missions.

As for the methods used for the TCS design, mostly widely verified programs were used like Excel. However, the thermal system was validated by putting in the values and checking the range stays in the beforehand stated operational temperatures. This was verified by a temperature of 300 K, as the system was designed based on this requirement.

6.5.6. Sustainability

In the design of the TCS, sustainability was also taken into account. This was mostly done in the choice of materials. However, due to thermal performance preferences, ammonia will be used, which is a toxic material. However, the TCS design still complies with requirement LMN.SUS.001, stating *'environmentally hazardous materials shall make up at most 0.1% of the total mass of the LUMEN system'*. As only the TCS and batteries make use of toxic materials, this requirement is still adhered to.

6.5.7. Sensitivity Analysis TCS

By far the most dominant part of the TCS by mass and volume, is the laser radiator. The design optimisation for mass and volume of this radiator is crucial. In this section, heat dissipation is varied, while keeping all other factors, like the type of laser, the materials and radiator type constant. The heat transfer characteristics of the radiators, including their geometry, surface area, and thermal conductivity, will also be considered consistent across the analysis. The heat that needs to be dissipated by the radiator is generated by the laser, with the assumption all energy not being transferred is converted into heat.

Figure 6.17 shows the linear relation between the required radiator area and the kW of heat generated by the lasers. The mass differs almost linearly with the area of the radiator. The only discontinuous factor is the mass of the deployment structure of 16.73 kg, which is constant and its relative percentage

[37] URL: https://www.desolutions.com/blog/2022/03/what-is-the-difference-between-thermal-shock-and-temperature-cycl [Cited 07/06/2023]

[38] URL: https://simpleflying.com/cold-soak-tests-guide/ [Cited 07/06/2023]

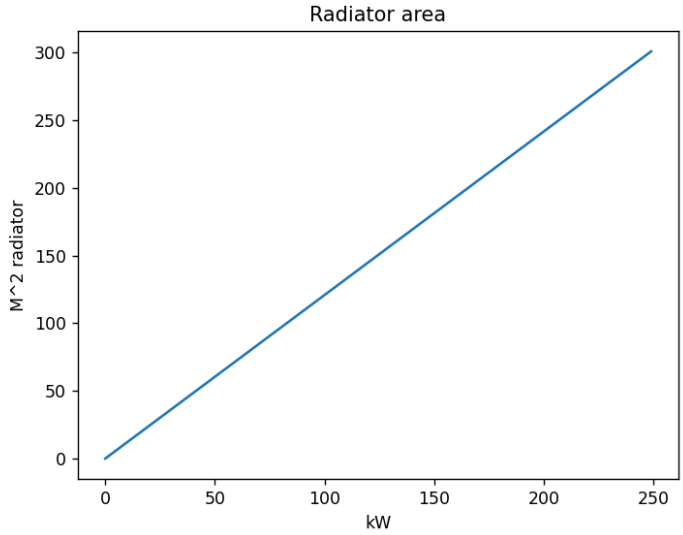

Figure 6.17: Required radiator area per heat input

of overall mass decreases with increased area, making the bigger radiators relatively more mass-efficient.

6.6. Propulsion Subsystem

In the mid-term report [7], two main solutions were proposed for the propulsion subsystem, namely cryogenic bipropellant and green monopropellant. The ΔV budged and consequent propellant mass and volume budgets are shown in the tables below:

Table 6.12: Mid-term mass, volume & ΔV budget

Manoeuvre	Δ**V** [m s^{-1}]
Lunar Orbit Insertion	826
Station Keeping	5 $\times$ 25 yrs
End of Life manoeuvre	220
Total	1171

Option	**Mass** [kg]	**Volume** [m^3]
Mono-propellant (AF-M315E)	231.8	0.157
Bi-propellant (LOX/CH_4)	146.5	0.172

However, the revision of the preliminary design led to changes in ΔV budget as well as in the whole mission profile. As specified in Section 5.5, the lunar transfer and orbit injection into lunar parking orbit will be provided by the Starship vehicle, therefore, the only manoeuvres that the main propulsion system has to be capable of are orbit change from parking to operational, EOL manoeuvre, eventual collision avoidance manoeuvre, occasional station keeping and orbit correction.

The new ΔV for each manoeuvre is listed in Table 5.8 and gives a total of $435.1\,\mathrm{m\,s^{-1}}$. Furthermore, the design of the subsystem is dictated by the following requirements, aside from the subsystem-specific requirements:

6.6.1. Propellant Selection

Even though both solutions proposed in [7] can fulfil the propulsion sub-system (LMN.PRP.001-009) and safety requirement (LMN.SAR.001), different issues might arise when considering the sustainability requirements, in particular LMN.SUS.003 (Table 6.13) which specifies the mission's 25 years of operational lifetime. Muratov et al. [91] emphasise the long-term storability complication in microgravity of cryogenic propellants due, among the others, to their low boiling point and the difficulties of venting boil-off vapour. This, together with the relatively low ΔV budget and the additional components needed for a bi-propellant system over a mono-propellant one, leads to the exclusion of the first option. The choice has therefore fallen on the green mono-propellant option. Among the available

Table 6.13: System Requirements driving the Propulsion subsystem design.

LMN.SYS.009	The LUMEN system S/C subsystems shall not consume more than 1250 W during peak power production.
LMN.SYS.011	The LUMEN system S/C propulsion subsystem and launcher shall be able to provide a combined ΔV of at least $4000\,\mathrm{m\,s^{-1}}$ for insertion from LEO into its operational orbit.
LMN.SYS.013	The LUMEN system S/C bus propulsion and AOCS subsystems shall be able to provide a ΔV of at least 33 m/s for End-Of-Life operations.
LMN.SAR.001	Less than 1% of the mass of the LUMEN system shall be made of materials and propellants that are toxic or hazardous to humans.
LMN.SUS.003	The LUMEN system, including its space segment, shall have a lifetime of at least 25 years.

option of green monopropellants in the Energetic Ionic Liquid (EIL) class, AF-M315E and LMP-103S have flown on the GPIM and PRISMA missions respectively and are classified as Progress to Mission Infusion (PMI) F [92, 93]. Even if those missions used 1N and 22N thrusters, development on higher thrust levels is ongoing, as a matter of fact, Bradford ECAPS has developed 200N class engines that work on LMP-103S[39]. Furthermore, this class of mono-propellant is particularly suitable for relatively high-thrust and impulsive manoeuvres, making it an option for AOSC thrusters as well.

An ionic liquid refers to a type of salt that has a melting point below $100\,^{\circ}$C. Ionic liquid monopropellants are compositions that combine an oxidizer salt, fuel, and water. The specific oxidizer salts used in the AF-M315E and LMP-103S green monopropellants are hydroxylammonium nitrate (HAN) and ammonium dinitramide (ADN) respectively [94]. AF-M315E is the former name for the Advanced SpaceCraft Energetic Non-Toxic (ASCENT) propellant, developed by the Air Force Research Laboratory[40]. It has theoretical vacuum I_{sp} up to 270s and adiabatic flame temperature of $1800\,^{\circ}$C [93, 95]. LMP-103S is the most mature among the ADN-base monopropellants [96]. It has a slightly lower adiabatic flame temperature than ASCENT, $1600\,^{\circ}$C), with a theoretical vacuum specific impulse of 250s [92, 97]. The most important characteristics of these propellants are listed in the table below:

Table 6.14: Performance and physical properties of the proposed EIL green monopropellants (2 MPa chamber pressure and $A_e/A_t 50:1$ at frozen equilibrium condition) [98, 99]

Propellant	**Theoretical Vacuum I_{sp} [s]**	**Density ρ [kg m^{-3}]**	**Volumetric ρI_{sp} [g s m^{-3}]**	**Chamber Temp. T_c [K]**	**Glass transition Temp. [°C]**	**PMI**
AF-M315E	266	1470	391	2166	<-80	F
LMP-103S	252	1240	312.48	1903	-7	F

It is in principle not clear what condition will lead to the selection of one propellant over the other, even if LMP-103S offers a lower chamber temperature and hence the possibility to select materials with a lower melting point, AF-M315E has a higher theoretical specific impulse, higher density and lower glass transition temperature, which will make it a preferable option for long term storability. Nevertheless, neither of the two selected propellants has been proven to be storable for a period longer than 5 years [92, 93]. On the other hand, studies are ongoing on modified versions of LMP-103S for storability periods of up to 20 years [100]. The combination of these aspects makes LMP-103S the best option in this phase of the design, leaving room for re-assessment of this choice at a later stage.

LMP-103S is an ADN-based liquid monopropellant composed for its 63% by ADN ($NH_4N(NO_2)_2$), 18.4% by methanol (CH_3OH) and 18.6% by Ammonia, 25% aqua (NH_4OH) [94] and a detailed set of its physical properties is given in the following:

[39] URL: `https://www.ecaps.space/products-200n.php` [Cited 15/06/2023]

[40] URL:`https://afresearchlab.com/technology/aerospace/successstories/advanced-spacecraft-energetic-non-toxic-asce`

Table 6.15: Physical properties of LMP-103S [94, 100]

Molecular Mass [g mol^{-1}**]**	**Freezing Temp. [**°C**]**	**Boiling Temp. [**°C**]**	**Specific Heat [**kJ kg^{-1} K^{-1}**]**	**Specific Heat Ratio**
46.9	-90	120	2.4	1.23

6.6.2. Engine Design & Performance

The vast majority of available data and tests using LMP-103S were performed at a combustion pressure of 2 MPa and nozzle expansion ratio 50:1. This is a typical value for these applications due to the very large expansion ratio usually employed by vacuum engines and thrusters and given also that the expansion ratios of commercially available options that uses LMP-103S as propellant ranges from 30:1 to 150:1[41]. In the following, the design of a 200 N of thrust, 50:1 expansion ratio is proposed; the key assumptions made in the design process are listed below:

- Combustion chamber pressure and temperature: $p_c = 2$ MPa, $T_c = 1903$ K;
- Isentropic flow after the combustion chamber;
- No friction;
- Constant physical and thermodynamic properties;
- Flow is stagnant in the combustion chamber.

Given the geometry (i.e. the expansion ratio) of the nozzle, the Mach number at any location x can be related to the local area ratio by the formula [101]

$$\frac{A_x}{A^*} = \frac{1}{M_x}\left[\frac{2}{\gamma+1}\left(1+\frac{\gamma-1}{2}M_x^2\right)\right]^{\frac{\gamma+1}{2(\gamma-1)}} \quad , \tag{6.22}$$

where the $*$ represents the throat condition, M is the Mach number, A is the cross sectional area of the nozzle, and γ is the specific hear ratio. Given the specific hear ratio in Table 6.15, the exit Mach number can be estimated from Equation (6.22). Being a quadratic equation, Equation (6.22) gives two roots (one for $M > 1$ and one for $M < 1$), the one of interest is the supersonic solution, resulting in a Mach number of 4.59.

Given the Mach number at the location x and the stagnation properties, in this case, assumed to be in the combustion chamber and denoted by the subscript 0, the pressure in the nozzle can be related to the above-mentioned quantities via isentropic relations [101]:

$$\frac{p_0}{p_x} = \left[1+\frac{\gamma-1}{2}M_x^2\right]^{\frac{\gamma}{\gamma-1}} \quad . \tag{6.23}$$

Substituting the combustion chamber pressure and the Mach number found previously gives $p_e = 2780$ Pa.

Having the pressure ratio and the design thrust level, the cross-sectional area for $M = 1$ (throat) can be found rearranging the following formula [101]:

$$F_T = p_c A^* \cdot \Gamma(\gamma)\sqrt{\frac{2\gamma}{\gamma-1}\left[1-\left(\frac{p_e}{p_c}\right)^{\frac{\gamma-1}{\gamma}}\right]} + (p_e - p_a)\frac{A^* \cdot \Gamma(\gamma)}{\sqrt{\frac{2\gamma}{\gamma-1}\left(\frac{p_e}{p_c}\right)^{\frac{2}{\gamma}}\left[1-\left(\frac{p_e}{p_c}\right)^{\frac{\gamma-1}{\gamma}}\right]}}, \tag{6.24}$$

$$\Gamma(\gamma) = \sqrt{\gamma\left(\frac{1+\gamma}{2}\right)^{\frac{1+\gamma}{1-\gamma}}} \quad ,$$

[Cited 15/06/2023]

[41] URL `https://www.ecaps.space/products-overview-ecaps.php` [Cited 16/06/2023]

where F_T is the thrust force and Γ is the Vandenkerckhove function. Setting $p_a = 0$, this results in a throat diameter of $8.2\,\text{mm}$ and a consequent exit diameter of $58.3\,\text{mm}$. Knowing the area at the throat, the mass flow rate and the exhaust velocity in choked flow condition can be calculated using the following formulas [101]:

$$\dot{m} = \frac{p_C \cdot A^*}{\sqrt{\frac{\mathcal{R}}{M_W} T_C}} \cdot \Gamma(\gamma) \quad , \tag{6.25a}$$

$$v_e = \sqrt{\frac{2\gamma}{\gamma - 1} \frac{\mathcal{R}}{M_W} T_C \left[1 - \left(\frac{p_e}{p_C} \right)^{\frac{\gamma-1}{\gamma}} \right]} \quad , \tag{6.25b}$$

where $\dot{m}$ is the mass flow rate, $\mathcal{R} = 8.314\,\text{J mol}^{-1}\,\text{K}^{-1}$ is the universal gas constant and M_W is the exhaust species molecular mass. Anflo et al. [100] give an overview of the exhaust species deriving from the combustion of LMP-103S and their mole fractions, from which the total average molecular mass can be calculated:

Table 6.16: Exhaust species and mole fraction of LMP-103S combustion products [100]

Species	H_2O	N_2	H_2	CO	CO_2
Mole fraction	50%	23%	16%	6%	5%

The value in Table 6.16 give a molar mass of $19.64\,\text{g mol}^{-1}$, resulting the mass flow rate and exhaust velocity of respectively $78\,\text{g s}^{-1}$ and $2469.4\,\text{m s}^{-1}$. However, these values are representative of the assumption made at the beginning of this chapter and therefore of ideal rocket theory. In order to account for non-ideal effects, the mass flow rate $\dot{m}$ is multiplied by a discharge correction factor ζ_d and the exhaust velocity v_e is multiplied by a velocity correction factor. Those values are given by the ratio of actual (real) and ideal conditions (the ones just calculated). Standard values for these coefficients are reported by Sutton and Biblarz [102] and are equal to 1.1 and 0.92 for the discharge and velocity correction factors respectively. Thus, the actual mass flow rate and exhaust velocity are $85.8\,\text{g s}^{-1}$ and

Knowing these values, the main performance parameters of the engine, namely characteristic velocity c^*, thrust coefficient C_F and specific impulse I_{sp}, can be calculated using the following relations [101]:

$$c^* = \frac{p_c A^*}{\dot{m}} = \frac{1}{\Gamma(\gamma)} \sqrt{\frac{\mathcal{R}}{M_W} T_c} \quad , \tag{6.26a}$$

$$C_T = \frac{F_T}{p_c A^*} \quad , \tag{6.26b}$$

$$I_{sp} = \frac{F_T}{\dot{m} g_0} \quad . \tag{6.26c}$$

Substituting the values leads to: $c^* = 1247.1\,\text{m s}^{-1}$, $C_T = 1.87$ and $I_{sp} = 238\,\text{s}$. This last value, in particular, is on the lower side of the theoretical vacuum I_{sp} reported in Table 6.14, resulting in a $5.6\,\%$ performance reduction with respect to ideal performance. In the following, the specific impulse just calculated will be used as more representative of the design engine.

6.6.3. Nozzle Design

To design the nozzle according to the specified characteristics and requirements, a methodology proposed by Rao in 1958 is employed. This approach was initially intended for engines operating in high-altitude conditions with extremely low ambient pressures, where the nozzle length is chosen to maximize thrust. The concept revolves around introducing a characteristic surface as a control surface for momentum, mass flow, and nozzle length. By determining the control surface and its

corresponding velocity distribution, the goal is to achieve maximum thrust while maintaining a constant mass flow rate. For a more comprehensive understanding of the relationship between maximum attainable thrust and nozzle length, it is recommended to refer to Rao's original paper [103].

Given the expansion ratio and the throat diameter, the geometry is described from the parameter given in the figure below:

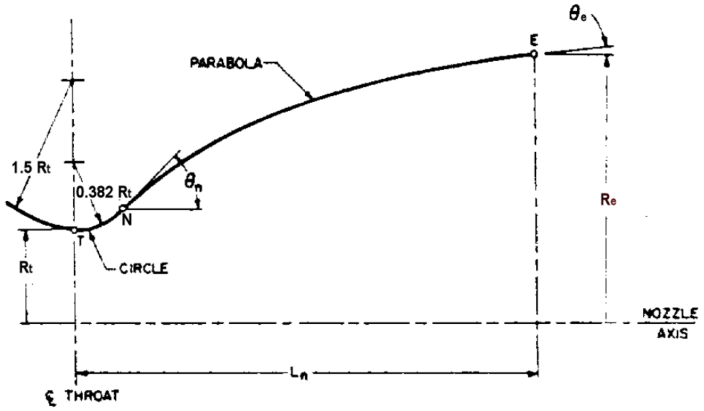

Figure 6.18: Rao nozzle characteristic parameters [104]

Figure 6.18 show the overall geometry of a bell nozzle called Rao nozzle that follows a parabolic shape; here R_t is the throat radius, L_n is the nozzle length, R_e is the exit radius, N and E are the design starting and end point of the parabola respectively, and θ_n and θ_e are the starting and end angle of the parabola tangent to throat curve. The curve of the converging section represents a circle of radius $1.5R_t$ spanning from an angle of $-135°$ to $-90°$. The first part of the diverging section represents a circle of radius $0.382R_t$, spanning from an angle of $-90°$ to $\theta_n - 90°$. The nozzle length is given by [103]:

$$L_n = \eta_n \left[\frac{(\sqrt{\epsilon} - 1)R_t}{\tan(15)} \right] \quad , \tag{6.27}$$

where η_n is the so-called length ratio and ϵ is the expansion ratio. An upper bound for nozzle efficiency of around 99% is typically achieved when the length ratio of the bell is 85%. Increasing the length ratio to 100% only provides a marginal additional performance gain of 0.2%. Therefore, 85% is commonly considered the practical upper limit. On the other hand, if the length ratio falls below 70%, the nozzle efficiency begins to decline. Due to these considerations, the 80% bell parabola is often selected as a suitable compromise [103, 104]. This results in a length of 79.2 mm. Lastly, the parabola angles θ_n and θ_e are functions of the expansion ratio and the length ratio η_n; their relationship is given in [104], resulting in θ_n = $32°$ and θ_e = $7.5°$. Given those angles, the unique parabola can be drawn, resulting in the geometry shown in Figure 6.19.

The nozzle and combustion chamber assembly need to withstand temperatures much higher when compared to hydrazine thrusters, for this reason, an iridium-lined rhenium (Ir/Rh) alloy was considered as material. In order to estimate the actual mass of the thruster, more information about the combustion chamber design and the nozzle thickness need to be known. Those detailed aspects are left for a later stage of the design process and the mass of the same thrust-level thruster developed by ECAPS[42] will be considered in this case, it being 6 kg. The same reasoning holds for the ignition mechanism, where a catalyst is used to start the reaction [100]. In order to estimate the power consumption for the process, the value from Bradford ECAPS is taken as a reference, ranging from 150 to 250 W. A CAD render of the proposed nozzle is shown in Figure 6.20

[42]URL: `https://www.ecaps.space/products-200n.php` [Cited 16/06/2023]

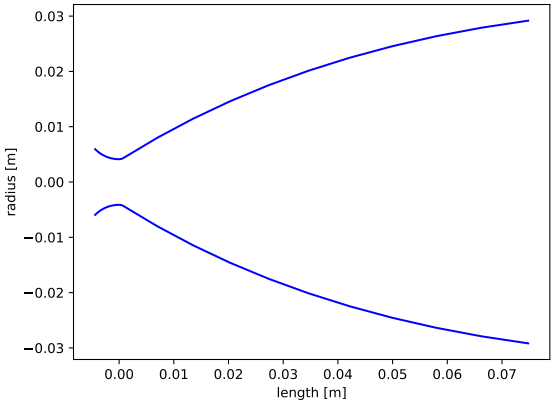

Figure 6.19: Nozzle shape according to Rao's Method

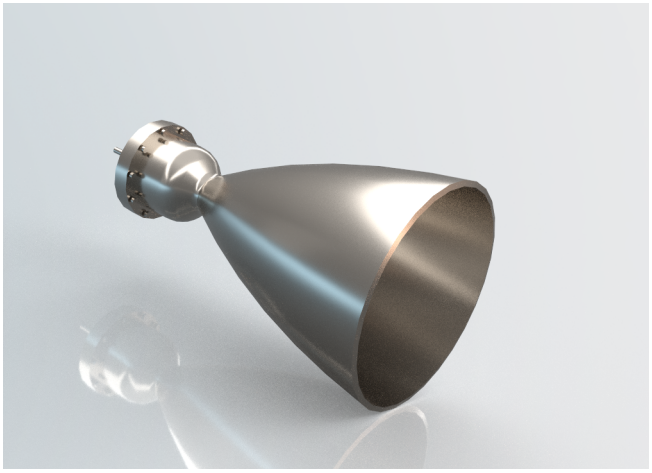

Figure 6.20: CAD render of the proposed nozzle geometry (combustion chamber dimensions for visualisation purposes only)

6.6.4. Propellant Tank

The propellant mass needed for the specified ΔV can be calculated using the rocket equation [55]

$$M_{prop} = M_{dry}\left(e^{\frac{\Delta V}{I_{sp} g_0}} - 1\right) \quad , \tag{6.28}$$

where M_{prop} is the propellant mass and M_{dry} is the S/C dry mass. Considering a dry mass of 888.92 kg and the propellant density listed in Table 6.14, the mass of LMP-103S is 174.4 kg. Given this propellant mass, a 20% margin is considered in this phase of the design [55]; this results in a total minimum propellant tank volume of 168.8 L; on top of this a 10 % is accounted for ullage.

In order to avoid performance losses and to keep the power budget to its minimum, a pressure-regulated system is preferred over a blowdown system, which was used during the PRISMA mission [92] but would require either a bigger engine or multiple thrusters. In order to estimate the amount of pressuring gas needed, a minimum feed pressure of 1.59 MPa was calculated to meet the requirement (LMN.PRP.009). For similarity of what has been done in the PRISMA mission, Helium will be used as pressurizing gas, also being by far the most used option for in-space propulsion applications [55, 92]. The maximum beginning of life pressure of the high-pressure tank is set to be 20 MPa and its temperature is assumed to be the average temperature of the S/C, being 300 K (Section 6.5). Wertz et al. [55] show the total pressuring gas mass is then calculated assuming that at the end of life, the fuel tank is completely filled with pressurising gas:

$$M_{gas} = \frac{pV_p}{R_{He}T - p/\rho} \quad , \tag{6.29}$$

where, M_{gas} is the total pressurizing gas mass, p is the minimum feed pressure defined above, V_p is propellant volume, R_{He} is the helium gas constan equal to $2079\,\mathrm{J\,kg^{-1}\,K^{-1}}$, T is the tank temperature and ρ is the pressurizing gas density, which at $20\,\mathrm{MPa}$ is $30\,\mathrm{kg\,m^{-3}}$ [55]. Solving for the mass gives a value of $445\,\mathrm{g}$ and a correspondent gas volume of $15\,\mathrm{L}$. The mass of the pressurising tank can be estimated via a parametric relation given in [55] that relates the tank mass in kg and pressuring volume times the pressurising tank pressure in $\mathrm{MPa\,m^3}$, resulting in a mass of $4.34\,\mathrm{kg}$.

During the PRISMA mission, a diaphragm tank was used [92]. Even in this case, a diaphragm tank was selected, given its simplicity and advantages, for example, to prevent pressurant gas mixing with the propellant and propellant sloshing in microgravity conditions. Looking at the commercially available options and material compatibility[43], model PDT-222 from MT Aerospace[44] was chosen, being representative of the above-mentioned volume budget. The selected tank has a mass of $17.1\,\mathrm{kg}$ and a volume of $221\,\mathrm{L}$.

In the following, the total mass, volume and power budget. For what concerns the power budget, the propulsion system modes can be split into operational and stand-day. During operational mode, the peak power will be needed to pre-heat the catalyst, initiate the combustion reaction and eventual thrust or mass flow regulations. The average power during the operational phase, an average power budget of $15\,\mathrm{W}$ was estimated based on previous missions employing similar systems but running on hydrazine which requires less heating power [55]. A similar approach was used to estimate the average power consumption during the standby phase, leading to a value of $5\,\mathrm{W}$. This value is on the lower side of previous missions that used hydrazine or MMH/NTO as propellant, however, it can be justified by taking into account the lass power needed for propellant storability, given the advantages of LMP-103S mentioned in Section 6.6.1 over more conventional propellants. For the dry mass, a safety margin of 1.2 is considered, as specified in Section 9.1.2, to account, among the others, for piping, fittings and valves.

Table 6.17: Propulsion system mass, volume and power budget. (Power budget when operational, for other mission phases, refer to Table 6.23)

Dry Mass [kg**]**	**Wet Mass [**kg**]**	**Volume [**$\mathrm{m^3}$**]**	**Peak Power [**W**]**	**Average Power [**W**]**
32	239.3	0.236	250	15

The tank and the whole main propulsion system will be placed at the bottom of the S/C, with the tank aligned with the centre of mass of the spacecraft to avoid any major lateral shift in the centre of gravity when the fuel tank gets emptied. Furthermore, the main engine will also be positioned on the same longitudinal axis of the centre of mass to avoid any undesired torque. The positioning of those elements in the context of the S/C is shown in Figure 6.21.

Figure 6.21: LUMEN S/C cut-out. It shows the location and position of the main propulsion system.

[43] URL:https://indico.esa.int/event/234/contributions/3743/attachments/3078/3783/2018CSID_CSmith_CompatibilityOfWeldedPropellantSystems.pdf [Cited 17/06/2023]

[44] URL:https://www.mt-aerospace.de/files/mta/tankkatalog/MT-Tankkatalog.pdf [Cited 17/16/2023]

6.6.5. Design Validation

In order to assess that the designed propulsion system is able to fulfil its requirements and is actually able to provide the thrust force it was designed for, validation of the design is proposed in the following. The developed nozzle is here compared to a similar thrust level commercially available option, namely the 200N Bipropellant Thruster by ArianeGroup[45]. This thruster was selected not only for the similar thrust level but also because it features the same expansion ratio and the same mass flow rate as the design proposed in Section 6.6.2. The specifications of this thruster are given below:

Table 6.18: Charteristic parameter and performance of the 200N Bipropellant Thruster as given on the ArianeGroup website[45].

Nominal Thrust	Nominal Flow Rate	Flow Rate Range	Nominal Chamber Pressure	Throat Diameter	Exit Diameter	Propellant
216 $\pm$ 10 N	78 g s^{-1}	60-100 g s^{-1}	0.8 MPa	12mm	95mm	MMH/MON-3

In Table 6.18 the characteristics parameter of the specific thruster are given, however, in order to assess whether the design tool developed is able to reproduce these parameters, additional information about the propellant and its combustion characteristics is needed. The propellant used by ArianeGroup MMH/MON-3 with a mixture ratio of 1.65. The combustion thermodynamic characteristics of the specific mixture are reported by Robert A. Braeunig[46], based on the freeware program STANJAN, and are reported in the following table:

Table 6.19: Physical properties of MMH/MON-3 combustion at 1.65 mixture ratio and 0.8 MPa chamber pressure [46]

Adiabatic Flame Temp.	Gas Molecular weight	Specific Heat Ratio
3200 K	20.8 g mol^{-1}	1.23

The procedure presented in Section 6.6.2 with the new input value given above, leads to the following results if a nominal thrust value of 216 N and a nominal chamber pressure of 0.8 MPa is assumed.

Table 6.20: Comparison between tool-estimated parameter and 200N Bipropellant Thruster Specifications

	Estimated	Actual	Discrepancy
Throat Diameter	13 mm	12 mm	8.3%
Exit Diameter	102.9 mm	95 mm	8.3%
Flow Rate	73 g s^{-1}	78 g s^{-1}	6.4%

Table 6.20 shows that the discrepancies between the values reported by ArianeGroup and the estimated values never exceed 9%. This gives confidence in the proposed design but, at the same time, shows the need for more in-depth analysis and investigation of the combustion process of the selected propellant LMP-103S. Furthermore, the combustion chamber design is left for a later stage of the design process, which will allow to clearly identify and design for the nominal conditions of the proposed engine.

6.6.6. Recommendation

Most of the architectures for High-Performance Green Propulsion (HPGP) Systems consist of Commercial off-the-shelf components that have an extensive flight heritage and can be adapted from their previous ”working environment”, namely hydrazine. Using those components could potentially reduce the cost and the timeline of development, production and certification of the propulsion system. As

[45] URL:https://www.space-propulsion.com/spacecraft-propulsion/bipropellant-thrusters/200n-bipropellant-thrusters.html [Cited 16/06/2023]

[46] URL: http://www.braeunig.us/space/comb-NM.htm [Cited 20/06/2023]

of the date of writing this report (21/06/2023), no 200N thrusters are available on the market, however, the development of a 200N LMP-103S thruster with orbit rise capabilities is ongoing at Bradford ECAPS [47]. This product is listed as Phase A development and TRL 3, therefore does not meet the LMN.PRP.005 requirement (The propulsion subsystem and its components shall have a minimum TRL of 6). If in the future this thruster will reach a sufficient TRL level, the employment of this solution is highly advised.

6.7. Structures & Mechanisms

The main function of a spacecraft structure is to provide protection and support to all the spacecraft subsystems, by transferring and sustaining mechanical loads. Additionally, it may include mechanisms required for specific spacecraft functionality. In this section, the main structure is fist sized for the static, vibrational, and buckling loads of launch, in Section 6.7.1. Section 6.7.2 then discusses additional precautions, to provide sufficient protection for micrometeoroid impacts. Finally, the most critical deployment mechanism, pertaining to the solar arrays, is discussed in Section 6.7.3.

6.7.1. Load-bearing Structure

As presented in [7], the spacecraft structure shall sustain axial compression and lateral launch loads of $6\,\mathrm{g}$ and $2\,\mathrm{g}$ respectively, with respective maximal frequencies of $15\,\mathrm{Hz}$ and $8\,\mathrm{Hz}$. However, the python tool developed in [7] was found to be unsuitable, requiring the structure sizing to be revised.

While the internal stress and buckling calculations were relatively accurate, the natural frequency results were not representative of the real structure. This is due to the short and thin-walled shape of the spacecraft structure, which reduces the accuracy of Euler-Bernoulli beam theory. The python tool used a conventional natural frequency formula for a tip-loaded cantilever beam, which neglects the effects of the exact shape of the structure cross-section. This lead to poor results for the thin-walled spacecraft structure, where shell vibration modes are predominant. For this reason, a different approach had to be considered for structure sizing.

One way to address the discrepancies caused by the short and wide shape of the structure, is to apply a more rigorous beam theory. The Euler-Bernoulli equations consider beams of high length-to-width ratio, where shear deformation and rotational bending effects can be neglected [105]. An alternative is the Timoshenko beam theory, which accounts for these effects [105]. However, solving the Timoshenko beam PDEs leads to a transcendental equations, which are not straight-forward to implement.

An alternative approach is to move to finite element analysis (FEA) tools, which have the advantage of being suitable for arbitrary geometries, unlike the beam equations, for which the cross-section must be constant and the cross-section properties must be individually implemented. Due to these advantages, the structural sizing was continued in the Simulia Abaqus FEA tool. There, multiple simulation scenarios were implemented, including linear static, buckling, and modal analyses.

Another change with respect to the preliminary design, was the shape of the primary structure. Rather than a square cross-section sized in [7], an octagonal cross-section is now considered. As can be inferred from Equation (6.30), it improves buckling strength thanks to the higher number of edges, which means that each individual plate has a smaller width b, therefore increasing its critical buckling stress [106]. In addition to that, it better accommodates the propellant tank shape, providing more possible mounting points. This new structure now has a width of $650\,\mathrm{mm}$ and a height of $1750\,\mathrm{mm}$, in order to accommodate for the propellant tank, and other internal subsystems.

$$\sigma_{cr} = C\frac{\pi^2 E}{12\left(1-v^2\right)}\left(\frac{t}{b}\right)^2 \tag{6.30}$$

The non-structural masses applied to the spacecraft bus were now also more accurately distributed, as shown in Figure 6.22. This mass distribution was defined in accordance with the spacecraft configuration described in Section 6.10.1. In Figure 6.22, the top mass represents the load of the laser and

[47] URL: `https://www.ecaps.space/products-200n.php` [Cited 21/06/2023]

transmission module, applied over the rop of the spacecraft walls. The two side masses correspond to the solar arrays in a stowed configuration, where the middle of the array is latched onto the spacecraft wall. The higher internal mass corresponds to the internal spacecraft subsystems, connected to the spacecraft walls via a shelf, as described in Section 6.10.1. Finally, the lower internal mass corresponds to the propellant tank, connected to the spacecraft walls.

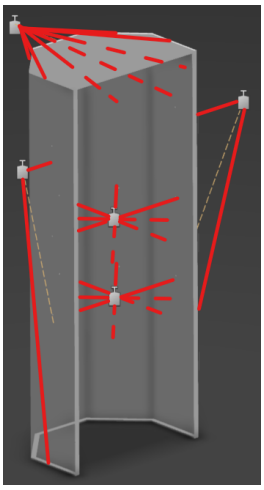

Figure 6.22: Section view of spacecraft structure with remote masses applied.

With these conditions, the structure's thickness was optimised, obtaining a minimal value of 9 mm, leading to a baseline structural mass of 103 kg. A summary of structural analyses for this thickness is displayed in Figure 6.23. As can be seen, the structure sustains the launch loads with a safety factor of 1.97. Likewise, its first mode frequency (28.026 Hz) exceeds the maximum launch load frequency (15 Hz) by a factor of 1.87.

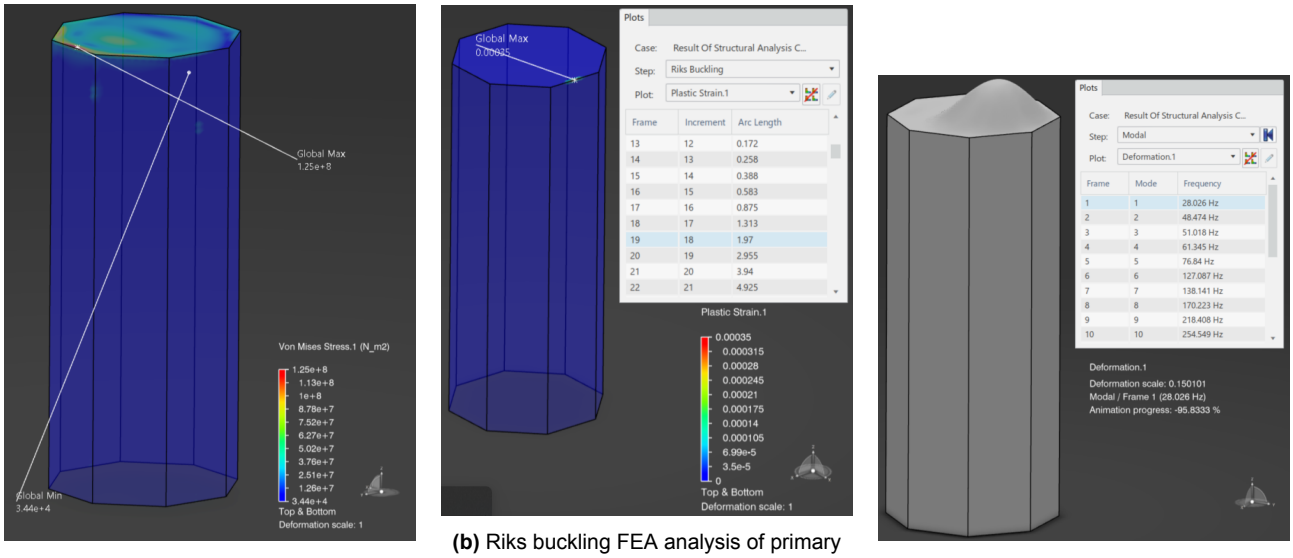

(a) Static FEA analysis of primary structure.

(b) Riks buckling FEA analysis of primary structure.

(c) Modal FEA analysis of primary structure.

Figure 6.23: FEA analysis results for primary structure.

6.7.2. Micrometeoroid Impact Protection

While the Moon's orbital environment does not include a significant amount of human-made space debris, a spacecraft in lunar orbit will still be subject to a similar risk of micrometeoroid impact, as in Earth orbit. This is due to the intersection of the Earth orbit with heliocentric orbits of micrometeoroids at 1AU, with the Moon being affected as Earth's satellite [107].

To estimate the flux of micrometeoroids of specific size, Equation (6.31), developed by Grün et al. [108], can be used. This equation takes the projectile mass m and spacecraft orbit altitude h, and

returns the flux of micrometeoroids with specified mass. The terms G_M and ξ act as correction factors for the gravitational and shielding effects of the moon, respectively.

$$F(m) = 3.15576 \cdot 10^7 \left[F_1(m) + F_2(m) + F_3(m)\right] \cdot G_M(h) \cdot \xi(h) \quad , \tag{6.31}$$

$$\begin{aligned} F_1(m) &= \left(2.2 \cdot 10^3 m^{0.306} + 15.0\right)^{-4.38} \quad , \\ F_2(m) &= 1.3 \cdot 10^{-9} \left(m + 10^{11} m^2 + 10^{27} m^4\right)^{-0.36} \quad , \\ F_3(m) &= 1.3 \cdot 10^{-16} \left(m + 10^6 m^2\right)^{-0.85} \quad , \end{aligned}$$

$$\begin{aligned} G_M(h) &= 1 + \frac{R_M}{R_M + h} \quad , \\ \xi(h) &= 0.5 \left(1 + \cos\left(\arcsin \frac{R_M}{R_M + h}\right)\right) \quad . \end{aligned}$$

The projectile mass can then be obtained by calculating the critical projectile diameter, with a typical micrometeoroid density of $500\,\mathrm{kg\,m^{-3}}$. This corresponds to the minimal projectile size to penetrate a spacecraft wall of a given thickness. Said diameter can be estimated using Equation (6.32) [109]. Here, t_t is the target (S/C wall) thickness, ρ_t is the target density, ρ_p - projectile density, v - projectile velocity, α - impact angle, K_f - failure factor, K_1 - material factor. The rest are empirical parameters, which depend on the type of target and theory used.

$$d_p = \left(\frac{t_t}{K_f \cdot K_1 \cdot \rho_p^{\beta} \cdot v^{\gamma} \cdot \cos(\alpha)^{\xi} \cdot \rho_t^{\kappa}}\right)^{\frac{1}{\lambda}} \tag{6.32}$$

Given these equations, an optimisation was performed, to limit the chance of a spacecraft being penetrated by micrometeoroid over the entire mission duration. The maximum acceptable penetration probability was set at $2\,\%$ by the reliability analyst. The minimal wall thickness was then calculated to be $11\,\mathrm{mm}$, at which failure probability falls just below the $2\,\%$ limit. Since this is only $2\,\mathrm{mm}$ above the designed thickness in Section 6.7.1, it was deemed preferable to increase the thickness, rather than add a Whipple shield, as said shield would increase complexity and mass due to fasteners. This new thickness now results in a primary structure mass of $126\,\mathrm{kg}$. With the addition of the two shelves, described in Section 6.10.1, the structure mass becomes of $146\,\mathrm{kg}$, leaving about of $9\,\mathrm{kg}$ for fasteners.

6.7.3. Solar Array Deployment

As discussed in [7], the solar array wings (SAWs) will utilise the Stretched Lens Array Square-Rigger (SLASR) deployment mechanism [18]. However, for increased performance and decreased mass, the SLASR system will be upgraded with flat Fresnel lenses and higher-efficiency photovoltaic cells, as discussed in Section 4.2.2. The use of flat Fresnel lenses is enabled by the lowered concentration of four suns and provides a decrease in mass and manufacturing cost.

The solar arrays have a total area of $331.658\,\mathrm{m^2}$, subdivided into 28 bays of $2.5\,\mathrm{m} \times 5\,\mathrm{m}$. This is then split into two solar array wings, with 14 bays per wing. In order to provide sufficient clearance for laser pointing, the solar arrays must be mounted asymmetrically, to prevent obstruction of the laser's field of view. The solar array bays can then be arranged into the configuration shown in Figure 6.24.

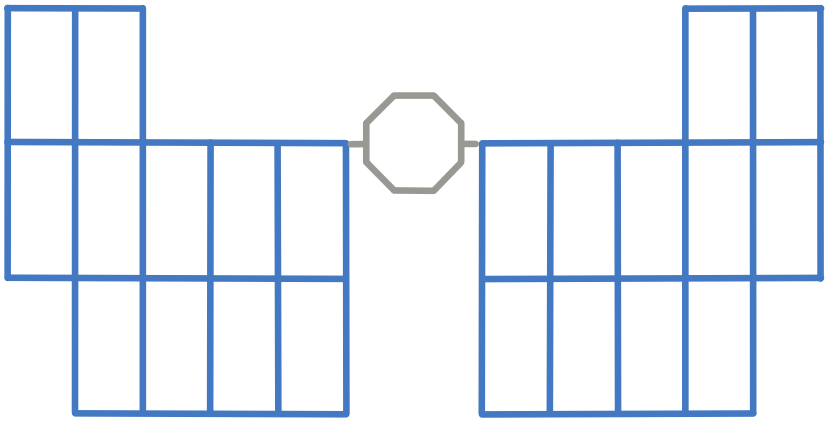

Figure 6.24: Configuration of solar arrays. Each blue rectangle corresponds to a bay. The grey octagon is the spacecraft bus.

6.7.4. Material characteristics

Among all the materials discussed in the different subsystems, the only two materials that are employed for structural elements are Aluminium and Carbon Fibre Composite. Those are used for the primary structure of the LUMEN S/C, and the supporting structure of the solar arrays respectively. The characteristics of these materials are listed in Table 6.21.

Table 6.21: Structural material characteristics

Material	Yield stress	Ultimate stress	Elastic Modulus
Al6061-T6	255 MPa	290 MPa	69 GPa
CFRP	N/A	400 MPa	144 GPa

6.7.5. Recommendations

The obtained structural design gives only a first indication of the general structural configuration, required by the mission. A number of recommendations are given to further iterate and improve the design in upcoming development stages.

Firstly, it is expected that the structural mass can be significantly decreased by increasing complexity. This can be achieved by employing isogrid walls, using a truss-structure covered with thinner skin panels, or applying topology optimisation to obtain an organic, numerically-optimised shape. The potential drawbacks of these approaches are that they increase manufacturing complexity, and may require a Whipple shield due to the reduction of skin thickness. However, the trade-off for lower mass is expected to be worthwhile.

Secondly, Al6061-T6 (described in Table 6.21) was considered as the primary structure material mainly due to its wide use in the aerospace industry, as well as its high strength-to-weight ratio. However, a more rigurous trade-off should be performed, considering diverse aluminium alloys, as well as other metals and potentially composites, as this may give an additional improvement in structural performance.

Finally, an additional consideration is the radiation environment of space. In order to protect the internal spacecraft subsystems, mounting radiation shielding on the spacecraft structure may be required. This shall be studied in collaboration with other subsystems in order to determine the optimal way to address radiation, either through individual subsystem shielding, or overall spacecraft bus coverage.

6.8. Electrical Power System

In order to successfully distribute the power from the solar panels to the lasers and the spacecraft bus, an Electrical Power System (EPS) is necessary. The EPS consists of the power conversion, the power management & distribution, and the batteries. In this section, the layout of this system will be expanded on. This includes the sizing and selection of the batteries and the power control of the solar array power.

6.8.1. Power Budget

In the earlier report Janssen et al. [7], a preliminary power budget estimation was performed based on empirical relations from Wertz et al. [55]. This power budget can be seen in Table 6.22.

Table 6.22: Preliminary power budget [7]

Type	Structure	Thermal	Power	TT&C	CDH	AOCS	Propulsion	Total
Average Power [W]	14	175	196	105	63	112	35	700

Now that the other subsystems have been sized in a more detailed matter, better estimates for the power budgets have been obtained. The power budgets are divided into a few power modes. First, coasting power is when the system is still connected to Starship. It is assumed that the power is provided by Starship. Deployement power refers to the power required during solar array deployment. The 100 W for the structures is necessary for 2 minutes. Assuming the arrays start collecting power as soon as they are deployed, this means that this power will have to be provided by the batteries, which will be explained in Section 6.8.2. EPS power budget includes losses during conversion and distribution, which is 3 % of the total collected power.

Table 6.23: Final peak power budget

Type	Structure	Thermal	TT&C	CDH	GNC	AOCS	Propulsion	Payload Structure	EPS	Transmitter	Total
Coasting Power [W]	0	0	0	3	0	0	0	5	0.24	0	3.1
Manoeuver Power [W]	0	0	16	3	120	102	250	0	14.7	0	505.7
Deployment Power [W]	100	0	16	3	120	102	5	0	10.4	0	351.2
Slew Power [W]	0	275	16	3	120	102	5	0	15.6	0	530.7
Operating Power [W]	14	275	16	3	120	102	5	335.7	3388.7	112099	116334
Eclipse Power [W]	0	0	0	3	61	18.4	5	0	2.6	0	90.0

With this revised budget, the number of batteries, the battery mass, and the battery volume can be found. Next to that, an overview of operating power distribution can be seen in Figure 6.25.

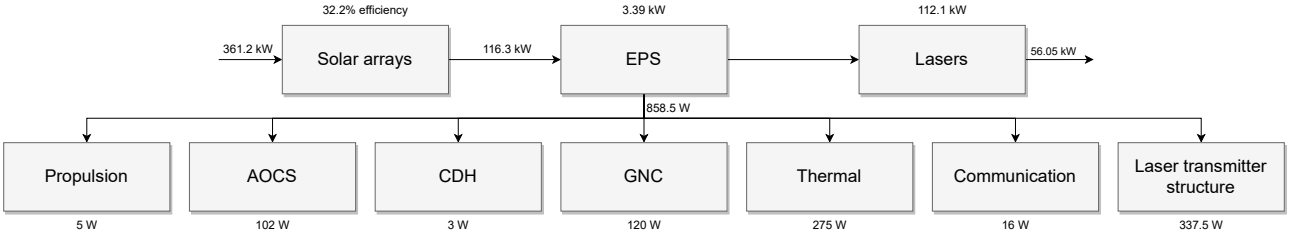

Figure 6.25: Operating power distribution Overview

6.8.2. Batteries Sizing

During power transmission to the lunar surface, the spacecraft will not encounter any eclipses. However, during other parts of the orbit where no transmission is done, eclipses might occur. Furthermore, as discussed in the previous section, the spacecraft will require power during the deployment of the solar arrays. From the determination of the orbit in Chapter 5, it was found that regular eclipses will occur for no more than 1.074 h of the 21.03 h orbit. However, the longest eclipse during the lifetime was found to be 4.94 h. During these eclipses, some subsystems will still require power for housekeeping,

meaning that batteries must be employed. In the preliminary design, the Eaglepicher Orbiter battery[48] was considered. Using the preliminary power budget, this resulted in one single 18 kg battery. However, reliability and redundancy concerns arise with this. First, if this single battery has a fault, the entire power storage system ceases to work. Furthermore, adding a second battery for redundancy would mean that the mass would be twice as high as necessary. Therefore, different batteries will be considered. The new batteries that will be used are the Eaglepicher 30 Ah Space Cell[49]. This is a Lithium-Ion, or more specifically, a Lithiated Nickel Cobalt Aluminum Oxide battery. Some of the important properties can be seen in Table 6.24:

Table 6.24: Battery Properties

Mass [kg]	Energy Density [Wh/L]	Specific Energy [Wh/kg]	Cycle Life
0.95	335	141	40000 cycles at 40% DoD

Considering the 25 year mission time and the orbital period of 21.05 h, a total of 10404 discharges will be done, meaning that the life time at 40 % Depth-of-Discharge (DoD) is sufficient. The required battery energy storage can be calculated using Equation (6.33):

$$E_{BAT} = \frac{P_{req} t_{eclipse}}{DoD \cdot \eta_{BAT}} \tag{6.33}$$

To size the battery, two cases must be considered: the eclipse case, and the manoeuver & deployment case, as the power in these phases will be provided by the batteries. First, the eclipse case will be considered. Using the required power of 90.0 W, an eclipse time of 4.94 h, a DoD of 40 %, and a battery discharge efficiency of 90 % [78], a total energy of 1130.7 W h is obtained. This would result in a total of 9 batteries needed. For redundancy, it was decided to apply a safety factor of 1.2 (this safety factor will be expanded on in Chapter 9). This adds two redundant batteries and 1.9 kg to the system, which is not significant in comparison with the rest of the system. Then, the total mass and volume of the batteries is 10.45 kg and 3.38 L respectively.
If the manoeuver & deployment case is considered, 505.7 W over 5 s for the manoever, and 351.2 W over 2 minutes for the deployment is needed. Using the same values for DoD and η_{BAT}, a total of energy of 35.54 W h is needed. It can be concluded that the batteries sizing according to eclipse time is the limiting case.

The mass and energy of the batteries are in accordance with requirements LMN.EPS.012 and LMN.EPS.013.

6.8.3. Harness

The power will be transferred through the spacecraft using wires. This network is called the spacecraft harness. The mass of the harness is a key driver of the total EPS mass. Usually, it is around 3 % of the total spacecraft dry mass [78]. Using a dry mass of 888.92 kg, a harness mass of 27 kg is obtained. Taking the GORE Type SPM (ESCC 3901/018) Variant No.39 cable[50], which has a specific mass of 4.4 kg km^{-1}, a total cable length of 4.3 km is used.

6.8.4. Power Converters

To correctly supply the power to each subsystem, power converters must be used. One of the main components are the laser modules, which each use 1200 W. A suitable power converter is the Vicor Isolated Regulated DC Converter[51], which is rated for 1300 W. As 188 lasers will be used, there will

[48] URL: https://www.eaglepicher.com/sites/default/files/LP%2033165%20MAVEN%20%200322.pdf [Cited 07/06/2023]

[49] URL: https://www.eaglepicher.com/sites/default/files/LP33081%2030%20Ah%20Space%20Cell%20%200123.pdf [Cited 07/06/2023]

[50] URL:https://www.gore.com/system/files/2019-10/GORE%20Space%20Cables%20-%20Catalog%20%28Traditional%20Space%29_10-28-2019%20%28A4%20Electronic%29_0.pdf [Cited 09/06/2023]

[51] URL: https://www.vicorpower.com/documents/datasheets/DCM5614xD0H36K3yzz_ds.pdf [Cited 21/06/2023]

also be 188 converters. On top of that, there will be a converter for each subsystem as well. Each converter has a mass of 215 g, which brings total converter mass to 40.42 kg.

6.8.5. Solar Panel Power Control & System architecture

The solar arrays might at times produce more than is required by the lasers and the subsystems. Therefore it is necessary to regulate the power from the arrays. This can be done in two ways: either using Direct Energy Transfer (DET) or Peak Power Tracking (PPT). In DET, shunts are used in parallel to open-circuit solar arrays to dissipate excessive power, while PPT changes systems extract only the required load power from the arrays [110]. DET has a lower part count, mass, and cost and higher efficiency, while PPT has a higher cost and lower efficiency at high powers; there is a loss of 4 - 7 % as they are connected in series [55]. Generally, PPT systems are beneficial for missions under five years. Therefore, it was opted to use a Direct-Energy-Transfer system, where sequential linear shunts will be used to regulate the power from the arrays. Next to that, bypass diodes will be used in parallel with the arrays, as specified by the solar cell datasheet[52]. The circuit layout of the solar arrays with the shunts can be seen in Figure 6.26a. As can be seen, the output power is compared to a reference desired power using an op-amp, which then regulates the power.

For power management, a similar-sized spacecraft was used as a reference for a flight-proven similar PMAD system. This spacecraft had a total PMAD mass of 27 kg [111].

Considering all of the masses discussed above, this brings the total mass to 107.23 kg. Using the aforementioned converters, the overall efficiency of the EPS system is 97 %.

A diagram of the system architecture can be seen in Figure 6.26b. As can be seen, the solar panels provide power to the batteries and the Power Management & Distribution (PMAD) system distributes the power to the lasers and the bus subsystem.

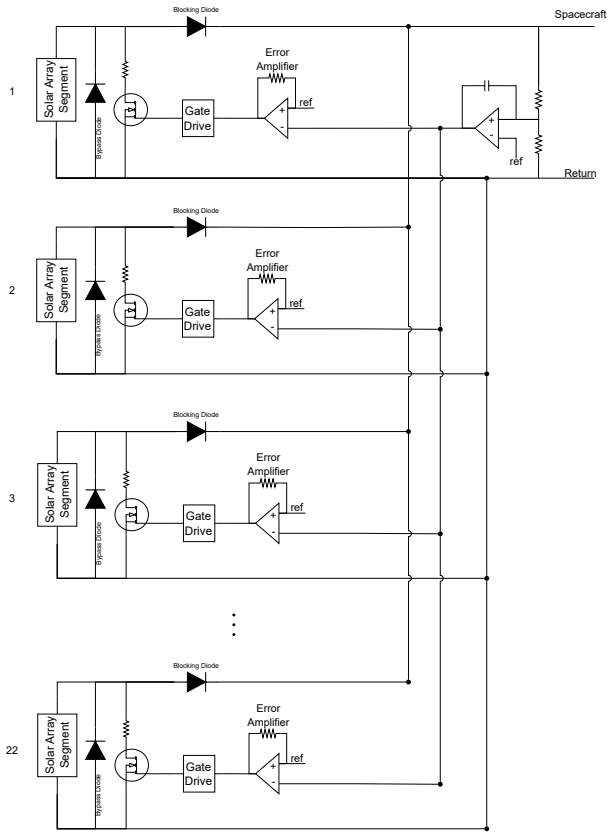

(a) Layout of solar panels with sequential shunts. Adapted from Hyder et al. [110]

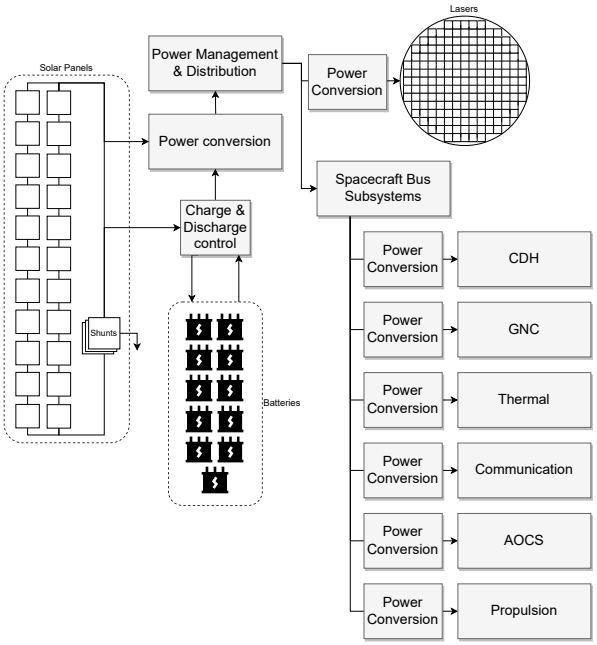

(b) Electrical Power System Architecture

Figure 6.26: Solar array layout & EPS system architecture

[52]URL: `https://www.spectrolab.com/photovoltaics/XTE-SF_Data_Sheet.pdf` [Cited 20/06/2023]

A render of the subsystem components can be seen in Figure 6.27. Note that this is a simplified layout; it only consists of the batteries (red), the power distribution unit (light grey), and the power converter units (dark grey). Also note that only the power converters for the subsystems are shown.

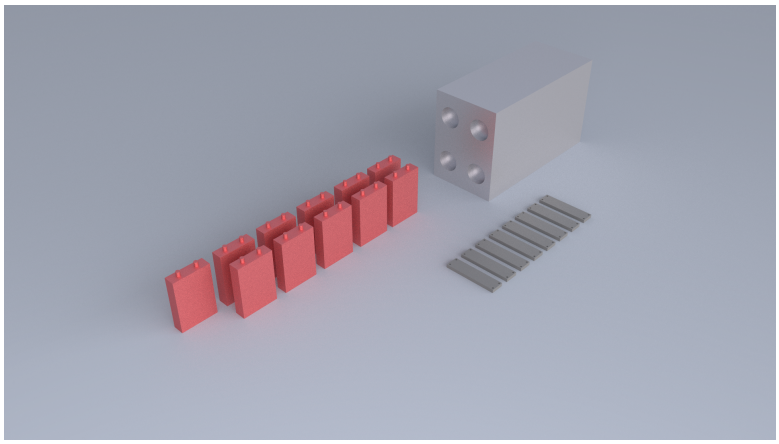

Figure 6.27: Render of the EPS Subsystem

An overview of the final values for the electrical power system can be seen in Table 6.25.

Table 6.25: EPS performance overview

Peak operational power (W)	Mass (kg)	Volume (m^3)
3388.5	107.23	0.03695

6.8.6. Materials & Sustainability

The materials and sustainability of the EPS system must be considered. One of the main concerns in this regard are the batteries. These contain Lithium, Nickel, Cobalt, and Aluminium.

- **Lithium** is one of the main materials for the batteries. Mining of the material harms the soil and causes air pollution[53]. Furthermore, 2.2 million litres of water is needed to produce one ton of Lithium.
- **Nickel** is the second main material that is used for the batteries. Just like Lithium, their mining is energy-intensive and poses ethical mining concerns[54]
- **Cobalt** also poses environmental concerns. A major Cobalt exporter is Congo, which is resonsible for $70\,\%$ of the world's Cobalt production[55]. There are concerns related to deforestation, water pollution, and air pollution.
- **Aluminium** is one of the most used materials in the Aerospace industry[56]. Nevertheless, mining and processing causes water, soil, and air pollution[57]. Furthermore, production of one ton of Aluminium requires 4-8 MW h.

Considering the above material considerations, it is still the optimal choice. Other types of batteries, such as Lead Acid batteries, pose sustainability concerns as well. With the higher energy density of Lithium-Ion batteries, fewer batteries and thus material is needed.

[53] URL: https://www.euronews.com/green/2022/02/01/south-america-s-lithium-fields-reveal-the-dark-side-of-our-elec [Cited 16/06/2023]

[54] URL: https://shoutlearning.org/the-environmental-impacts-of-nickel-mining-and-production.html [Cited 16/06/2023]

[55] URL: https://earth.org/cobalt-mining-in-congo/#:~:text=Cobalt%20is%20fast%20turning%20from,are%20vital%20for%20soil%20fertility. [Cited 16/06/2023]

[56] URL: https://www.techbriefs.com/component/content/article/tb/pub/features/articles/33914 [Cited 16/06/2023]

[57] URL: https://blog.thepipingmart.com/metals/environmental-impact-of-aluminum-production/#:~:text=The%20process%20of%20extracting%20aluminum,be%20harmful%20to%20aquatic%20life. [Cited 16/06/2023]

6.8.7. Sensitivity Analysis

To investigate the influence of certain parameters on the EPS mass, a sensitivity analysis is performed. The parameters that are considered are the eclipse time, the number of laser modules, the spacecraft dry mass, and the battery Depth-of-Discharge. The influence of these parameters can be seen in Figure 6.28.

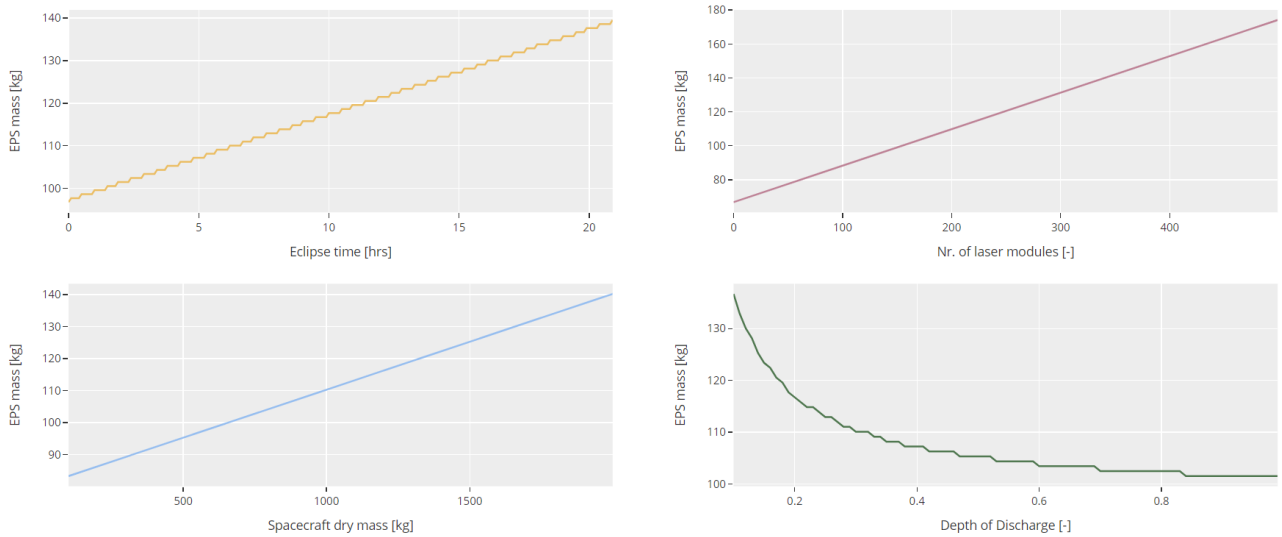

Figure 6.28: EPS mass sensitivity

For the eclipse time, it can be seen that the mass increases step-wise. For every 0.4 h of eclipse time, one battery, or 0.95 kg is added. Also, notable, due to the relatively low mass of the batteries, doubling the eclipse time only increases the EPS mass by 10 kg.

For both the number of laser modules and spacecraft dry mass, it can be seen that the EPS mass varies linearly with these respective parameters. These two parameters are also the only ones that heavily depend on the number of spacecraft.

Lastly, the depth-of-discharge was considered. From the data sheet, only values of lifetime for 40 % (40000 discharges) and 100 % (2000 discharges) were available. While the mission only requires 10404 discharges, it was still opted to use 40 %. From the graph, it can be seen that the total difference in mass between 40 % and 100 % is about 6 kg, or 0.66 % of the total dry mass. Therefore, it can be concluded that while it is over-designed, the influence on the total mass is acceptable.

6.8.8. Verification & Validation

For the calculations, Python was used. All equations were verified by comparing them to a calculation done by hand. As they were consistent, it could be concluded that the written code is correct.

For validation, it is possible to look at similar missions. First, the power usage by the electrical power system is considered. From Table A-11 in Space Mission Analysis and Design Wertz et al. [55], it is found that this power usage ranges between 1 and 21 % of the total spacecraft power, with a mean of 10 %. While the value of 3 % for this design is on the lower side of this range, it is still realistic. Next, the power budget of the systems during operating mode can be investigated. For this, the transmitter power and EPS power will be neglected as these are significantly higher than any other mission ever. While this makes this comparison less accurate, it can still be useful to perform it. The operating power of a LUMEN spacecraft then is 851.7 W. Still from Table A-11 in [55], it can be seen that the power ranges between 234 and 1338 W with a mean of 749 W. With a power slightly higher than the mean, but still below the maximum, it can be concluded that this power usage is reasonable.

6.9. Launcher

To estimate the total number of launches needed, the launch vehicle payload fairing, and the total mass transportation that it can provide, need to be taken into account. The dimensions of the payload

fairing for the Starship launch vehicle can be found in Figure 6.29.

Firstly, the bounding box of one of the LUMEN S/C needs to be estimated in its undeployed state. The solar arrays in the folded configuration are stored in a 2.5 m long bay; the collimator dish has a diameter 2.4 m, this adds up to the additional lateral space to fold the solar arrays, which is estimated to be 0.3 m, giving a total of 2.7 m in the lateral direction; lastly, to estimate the depth of the S/C, the CPM boom is assumed to be foldable, having a total width of 1.1 m which adds up to the 0.7 m wide S/C bus, making a total of 1.8 m.

With these dimensions, it is expected that 8 spacecraft can fit in the cylindrical part of the payload fairing per layer [58]. Three layers can fit within the height of the cylindrical part. In the conic-like part of the fairing, the amount of spacecraft that fits per layer will decrease. An additional four layers fit in the conical part, the first of which will contain 6 spacecraft, the next will contain 5, the layer after that will contain 3, and the final layer will contain 1 satellite.

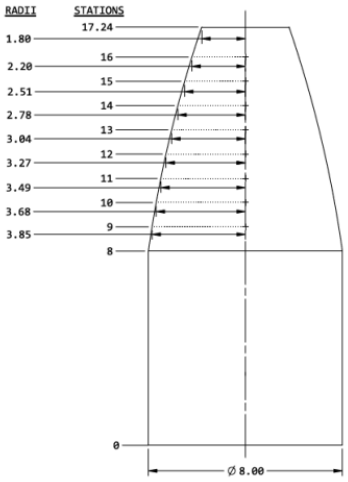

Figure 6.29: Starship payload fairing [112]

This leads to a total of 39 S/C that can be arranged in one single launch vehicle per launch. This number of spacecraft has a combined mass of $42\,751.8$ t to determine if the configuration is mass-limited or volume limited, the ΔV budget must be analysed.

Given the total ΔV budget [7], it is crucial to assess whether the Super Heavy-Startship launch vehicle will be able to deliver the required mass to moon orbit. SpaceX states that the selected launch vehicle can deliver >100 t of payload to LEO in a single launch but no indication for a single launch mass-to-moon is available, therefore a feasibility study is needed [112]. Using ideal rocket theory, data provided by SpaceX [112], can be replicated:

$$\begin{aligned} \Delta V_{SH} &= I_{sp_{SH}} g_0 \ln\Big(\frac{M_{dry_{SH}} + M_{prop_{SH}} + M_{dry_{SS}} + M_{prop_{SS}} + M_{PL}}{M_{dry_{SH}} + 0.1M_{prop_{SH}} + M_{dry_{SS}} + M_{prop_{SS}} + M_{PL}}\Big) \quad , \\ \Delta V_{SS} &= I_{sp_{SS}} g_0 \ln\Big(\frac{M_{dry_{SS}} + M_{prop_{SS}} + M_{PL}}{M_{dry_{SS}} + M_{PL}}\Big) \quad , \end{aligned} \tag{6.34}$$

where the subscript *SH* refers to the Super Heavy booster, the subscript *SS* refers to Starship and M_{PL} is the payload mass. Maiwald and Westphal [113] confirms what SpaceX founder stated in a recent interview[59], addressing that the dry mass of the booster ($M_{dry_{SH}}$) is estimated to be between 160 and 200 t, therefore a value of 180 t was selected for the specific calculation. The same sources report that Starship's dry mass ($M_{dry_{SS}}$) is between 85 and 120 t, hence a value of 100 t was selected. The propellant masses can be retrieved from SpaceX website[60] being for Super Heavy and Starship

[58] URL: `https://erich-friedman.github.io/packing/squincir/` [Cited 24/06/2023]
[59] URL: `https://everydayastronaut.com/starbase-tour-and-interview-with-elon-musk/` [Cited 08/06/2023]
[60] URL: `https://www.spacex.com/vehicles/starship/` [Cited 08/06/2023]

3400 and 1200 t respectively. For what concerns the specific Impulses (I_{sp}), the booster comprises 33 Raptor V2 engines with specific impulse at sea level of 330 s and vacuum specific impulse of 355 s; the Starship vehicle comprises a total of six engines, three Raptor V2 engines and three Raptor vacuum engines with a vacuum specific impulse of 380 s, as specified by SpaceX CEO in the two most recent Starship updates[61]. As a consequence, for the Starship ΔV calculation, the average of the two specific impulses was taken. Furthermore, the low launch cost of the selected launcher is dictated by its reusability, for this reason, 10 % of the booster propellant mass is kept in the booster after stage separation to allow for a safe landing. This result in a total maximum ΔV to LEO (up to 500 km circular orbit at up to 98.9° inclination [112]) of 9852 m s^{-1} with 100 t of payload.

To check whether Starship itself can reach the moon in a single launch, the payload mass (M_{PL}) was set to 0 in Equation (6.34), resulting in a total ΔV of 12 113 m s^{-1}. The ΔV needed for reaching the desired LEO orbit proposed in [7] was subtracted resulting in an extra ΔV of 2297 m s^{-1}, which is not enough to perform the lunar transfer. It can be concluded that on-orbit refilling is necessary to accomplish the mission, even though this will result in additional launch costs.

The on-orbit refilling operation will take place by means of a tanker vehicle, which essentially is a second Starship with refilling purposes[60]. At the moment, no extensive information is available about this procedure, however, given that the maximum payload capacity is one order of magnitude less than the Starship propellant capacity, multiple tankers will be needed to provide the propellant necessary to reach lunar orbit. The total ΔV's needed for performing the lunar transfer and the lunar orbit injection are summarised in Table 5.8, giving a total of 3.66 km s^{-1}. The propellant mass to be refilled for achieving the above-mentioned velocity change can be estimated using again the rocket equation:

$$M_{prop_{SS}} = (M_{dry_{SS}} + M_{PL})\left(e^{\frac{\Delta V_{LT}+\Delta V_{LOI}}{I_{sp}g_0}} - 1\right) \quad , \tag{6.35}$$

where ΔV_{LT} and ΔV_{LOI} are respectively the velocity change needed for lunar transfer and lunar orbit injection (Table 5.8). Working this out, considering an average payload mass per launch of 68 t leads to a total propellant mass to be refilled of 164.8 t.

The total mass of propellant that can be refilled by a single tanker launch is assumed to be the total payload capacity of the Starship, which in this case will be occupied by propellant, resulting in 100 t of propellant that can be transferred for each tanker launch. As a result, a total of two additional launches are needed in order to successfully inject Starship with LUMEN satellites as payload into lunar orbit.

Thus the launcher is volume limited and the full 39 satellites per launch can fit. This results in four payload launches being necessary with eight refuelling launches.

6.10. Design Summary

6.10.1. Configuration and Layout

Once all subsystems have been designed, these have to be efficiently organised inside and outside of the spacecraft structure. The internal components must be packed as compactly as possible, while the external ones need to be mounted such that the space in the launch vehicle occupied by a spacecraft is minimised, and loads are transferred efficiently. It is important to note, that all the subsystems shall be placed such that their functionality is uncompromised.

Firstly, the internal subsystems were organised. This was primarily constrained by the structure width, set by the propellant tank. Said propellant tank is placed at the bottom of the spacecraft bus, to provide a short connexion to the main thruster. The pressurant tank is then mounted on directly on top of the propellant tank. The remaining components are placed on two shelves, for easier integration.

The first shelf contains the power distribution unit, an assembly of four reaction wheels, 11 batteries, and the onboard computer. In addition to that, the reaction wheels and onboard computer are paired with a power conversion unit (PCU). Meanwhile, the second shelf supports the laser modules, two

[61] URL: `https://www.youtube.com/watch?v=sOpMrVnjYeY`, `https://www.youtube.com/watch?v=3N7L8Xhkzqo` [Cited 08/06/2023]

inertial measurement units, two clocks, as well as a box with miscellaneous TT&C components. Here again, each distinct component is paired with a PCU. An exploded view of this configuration can be seen in Figure 6.30a.

As for the outside of the spacecraft, shown in Figure 6.30b, it can be separated into the Sun-facing, Sun-opposite, Moon-facing, and Moon-opposite, as well as a left and right horizon face. The subsystems are organised on a combination of these phases.

The largest subsystem is the two solar arrays, and these are mounted on the two horizon-facing sides of the spacecraft. Their long side is facing away for the Moon, in order to provide a larger field-of-view for the transmitter. Said solar arrays are placed as close as possible to the Sun-facing end, in order to be unobstructed by other subsystems.

Two of the radiators are positioned directly behind the solar arrays, such as to be completely covered from the Sun. This minimises the incident heat on the radiators, maximising their heat-dissipation efficiency. One additional radiator is placed on the Moon-opposite side, however, its thin Sun-facing edge can still minimise the incident heat.

Moving on, several smaller components are placed around the outside of the spacecraft. The main thruster is placed on the Sun-facing side, which is the bottom of the spacecraft. Two monopole antennae are mounted to the diagonal walls between the Moon-facing wall and the horizon walls, ensuring their orthogonality. Four blocks of three AOCS thrusters are positioned on the Sun-facing and opposing sides of the spacecraft, providing the highest moment arm for attitude control. Two star sensors are placed on the diagonal walls between the Moon-opposing and horizon walls. Finally, the transmitter antenna is mounted on the Moon-facing wall, close to the top of the spacecraft.

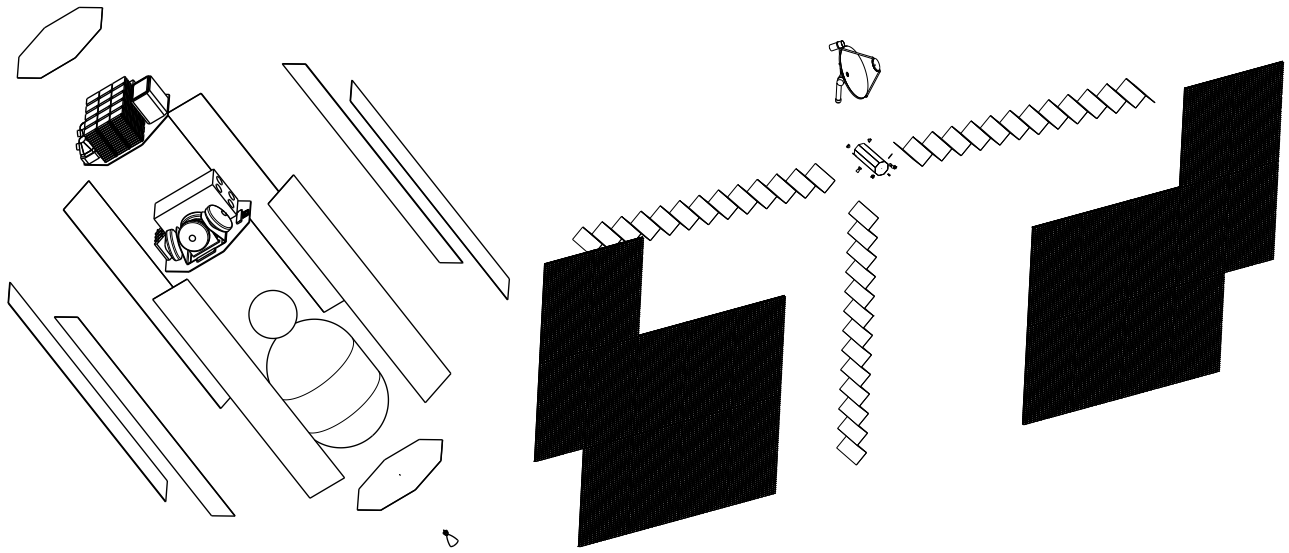

(a) Exploded view of the internal configuration.

(b) Exploded view of external configuration.

Figure 6.30: Exploded views of spacecraft internal and external configurations.

6.10.2. Performance Overview

Having determined the requirements for the subsystems of the spacecraft, along with the configuration and layout, an overview of the performance can be given. The performance overview will be given in Table 6.26, and consists of the mass and power budgets of each subsystem, along with the total mass of the spacecraft and of the entire system.

Table 6.26: An overview of the performance in terms of mass and power of the subsystems, and spacecraft of the LUMEN system.

Item	Mass [kg]	Average Operational Power [W]
Transmission	75.2	-
AOCS	70.0	112
GNC	24.5	120
CDH	0.02	3
TT&C	8.4	16
Thermal	166.0	275
Propulsion	32.0	15
propellant	207.3	-
Structure	155.0	14
EPS	107.3	3388.5
batteries	10.45	-
Optics	75.9	337.5
Solar array	174.6	-
Total Dry	888.92	3943.5
Total Wet	1096.2	3943.5
System Total Dry	118,226	524,486
System Total Wet	145,797	524,486

6.10.3. HW and SW

In the midterm report [7], the Hardware and Software Diagram was presented. This has been updated and is shown in Figure 6.31.

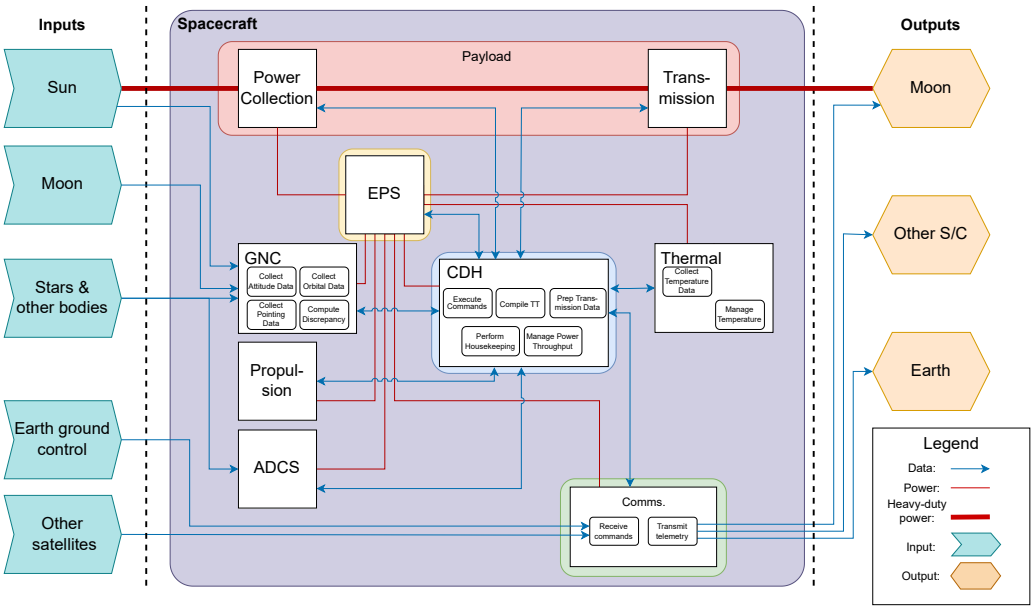

Figure 6.31: Updated Hardware and Software Diagram

The Hardware and Software Diagram shows the connections, flows of data and power through the different subsystems of the spacecraft, as well as the outside environment. During nominal operations, the overall functioning of the spacecraft can roughly be divided into two parts, continuous and transmission. In Figure 6.32, a more detailed look at the different functions and data flows in each subsystem is given, as well as showing how these relate to one another.

In particular, the continuous functions include most of the loops between AOCS and GNC such as the sun pointing and the orbit and attitude control. As well as data storage, communication and thermal control. Lastly, continuous system health monitoring will ensure that the satellite's subsystems

are in working order. For what concerns functions during transmission, to establish the required transmission accuracy, the GNC's guiding laser will start using the rough pointing knowledge obtained from the beacon communication in order to find the retroreflector and commence the fine pointing loop. Following this, the large power circuit will be closed and the power transmission laser modules will start their function until the transmission window has passed.

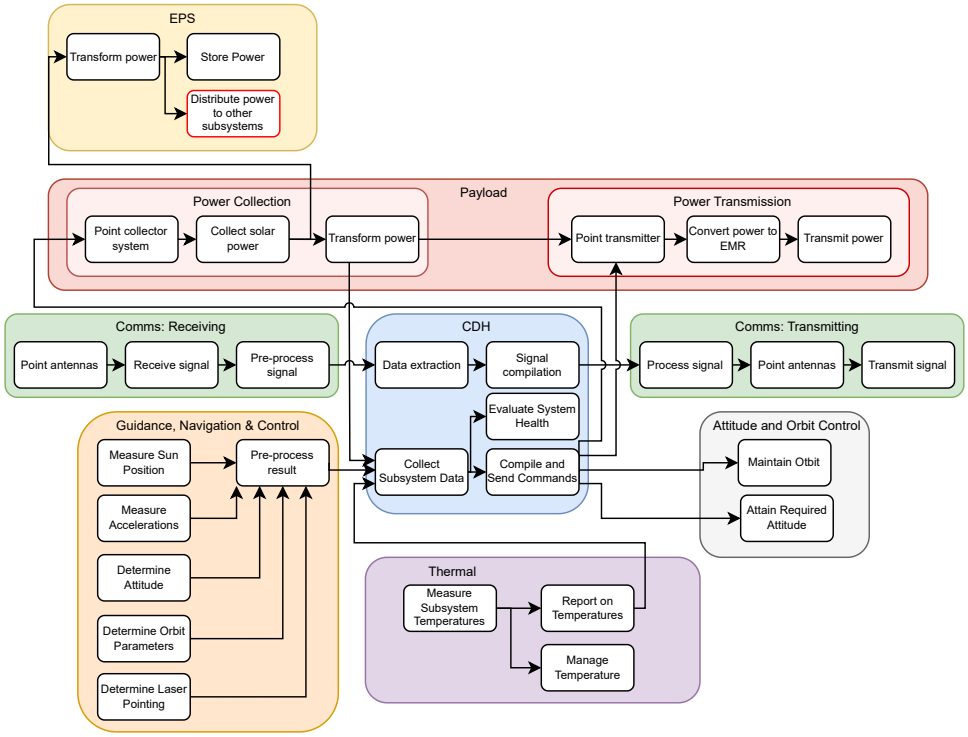

Figure 6.32: Detailed functions for each subsystem

7.1. Cost Analysis

In this section, the total cost of the mission is indicated. This is done by use of the complexity-based cost estimation tool that was previously developed [7]. Next, the reliability cost will be detailed, highlighting the options the client has in terms of cost and risk. First, the cost breakdown structure can be seen in Figure 7.1.

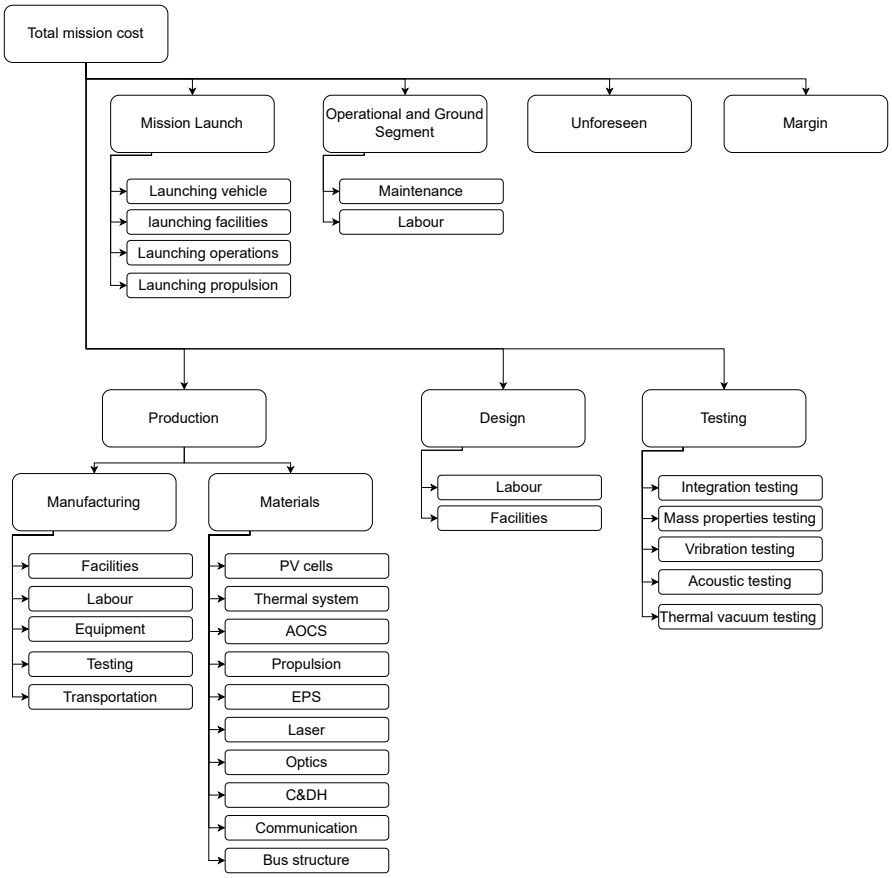

Figure 7.1: Cost Breakdown Structure

7.1.1. Complexity-Based Cost Estimation

Conventionally cost estimations are based on the mass of the spacecraft of the mission in question. While this estimation method uses historical data points which makes it robust for conventional missions, it does not provide support for missions that significantly deviate from those 'normal' missions, as is the case for the LUMEN mission.

Especially development cost is a large part of the cost budget that is usually estimated via mass. To still be able to obtain a development cost estimation, a tool was developed that is not directly governed by satellite mass. Rather, it uses the 'complexity' of a system to identify the associated development cost.

This novel method looks at the relative fractions of the power and mass budget and compares those to historical relative proportions. Depending on which way they deviate from those historical proportions, a complexity index is attributed to the system. That then drives the cost estimation as the mission complexity is compared to the complexity index of previous missions. For more detail on the software architecture of the tool, the reader is referred to Janssen et al. [7].

In the previous version of the tool, the relative proportions of the subsystem budgets were largely taken from literature and remained fixed regardless of the number of satellites. However, this approximation is inaccurate as different numbers of satellites result in different relative fractions of the power and muss budgets. The updated version of the tool now takes the change in relative proportions into

account. Moreover, due to design iterations, the subsystem budgets were changed from estimated values from literature to fractions obtained from the design process.

Due to this change in relative fractions, the complexity index of the spacecraft changed which in turn resulted in a different cost estimation of the system. Unfortunately, this (in part) resulted in the cost requirements being exceeded, as the mission is now estimated to cost 3.682 billion euros. This value includes development, production, AIT, launchers, operations, and reliability. The relevance of the reliability cost is explained in Section 7.1.2. The breakdown structure can be found in Figure 7.1. An overview of the costs per segment can be seen in Table 7.1.

Table 7.1: The cost budget per segment of the LUMEN mission.

Segment	**Cost** [FY23M€]
Design and Development	1708
Assembly Integration & Testing	194
Production	998
Buffer	500
Launch	120
Operations	112.7
Total	3.779

7.1.2. Reliability Cost

The LUMEN system was designed for a specific number of satellites. However, due to the reliability of the satellites, the probability of the mission succeeding with just the designed-for satellites is less than 1%. Thus, a 'buffer' is necessary to increase the system-level reliability. The determination of the size of the required buffer is presented in Chapter 9.

There are multiple financial considerations to take into account when selecting the buffer size. These choices are related to how much risk the client would like to take. Using fewer satellites in the buffer decreases the production cost of the buffer but decreases the likelihood of the mission succeeding. Having more satellites in the buffer makes it more likely for the mission to succeed but comes at a higher cost, as well as diminishing returns per additional satellite.

The relationship between cost and reliability can be found in Figure 7.2. There are a few important things to note in Figure 7.2. The total cost (the solid blue line) is comprised of the addition of the 'cost of risk' and the 'cost of buffer'. The total cost should be considered when making a decision for the size of the buffer, as the two parts individually are not representative.

The cost of risk is the expected value that a failure will have, and is determined by multiplying the cost of the mission by the probability that it will fail. This cost is not a 'real' cost in the sense that the mission will cost will not decrease with increasing buffer size. Rather, it states the expected losses that will be incurred. This is visualised by the red line in Figure 7.2 The expected loss can be decreased by including mitigation measures.

The mitigation measures are of course taken into account when designing the product. However, this mitigation can only be done to a certain extent. The other mitigation measure is, in the case of the LUMEN mission, to include additional buffer satellites. These additional satellites decrease the likelihood of the mission failing but cost money to produce. This cost is the green line in Figure 7.2.

The total cost gives the cost of the mission given the cost of risk and the cost of buffer. This optimal point, financially speaking, is the minimum of the total cost line. However, as the cost of risk is not *real*, the additional cost on top of the mission cost can be decreased by reducing the buffer size, though the risk of the mission failing will be increased.

According to requirement LMN.SAR.002 the system should have a reliability of 95%. This corresponds to a total cost of approximately 698 million euros of which around 500 million is attributed to producing additional satellites. This is however not the optimal point as increasing the number of satellites decreases the cost of risk more than the increased production cost, giving a lower total cost

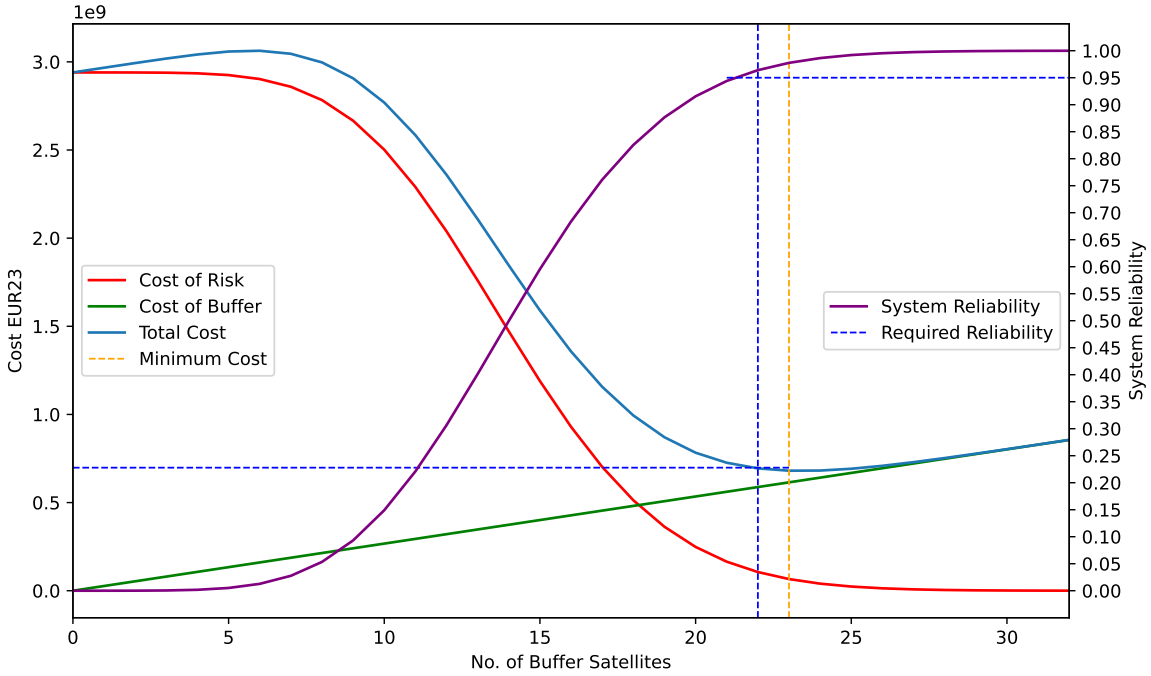

Figure 7.2: The relationship between cost and reliability depending on the number of satellites in the buffer.

and increasing the system level reliability. However, the production cost also increases to 540 million euros.

Depending on how much the client wants to spend on cost of risk and on production, the buffer can be chosen. Taking only the reliability requirement into account, the buffer should contain 25 satellites (the dashed blue line). Taking the best financial strategy into account, the buffer should consist of 27 satellites (the dashed yellow line). Opting for a different number of satellites is possible though it should be taken into account that taking less satellites quickly decreases system reliability. Increasing the number satellites gives diminishing returns; past 30 satellites the reliability increases minimally while the production cost continues increasing linearly.

7.1.3. Additional Costs

Some costs are not accounted for in the novel complexity-based cost estimation of Section 7.1.1. An overview of the additional cost can be seen in Table 7.2.

Table 7.2: Additional Cost

ID	name	FY23M€
A	**Additional costs**	**232.7**
A.1	Launch	120
A.2	Ground station and operational budget	112.7

Launch Cost

For the launch cost, some adaptions to the cost of the Midterm report [7] were made. A single launch of a Starship will still cost 10 M€ however, the performance of the Starship differs to those stated in the Midter report. Per launch of the Starship, two additional Starships must be launched to refuel the Starship with payload. This results in a $30M dollars per launch. Moreover, the packing of the satellites in the payload fairing is now taken into account. This results in being able to take less mass per launch into orbit, which in turn increases the amount of launches necessary to bring the entire system into orbit. Using a bounding box of $2x2x3$m, around 39 will fit per launch, as specified in

Section 6.9. This means a total of 4 launches will be necessary to place all satellites in the system in orbit, with a total cost of $120M US dollars (including the refuelling of the payload launcher).

Ground Station and Operational Cost

The maintenance cost are both estimated using Space Mission Analysis and Design by Wertz et al. [55], where labour cost is a summation of the contract cost ($160 FY00 per staff year) and the government labour ($110 FY00 per staff year) which equals to an M€0.45 FY23 for 1 year, so M€16.2 for 35 years of operational life and 1 year EOL phase. The maintenance is calculated by $0.1 \cdot 0.66 \cdot Cost_{\text{dev}}$[55]. The development cost from subsection 7.1.1 was 1708 M€, which results in a cost of 112.7 M€ for the maintenance.

7.2. Resource Management

7.2.1. Resource Allocation

The resource allocation and the budget breakdown presented in the previous baseline report [6] is reviewed and expanded upon for further mission phases. These phases were defined using the guidelines provided by ESA[62] as (0) Mission Analysis and identification, (A) Feasibility, (B) Preliminary Definition, (C) Detailed Definition, (D) Qualification and Production, (E) Utilisation, (F) Disposal. The resources are split up into human resources, technical resources and sustainability resources. Each was given their individual breakdown through the different phases of the project. The budget breakdown consists of budgets for mass, power, volume and cost.

7.2.2. Human Resources

No significant changes were made to the human resources allocation. Although some overtime had to be made to meet the deadlines of the reports, it was not a significant amount. As noted in the baseline, the total amount of experts and time needed in later phases will likely differ from what was presented, however, this will have to be negotiated with the different companies and government agencies which will be contacted for the various components and mission elements.

7.2.3. Technical Resources

The technical resources consist of the different tools and facilities to be used during the different phases. For phases 0, A, B, C, E and F, no notable changes were made from the baseline report. The tools and facilities used in the production phase will once again be dependent on the companies which will produce the different components. The estimates provided remain sufficient at the time of producing this report.

7.3. Market Analysis

In this section, the market analysis of the system will be done. The market analysis investigates the competition space-based solar power would encounter. First, current and possible future markets related to the lunar network will be discussed in Section 7.3.1. Then, the market for power provision to Earth will be investigated in Section 7.3.2.

7.3.1. Moon Market

Between now and 2035, it has been projected that more than 200 people will live on the Moon [114]. Like humans, the lunar inhabitants will require a constant power supply for life support and machinery. One potentially interesting place is the lunar South Pole. Thanks to permanent shadows at the lunar South Pole, some areas or craters could potentially contain water ice. However, due to these permanent shadows, surface-based solar panels are not feasible. Furthermore, common nuclear-based spacecraft energy generation technologies, such as Radioisotope Thermoelectric Generators (RTGs), which usually use Plutonium, have limited power conversion efficiencies and pose environ-

[62] URL: https://www.esa.int/Science_Exploration/Space_Science/How_a_mission_is_chosen [Cited on 15/06/2023]

mental risks[63,64]. They usually provide no more than 1 kW, meaning that more than 1000 RTGs would have to be employed.

Taking this into consideration, there is a market for a sustainable, safe, high-power energy generation system on the Moon. This is where space-based solar power can make a difference.

Market Segmentation & Potential Clients

There are several potential clients. These can be divided into governmental institutions or agencies, and private companies [65,66,67]. Some potential end-users can be seen in Table 7.3.

Table 7.3: Market segmentation analysis

Agency	Firmographic
ESA	Governmental
NASA	Governmental
JAXA	Governmental
ISRO	Governmental
UNAM	Governmental
ispace	Private

Company	Firmographic
Astrobotic	Private
Intuitive Machines	Private
Firefly Machines	Private
Draper	Private
Space IL	Private
SpaceX	Private

The list will most likely grow as time goes on and interest in the Moon industry grows.
These potential end-users may use the power for several different reasons. Some are listed in Table 7.4.

Table 7.4: Existing and future applications for the system.

Applications	Rationale
Crewed lunar outposts	There are future plans for crewed lunar outposts, which can function for scientific research or military purposes. The water ice at the South Pole makes a base enticing, as this can be used to obtain drinkable water and oxygen[68].
Lunar rovers	Currently, there are existing rovers conducting scientific research on the lunar surface. Currently, these rovers can be battery-powered, or equipped with solar panels. With the LUMEN mission, roves could potentially get recharged at the receiver station.
Uncrewed lunar outposts	In the future, there is a possibility of uncrewed lunar outposts, which may serve for scientific research or military purposes.
Moon mining	Currently, it is known that the lunar surface consists of usable resources such as He-3, water ice, and other valuable resources which could potentially be mined. As such, the LUMEN mission could provide power to these mining stations.
In-situ production plants	In the future, there may be in-situ production of propellants and other raw materials, which will also require power.
Communication	Communication relay stations on the Moon may potentially make use of the LUMEN system.

As can be seen, there are many potential end-users for the LUMEN mission. Furthermore, the investment in space-based solar power technologies can lead to spin-offs on Earth. For instance,

[63] URL: http://large.stanford.edu/courses/2013/ph241/jiang1/ [Cited 14/06/2023]
[64] URL: https://archive.nytimes.com/www.nytimes.com/library/national/science/090897sci-nasa-saturn.html[Cited 14/06/2023]
[65] URL: https://www.theverge.com/2019/8/23/20828312/Moon-companies-ispace-intuitive-machines-nasa-private-landing [Cited 13/06/2023]
[66] URL: https://www.nature.com/articles/d41586-023-01045-6 [Cited 13/-6/2023]
[67] URL: https://www.bbc.com/news/science-environment-64002977 [Cited 13/06/2023]
[33] URL: https://nssdc.gsfc.nasa.gov/planetary/ice/ice_moon.html [Cited 14/06/2023]

investments in more efficient and more durable solar cells could become beneficial for Earth applications. Next to that, long-range power transfer could be used on Earth as well, e.g. for wireless power transfer to aerial vehicles such as drones, helicopters or aeroplanes.

Swot Analysis

One important aspect of a market analysis is the Strengths, Weaknesses, Opportunities & Threats (SWOT) analysis. Doing so, the internal helpful aspects (strengths), external helpful aspects (opportunities), internal harmful aspects (weaknesses), and external harmful aspects (threats). This analysis can be seen in Figure 7.3.

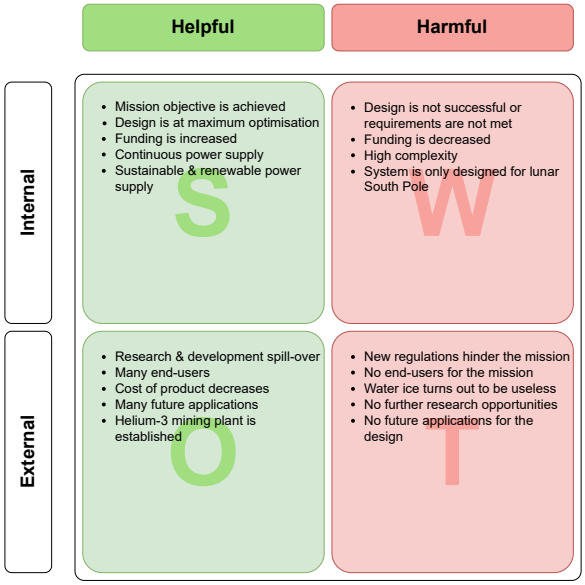

Figure 7.3: SWOT Analysis for Moon applications

7.3.2. Earth Market

On Earth, the competitive landscape is significantly different. Energy production is something that has been done for centuries already, meaning that breaking into this market is not trivial. However, this does not mean that there is no place for space-based solar power on Earth. In this section, the application for Earth of an SBSP system will be investigated.

The need for renewable energy production has increased significantly in the past two decades, as seen in Figure 7.4, with an increase of nearly $300\,\%$ since 2000.

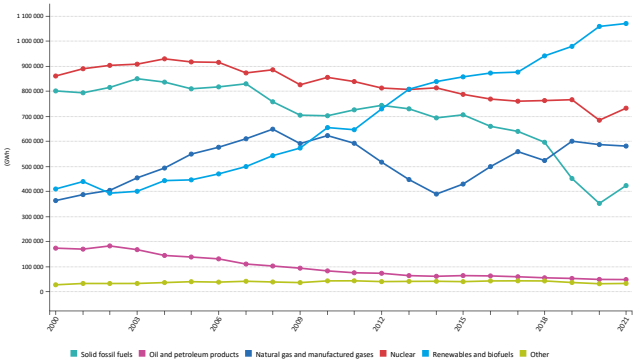

Figure 7.4: Gross electricity production by fuel, EU 2000-2001. Source: Eurostat[69]

Furthermore, the use of nuclear energy has been decreasing as well due to safety concerns, resulting

[69] URL: https://ec.europa.eu/eurostat/statistics-explained/index.php?title=Electricity_and_heat_statistics#General_overview [Cited 13/06/2023]

in some countries such as Germany closing down all their nuclear power plants[70]. Therefore, there is potential for new technologies to enter the market. In Section 7.3.2, a comparison of the LUMEN system with other energy production methods is compared.

Levelised Cost Of Energy

One way to compare the cost of different energy production methods is the Levelised Cost of Energy (LCOE), which is a metric that measures the lifetime costs over the energy production. It also allows for comparison between different technologies of unequal life spans, project size, different capital cost, risk, return, and capacities. A plot of different energy production methods and their associated LCOE can be seen in Figure 7.5.

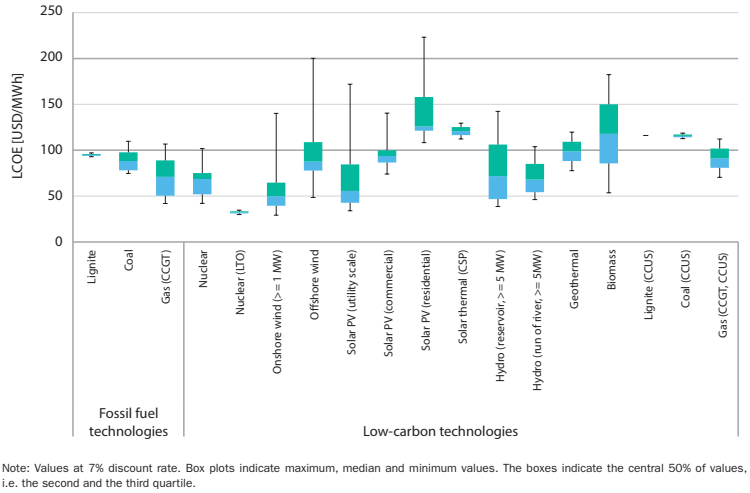

Figure 7.5: Levelised Cost of Energy by technology (FY 2018). Source: International Energy Agency [115]

As such, it is useful to compute the LCOE for an SBSP system for Earth to assess the competitivity. For a photovoltaic system, the LCOE can be calculated using Equation (7.1).

$$\text{LCOE} = \frac{\sum_{t=0}^{n} \frac{I_t + M_t}{(1+r)^t}}{\sum_{t=1}^{n} \frac{E_t}{(1+r)^t}} \tag{7.1}$$

where I_t are the capital investments in year t, M_t are the maintenance and operational costs in year t, r is the discount rate (set at $7\,\%$ as in Figure 7.5), and E_t is the used energy in year t (in MW h).

Some assumptions for the scaled system will be made:

- Just as for the lunar system, 1 MW will be produced at the receiver.
- It is assumed that the budget (€3.8 billion FY2023) to set up the system to continuously produce 1 MW is the same as for the Moon.
- The same losses and efficiencies as for the lunar system are considered, hence the receiver is of the same size.
- The lifetime of the Earth system is also 25 years.
- Maintenance and operational costs mainly include operational costs, except for the receiver.
- A yearly degradation factor of $0.5\,\%$ for the receiver and $0.3\,\%$ for the collectors are assumed.
- The maintenance cost of the receiver is similar to a normal photovoltaic farm, assumed to be 17 United States Dollars (USD) (FY2020) per kilowatt per year[71]. Assuming one megawatt, this results in 17000 USD per year. In FY18 USD, this is 16500 USD per year.

[70] URL: `https://www.cleanenergywire.org/news/qa-why-germany-phasing-out-nuclear-power-and-why-now` [Cited 13/06/2023]

[71] URL: `https://www.pv-magazine.com/2020/06/03/pv-plants-lasting-longer-with-lower-operational-costs/` [Cited 13/06/2023]

- The exchange rate from Euro to USD in 2018 is 1.17[72].
- The total euro inflation ratio between 2018 and 2023 is 1.2[73].

The operational costs are calculated using the methods by Wertz et al. [55], where 26 engineers and 8 technicians are employed. This results in a yearly operational cost of $\$7.02$ M (FY18), or $€7.2$ M (FY23). Taking this into consideration, the Levelised Cost of Operation results in $31330 USD (2018) per MWh. In Figure 7.5, the largest outlier is found in residential solar PV, at approximately 225 USD/MWh. This means that the space based solar power system LCOE would be 1392 % higher than the highest outlier.With this, it can be concluded that in order to apply space based solar power to Earth, the power output must be increased significantly; at least by a factor of 139, to make it fall into a feasible range. Furthermore, the cost must not increase with this increase in power. Of course, this is just a high-level estimate and the exact cost will most likely not be the same. The system was specifically designed for lunar applications, and increasing the total power generation by a factor of 1000 will most likely not increase costs by a factor of 1000. For instance, a 1 GW nuclear power plant costs around $6 billion to $9 billion to construct [116]. This is an increase of a factor of 1000 in power output compared to SBSP, with only a 4 to 6 times increase in price. Furthermore, a study by Frazer-Nash Consultancy [117] showed that a 1 to 2 GW SBSP system (single satellite in Geostationary orbit) would cost $9.8 billion. This would also result in a LCOE of €206/MWh, potentially decreasing to €69/MWh, making it more cost-competitive than many other methods. A more in-depth scalability analysis for Earth applications will be done in Section 8.2

SWOT Analysis

Just as for the Moon, a SWOT analysis can be done for Earth applications. This SWOT analysis can be seen in Figure 7.6.

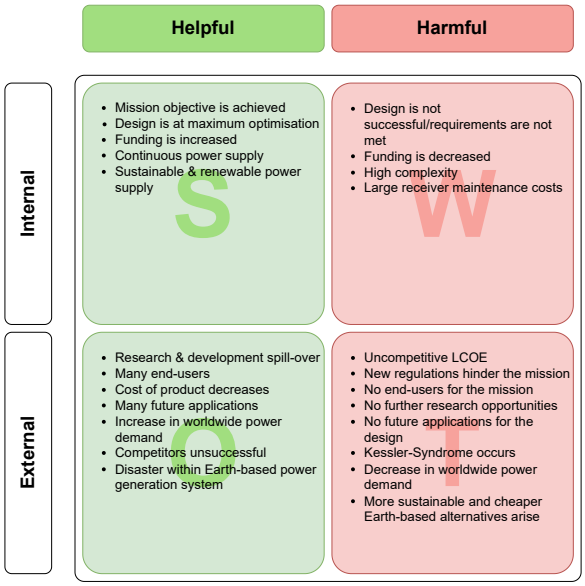

Figure 7.6: SWOT Analysis for Earth applications

To conclude, some of the main advantages of a SBSP system are the following:

- There is potential to use one system to power several countries. If the orbit is not geostationary, the spacecraft could pass over several countries; all that is needed is a receiver.
- It is potentially more sustainable than coal or other non-renewable energy source.
- Unlike earth-based solar power, it is possible to provide power at night, as GEO orbits receive power 99 % of the time [117].
- It is not dependent on weather conditions as is for wind turbines.

[72] URL: `https://www.statista.com/statistics/412794/euro-to-u-s-dollar-annual-average-exchange-rate/` [Cited 13/06/2023]

[73] URL: `https://www.inflationtool.com/euro/` [Cited 13/06/2023]

8. System Analysis

This chapter aims to give an overview of two analyses that have been performed on LUMEN's design: an analysis of its exergy, a measure for the amount of useful work that can be extracted from a system in equilibrium with its environment, and an analysis on its scalability, where the possibility of scaling the system for Earth applications is assessed. These analyses are useful tools in assessing how feasible a system such as LUMEN would be for its intended use, and how feasible the concept of a Space-Based Solar Power system would be in general for future applications.

8.1. Exergy Analysis

Exergy is defined as the measure of useful work generated by a system. It is a concept based on the second law of thermodynamics, wherein a non-perfect system entropy will always increase.

The general formula for Exergy is given by Equation (8.1).

$$E_{x,in} = E_{x,out} + E_{x,destroyed} \tag{8.1}$$

Here, $E_{x,in}$ represents the incoming exergy, $E_{x,out}$ the outgoing exergy and $E_{x,destroyed}$ the destroyed exergy. To analyse the exergy balance of a system, it is important to properly define the boundaries of the system.

In the case of the LUMEN system, the boundaries are chosen in a way that they encompass a static satellite and the receiver so that the outgoing exergy is in the form of electricity and thermal radiation. Differentiating exergy from energy is done by a conversion factor, which is dependent on the type of energy or exergy in consideration. A list of conversion factors for common energy types is given in [118]. With the boundaries now defined, the different exergies can be analysed. First, the method will be shown using BOL efficiencies, after that the evolution of the exergy over mission time will be discussed and finally a comparison to a solar panel on the Moon will be made.

8.1.1. Incoming Exergy

The incoming exergy in the system is in the form of solar radiation on the solar panels. This represents the total energy or exergy with which, potentially, work could be done. The total amount of energy that enters the sum is equal to the solar radiation density times the area of the solar panels, and the conversion factor of photon radiation is given by Equation (8.2). Here, T_{ref} represents the ambient temperature outside the system, and T is the temperature of the object in consideration, both expressed in Kelvin.

$$\zeta = 1 - \frac{T_{ref}}{T} \tag{8.2}$$

Since the temperature of space can be approximated to be $2.73\,\mathrm{K}$[74] and the design operating temperature of the solar panels (and the entire spacecraft) is around $300\,\mathrm{K}$, ζ is 0.991 in this case. Thus the incoming exergy is almost the same as the total solar radiation covered by the solar panels for the LUMEN mission, and it can be calculated in Equation (8.3)

$$E_{x,in} = \zeta A_{PV} I_{Sun} = 0.991 \cdot 224.22\,\mathrm{m}^2 \cdot 1366\,\mathrm{W\,m}^{-2} = 303\,527\,\mathrm{W} \tag{8.3}$$

8.1.2. Outgoing Exergy

The outgoing exergy defines the exergy which exits the system. In LUMEN's case, it comes in the form of the electricity going out of the receiver on the Moon, along with thermal radiation exergy.

$$E_{x,out} = E_{x,elec} + E_{x,thermal} = E_{x,elec} + E_{x,thermal,Solarcell} + E_{x,thermal,laser} + E_{x,thermal,subsystems} \tag{8.4}$$

[74] URL: https://www.esa.int/Science_Exploration/Space_Science/Planck/Planck_and_the_cosmic_microwave_background [Cited 23/06/2023]

With the list of all system efficiencies, the total system efficiency is a measure of how much solar energy is converted into electrical energy. The exergy conversion factor for electrical energy is also given as being 1 in [118], thus the outgoing electrical exergy equals the outgoing electrical energy.

$$E_{x,elec} = \zeta \eta_{total} A_{PV} I_{Sun} = 1 \cdot 0.0503 \cdot 224.22\,\mathrm{m}^2 \cdot 1366\,\mathrm{W\,m}^{-2} = 15\,406\,\mathrm{W} \tag{8.5}$$

The thermal exergy then can largely be divided into three elements. The first is the exergy to be radiated due to the solar panels.

$$\begin{aligned} E_{x,thermal,solarcell} &= \zeta Q_{radiated,solarcell} = \zeta(1-\eta_{PV}) A_{PV} I_{Sun} \\ &= 0.991 \cdot 0.7067 \cdot 224.22\,\mathrm{m}^2 \cdot 1366\,\mathrm{W\,m}^{-2} = 214\,503\,\mathrm{W} \end{aligned} \tag{8.6}$$

Second, is the thermal exergy to be radiated due to the transmission laser. The thermal energy is equal to one minus the efficiency of the lasers times the energy which enters the laser modules.

$$E_{x,thermal,laser} = \zeta Q_{radiated,laser} = \zeta(1-\eta_{laser}) P_{intolaser} = 0.991 \cdot 0.5 \cdot 94\,853\,\mathrm{W} = 47\,000\,\mathrm{W} \tag{8.7}$$

The total efficiency for the subsystems was discussed in Section 6.5 and was assumed to be 55%, thus the thermal energy they produce is relative to one minus this efficiency.

$$\begin{aligned} E_{x,thermal,subsystems} &= \zeta Q_{radiated,subsystems} = \zeta(1-\eta_{subsystems}) P_{intosubsystems} \\ &= 0.991 \cdot 0.45 \cdot 1100\,\mathrm{W} = 491\,\mathrm{W} \end{aligned} \tag{8.8}$$

These outgoing exergies do not cover every aspect of the spacecraft, and as such some unaccounted for exergy will exist. These can be found later during the balance setup.

8.1.3. Destroyed Exergy

Destroyed exergy can be seen as the amount of energy which goes through an irreversible process, and thus can never be used to provide useful work. In the case of a LUMEN satellite, the most obvious source of irreversible is the mechanical energies consumed by components such as the actuators.

$$\begin{aligned} E_{x,dest,subsystems} &= \zeta Q_{used,subsystems} = \zeta \eta_{subsystems} P_{intosubsystems} \\ &= 0.991 \cdot 0.55 \cdot 1100\,\mathrm{W} = 600\,\mathrm{W} \end{aligned} \tag{8.9}$$

8.1.4. Exergy Efficiency

With these values, an exergy balance can be made. When subtracting the sum of the outgoing exergies and the destroyed exergies from the incoming exergy, it can be seen that about 31 kW of exergy has been unaccounted for. While this will most likely not affect the useful exergy efficiency, in a more detailed analysis this has to be eliminated. The exergy efficiency is calculated by dividing the useful exergy, $E_{x,elec}$ in this case, by the incoming exergy. The above calculations can be performed for each year, taking into account the degradation of the collection, transmission and receiver subsystems. An area graph showing the relative percentages of the different exergies is shown in Figure 8.1 and a more detailed breakdown of the BOL and EOL efficiencies is given in Table 8.1.

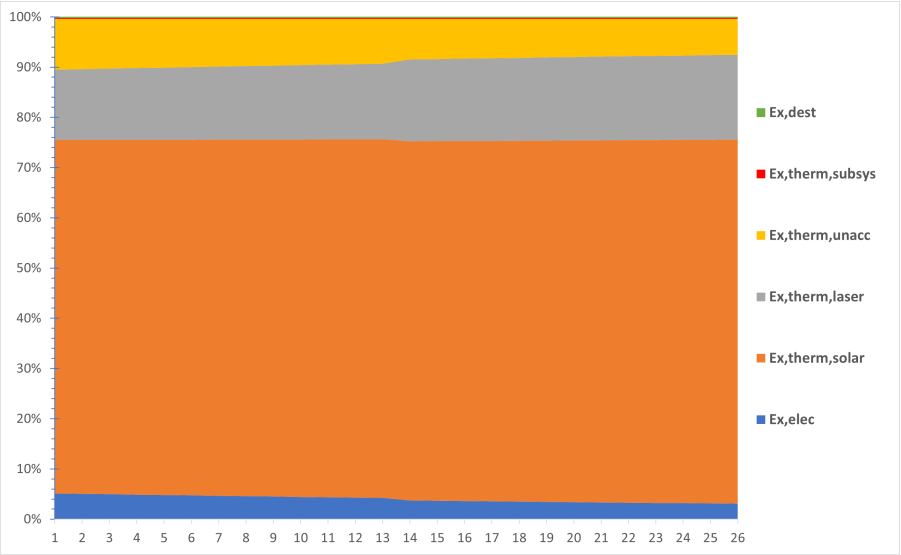

Figure 8.1: Exergy percentage breakdown over the system's lifetime.

Table 8.1: BOL and EOL percentage breakdown

Exergy type	BOL percentage	EOL percentage
Electrical	5.134	3.085
Thermal, Solar cell	70.672	72.794
Thermal, Laser	14.051	16.95
Thermal, subsystems	0.161	0.161
Thermal, unaccounted	10.179	7.208
Destroyed	0.197	0.197

8.1.5. Comparison and discussion

To figure out the differences of this system to a 'regular' solar panel on the Moon's surface, an exergy analysis will have to be performed for this solar panel. In this situation, parameters will be used from Section 4.1.1. In this section, it is discussed how a solar panel array on the crater trim would need about 11.6 km of cabling to reach the same location as the receiver. In [119], analysis is performed on cabling on the lunar surface with different lengths, input powers and voltages. For a cable with a length of 10 km, a power in overpower out factor of 1.39 is calculated. Extrapolating this result to 11.6 km, gives a factor of 1.438. This factor represents the loss of the cable and the power converters and will be assumed to be radiated away in the form of heat with a reference or outside temperature of 2.73 K. The solar panel efficiencies and degradation will be the same as in the LUMEN mission. With these values and equations, the total solar panel area needed can be calculated to be $3870\,\mathrm{m}^2$.

The exergy of this system can then be calculated in a similar way to the sections above. The incoming exergy is the solar irradiance on the solar panels, the outgoing exergy consists of the electrical energy delivered and the thermal radiation by the solar panels, the cable and the converters. The qualitative breakdown of the exergy for this solar panel can be seen in Figure 8.2.

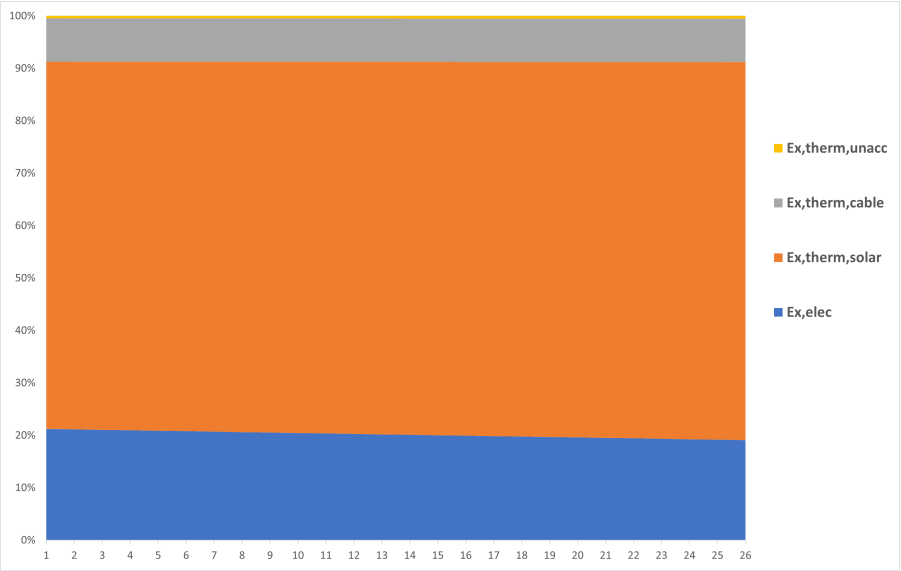

Figure 8.2: Exergy breakdown for a solar panel on the Moon

This breakdown is only a high-level one, as the exact parameters of the study in [119] do not line up with the ones which would be needed by LUMEN. The degradation of the cable was also neglected alongside the extra degradation the solar panel array would see due to lunar dust and other elements.

Comparing both breakdowns to one another, it can be seen that a solar panel placed on the lunar is for now the more exergy-efficient option. This is mainly due to the large unaccounted-for cable and conversion losses, as well as the low efficiency of the laser. The solar panel efficiency of course is the same in both cases, and thus improvements in this aspect would increase the overall exergy efficiency. Another point of improvement which could be made is the use of thermal-to-electrical conversion methods, which would help turn some of the 'wasted' thermal exergies into useful electrical exergy.

8.2. Scalability Analysis

While LUMEN was designed specifically for lunar applications, the system is also intended to represent a proof of concept for larger-scale systems in Earth orbit, catering to terrestrial applications. Developing a new complex system like LUMEN from the ground up requires considerable time, financial and personnel resources. However, the possibility of (partially) reusing LUMEN's design could significantly reduce these resource requirements. This section focuses on evaluating the scalability of LUMEN's system for Earth-based scenarios. Three cases are considered: a single LUMEN spacecraft, the 133 LUMEN spacecraft used for the lunar case and a significantly higher number of spacecraft.

8.2.1. Considerations for Earth Scalability

When scaling the system for Earth applications, changes in the environment and thus also its requirements should be considered. The terrestrial environment poses new challenges for the system, while also providing new opportunities. This section will give an overview of relevant changes, both positive and negative, arising when scaling LUMEN to Earth applications.

In many regards, the Earth's environment is more complex than the Moon's environment, leading to more stringent system constraints:

- **Earth's effect on the SBSP environment:**. For an SBSP system, the most notable change is the presence of the Earth's atmosphere, significantly affecting laser power transmission losses due to atmospheric attenuation and turbulence. Atmospheric drag, along with the presence of the Earth's magnetic field and its deeper gravity well also result in increased disturbances on a spacecraft's attitude and orbit, especially in LEO. Earth also has a higher albedo, so more heat is reflected towards the spacecraft, resulting in higher temperatures.

- **Debris:** Space debris around the Earth is a growing concern[75]. Consequently, the satellites employed within the SBSP system face an increased risk of encountering high-velocity collisions when in Earth's orbit as compared to the lunar orbit. Such collisions would likely lead to catastrophic spacecraft failures, posing a potential threat to other nearby spacecraft.
- **Van Allen belts:** For the Earth case, the SBSP system's orbit will need to be designed to take into account the increased radiation in the Van Allen belts compared to the lunar orbit. The high density of energetic charged particles in these zones can break sensitive electronics in the satellite and accelerate the degradation of photovoltaics. Next to this, atomic oxygen is present, especially in lower orbits. It is one of the main drivers of satellite degradation in LEO and has the potential to decrease the lifetime of the system significantly. Its effect on the transmittance and structural integrity of the concentrator lenses is a key concern.
- **Interference:** LUMEN's laser-based power transmitter could interfere with existing optical communication systems. Due to the continuous wave lasers, this interference could be filtered out easily. However, the main concern is the high intensity of the beam, which could damage the optical communication sensors. The potential for sensor damage is even more important for astronomical observatories. While telescopes operating at infrared wavelengths are far less popular than radio telescopes, their sensors are highly sensitive and would likely be instantly destroyed if hit by LUMEN's power beam.

In other regards, the Earth's environment also allows for alleviating some of the system constraints:

- **Orbit possibilities:** Using either sun-synchronous or GEO orbits could result in less total spacecraft required.
- **Receiver size :** For Earth application, a significantly larger receiver can be built for a fraction of the price of a lunar receiver. A larger receiver can result in less stringent pointing requirements, simplifying the pointing mechanisms of the power transmitter.
- **Accessibility:** An Earth-orbiting satellite is easier to reach than a Moon-orbiting satellite and thus easier to replace or even repair if it were needed. This could reduce the risk of having a non-functioning system.

Finally, perhaps the most important change in scaling LUMEN to Earth applications is how its mission objective would change:

- **Larger scale:** For Earth applications, the power requirement of $1\,\mathrm{MW}$ is too low to be truly useful, as there exist more than 11700 utility-level solar power plants with a peak power production capacity above $4\,\mathrm{MW}$ (AC)[76]. Furthermore, $>440\,\mathrm{GW}$ of renewable power capacities are expected to be added in 2023 alone[77], with this value expected to grow year-by-year. For the purposes of this terrestrial scalability analysis, a power capacity target of $1\,\mathrm{GW}$ is assumed to provide a significant increase in the yearly renewable power capacity addition.
- **Business case:** Energy generation is already being done in various ways on the Earth's surface, so it is harder to make an economically viable system. While an SBSP system could provide power 24 hours a day, the time-averaged cost per watt must be competitive with conventional terrestrial solar power plants to achieve viability. It should be noted that the footprint of the SBSP receiver can be significantly smaller than that of a conventional solar power plant. Furthermore, by using a combination of PV junctions tuned to the laser's wavelength and junctions tuned to the solar spectrum, such a receiver would generate additional power during the day.

8.2.2. Losses and efficiency

Due to the presence of Earth's atmosphere, a fraction of the transmitter laser will be lost through scattering and absorption. Three main mechanisms lower the atmospheric transmittance: Rayleigh

[75] URL: `https://www.esa.int/Space_Safety/Space_Debris/About_space_debris` [Cited 20/06/2023]

[76] URL: `https://www.wiki-solar.org/analysis/` [Cited 23/06/2023]

[77] URL: `https://www.iea.org/reports/renewable-energy-market-update-june-2023/executive-summary` [Cited 23/06/2023]

scattering, aerosol scattering and molecular absorption. The laser power transmission system employed on LUMEN operates in the near-infrared at 976 nm - at this wavelength, the predicted zenith transmittance is around 82.5 % [120]. It should be noted that 976 nm lies within a few nm of an H_2O molecular absorption line (978 nm). Should wavelength drift of the laser occur, it could significantly reduce the transmittance for Earth applications, as H_2O makes up about 4% of the Atmosphere[78]. Furthermore, the transmittance may vary heavily in time due to cloud coverage and the resulting [120] - for an optically thick cloud, the transmittance approaches 0 %. For the purposes of this analysis, cloud cover effects shall be neglected, as the GEO orbit makes the best receiver locations around the equator, where cloud cover is minimal. The atmospheric transmissivity of 82.5 % for100 km of the atmosphere is scaled by the beam propagation distance through the atmosphere at varying incidence angles.

Atmospheric turbulence is an unavoidable loss and effectively manifests as a dilution of the laser beam. According to Dakar et al. [121], the RMS difference in beam width (diameter containing 85 % of the power) is around 0.18 m at a distance of 30 km and with a laser of 1.55 µm. Unfortunately, no data is available past a distance of 30 km and the RMS seems to become linear with increasing distance. Therefore, it was decided to extrapolate the data from [121]. The estimated additional beam width RMS after 100 km is therefore 0.74 m. Furthermore, to account for the 99 % power Gaussian beam instead of 85 %, a factor of 1.52 is added, resulting 1.125 m. This is likely an optimistic estimation and should be viewed critically, so a safety factor of 1.5 is applied, resulting in an additional 1.7 m RMS 99 % power beam width.

With more than one spacecraft, an appropriate separation distance must be kept in their orbit to reduce the risk of collisions. The separation distance is initially assumed to be the same as for the lunar case, namely 164.47 km (from Table 5.7). This separation causes an incidence angle and increases receiver reflectivity losses as described in Section 4.1.3. However, for the GEO case, the incidence angle has only 1 component, as the inclination of the orbit is 0 and the receiver is assumed to be on the equator. To determine the relationship between the incidence angle and the reflectivity of the receiver coverglass with an anti-reflective coating at 976 nm, measurements from [15] is again used. Unlike for the lunar receiver, the mean of these incidence angles is centred at $0\,^\circ$, meaning the full dataset shown in Figure 8.3 with $0\,^\circ \leq \phi \leq 60\,^\circ$ is used, with an additional datapoint at $\phi = 90\,^\circ$, where there is 100 % loss. To this data, a quartic trendline was fit, resulting in the relation shown in Figure 8.3 with y the loss coefficient as a fraction.

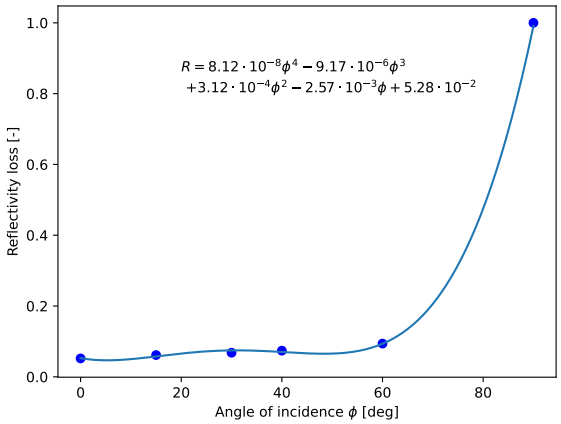

Figure 8.3: Reflectivity measurements with quartic fit sourced at 976 nm from [15].

The reflectivity relation is used in combination with the atmospheric losses to obtain the combined efficiency due to reflectivity and atmospheric losses. These efficiencies versus the number of spacecraft are shown in Figure 8.4. The transmission window of the constellation is limited to incidence angles smaller than $85\,^\circ$, as this is the value used by most other satellites. However, this angle must

[78]URL: `https://www.noaa.gov/jetstream/atmosphere` [Cited 21/06/2023]

be revised after the safety of the design is evaluated. For this cutoff and spacing of 164.47 km (Table 5.7), the maximum number of satellites in one track in GEO is 730, as can be seen in Figure 8.4. The overall constellation transmission efficiency is around 71 %.

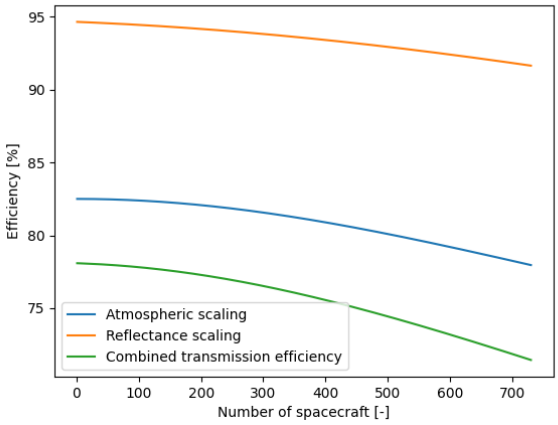

Figure 8.4: Efficiencies for terrestrial power transmission versus the number of spacecraft in GEO with a spacing of 164.47 km.

8.2.3. Single LUMEN spacecraft in GEO

The receiver size is first calculated for a singular unmodified LUMEN spacecraft is calculated the same way as the lunar case, using Equation (4.1). The additional beam divergence due to turbulence in the ≈ 100 km of the atmosphere is accounted for by adding it onto the receiver size. When not accounting for atmosphere, a receiver diameter of 187.37 m is calculated. Correcting for atmospheric effects results in a receiver diameter of 189.07 m. This diameter is around 2.2 times larger than the lunar receiver; its area is 4.8 times larger. It must be noted that the size can heavily depend on atmospheric turbulence and is likely to be underestimated. However, even if it is, a terrestrial receiver of this size is easily feasible, as many photovoltaic power stations are significantly larger than this.

Based on the relation presented in Section 8.2, a reflectivity of 5.35 % is taken. Keeping all other efficiencies constant, a single LUMEN spacecraft directly over the receiver in GEO orbit is expected to produce 15.64 kW at BoL. After 25 years, this value decreases to 9.399 kW. The BOL and the EOL efficiencies for a single LUMEN spacecraft in GEO are 4.33 % and 2.60 % respectively. The LUMEN system is less efficient in the Earth case compared to the lunar case, as the atmospheric losses outweigh the lower reflectivity.

8.2.4. Unaltered LUMEN constellation in GEO

As can be concluded from Section 8.2.3, putting a single LUMEN spacecraft in GEO would result in low power outputs, especially when compared to the 1 GW goal for Earth applications. A possible solution to this problem would be to increase the number of spacecraft in orbit: in this case, the result of placing all 133 LUMEN spacecraft in GEO is assessed.

With an increasing number of spacecraft, the efficiency of the LUMEN system decreases due to the notion that all spacecraft have a finite size and should have a certain relative spacing in orbit. Thus, when increasing the number of spacecraft in orbit, all additional spacecraft will have to be placed next to the spacecraft directly above the receiver. This will increase losses by increasing the average angle of incidence of all transmitting spacecraft, leading to higher reflectivity losses, and by increasing the average distance over which the spacecraft has to transmit power, leading to higher atmospheric losses.

For the case of 133 LUMEN spacecraft in GEO orbit, spacecraft are assumed to be spaced 164.47 km apart - the minimum value encountered for the lunar LUMEN constellation presented in Table 5.7. While some spacecraft in GEO are sometimes spaced less than 100 km apart, choosing this larger separation would reduce the risk of collisions. Using this separation, the atmospheric transmission

and reflectivity efficiencies are $82.3\,\%$ and $94.4\,\%$. The overall system's BOL and EOL efficiencies are $4.22\,\%$ and $2.54\,\%$, respectively. This results in an average useful power provided per spacecraft of $15.25\,$kW at BOL and $9.162\,$kW at EOL. The combined useful power output of this constellation is therefore $2.0275\,$MW at BOL and $1.219\,$MW at EOL. This is higher than the lunar LUMEN system, as all 133 S/C are in view at all times due to the GEO orbit.

8.2.5. Gigawatt-scale LUMEN in GEO

The number of LUMEN spacecraft must be significantly higher to generate $1\,$GW of electrical utility power on the Earth. Due to the angular separation between the spacecraft in GEO and the resulting incidence angles, the reflectivity losses increase compared to the singular and 133 LUMEN spacecraft cases.

However, with a separation of $164.47\,$km, only around 730 spacecraft can be in view of the receiver. Dropping the separation down to $70\,$km or the size of a typical GEO "box" separating satellites[79] results in 1710 satellites in one track. This is not nearly enough lunar LUMEN spacecraft to provide $1\,$GW of power, so the spacecraft must either be larger or more tracks need to be used. By relaxing the orbit to geosynchronous instead of geostationary, more orbital tracks can be added - the Inter-Agency Space Debris Coordination Committee defines this region with inclinations within $\pm 15\,°$ of geostationary. The maximal 1710 spacecraft can provide a combined $24.171\,$kW of power. The atmospheric efficiency, reflectivity efficiency and the combination of the two for the 1710 satellites per track are shown in Figure 8.5.

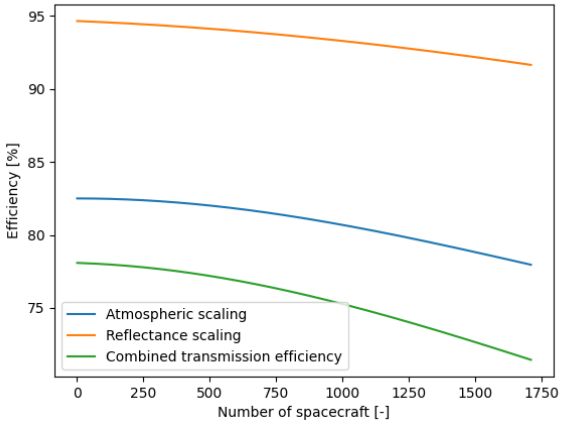

Figure 8.5: Transmission and reflectivity efficiencies versus number of spacecraft for $70\,$km spacing.

To achieve $1\,$GW, 41.37 tracks of 1710 spacecraft are therefore required. A spacing of $70\,$km results in a separation of around $0.112\,°$ on the sky - with 42 tracks the total angular span is around $4.5\,°$, which falls well within the $\pm 15\,°$ criterion. The total required number of spacecraft summed over the 42 orbital planes is therefore 707427.

However, assuming the same 36 S/C per launch as for the lunar case, this results in 1966 Starship launches with S/C as payload. While with a payload mass of $\approx 40\,$t, refuelling is necessary to reach GEO, this only needs to happen once compared to twice for the lunar case. If the number of spacecraft per launch were reduced, non-refuelled $20\,$t launches could be cheaper than refuelling, depending on the cost of the Starship. However, the >2000 launches is an incredibly high number - in 2022, 180 orbital launches were performed[80]. For this reason, larger spacecraft should be considered, potentially including in-orbit assembly and integration.

[79] URL: `https://thespacereview.com/article/1634/1` [Cited 22/06/2023]
[80] URL: `https://www.nature.com/articles/d41586-023-00048-7` [Cited 22/06/2023]

8.2.6. Terrestrial LUMEN Design Alterations

As mentioned before, Earth applications do not only lead to new challenges but also allow for more opportunities. Tailoring LUMEN's design to Earth applications requires changes on different levels of its design. This section describes which changes could be considered for increasing LUMEN's Earth-based performance.

Orbit Alterations

Moving to the Earth, putting spacecraft into GEO becomes possible. For a number of reasons, this choice of orbit provides such important advantages to the SBSP system that choosing it would be obvious:

- **Contact time**: As GEO allows for constant contact between spacecraft and the receiver, the system's mass can significantly be reduced, as illustrated by the following example. Consider a case where every spacecraft is designed to provide 10% of the total power that should be transmitted to the Earth. This design choice would impose the requirement that at least 10 spacecraft should have contact with the receiver at all times. While putting these spacecraft into GEO would then allow for only using 10 spacecraft, seeing as contact is constant, choosing any other orbit would require a significantly larger number of these same spacecraft to account for times at which these spacecraft are not in view.
- **Efficiency**: Putting a spacecraft into GEO significantly increases time-averaged system efficiency by decreasing transmission-receiver losses. For a general orbit, the spacecraft's elevation with respect to the receiver will vary over time, causing its laser's angle of incidence with respect to the receiver to also vary. As the angle of incidence of the laser increases, the efficiency of the transmission-receiver segment will drop. Considering incidence losses should be zero when the elevation is exactly equal to $90\,^\circ$ (when the spacecraft is directly above the receiver), and seeing as for GEO this can be satisfied at all times, a spacecraft in GEO should have a higher efficiency on average. This is strengthened by the fact that being directly above the receiver minimises the distance the laser has to travel through the atmosphere. This decreases losses even further compared to the general case, where the varying elevation angle would on average increase the length of the atmosphere the laser would have to travel through.
- **Pointing**: For a spacecraft in GEO, locating the receiver would be significantly easier, seeing as its position with respect to the satellite remains constant. While GEO is characterised by very high altitudes, which would make pointing requirements more stringent, Earth applications would also allow for increasing the receiver size, which could (partially) solve this problem: for Moon applications, receiver size is mostly constrained by the difficulty of transportation and manufacturing, but for Earth applications, these considerations do not constrain the design.
- **Degradation**: As GEO spacecraft can transmit continuously because of their constant contact times, the system's lasers would never have to be turned off. As laser degradation mostly has to do with the number of thermal cycles, reducing the laser transmission to continuous firing could help to increase the laser modules' lifetimes.
- **Safety**: An important consideration for Earth applications would be safety, seeing as the Earth is home to large numbers of organisms, all of which are susceptible to injury due to laser absorption. Also, LUMEN's laser transmission could interfere with air traffic and telecommunications. Since a GEO configuration would allow a laser's path to remain constant, safety issues could largely be solved by fencing the area surrounding the receiver and imposing a no-fly zone. Furthermore, more ΔV should be budgeted for potential avoidance manoeuvres.

Seeing as putting the spacecraft into GEO is of uttermost importance to the system's performance, redesigning LUMEN around its compliance with this orbit makes a lot of sense: the switch from ELFO to GEO will thus largely drive other changes to be made to the design. One of the most important changes this switch in orbit induces is to significantly decrease the system's number of spacecraft.

Another important impact that the change to a GEO brings forth is that the GEO orbit a daily eclipse of maximum $70\,\text{min}$[81] has. This maximum eclipse happens when the Earth is at equinox and the system

[81] URL: `https://www.noaa.gov/jetstream/atmosphere` [Cited 21/06/2023]

should be designed for this value. To provide power during the eclipse there are two design options to take into account:

- **Extra batteries:** the SBSP systems batteries will need to be able to store an extra 43.17 MW h in total if full functionality is needed at eclipse.
- **Extra upscaled satellites:** As the eclipse in only 5 % of the orbit time, not taking the penumbra into account, other SBSP satellites in sunlight can still provide power to the receiver. The other GEO-stationary satellites of the SBSP system will have an incidence angle higher than 0 °, so extra incidence angle and atmospheric losses will also need to be taken into account.

Finally, in-orbit assembly could be taken into account if the number of spacecraft is low and the system cannot fit into one launcher anymore.

Collection Alterations

As the whole LUMEN system will have to be scaled for Earth applications and the 1 GW requirement, the collection system will also need to be altered. The best option is to increase the area of the collection subsystem. To achieve 1 GW, over 70700 unaltered spacecraft are needed. Increasing their size would reduce the atmospheric losses as there are fewer spacecraft beaming at high incidence angles. Furthermore, fewer power transmitter collimators would be required with fewer, larger spacecraft, as the collimator diameter does not scale with the spacecraft power. Using higher concentration factor collector lenses could cut costs, as fewer PV cells are then required. The combination of these two recommendations could significantly reduce the cost of a terrestrial lumen system but it would require a significant redesign.

Transmission-Receiver Alterations

As a GEO-stationed SBSP system has been chosen, it is opted to keep the laser transmission and not change to the microwave transmission technology. Using microwave technology at GEO altitude leads to unreasonable receiver and transmission sizes, as the beam width of a microwave is too high. However, it is much more feasible to build a kilometre-scale receiver on the Earth than on the Moon. Keeping the laser transmission does however not mean that the exact same laser can be used, because the laser wavelength should be changed, as explained in Section 8.2.2.

The turbulence effects, as explained in Section 8.2.2 could be compensated for using adaptive optics (depicted in Figure 4.8) such as deformable mirrors [36]. This technology depends on measuring the atmospheric turbulence using a guidance laser, which would be less effective and more difficult to do at GEO distances, as the guidance laser would be faint. Furthermore, the round-trip time delay is around 0.24 s, reducing the effectiveness of the feedback loop with fast-steering optics. As it was considered out of the scope of this preliminary analysis, turbulence is not compensated for.

8.2.7. Conclusion

In conclusion, the scalability analysis of the LUMEN system for Earth applications reveals both challenges and opportunities. The Earth's environment poses new constraints, such as the presence of the atmosphere, atmospheric losses, increased disturbances from Earth's gravity and magnetic field, higher albedo, and the risk of space debris collisions. However, it also offers advantages, including the possibility of using different orbits, larger receiver sizes and easier accessibility for maintenance and repairs.

To fully explore the scalability potential of the LUMEN system for Earth applications, further analysis is required considering larger spacecraft and different transmitter wavelengths. Moreover, the economic viability and competitiveness of an Earth-based SBSP system need to be carefully evaluated, taking into account the existing power generation options and cost factors.

Overall, while the challenges of scaling the LUMEN system for Earth applications are significant, the potential benefits in terms of increased power capacity, reduced reliance on conventional power plants, and the ability to provide continuous power could make it a compelling option for future energy generation on Earth. Modifications or alternative designs to the LUMEN system could be explored to optimize it for terrestrial use, potentially reducing the required number of spacecraft and improving its feasibility and cost-effectiveness.

9. Reliability, Availability, Maintainability and Safety Analysis

A Reliability, Availability, and Maintainability Study (RAMS) must be performed on the mission design, to identify potential issues or areas critical to the throughput of the mission operation. Moreover, the potential causes of losses of operational availability of the system are investigated.

9.1. Reliability

Of the 3 factors of the RAMS, the reliability of the system is an essential driver in the design process with ramifications in the philosophies of redundancy, safety margin and spacecraft reliability. With a lifetime of 25 years and a key requirement on the system reliability, redundancy had to be implemented in every subsystem design.

On a system level, each spacecraft is responsible for generating approximately 7.6 kW of power. If a singular satellite were to experience a catastrophic failure, the power generation responsibility of the single spacecraft would have to be shared amongst the rest of the constellation. The relation between the singular spacecraft reliability and system (constellation) reliability was modelled as an inverse binomial cumulative distribution function. This can be found in Equation (9.1).

$$\alpha \leq \sum_{k=0}^{b} \binom{n+b}{k} (1-p)^{n+b-k} \cdot p^{k} \tag{9.1}$$

In this equation, α is the system-level reliability, b is the amount of 'buffer' satellites (i.e. satellites that can fail without the mission being compromised) and is the running variable, k is the instance variable for the summation, and p is the probability of a satellite failing over the mission lifetime including the probability of a critical failure due to a micrometeoroid impact. The latter is described in Section 6.7.2, and was found to be 2.16%.

The output of the program identifies how many additional *buffer* spacecraft (b) are required to add to the constellation, given system-level reliability, spacecraft reliability, and the number of satellites the mission was sized for. The system reliability was set to be 0.95, as per requirement LMN.SAR.002. The spacecraft reliability is also essential in determining the number of buffer satellites necessary. This is complex as to determine this, the reliability of all components must be taken into account together with the interactions between the components as certain failures may cause a cascade of failures.

At this stage of the design, a component-level reliability analysis cannot be performed. Therefore, a statistical approach will be taken in modelling the reliability of the spacecraft. According to Castet and Saleh [122], spacecraft reliability can be modelled as a Weibull distribution. This distribution can be fit to reliability data of previous missions with an $R^2 = 0.92$ giving a relatively accurate estimation of the reliability of spacecraft. The equation in question is described by Castet and Saleh [122], and can be found in Equation (9.2)

$$R = e^{(-t/\theta)^{\beta}} \tag{9.2}$$

In this equation, R is the spacecraft reliability, θ and β are shape parameters of the distribution, and t is the lifespan of the mission. The shape parameters were empirically determined to be $\theta = 0.3875$ and $\beta = 8316$. For a nominal mission lifetime of 25 years, as is the case for LUMEN, the spacecraft reliability is 0.9. This reliability was subsequently used in Equation (9.1) to determine the required buffer, where $p = 1 - R$.

Having the reliability values necessary for Equation (9.1), the buffer can be determined. As no closed form of the inverse binomial cumulative distribution function exists, the buffer is determined by looping through different buffer sizes. Whenever the associated α level equals or exceeds the required system-level reliability (0.95), the respective buffer size is returned. Adding satellites to the buffer increases the scenarios in which the mission is still successful. For example, a system with a buffer

of 8 satellites contains nine scenarios that are acceptable, being zero failures up to and including the failure of all eight buffer satellites. An important note is that the buffer satellites do not differ from the 'normal' satellites; they are fully functional satellites that perform at an equal level, and no specific satellite is necessarily labelled as being a *buffer satellite*. Depending on the wishes of the client, the additional spacecraft can be employed in two ways.

One method is to set the extra satellites to a 'dormant' mode to minimise component degradation. It would then only be activated when an operational satellite fails. This has the benefit that the dormant satellite will perform better than the failed satellite due to less degradation and is less likely to fail. However, the dormant satellite is not used for power generation thus having unused resources and the possibility of not having been used at all at the end of the mission, in the case that other satellites do not fail.

The second method is to utilise all satellites that are in orbit, including the buffer satellites. This has the benefit of additional power reaching the receiver that can then be used. The downside of this method is that the buffer satellites will experience increased degradation compared to the previous method and that their reliability is thus lower compared to the dormant satellites.

It is up to the client to decide what method they prefer, trading additional power for the increased probability of mission success. A hybrid option is, of course, also possible where some satellites are dormant and some are active, striking a balance between optimal resource utilisation and reliability.

For the configuration used in the LUMEN system, the required reliability is specified by requirement LMN.SAR.002, is 0.95, and the satellite reliability, as previously described, is 0.90. This gives a buffer size of 25 to reach the required system reliability. This buffer, of course, affects the mission cost. A detailed description of the financial considerations can be found in Section 7.1.2.

9.1.1. Subsystem Reliability

On a subsystem level redundancy is integrated differently. For example, for GNC there are 2 of each sensor, avoiding any chance of single points of failure. As for AOCS, redundancy is implemented by using a 4-wheel reaction wheel assembly, as well as using four 3-axis thruster components, hence providing redundancy in all axes. In the TT&C subsystem, two of each component are implemented, except for the RF Distribution Network. For the command and data handling subsystem, two complete PCBs are implemented in the spacecraft. Each board contains extra storage for redundancy reasons, also accounting for cycling degradation reliability. As for the EPS subsystem, a total of 4 batteries are required to maintain the S/C subsystems in eclipses of which two are added as margins. In the collector of the payload design, it is ensured that all photovoltaic cells are placed in parallel so that no cell failure leads to inoperative sets of cells. The reliability of the transmission part is increased by having a large number of smaller laser modules, instead of a single large component, hence, allowing for an additional

For other subsystems, such as Structures, Thermal and Propulsion, a different approach is adopted. Here the complexity of the subsystem is reduced as much as possible, favouring simplicity. This is similar to the well-known philosophy of SpaceX "The best part is no part". By strongly decreasing the number of parts, the inter-dependencies of mechanisms and subsystem components are kept to a minimum, reducing the propagation possibilities of failures. Moreover, designing for fewer parts allows for a more detailed analysis of the performances of the design with margins.

9.1.2. Factor of Safety

Factors of safety or safety margins are essential in engineering design to design with a margin over the predicted loads and are the core philosophy for redundant design.

Furthermore, there are many aspects to consider when implementing a safety factor, such as design maturity, system environment, agency policies, etc. ECSS Secretariat ESA-ESTEC [123] was consulted to verify which factors were to be considered and with what magnitude to implement the safety factor. When designing for loads, [123], prescribes the implementation of a model factor - K_M - that takes into account the accuracy of mathematical models, project factor - K_P - that takes into account project maturity and possible evolution, qualification test factor - K_Q - that defines the qualification

test loads. Other factors mentioned in [123] are the margin policy factor - the margin applied to launch vehicles to account for the policy margin of the mission - and also the acceptance test factor (analogous to the qualification test factor). Nevertheless, the margin policy factor does not apply to the system design and the acceptance test factor is equal to 1 if the qualification factor is already included when looking at global flight loads on the satellite. Therefore, the factor of safety for limit load design is Section 9.1.2.

As for the magnitudes of the factors, [123] recommends minimum values that then evolve over time. For example, a model factor of 1.2 is recommended at the beginning of satellite development, and can progressively be reduced to 1. As for the qualification test factor, [123] prescribes a magnitude of 1.25 when analysing the global flight loads of a satellite. Finally, the project factor is not prescribed but outlines areas to consider to size this factor. For this project, an initial project factor of 1.5 is implemented due to the low maturity of the design and the flexibility of the specifications of the design. At an early stage, this magnitude allows for a programmatic margin that can then spare potential for growth for the system. However, during the development of the project, the project factor magnitude, especially for subsystem designs not directly involved with loads, is decreased to 1.2. This is because as the mass budget stabilises and the design consolidated, the confidence of the specifications grows.

$$K = K_M \times K_P \times K_Q = 1.2 \times 1.5 \times 1.25 = 2.25$$

For various aspects within the subsystem design that do not directly relate to the loads of the satellite, the project factor is used as the driving safety factor. As mentioned before the safety margin at the advanced design stage is thus 1.2.

9.2. Availability

Further key items for the RAMS analysis are the considerations about the availability of the designed system. A driving requirement for the system is the requirement that 1MW is to be transmitted uninterruptedly for the mission's lifetime. Therefore, the availability shall be constant. However, as discussed in Chapter 5, during the mission lifetime, there will be Earth eclipses, shadowing the spacecraft and blocking the transmission possibilities by the satellites. These eclipses have a period of at most 4.94 h where no sunlight is available during transmission. To account for this, a system on the lunar surface must be in place to mitigate this unavailability of power.

However, storing 4.94 MW h is not trivial. If this were to be stored using $141\,\mathrm{W\,h\,kg^{-1}}$ lithium-ion batteries (as is on the spacecraft), a total battery mass of $97\,322.75$ kg would be needed. Another option is to consider the In-Situ-Resource-Utilisation (ISRU) of the lunar regolith to store energy. This would consist of heating up the lunar regolith, which would retain the heat during the eclipse. Then, using a Stirling engine, the heat would be converted to electricity. A study by Universitat Politècnica de Catalunya-BarcelonaTech [124] has come up with a system for 10 kW with a mass of $18\,919$ kg. Scaling this up to 1 MW would result in a mass of about $733\,813$ kg, as not all aspects of the system scale linearly.

As can be seen, storing 1 MW would require masses in the same order of magnitude as the whole LUMEN system. Therefore, some mitigation strategies must be considered. For instance, the ISS power usage is 75 - 90 kW[82]. If it is assumed that the life support system of a moon base would be the most critical power user, a possible assumption could be to lower the power provision to 100 kW. In this case, 9734.65 kg of batteries would be needed. This could fit within the launch of the receiver to the lunar surface.

Therefore, as a business case, a singular payload-bearing Starship could be launched, including both the receiver and the batteries for eclipse periods. According to EnerVenue CEO Jorg Heinemann, space-grade batteries can cost as much as $\$20,000$ per kW h[83], which converted to Euros is $18,320$

[82] URL: https://www.edn.com/international-space-station-iss-power-system/#:~:text=The%2075%20to%2090%20kilowatts,than%2040%20homes%20on%20Earth. [Cited 18/06/2023]

[83] URL: https://www.powermag.com/battery-technology-used-in-outer-space-could-be-a-gamechanger-on-earth/#:~:text=The%20batteries%20used%20in%20space,%2FkWh%2C%20according%20to%20Heinemann. [Cited 21/06/23]

€/kWh. Applying this to the aforementioned batteries with a rating of $494\,\text{kW h}$ the batteries alone would cost $9,050,080$ €. Using the cost estimation mentioned in Section 4.1.3 and the receiver diameter of 90m, the cost of the receiver would total $1,100,000$ €. To both of these costs, the launch costs need to be added, which attribute to the original launch and 3 launches for in-orbit refuelling. The refuelling is necessary especially for this payload-bearing Starship to land on the Moon. As of [7], the cost per launch for Starship is $\$10$ million, which converted equates ≈ 9.16 million €. Finally, the total cost for a customer for the receiver and batteries is 19.31 million € for continuously available power.

9.3. Maintainability

Maintainability as a concept can be defined in many ways, depending on the perspective. For this project, maintainability is defined as the ability of a system to regain operational capacity and hence is analysed below with this definition.

As to maintenance, there are not many feasible maintenance strategies for LUMEN, as the system is orbiting the Moon. While a lunar base might be present, additional launch capabilities cannot be assumed available. Launching robotic or manned missions from the Earth for repairs is costly and most likely more expensive than sending replacement satellites, as the technology for repair is not developed at this moment. Manned missions that are intended for the lunar base are not designed for such repair missions and can, thus, not be considered a feasible maintenance strategy.

The LUMEN spacecraft do possess software maintenance capabilities as software updates can be transmitted to the spacecraft via the communication subsystem. Storage space onboard the spacecraft is reserved for potentially increased operating system size. While these updates are limited to virtual changes, they may affect the operation parameters of certain components that could, for example, reduce usage degradation. This is of course not as effective as repair or replacement, it is both faster and less expensive.

Moreover, under the definition of maintainability provided above, the software department of the spacecraft possesses further responsibilities. The ability to regain the operational capacity of the system is essential, both for the performance of the constellation, as well as for the safety with regards to the other spacecraft in the same orbit. Therefore, a clear consideration of the safe modes of the satellites is made and their status is consistently monitored. Moreover, despite the integration of verified, validated and quality-assured software onboard the S/C, a commitment is made to regain operation of the system within 1 orbital period ($21.03\,\text{h}$), of the first loss of operation.

In terms of orbit maintenance, the spacecraft is not equipped with propellants for station-keeping manoeuvres. Hence, the orbit naturally oscillates during its lifetime. No additional maintenance is required as the system was designed to perform within the bounds of these natural oscillations.

Should launch capabilities from the lunar surface be available for either manned repair missions or servicing robots these can be considered for maintenance. Due to weaker gravity at the moon and the shorter trip distance, servicing satellites is substantially cheaper and therefore possibly cheaper than sending a replacement. However, as this assumption cannot be substantiated it was not considered for maintainability.

Important to note is that 'buffer' satellites were taken into account to achieve the system-level reliability, as described in Section 9.1. These additional satellites can experience a critical failure without compromising the mission objective. While any failures should be kept to a minimum, servicing the failed satellites is not essential in keeping the system nominal.

It is clear that the spacecraft were not designed for maintainability. Rather, the system was designed to operate nominally taking into account the degradation and reliability over the lifetime of the system.

9.4. Safety

Within this project, safety is defined as the probability of harming something or someone within the lifetime of the mission. On top of this, various considerations can be made with regard to spacecraft safety, inter-spacecraft safety, receiver safety and environmental safety. All of the mentioned topics are addressed in detail below.

Firstly, the spacecraft design not only considers reliability, but also safety of the spacecraft from external disturbances. For example, in Section 6.3 the design of the CD&H subsystems considers the effects of external radiation and the possible consequence of bit flipping. This is taken into consideration by selecting radiation-hardened components. Moreover, in Section 6.7 the structure design is developed, considering also the impact of micro-meteoroids, hence integrating additional thickness as an impact protection layer. Thus, the design is strengthened for externally-caused failures.

As to inter-spacecraft safety, both in Chapter 5 and Section 6.2, analyses are performed as to the distance between the spacecraft, the spacecraft position knowledge box and the possibility of object avoidance manoeuvres. These analyses finalise themselves with the aforementioned commitment in Section 9.3 on the ability to regain the operational capacity of each spacecraft within a given time. These are all considerations to enhance the safety of spacecraft in the same orbit.

Considering the definition of safety, environmental safety is a critical consideration to be made with regard to the mission. For this, an End-Of-Life plan has been developed to dispose of the system safely, with limited implications for the lunar environment. For the details of this EOL plan see Section 5.5.1. Within this plan, the Gamow crater is used as a debris graveyard. This heavily concentrates the waste material and maximises the distance from the south-pole lunar assets. Being so far from the lunar base on the south pole ensures also the safety of any equipment and instrumentation that could be affected by the debris produced from the de-orbiting manoeuvres.

The main safety concern of the mission is the high-power laser that is being beamed down to the lunar surface. Due to the wavelength of the laser ($976\,\text{nm}$), this can already pierce the cornea and reach the retina to cause permanent damage to the human eye[84]. Though the humans on the Moon would need a spacesuit with integrated optical filters on the glass, which would mitigate this danger. Moreover, the current terrestrial standards for outdoor laser use, are not of relevance, as these are mainly driven together with the aviation industry to limit the distractions or harms caused to pilots' eyes (see ANSI Z136.6: American National Standard for Safe Use of Lasers Outdoors). Nevertheless, of crucial importance is the intensity of the laser at the receiver, which on average is $\approx 150\,\text{W}\,\text{m}^{-2}$. This classifies the laser as a class 4 laser and has extreme implications for health safety with regard to humans. The skin may at no time come in contact with the laser. Moreover, any material within the area of the receiver must be protected and hardened, so as not to burn from the laser beam [85]. Therefore, no instrumentation or material that is not qualified to handle such intensities should remain at least $500\,\text{m}$ away from the receiver, and for human eye safety at least $710\,\text{m}$ away[86].

[84] https://www.nasa.gov/sites/default/files/atoms/files/17_regulatory_considerations_laser_safety_and_the_emerging_technology_of_laser_communication_b_edwards.pdf [Cited 24/06/2023]

[85] URL: https://www.lasersafetyfacts.com/laserclasses.html [Cited 25/06/23]

[86] URL: https://www.lasersafetyfacts.com/laserclasses.html [Cited 25/06/23]

10. Requirement Compliance

In this chapter, the requirement compliance and the feasibility analysis will be performed. The requirement compliance will be done in the form of a compliance matrix, which indicates which subsystems adhere to the requirements and which do not. This compliance is done according to the updated requirements, meaning that the requirements discussed in Section 2.2.2 are struck out.

Figure 10.1: Requirement Compliance matrix

As can be seen, the cost requirements have not been met. This is due to the minimal knowledge about the project when this requirement was set up. Therefore, a renegotiation of the cost budget with the customer will be necessary.
Furthermore, the requirement to provide 1 MW is only partially met. While on average, 1 MW is provided, there will be eclipses where the power will be lowered to 100 kW, provided by batteries as discussed in Chapter 9.
Requirement LMN.LAU.011 has been coloured in yellow, as there is not sufficient information provided by the launch provider regarding the injection accuracy.
It can be concluded that for the mission to be feasible, the budget must be increased.

11. Future Developments

As the DSE is a phase-0 study, more work needs to be performed to realise the project. Key activities are identified to create a plan for the activities that should occur after the DSE. This is not limited to detailed designing but also includes manufacturing and production, and operations and logistics. In this chapter, a high-level project plan is described, together with the activities that should occur and what they entail.

11.1. Project Design & Development Logic

The project design & development logic shows the steps that will be executed in the post-DSE phases of the project before the operation starts. This information is systematically recorded in Appendix C. In this diagram, a description of activities is given in a time-wise order from top to bottom, with parallel activities next to each other on the horizontal axis. Regarding the LUMEN production, the assumption is made that the number of spacecraft is high enough to sustain a production line, like previously also done with large-amount-of-spacecraft missions such as SpaceX's Starlink.

When the DSE is finished and reviewed, the preliminary design, phase 0 and partly phase A will be done. To be compliant with the client, feedback then can be given. When feedback is implemented and the preliminary design is successful, the set-up for the detailed design can begin. In this stage, all preparations for design until production will be made. Afterwards, the mission will be designed in detail, the setup for ground, and launching operations will be done and regulatory compliance verification and validation will be done, to make sure the mission is legally accepted. Leading up, the detailed design will be fine-tuned with respect to the ground, and launching systems. This goes parallel with the set-up of the verification and validation methods and the set-up of the production methods. When these phases are finished, the critical design review will be done, and in case of failure, the detailed design will be redone.

After the critical design review, The production of the first spacecraft prototype will start. Parallel to this, both the subsystems and the assembled spacecraft will be verified and validated. This will also be done with respect to the receiver and the ground station, therefore most importantly testing the transmission system and communication system. When the verification is a success, the production line will start and the complete mission system will be manufactured. Parallel to this, the market strategy will be started to inform the public and also potential Lunar energy investors. Lastly, when the whole system is produced and verified, the acceptance review can be completed, giving a start to the actual mission operations.

Using the key events from the project plan and development logic, a schedule can be made to give a time indication of the length of the project. To identify the project phases and task dependencies, a Gantt Chart is made. The Gantt chart for the post-DSE activities can be found in Figure 11.1.

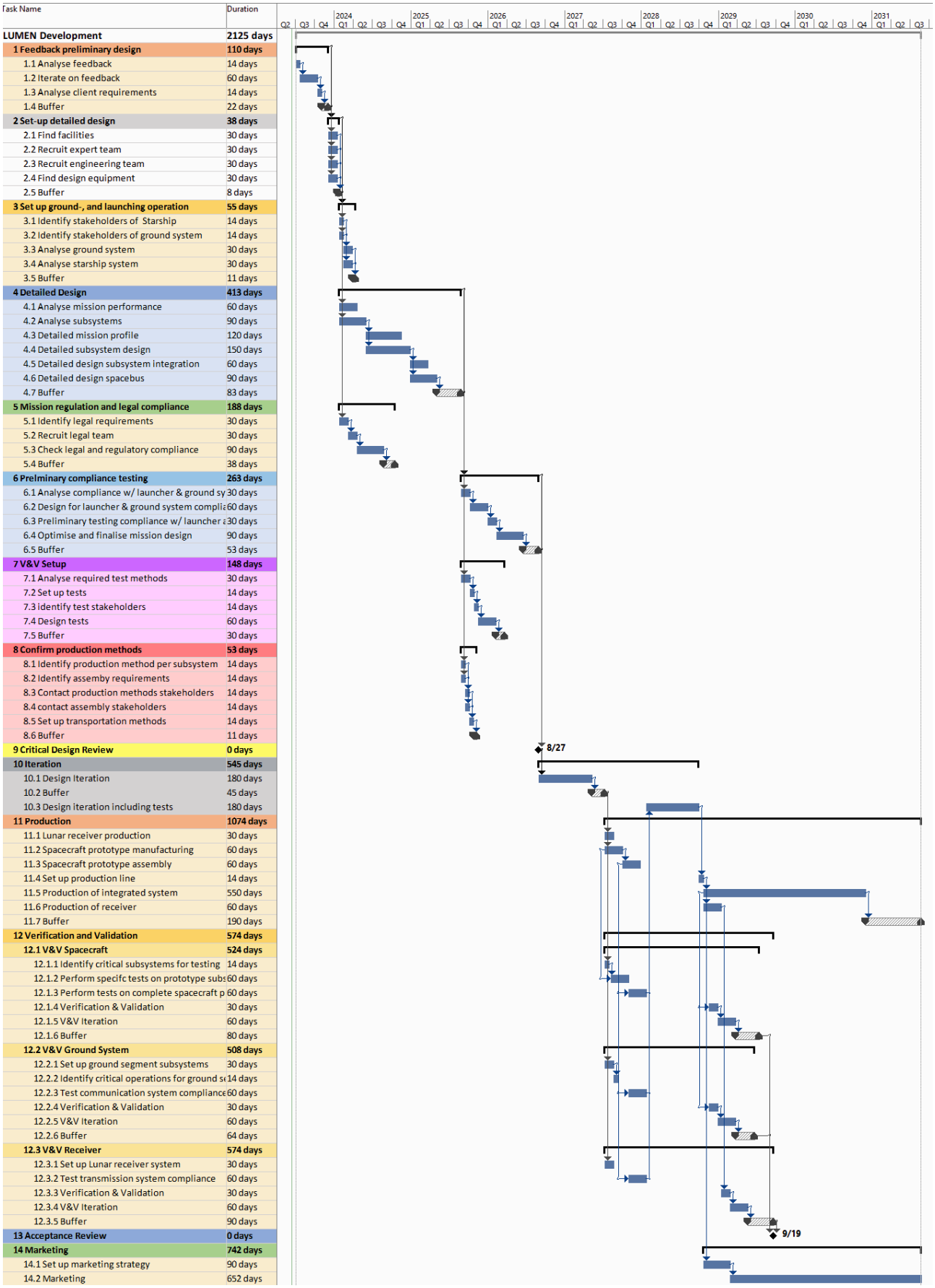

Figure 11.1: The Gantt Chart for the activities post-DSE until the Acceptance review (including iteration tasks in case of non-compliance).

11.2. Manufacturing, Assembly and Integration Plan

The manufacturing, assembly and integration plan is an important part of the mission development. The production of the LUMEN system has to be carefully planned, so no delays will happen and the planned maiden launch date of 2030 can be achieved. Next to this, any mistake in production can lead to catastrophic consequences for the mission, either in the manufacturing phase or in the operational phase.

In Figure 11.2 the Manufacturing, Assembly and Integration (MAI) flow can be seen. It starts with acquiring the materials needed to start the subsystem assembly, these will have to be transported (or delivered) to the manufacturing facilities. In the manufacturing phase, all the non-off-the-shelf parts will be manufactured and moved to a storage room. At the same time, the off-the-shelf components are acquired, transported and stored. From the storage, the sub-assemblies will be done, in which all the subsystems are to be assembled. All these assembled subsystems are mass and performance tested, to check whether they meet the specified requirements. From the results of the testing, the flow will either go on transport to the storage room or back to either the part manufacturing phase or the sub-assembly phase. If all tests are passed successfully, the sub-assemblies are collected in a storage room before starting the integration phase. If everything fits together and if the integration test is passed they will be assembled. From the assembly, they will be stored until the final testing phase can be started, in which the assembled system will undergo mass properties testing, vibration testing, acoustic testing, radiation testing, and thermal vacuum testing. The final tested assemblies are stored until they can move to the launch phase.

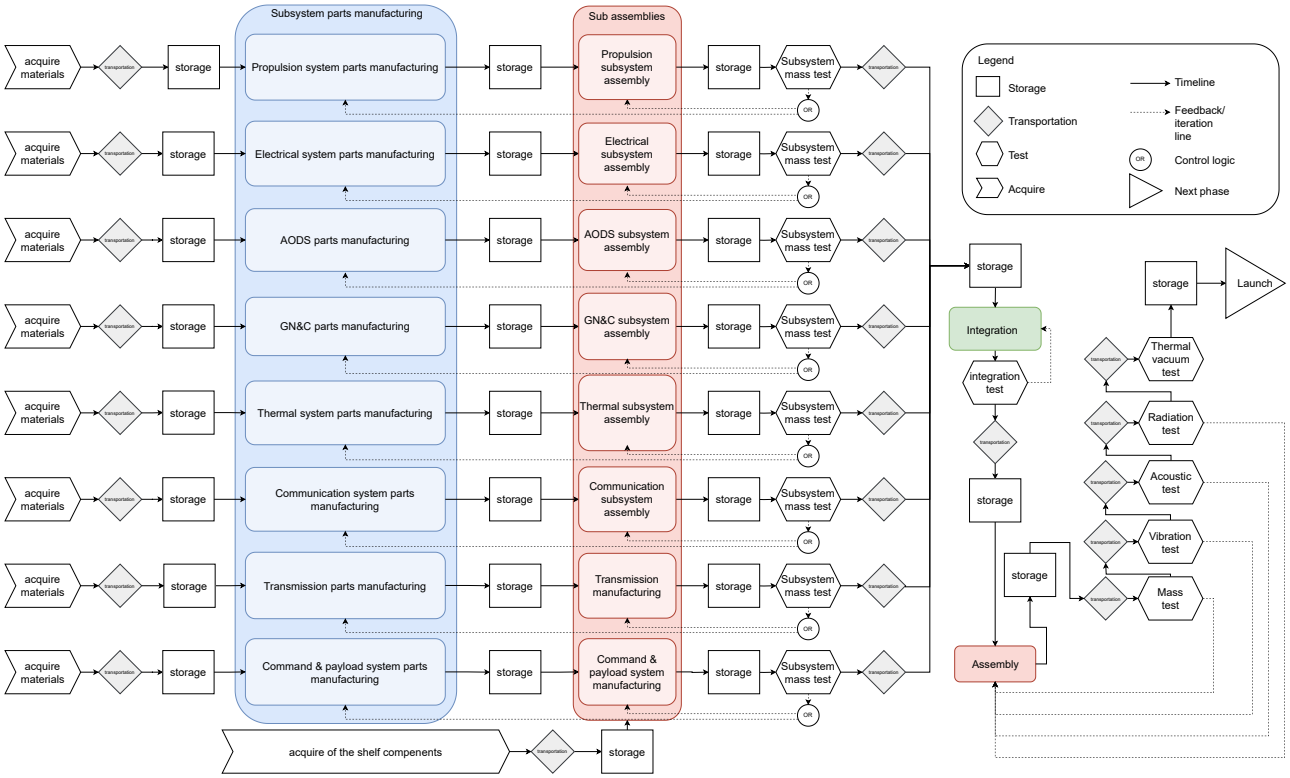

Figure 11.2: Manufacturing, Assembly and Integration Flow

11.3. Operations and Logistics

An operation flow diagram for the post-development phase, the phase starting from launch until EOL has been made to illustrate the operation communication flows. This diagram can be seen in Figure 11.3.

Estrack has been chosen as the main communication network and will have communication links with the launcher during the launch and transfer phase. For complete coverage, collaboration with DSN is also possible. During the insertion phase, the space segment will be released from the launcher and will start its operations after deployment. In this phase Estrack or DSN will be in contact with both the

space segment, once deployed, and the launcher. During the operational phase, Estrack will receive health check info from the space segment and send commands to the space segment if needed. At the beginning of EOL Estrack send its final command to perform the EOL manoeuvre, after which no communication link will be present anymore.

The launcher ground station will keep a communication link while the launcher is still in use, and will only have a link with the launcher itself. After the insertion, the launcher is not connected to the space segment anymore, so other communication links with the launcher after insertion have not been taken into account in the scope of the LUMEN mission.

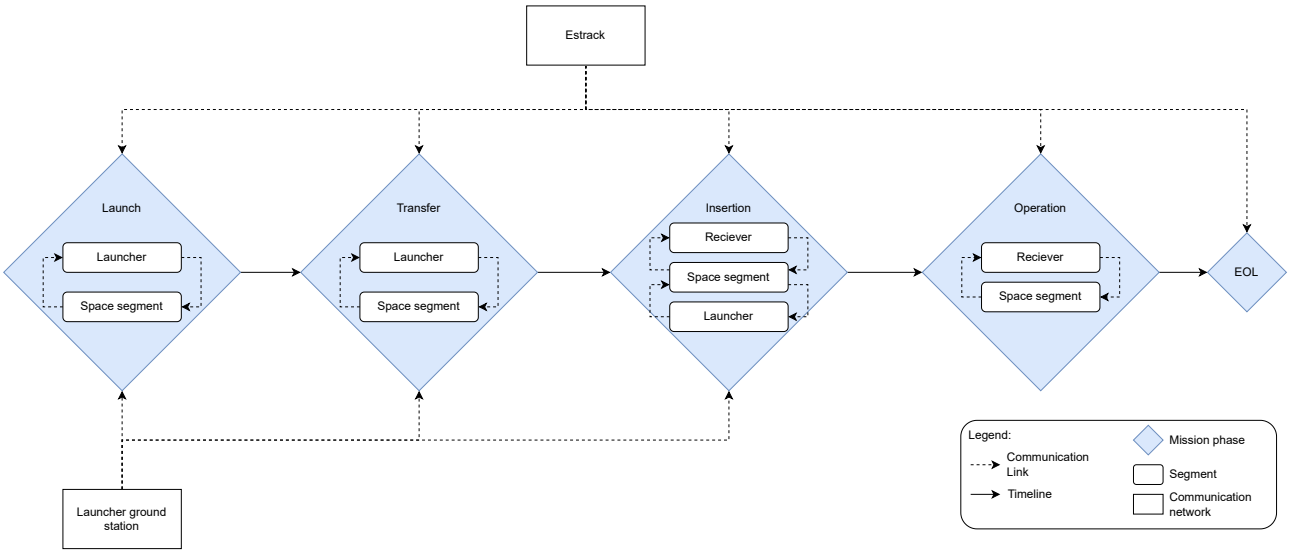

Figure 11.3: Operation flow diagram launch phase until EOL

11.3.1. SpaceX Launch Operations

During launch, the LUMEN team is placed within the spacecraft control centre, which has a live video, sound and data connection with the SpaceX launch control, located on the launch site. Here the LUMEN team can check the process of the launch, receive all the latest data and check up on the health of the LUMEN system.

The design of Falcon launch vehicle systems and operations incorporates the ability to engage in recycling procedures when deemed suitable. While each recycles occurrence and launch window demand are all unique, SpaceX vehicles and launch control and operation possess the capability to execute multiple recycles within a designated launch window, thereby eliminating some launch delays. Due to the current low TRL of the Starship, its operations have been assumed to be similar to the Falcon 9, which has a high TRL[87].

11.3.2. Estrack Operations

The ESA Estrack communication network has nine ESA-owned stations and the 3 other supporting cooperative stations, providing spacecraft support during both critical and routine mission phases, for multiple external users.[88] In order to coordinate the number of Estrack users and the network efficiently, an automated planning and coordination system is being developed by ESA, called the Estrack management system (EMS). Communication flow of the EMS can be seen in Figure 11.4[89]. With this management system, it is possible to plan all the necessary contact times and request the

[87] URL: https://www.google.com/url?sa=i&rct=j&q=&esrc=s&source=web&cd=&cad=rja&uact=8&ved=0CAIQw7AJahcKEwj4sYnX58f_AhUAAAAAHQAAAAAQAw&url=https%3A%2F%2Fwww.spacex.com%2Fmedia%2Ffalcon-users-guide-2021-09.pdf&psig=AOvVaw3VX_9-xObZDDP8Q6-CzScH&ust=1687005583731658 [Cited 16/06/2023]

[88] URL: https://www.eoportal.org/other-space-activities/estrack#estrack-esas-tracking-stations-network [Cited 16/06/2023]

[89] URL: https://www.esa.int/Enabling_Support/Operations/Introduction_to_the_ESTRACK_Management_System [Cited 16/06/2023]

use of the Estrack system.

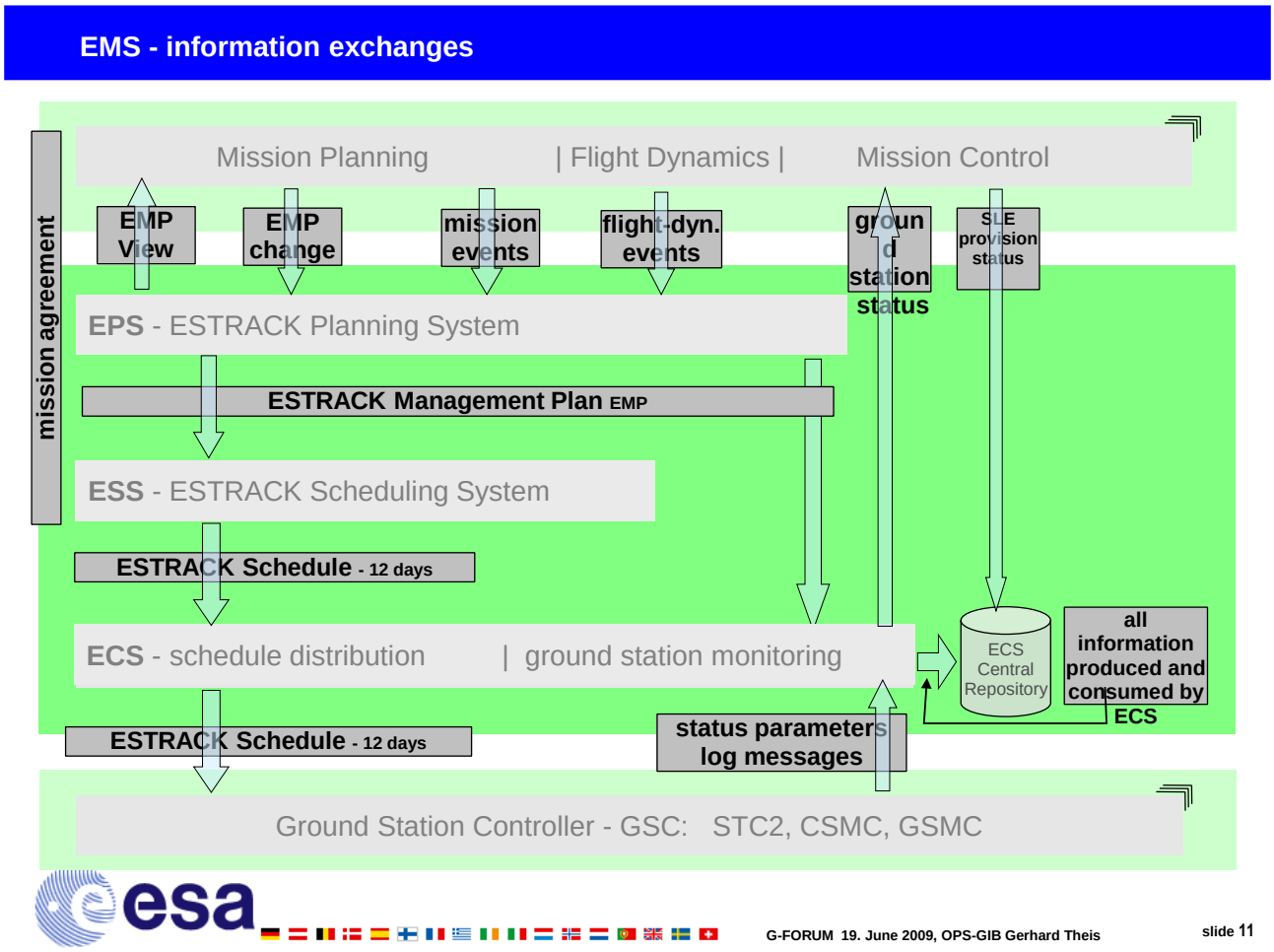

Figure 11.4: EMS information exchanges.

12. Conclusion & Recommendations

After 10 weeks, the team has finalised the design of a Space-Based Solar Power (SBSP) system for assets on the lunar south pole. This Phase A study was performed on request by the European Space Agency and the TU Delft. The mission name has been chosen to be LUMEN: Laser-based Uninterrupted Moon Energy Network.

The goal of the project was to design a SBSP system that provides 1 MW continuously for 25 years. The location of the receiver was identified to be the Shackleton crater on the lunar South Pole, which contains areas in permanent shadow, which may imply the presence of ice water. This makes it an interesting area to investigate by rovers or potentially a lunar base.

This concluding chapter encompasses the report's key conclusions, summarising the main findings. Moreover, it offers recommendations for future research endeavours.

12.1. Conclusion

After a thorough design trade-off, it was opted to use laser transmitters for beaming the power to the surface. While microwave transmission provides better transmitter and receiver conversion efficiencies (83 % and 83 % for microwaves versus 50 % and 40 % for lasers), they have a considerably larger divergence, increasing the receiver diameter on the Moon by at least an order of magnitude.

For the orbit, it was decided to place the spacecraft in a highly-elliptic frozen lunar orbit. In this orbit, the apoapsis passes above the lunar South Pole at a maximum altitude of $14\,041.79$ km. This way, more spacecraft are in view of the receiver at any time, requiring a lower power generation per spacecraft. As can be expected, this makes the required pointing accuracy for the laser more stringent.

Considering the number of spacecraft, an analysis based on mass, number of launches, and cost was performed to find the optimal number of spacecraft. Decreasing the number of spacecraft increases the required power generation per spacecraft and thus the solar array and thermal subsystem mass, which is less desirable. Conversely, increasing the number of spacecraft also increases the assembly, integration and testing costs, despite an application of a learning curve. Therefore, a middle point between these two had to be found, which was found to be 110. On top of this, 23 spacecraft were added as redundancy to meet reliability requirements. From this, the number of spacecraft that are in view at any time is 77.

Each spacecraft will collect 117 kW with its solar arrays and transmit the power down using 188 lasers. While only half of the lasers are used at a time, the other half is used when the first half has degraded. This increases the system efficiency considerably at the expense of double the laser module mass. With an end-of-life efficiency of 3.03 % from the incident sunlight on the spacecraft's solar arrays to the ground-based receiver, the dry and wet mass of each spacecraft is projected to be 888.92 kg and 1096.2 kg respectively.

12.2. Recommendations

While the concept of Space-Based Solar Power is not a new idea, considerable progress has been made since its inception and recently it has re-emerged as a point of interest for researchers. In the past, much of the technology necessary for such a system was not at the right technology readiness level yet. Furthermore, with a recent decrease in launch costs, the launch of large systems becomes more feasible year by year. Nevertheless, several recommendations can still be made regarding the level of certain technologies:

- It will be necessary to design some components specifically for this mission. In this design phase, many off-the-shelf components are considered. However, it is important to consider the development of low-mass, high-power components related to the electrical power system.
- The pointing accuracy of lasers is another important aspect to consider. The higher the accuracy, the smaller the receiver area, and the lower the potential launch costs.
- Due to the long mission time of 25 years, special considerations must be made for degradation and reliability. With this, it is important to consider the improvement of the laser module's

lifetime. In the design, the amount of necessary lasers is doubled to increase the end-of-life efficiency. This means that at all times, only half of all lasers are operating and the other half is unused mass. Therefore, the development of lasers that are able to operate in the lunar orbital environment for at least 25 years is recommended.

- The laser modules that are used as references in the design are generic components and are not proofed for space uses. Therefore, it is necessary to develop dedicated laser modules specifically designed for power transmission from orbit.
- To concentrate the laser beam, a telescope is used. However, unlike many other components of the system, this is not an already existing off-the-shelf component as it requires integrated cooling. Furthermore, it is recommended to optimise the telescope to minimise spherical aberration to keep the divergence low.
- In this design, the solar power was collected using solar arrays with an efficiency of around $30\,\%$. A possibility to circumvent this is the use of solar-pumped lasers. These turn sunlight directly into the laser, avoiding part of the around $70\,\%$ loss in power. Currently, however, the state-of-the-art solar pumped lasers only provide an energy density of $18\,\mathrm{W\,m^{-2}}$. Therefore, improvements in this technology could greatly help future SBSP systems.
- There will be eclipses of maximum $4.94\,\mathrm{h}$ (at most twice per year) where no power can be generated. In this report, a strategy was described in the case of these eclipses, where it was concluded to reduce the power provision to $100\,\mathrm{kW}$, just for life-support systems. This will be done through around $9700\,\mathrm{kg}$ of batteries. In the future, more research into power generation and thermal energy storage through lunar regolith can be useful, as currently, the specific power is still low, at $0.53\,\mathrm{W\,kg^{-1}}$ for a $10\,\mathrm{kW}$ generator.
- Lastly, for the subsequent design phases, it would be useful to optimise the high-inclination elliptical lunar frozen orbit.

Acknowledgements

Now that 10 weeks have passed and the Design Synthesis Exercise comes to an end, we want to express our deepest appreciation to our tutor, Dr Angelo Cervone for providing substantial support during all phases of the DSE. We would also like to thank our Coaches, Dr Nan Yue and PhD. candidate Guanqun Xu, for their meaningful contributions. Next, we want to express our gratitude to our customer, Dr Sebastien Vincent-Bonnieu from the European Space Agency, for taking his time to attend our meetings and providing useful input in our design choices. Finally, we would like to express our gratitude to Yannick Heumassej, who generously offered his expertise in many of our project's aspects.

Next to that we also want to thank several other people for their help:

- Alessandro Battegazzore, for his help with project management and systems engineering aspects of the project.
- Joshua Spaanders, for his expertise in lasers and their pointing systems.
- Assistant Prof. Pierre Piron for his aid with the optical systems.
- Prof. Jian Guo, for his help with the Guidance, Navigation & Control system.
- Prof. Stefano Speretta, for his help with the Guidance, Navigation & Control system.
- Mark O'Neill (`https://www.markoneill.com/`), for his expertise in concentrated photovoltaics and laser power beaming.
- Prof. Erwin Mooij and Prof. Ron Noomen, for their expertise in astrodynamics.
- Emre Halici, for sharing his practical satellite cost expertise.
- Ines Uriol Balbin, for sharing expertise on spacecraft structural design.
- Prof. Sergio Turteltaub, for aiding with advice on vibrational analysis.
- Prof. Piero Colonna and PhD candidate Dabo Krempus, for sharing their epertise on thermodynamics.

Bibliography

[1] O'Neill, M., McDanal, A. J., Brandhorst, H., Spence, B., Iqbal, S., Sharps, P., McPheeters, C., Steinfeldt, J., Piszczor, M., and Myers, M., "Space photovoltaic concentrator using robust Fresnel lenses, 4-junction cells, graphene radiators, and articulating receivers," Institute of Electrical and Electronics Engineers Inc., 2017. doi: 10.1109/PVSC.2017.8366274.

[2] Brandhorst, H., Piszczor, M. F., O'neill, M. J., Eskenazi, M. I., and Brandhorst, H. W., "Stretched lens array (SLA) photovoltaic concentrator hardware development & testing," , 2003. URL https://www.researchgate.net/publication/224749074.

[3] Cierny, O., "Precision Closed-Loop Laser Pointing System for the Nanosatellite Optical Downlink Experiment," , 2017.

[4] Guijarro, J., Auriol, A., Costes, M., Jayles, C., and Vincent, P., "MWR and DORIS-Supporting Envisat's Radar Altimetry Mission Figure 3. The MWR radio-frequency (RF) front-end (courtesy of EMS) Figure 2. The 36.5 GHz Dielectric Resonator Oscillator (DRO) (courtesy of COMDEV)," , 2000.

[5] Janssen, E., Kok, K., Korycki, J., Maximchuk, M., Pauwels, E., Pulimeno, A., Scaglioni, M., Schramade, D., Simoens, M., and Teixeira Pijpers, T., "Project Plan AE3200 Design Synthesis Exercise - Group 27," , 2023.

[6] Janssen, E., Kok, K., Korycki, J., Maximchuk, M., Pauwels, E., Pulimeno, A., Scaglioni, M., Schramade, D., Simoens, M., and Teixeira Pijpers, "Baseline Report - Group 27," , 2023.

[7] Janssen, E., Kok, K., Korycki, J., Maximchuk, M., Pauwels, E., Pulimeno, A., Scaglioni, M., Schramade, D., Simoens, M., and Teixeira Pijpers, T., "Midterm Report LUMEN: Laser-based Uninterrupted Moon Energy Network Final Version," , 6 2023.

[8] Masse, R. K., Allen, M., Driscoll, E., Spores, R. A., Arrington, L. A., Schneider, S. J., and Vasek, T. E., "AF-M315E propulsion system advances & improvements," American Institute of Aeronautics and Astronautics Inc, AIAA, 2016. doi: 10.2514/6.2016-4577.

[9] Thomson, B. J., Bussey, D. B., Neish, C. D., Cahill, J. T., Heggy, E., Kirk, R. L., Patterson, G. W., Raney, R. K., Spudis, P. D., Thompson, T. W., and Ustinov, E. A., "An upper limit for ice in Shackleton crater as revealed by LRO Mini-RF orbital radar," Geophysical Research Letters, Vol. 39, No. 14, 2012. doi: 10.1029/2012GL052119.

[10] Schlüter, L., and Cowley, A., "Review of techniques for In-Situ oxygen extraction on the moon," Planetary and Space Science, Vol. 181, 2020, p. 104753. doi: 10.1016/j.pss.2019.104753.

[11] Haruyama, J., Ohtake, M., Matsunaga, T., and Morota, T., "Lack of Exposed Ice Inside Lunar South Pole Shackleton Crater," Science, Vol. 322, No. 5903, 2008, pp. 938–939. doi: 10.1029/2007GC001743.

[12] Fathi-Hafshejani, P., Soltani-Tehrani, A., Shamsaei, N., and Mahjouri-Samani, M., "Laser incidence angle influence on energy density variations, surface roughness, and porosity of additively manufactured parts," Additive Manufacturing, Vol. 50, 2022, p. 102572. doi: 10.1016/j.addma.2021.102572.

[13] Algora, C., García, I., Delgado, M., Peña, R., Vázquez, C., Hinojosa, M., and Rey-Stolle, I., "Beaming power: Photovoltaic laser power converters for power-by-light," , 2 2022. doi: 10.1016/j.joule.2021.11.014.

[14] Fafard, S., and Masson, D. P., "74.7% Efficient GaAs-Based Laser Power Converters at 808 nm at 150 K," Photonics, Vol. 9, No. 8, 2022. doi: 10.3390/photonics9080579.

[15] Sharma, R., "Effect of obliquity of incident light on the performance of silicon solar cells," Heliyon, Vol. 5, No. 7, 2019. doi: 10.1016/j.heliyon.2019.e01965.

[16] Allen, D. M., Schaffer, W. J., Jones, A. P. A., Murphy, D. M., and Piszczor, M. F., "The Scarlet Light Concentrating Solar Array," , 1996.

[17] Jenkins, P., Bentz, D., Barnds, J., and Binz, C., "TACSAT-4 solar cell experiment: Two years in orbit," Noordwijk, 2014.

[18] Piszczor, M., O'Neill, M., Eskenazi, M., and Brandhorst, H., "The Stretched Lens Array SquareRigger (SLASR) for Space Power," American Institute of Aeronautics and Astronautics, San Diego, California, 2006. doi: 10.2514/6.2006-4137.

[19] O'neill, M., Mcdanal, A. J., Landis, G., Pricone, R., Kumar, C., and Puglia, M., "Space PV Concentrators for Outer Planet and Near-Sun Missions, Using Ultra-Light Fresnel Lenses Made with Vanishing Tools," , 2019.

[20] Mceachen, M. E., Haynes, P., Peterson, C., Rodgers, W., Spink, J., Eskenazi, M., and Sharps, P., "Point-Focus Concentration Compact Telescoping Array EESP Option 1 Phase Final Report for Public Release," , 2019. URL http://www.sti.nasa.gov.

[21] Raya-Armenta, J. M., Bazmohammadi, N., Vasquez, J. C., and Guerrero, J. M., "A short review of radiation-induced degradation of III–V photovoltaic cells for space applications," , 12 2021. doi: 10.1016/j.solmat.2021.111379.

[22] ECSS Secretariat ESA-ESTEC, “Space engineering - Photovoltaic assemblies and components,” , 2022.

[23] Ebert, C., Guiney, T., Braker, J., Stapleton, D., Alegria, K., and Irwin, D., “High-power pump diodes for defense applications,” SPIE, 2017. doi: 10.1117/12.2265028.

[24] Könning, T., Ahlert, S., Weimar, J., Steinborn-Knuth, R., Ahnepohl, F., Kissel, H., Köhler, B., Klein, M., Liu, G., and Lehkonen, S., “Advances in fiber coupled high power diode laser modules at 793nm and 976nm for defense applications,” SPIE-Intl Soc Optical Eng, 2022. doi: 10.1117/12.2606176.

[25] Ebert, C., Guiney, T., Braker, J., Stapleton, D., Alegria, K., and Irwin, D., “Advances in the power, brightness, weight and efficiency of fiber-coupled diode lasers for pumping and direct diode applications,” SPIE, 2017. doi: 10.1117/12.2253116.

[26] Könning, T., Ahlert, S., Weimar, J.-N., Steinborn-Knuth, R., Ahnepohl, f., Kissel, H., Köhler, B., Liu, G., and Lehkonen, S., “Wavelength stabilized fiber coupled modules at 79x nm, 88x nm, and 97x nm with up to 600W output power based on single emitters,” SPIE-Intl Soc Optical Eng, 2021. doi: 10.1117/12.2577691.

[27] Häusler, K., Zeimer, U., Sumpf, B., Erbert, G., and Tränkle, G., “Degradation model analysis of laser diodes,” Journal of Materials Science: Materials in Electronics, Vol. 19, No. SUPPL. 1, 2008. doi: 10.1007/s10854-007-9534-8.

[28] Gale, P., “Estimating Laser Diode Lifetimes and Activation Energy Reference Estimating Laser Diode Lifetimes and Activation Energy,” , 2008. URL www.ilxlightwave.com.

[29] Jiménez, J., “Laser diode reliability: crystal defects and degradation modes,” Comptes Rendus Physique, Vol. 4, No. 6, 2003, pp. 663–673. doi: 10.1016/S1631-0705(03)00097-5.

[30] Gale, P., “Estimating Laser Diode Lifetimes and Activation Energy Reference Estimating Laser Diode Lifetimes and Activation Energy,” , 2008. URL www.ilxlightwave.com.

[31] Joyce, W. B., Liou, K. Y., Nash, F. R., Bossard, P. R., and Hartman, R. L., “Methodology of Accelerated Aging.” AT&T Technical Journal, Vol. 64, No. 3, 1985, pp. 717–764. doi: 10.1002/j.1538-7305.1985.tb00446.x.

[32] Nakatsu, Y., Nagao, Y., Kozuru, K., Hirao, T., Okahisa, E., Masui, S., Yanamoto, T., and Nagahama, S.-i., “High-efficiency blue and green laser diodes for laser displays,” SPIE-Intl Soc Optical Eng, 2019. doi: 10.1117/12.2505309.

[33] Smith, L., Benner, R., Gray, G., Pan, M.-W., and Rallison, R., “Raman spectroscopy apparatus and method using external cavity laser for continuous chemical analysis of sample streams,” , 2000.

[34] Asbury, C. G., Dorsky, L. I., Nerheim, N. M., Forouhar, S., Rider, D. M., Chu, E. Y., Fisher, B. M., Valencia, R. S., Montero, M. R., and Kane, T. J., “Space- and ground-based non-accelerated long lifetime data for ruggedized commercial NPRO lasers,” SPIE-Intl Soc Optical Eng, 2019. doi: 10.1117/12.2535964.

[35] Hoos, F., Li, S., Meyrath, T. P., Braun, B., Giessen, H., Moser, M., Biswal, S., Nees, J., Braun, A., Mourou, G. A., Johannsen, I., Giessen, A., Seeber, W., and Keller, U., “Thermal lensing in an end-pumpedYb:KGW slab laser with high powersingle emitter diodes,” Optics Express, Vol. 16, No. 9, 2008. URL http://www.ekspla.com/en/main/products/1/.

[36] Kaushal, H., and Kaddoum, G., “Applications of Lasers for Tactical Military Operations,” IEEE Access, Vol. 5, 2017, pp. 20736–20753. doi: 10.1109/ACCESS.2017.2755678.

[37] Ackermann, M. R., Mcgraw, J. T., and Zimmer, P. C., “Five lens corrector for Cassegrain-form telescopes,” , 2008.

[38] Keski-Kuha, R. A., Bowers, C. W., Quijada, M. A., Heaney, J. B., Gallagher, B., McKay, A., and Stevenson, I., “James Webb Space Telescope optical telescope element mirror coatings,” SPIE, 2012. doi: 10.1117/12.925470.

[39] Cierny, O., “Precision Closed-Loop Laser Pointing System for the Nanosatellite Optical Downlink Experiment,” , 11 2017.

[40] Han, W., Shao, S., Zhang, S., Tian, Z., and Xu, M., “Design and modeling of decoupled miniature fast steering mirror with ultrahigh precision,” Mechanical Systems and Signal Processing, Vol. 167, 2022. doi: 10.1016/j.ymssp.2021.108521.

[41] Lv, T., Ruan, P., Jiang, K., and Jing, F., “Modeling and analysis of fast steering mirror disturbance effects on the line of sight jitter for precision pointing and tracking system,” Mechanical Systems and Signal Processing, Vol. 188, 2023. doi: 10.1016/j.ymssp.2022.110002.

[42] E Siegman Edward L, P. A., “How to (Maybe) Measure Laser Beam Quality,” , 1997.

[43] Whitley, R., and Martinez, R., “Options for Staging Orbits in Cis-Lunar Space,” , 2015.

[44] Folta, D., and Quinn, D., “Lunar frozen orbits,” 2006. doi: 10.2514/6.2006-6749.

[45] Ely, T. A., “Stable constellations of frozen elliptical inclined lunar orbits,” , 7 2005. doi: 10.1007/bf03546355.

[46] Curtis H, “Orbital Mechanics for Engineering Students,” , 2005.

[47] Yang, K., Feng, W., Xu, L., and Liu, X., "Review of research on lunar dust dynamics," 2022. doi: 10.1007/s10509-022-04094-x, URL http://arxiv.org/abs/2207.13883http://dx.doi.org/10.1007/s10509-022-04094-x.

[48] Martin, M., Houghton, B., Craig, M., Tooley, R., Richard, M., and Saylor, S., "Mission Design and Operations Considerations for NASA's Lunar Reconnaissance Orbiter," , 2007.

[49] Ellegood, E., Eleazer, W., For, C. A., Wayne Eleazer, B., and Ellegood, E., "Challenges For A South Texas Spaceport Challenges For A South Texas Spaceport Safety Challenges for a South Texas Spaceport," , 2014. URL https://commons.erau.edu/stm/2014/wednesday/17.

[50] Janssen, E., Kok, K., Korycki, J., Maximchuk, M., Pauwels, E., Pulimeno, A., Scaglioni, M., Schramade, D., Simoens, M., and Teixeira Pijpers, T., "Project LUMEN - System and subsystem requirements," , 2023.

[51] SpaceX, "Starship Users Guide," , 2020.

[52] Guardabasso, P., Lizy-Destrez, S., and Ansart, M., "LUNAR ORBITAL DEBRIS MITIGATION: CHARACTERISATION OF THE ENVIRONMENT AND IDENTIFICATION OF DISPOSAL STRATEGIES," , 2021. URL http://conference.sdo.esoc.esa.int,.

[53] Hughes, S. P., Qureshi, R. H., Cooley, D. S., Parker, J. J., and Grubb, T. G., "Verification and validation of the general mission analysis tool (GMAT)," American Institute of Aeronautics and Astronautics Inc., 2014. doi: 10.2514/6.2014-4151.

[54] Carpenter, J. R., and Alfriend, K., "NAVIGATION ACCURACY GUIDELINES FOR ORBITAL FORMATION FLYING," , 2003.

[55] Wertz, J. R., Larson, W. J., Kirkpatrick, D., and Klungle, D., Space mission analysis and design, Microcosm, 1999.

[56] Rinard, L. A., Chapman, E. L., and Ringler, S. C., "Reaction Wheel Supplier Survey," , 2011.

[57] AccuBeat, "Ultra Stable Oscillator (USO) for Deep Space Exploration," , 2023. URL http://www.accubeat.com.

[58] Terma, "T1 Star Tracker," , 2023.

[59] Honeywell, "HG9900 Inertial Measurement Unit," , 2018.

[60] S. Schmidt, "SatCatalog_-_Lens_RD_-_BiSon64-ET-B_-_Datasheet," 2018.

[61] Mazarico, E., Rowlands, D. D., Neumann, G. A., Smith, D. E., Torrence, M. H., Lemoine, F. G., and Zuber, M. T., "Orbit determination of the Lunar Reconnaissance Orbiter," Journal of Geodesy, Vol. 86, No. 3, 2012, pp. 193–207. doi: 10.1007/s00190-011-0509-4.

[62] AAC Clyde Space, "satsearch_datasheet_uqbcoq_aac-clyde_tx-2400," , 2023.

[63] KUHNE electronic, "S-Band KU PA 200270-10 A, GaN-HEMT Power Amplifier," , 2023.

[64] KUHNE electronic, "OMNI-A0142 High Gain S-Band Omni," 2023.

[65] AAC Clyde Space, "satsearch_datasheet_fnjp6v_aac_clyde_ac_2000," , 2023.

[66] AAC Clyde Space, "satsearch_datasheet_vh696v_aac-clyde_rx-2000," , 2022.

[67] Cierny, O., and Cahoy, K. L., "On-Orbit Beam Pointing Calibration for Nanosatellite Laser Communications," , 2018. URL https://hdl.handle.net/1721.1/124154.

[68] Figura, J., Haughwout, C., Cahoy, K., Welle, R., Hardy, B., Pack, D., and Bosh, A., "Initial Demonstration of an Uplink LED Beacon to a Low Earth Orbiting CubeSat," , 2018. URL www.jossonline.com.

[69] Micron Technology Inc., "Image sensor 1/2.5-inch 5-Mp digital image sensor data sheet," , 2006.

[70] Balluff, "MATRIX VISION Industrial Cameras mvBlueFOX-IGC Series-Standard," , 2023. URL www.balluff.com.

[71] Imaging Corporation, A., "MT9J003: 1/2.3-Inch 10Mp CMOS Digital Image Sensor Features Aptina Confidential and Proprietary," , 2023. URL www.aptina.com.

[72] Basler, "Ace data sheet," 2023.

[73] RPMC Lasers, "455nm 5.5W Collimated Laser Diode High Power LD| High Power Output Power| Collimation Beam 450nm~455nm 5.5W LD | Small Compact Package| Blue Diode Laser RWSLD-455-5500m-K," , 2023.

[74] Celestron, "Advanced VX Telescope Series_Manual_5lang_2021," 2023.

[75] Edmund Optics, "prnt_65080," 2023.

[76] CCSDS, "Recommendation for Space Data System Standards TM SYNCHRONIZATION AND CHANNEL CODING RECOMMENDED STANDARD BLUE BOOK," , 2022.

[77] CCSDS, "Blue Book - TELECOMMAND - Part 3 Data Management Service Architectural Specification," , 1987. URL http://public.ccsds.org/publications/.

[78] Zandbergen, B. T. C., "AE1222-II Aerospace Design & Systems Engineering Elements I Part: Spacecraft (bus) design and sizing," , 2020.

[79] Joseph Lazio, "The Deep Space Network Radio Astronomy User Guide," , 2021.

[80] CCSDS, “Recommendations for Space Data System Standards RADIO FREQUENCY AND MODULATION SYSTEMS-PART 1 EARTH STATIONS AND SPACECRAFT,” , 2018.
[81] Speretta, S., “AE2111-II Aerospace Design and Systems Engineering Elements II Lecture S4 Spacecraft Telecommunications,” , 2021.
[82] Rickman, S. L., “A Simplified, Closed-Form Method for Screening Spacecraft Orbital Heating Variations,” , 2023.
[83] Rickman, S. L., “Introduction to On-Orbit Thermal Environments,” , 2014.
[84] Mermer, E., and Ünal, R., “Passive thermal control systems in spacecrafts,” , 3 2023. doi: 10.1007/s40430-023-04073-5.
[85] Deng, B., Yang, S., Xie, X., Wang, Y., Bian, X., Gong, L., and Li, Q., “Study of the thermal performance of multilayer insulation used in cryogenic transfer lines,” Cryogenics, Vol. 100, 2019, pp. 114–122. doi: 10.1016/j.cryogenics.2019.01.005.
[86] Koebel, M., Rigacci, A., and Achard, P., “Aerogel-based thermal superinsulation: An overview,” , 9 2012. doi: 10.1007/s10971-012-2792-9.
[87] Juhasz, A. J., “Design Considerations for Lightweight Space Radiators Based on Fabrication and Test Experience With a Carbon-Carbon Composite Prototype Heat Pipe,” , 1998.
[88] Cabeza, L. F., Castell, A., Barreneche, C., De Gracia, A., and Fernández, A. I., “Materials used as PCM in thermal energy storage in buildings: A review,” , 4 2011. doi: 10.1016/j.rser.2010.11.018.
[89] Wang, S., Hou, X., Yin, J., Xing, Y., and Wang, Z., “Comparative Study of the Thermal Enhancement for Spacecraft PCM Thermal Energy Storage Units,” Aerospace, Vol. 9, No. 11, 2022, p. 705. doi: 10.3390/aerospace9110705.
[90] Bierwagen, G. P., He, L., Li, J., Ellingson, L., and Tallman, D. E., “Studies of a new accelerated evaluation method for coating corrosion resistance-thermal cycling testing,” , 2000.
[91] Muratov, C. B., Osipov, V. V., and Smelyanskiy, V. N., “Issues of Long-Term Cryogenic Propellant Storage in Microgravity,” , 2011. URL http://www.sti.nasa.gov.
[92] Anflo, K., and Crowe, B., “In-space demonstration of an ADN-based propulsion system,” American Institute of Aeronautics and Astronautics Inc., 2011. doi: 10.2514/6.2011-5832.
[93] Spores, R. A., Masse, R., Kimbrel, S., and McLean, C., “GPIM AF-M315E propulsion system,” American Institute of Aeronautics and Astronautics Inc., 2013. doi: 10.2514/6.2013-3849.
[94] Gohardani, A. S., Stanojev, J., Demairé, A., Anflo, K., Persson, M., Wingborg, N., and Nilsson, C., “Green space propulsion: Opportunities and prospects,” , 11 2014. doi: 10.1016/j.paerosci.2014.08.001.
[95] Masse, R. K., Overly, J. A., Allen, M. Y., and Spores, R. A., “A new state-of-the-art in AF-M315E thruster technologies,” 2012. doi: 10.2514/6.2012-4335.
[96] Wilhelm, M., Negri, M., Ciezki, H., and Schlechtriem, S., “Preliminary tests on thermal ignition of ADN-based liquid monopropellants,” Acta Astronautica, Vol. 158, 2019, pp. 388–396. doi: 10.1016/j.actaastro.2018.05.057.
[97] Nosseir, A. E., Cervone, A., and Pasini, A., “Modular impulsive green monopropellant propulsion system (Mimps-g): For cubesats in leo and to the moon,” Aerospace, Vol. 8, No. 6, 2021. doi: 10.3390/aerospace8060169.
[98] Nosseir, A. E., Cervone, A., and Pasini, A., “Review of state-of-the-art green monopropellants: For propulsion systems analysts and designers,” Aerospace, Vol. 8, No. 1, 2021, pp. 1–21. doi: 10.3390/aerospace8010020.
[99] Wingborg, N., “Chapter Glossary,” , 2004.
[100] Anflo, K., Thormählen, P., and Persson, M., “Hot-Firing tests using a low temperature derivative of LMP-103S,” , 2013.
[101] James John, and Theo Keith, Gas Dynamics, 3rd ed., Pearson, Uppear Saddle River, new Jersey, 2006.
[102] Sutton, G. P., and Biblarz, O., ROCKET PROPULSION ELEMENTS, 9th ed., John Wiley & Sons, Hoboken, New Jersey, 2017.
[103] Rao, G. V. R., “Exhaust Nozzle Contour for Optimum Thrust,” Journal of Jet Propulsion, Vol. 28, No. 6, 1958, pp. 377–382. doi: 10.2514/8.7324.
[104] NASA, “NASA SPACE VEHICLE DESIGN CRITERIA (CHEMICAL PROPULSION),” , 1976.
[105] Timoshenko, S. P., “X. On the Transverse Vibrations of Bars of Uniform Cross-Section,” The London, Edinburgh, and Dublin Philosophical Magazine and Journal of Science, Vol. 43, No. 253, 1922, pp. 125–131. doi: 10.1080/14786442208633855.
[106] Rans, C., and Melkert, J., “Structural Analysis & Design Slides,” , 2022.
[107] Badyukov, D. D., “Micrometeoroids: The Flux on the Moon and a Source of Volatiles,” Solar System Research, Vol. 54, No. 4, 2020, pp. 263–274. doi: 10.1134/S0038094620040024.
[108] Grün, E., Zook, H. A., Fechtig, H., and Giese, R. H., “Collisional Balance of the Meteoritic Complex,”

Icarus, Vol. 62, No. 2, 1985, pp. 244–272. doi: 10.1016/0019-1035(85)90121-6.

[109] Christiansen, E. L., and Kerr, J. H., "Ballistic Limit Equations for Spacecraft Shielding," International Journal of Impact Engineering, Vol. 26, No. 1-10, 2001, pp. 93–104. doi: 10.1016/S0734-743X(01)00070-7.

[110] Hyder, A., Wiley, R., Halpert, G., Flood, D., and Sabripour, S., Spacecraft Power Technologies, Imperial College Press, 2000.

[111] Jackson, B., "XMM's Electrical Power Subsystem," , 12 1999.

[112] SpaceX, "Starship Users Guide," , 2023.

[113] Maiwald, V., and Westphal, B., "Critical Analysis and Review of Current Mars Mission Scenarios for SpaceX Starship Space Sustainability and Sustainable Development (S3D) View project Gravity-assist Optimization for Low-thrust Trajectories (GOLT) View project Critical Analysis and Review of Current Mars Mission Scenarios for SpaceX Starship," , 2022. URL https://www.researchgate.net/publication/363753314.

[114] Scatteia Luigi, and Perrot Yann, "Lunar market assessment: market trends and challenges in the development of a lunar economy," , 2021.

[115] International Energy Agency, "Projected Costs of Generating Electricity," , 2020.

[116] Schlissel, D., and Biewald, B., "Nuclear Power Plant Construction Costs," , 2008.

[117] Frazer-Nash Consultancy, "Space-Based Solar Power - A Future Soure of Energy For Europe?" , 2022. URL www.fnc.co.uk.

[118] Gong, M., and Wall, G., "Exergy analysis of the supply of energy and material resources in the Swedish society," Energies, Vol. 9, No. 9, 2016. doi: 10.3390/en9090707.

[119] Kerslake, T. W., "Lunar Surface-to-Surface Power Transfer," , 2007. URL http://www.sti.nasa.gov.

[120] Blake, C. H., and Shaw, M. M., "Measuring NIR Atmospheric Extinction Using a Global Positioning System Receiver," , 2011. URL http://www.naoj.org/Projects/HSC/index.html.

[121] Dakar, E., Golbraikh, E., Kopeika, N. S., and Zilberman, A., "Effect of the zenith angle on optical wave propagation in anisotropic non-kolmogorov atmospheric turbulence: A new experiment-based model," IEEE Transactions on Antennas and Propagation, Vol. 68, No. 8, 2020, pp. 6287–6295. doi: 10.1109/TAP.2020.2986720.

[122] Castet, J. F., and Saleh, J. H., "Satellite reliability: Statistical data analysis and modeling," Journal of Spacecraft and Rockets, Vol. 46, No. 5, 2009, pp. 1065–1076. doi: 10.2514/1.42243.

[123] ECSS Secretariat ESA-ESTEC, "ECSS-E-ST-32-10C," , 8 2019.

[124] Universitat Politècnica de Catalunya-BarcelonaTech, "Executive Summary Report - Lunar ISRU Energy Storage and Electricity Generation (LIESEG) project," , 2 2020.

Appendix A

Functional Flow Diagram

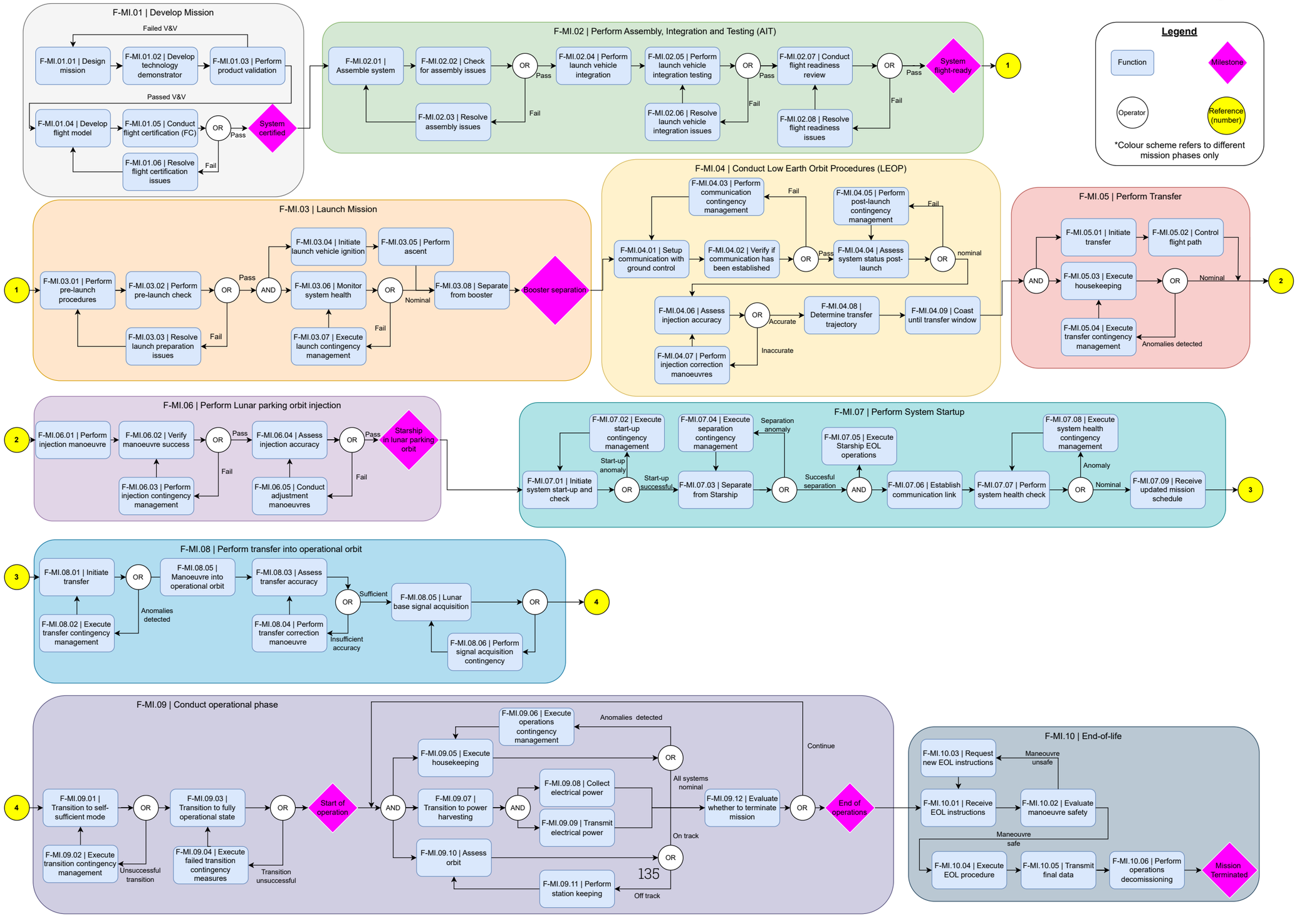

Figure A.1: *Functional Flow Diagram - Final report*

Appendix B
Functional Breakdown Structure

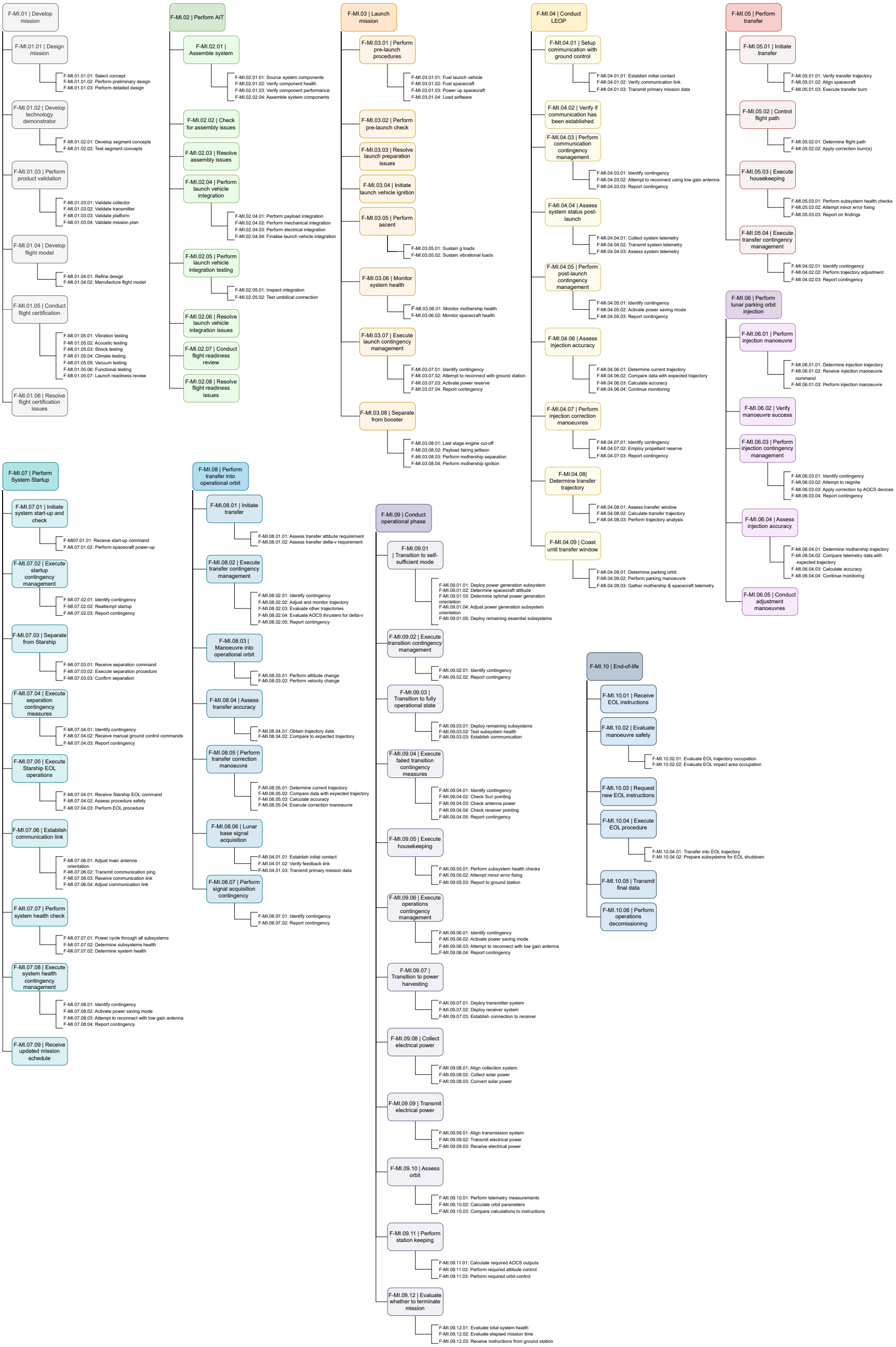

Figure B.1: *Functional Breakdown Structure*

Appendix C
Project Design & Development Logic

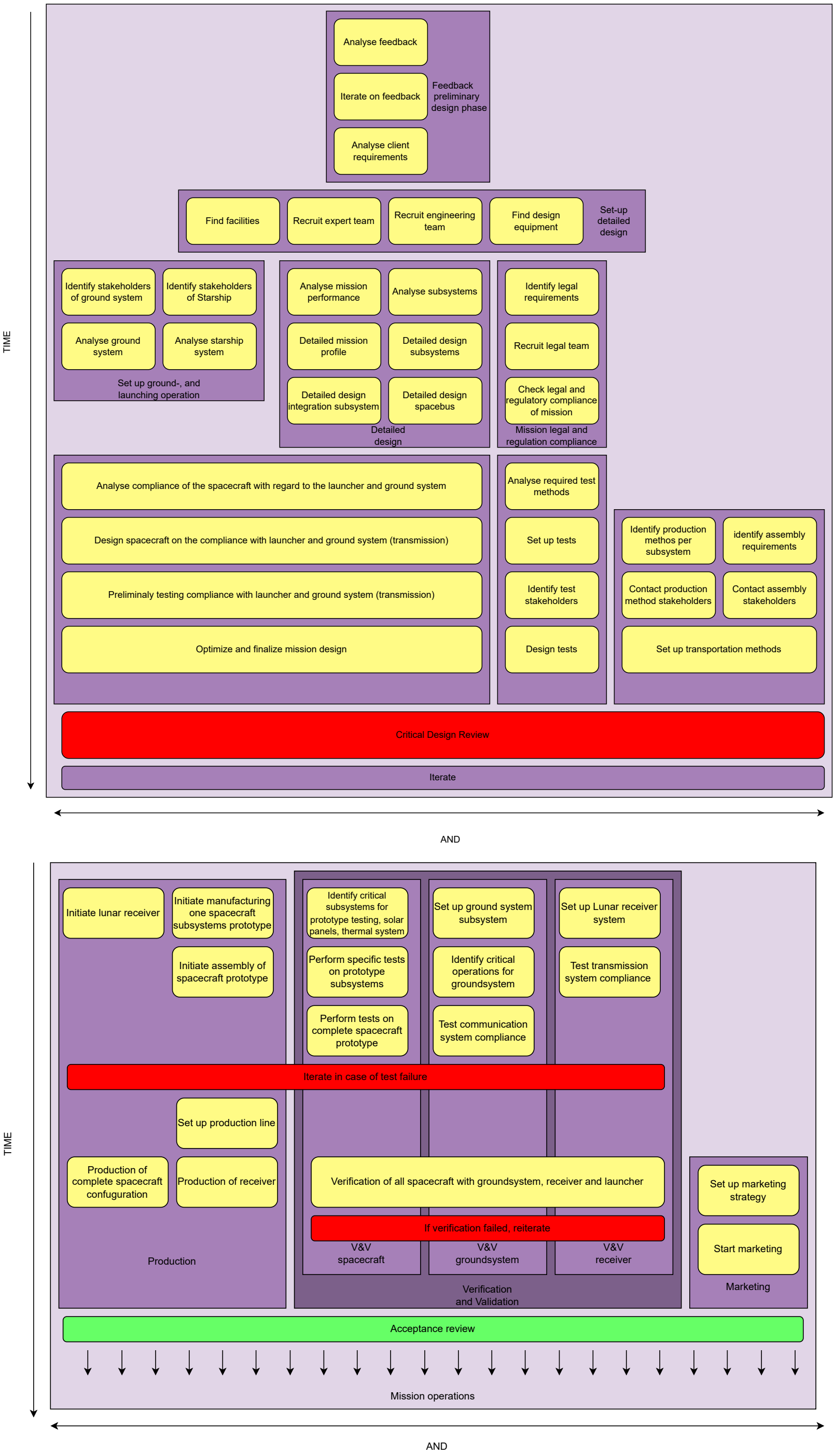

Figure C.1: *Project Design & Development Logic*